DESIGN, DEVELOPMENT AND ANALYSIS OF COMPACT MULTIPORT ANTENNA FOR ULTRA-WIDEBAND MIMO COMMUNICATIONS

Thesis submitted by

ROSHNA T. K.

in partial fulfilment of the requirements for the degree of

DOCTOR OF PHILOSOPHY

Under the guidance of

Prof. P. MOHANAN

Department of Electronics

Faculty of Technology

Cochin University of Science and Technology

Cochin - 682 022, Kerala, India

August 2018

Design, development and analysis of compact multiport antenna for ultra-wideband MIMO communications

Ph.D. Thesis under the Faculty of Technology

Author

Roshna T. K.
Centre for Research in Electromagnetics and Antennas (CREMA)
Department of Electronics
Cochin University of Science and Technology
Cochin - 682 022, Kerala, India.
Email: roshnatk03@gmail.com

Supervisor

Dr. P. Mohanan
Professor (UGC BSR)
Centre for Research in Electromagnetics and Antennas (CREMA)
Department of Electronics
Cochin University of Science and Technology
Cochin - 682 022, Kerala, India.
Email: drmohan@gmail.com

Department of Electronics

Cochin University of Science and Technology

Cochin - 682 022, Kerala, India.

www.doe.cusat.edu

August 2018

Dedicated to the Almighty... Teachers...
Parents... & Dear Ones...

DEPARTMENT OF ELECTRONICS
COCHIN UNIVERSITY OF SCIENCE AND TECHNOLOGY
COCHIN-682 022, INDIA.

Dr. P. Mohanan
(Supervising Guide)
Professor (UGC BSR)
Department of Electronics
Cochin University of Science and Technology.

Certificate

This is to certify that this thesis entitled " **Design, development and analysis of compact multiport antenna for ultra-wideband MIMO communications**" is a bonafide record of the research work carried out by **Ms. ROSHNA T. K.** under my supervision and guidance in the Centre for Research in Electromagnetics and Antennas (CREMA), Department of Electronics, Cochin University of Science and Technology in partial fulfilment of the requirements for the Ph.D. degree under the Faculty of Technology. The results embodied in this thesis or parts of it have not been presented for the award of any other degree. All the relevant corrections and modifications suggested by the audience and recommended by the doctoral committee of the candidate during the pre-synopsis seminar have been incorporated in the thesis.

Cochin – 22
August 2018

Prof. P. Mohanan

Declaration

I hereby declare that the work presented in this thesis entitled " **Design, development and analysis of compact multiport antenna for ultra-wideband MIMO communications**" is based on the original research work carried out by me under the supervision and guidance of Dr. P. Mohanan in the Centre for Research in Electromagnetics and Antennas (CREMA), Department of Electronics, Cochin University of Science and Technology in partial fulfilment of the requirements for the Ph.D. degree under the Faculty of Technology and that no part of this thesis has been submitted before for the award of any other degree.

Cochin − 22

August 2018

Roshna T. K.

Research Scholar

Department of Electronics

CUSAT

Acknowledgements

First and foremost, I would like to thank God Almighty for giving me the strength, knowledge, ability and opportunity to undertake this research study and to persevere and complete it satisfactorily. Without his blessings, this achievement would not have been possible.

In my journey towards this degree, I have found a teacher, Dr. P. Mohanan, Professor (UGC BSR), Department of Electronics, Cochin University of Science and Technology (CUSAT), who took me to the throbbing world of ElectroMagnetics and stood as a source of inspiration for me. He has been there providing his heartfelt support and able guidance at all times and has given me valuable suggestions in my quest for knowledge. I cherish the period of learning under him. Without his able guidance and immense patience, this thesis would not have been possible and I shall eternally be grateful to him for his assistance.

I have great pleasure in acknowledging my gratitude to Prof. K. G. Nair for his vision in setting up Center for Research in Electromagnetics and Antennas (CREMA) at CUSAT.

I take pride in acknowledging the insightful guidance of Dr. K. Vasudevan, Emeritus Professor, Dept. of Electronics, CUSAT and Dr. C. K. Aanandan, Head, Dept. of Electronics, CUSAT, for sparing their valuable time whenever I approached them and showing me the way ahead.

I express my sincere thanks to Dr. James Kurian, Dr. M. H. Supriya, Dr. Tessamma Thomas, Dr. K. T. Mathew, Dr. P. R. S Pillai and all other faculty members at the Dept. for their moral support and timely advice which paved a smooth path for my research at the Department of Electronics, CUSAT.

I have great pleasure in acknowledging my gratitude to my fellow research scholars at Dept., Dr. C. M. Nijas, Dr. V. P. Sarin, Dr. Sajitha V. R., A. O. Lindo and Suraj Kamal for being there at times when I required motivation

and their encouragement & credible ideas have been great contributors to the completion of the thesis.

I would also like to express my gratitude to Vinisha C. V., Vivek R., Vinesh P. V., Manoj M., Remsha M., Prakash K. C., Dr. Shameena V. A., Dr. Sumitha Mathew, Mohammed Ameen, Anju P. Mathews, Dibin Mary, Sreekala P. S., Liby V. A., Dr. Sreenath S., Paul Bert, Neeraj K. Pushkaran, Nelson K. J., Cyriac M. O., Tony D., Sruthi Dinesh, Prasanth, Aji Goerge, Mithun M. S., Ann Varghese, Navya Mohan, Prasanth P. P. Athul Thomas, Satheesh Chandran, Limna, Suja S., Tina P. G., Deepthi Dilish, Sangeetha R. Theresa B. and all other fellow research scholars at Dept. of Electronics, who have been so helpful & cooperative in giving their support at all times to help me achieve my goal and who never let things get dull or boring.

My acknowledgement would be incomplete without thanking the biggest source of my strength, my family. The blessings of my parents Mrs. Shobhana T. K. & Mr. Purushothaman P.K., the love and care of my brother Rohith P.K., and my parents-in-law Mrs. Leelavathi M. P. and Mr. Unnimadhavan V. P, have all made a tremendous contribution in helping me reach this stage in my life. I thank them for putting up with me in difficult moments where I felt stumped and for goading me on to follow my dream of getting this degree. This would not have been possible without their unwavering and unselfish love and support given to me at all times.

Above all, I thank my prime source of ideas, my husband Deepak U, for his love & persistent confidence in me and inspiring me with his pursuit of learning. He stood as a pillar of support in all my difficult situations. And, I appreciate my son Vedik Dev for his immense patience, love and support to his mother during this period.

Last but not the least, I would like to thank everybody who became a cause to the successful realization of this thesis, as well as expressing my apology that I could not mention personally one by one.

Roshna T. K.

Abstract

The era of emerging wireless communication systems demand high data-rate and highly reliable communication strategies. A UWB system is well-known for their exploitation of a huge frequency band of 3.1 to 10.6 GHz, which provides great potential for increasing data transmission rates according to the Shannon theorem. This made a visible trend for products/services based on short-range WBANs, WPANs etc. However, due to the limitations in their power spectral density by the Federal Communications Commission (FCC), the data transmission rate will be limited. Incorporating the MIMO technique into UWB provides a viable solution for the bottleneck problem of power limit. A multi-antenna system can provide high spectrum efficiency and improved quality of service for next generation wireless systems. Inspired by these factors, this thesis presents the valuable insights in the design of compact, novel antennas for efficient UWB-MIMO communications.

In the course of present research work, two coplanar UWB antennas have been proposed, and using those UWB antennas three co-located UWB-MIMO antennas has created. The thesis examines the potential and credibility of the co-located UWB antennas for the operation in a MIMO communication system with the help of certain figures-of merit which evaluates the antenna's MIMO/diversity performances and channel performances. The thesis also demonstrates the efficient methods of isolating the antenna-elements within the space constraints as well as for wide band operation, which is a challenge. Further, this thesis investigates the transfer properties and stability performance of the antenna in the required 3.1 — 10.6 GHz UWB band, in order to check their suitability for portable pulsed-UWB systems. The ultimate aim of this thesis is to investigate and enhance the MIMO/diversity performance of multiple antenna systems for future UWB communications.

Table of contents

List of figures

List of tables

Chapter 1

Introduction

The birth of communication network happened in the pre-industrial age, where information was transmitted over line-of-sight distance (later extended by telescopes) by using smoke signals, flashing mirrors, torch signalling, signal flare or semaphore flags. Combinations of these rudimentary signal were used to convey complex messages. These early communication networks got outdated with the invention of the telegraph network by Samuel Morse [181] in 1858 and later with the telephone by Alexander Graham Bell [181] in 1876. However, the term 'wireless' was originated after the demonstration of electric wave communication mechanism by Henrich Rudolf Hertz [181] in 1888, who experimentally proved the unified theory of electricity and magnetism formulated by his teacher James Clerk Maxwell. This inspired Guglielmo Marconi to establish the first radio link between a land-based station (Isle of Wight) and a tugboat 18 miles away [181] (in 1895), and thus the radio communication was born. Later in 1901, Marconi performed the historic Transatlantic experiment, by transmitting the letter S (three dots in Morse code), over a distance of 700 nautical miles, by drawing inspiration from the works of Jagdish Chandra Bose [28] and Hertz. By this, the era of wireless communication networks started. Since then, the wireless communication systems have evolved substantially with a furious pace.

Out of all wireless services, the birth of mobile communication network changed our day-to-day life tremendously with its continuing phases of evolution. Its first generation (1G) allowed only analogue voice communication, while the second generation (2G) realized the digital voice communication, along with
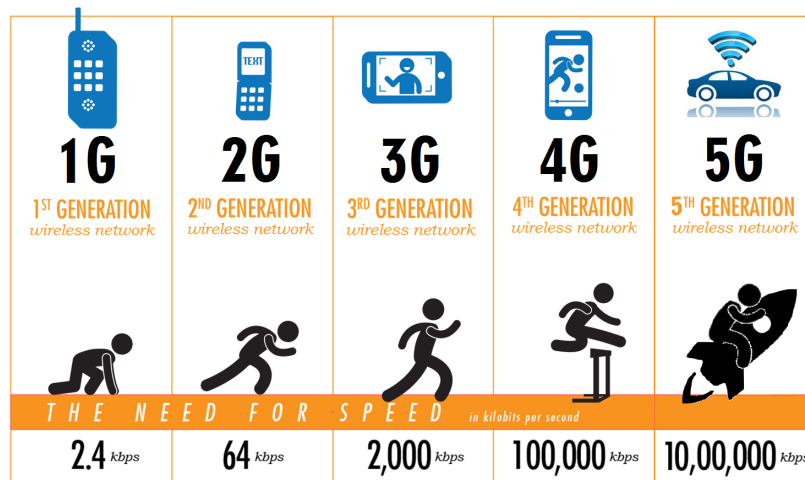
Fig. 1.1 Evolution of the wireless communication technologies

text messages, picture messages and multi-media messaging services. The third generation (3G) provided video telephony, Internet access, digital voice services as well as video/music download services. Currently, the fourth generation (4G) can provide on demand high quality audio & video services, global mobility support, integrated wireless solutions and is known as true mobile broadband. In the near future, the fifth generation (5G) will be able to offer TV programs with HD quality, large clarity audio/video and interactive multimedia, voice, streaming video, Internet & others. A brief evolution of the wireless communication technologies from 1G to 5G is shown in Fig. 1.1.

On the other hand, wireless networks enabled people to communicate and access applications & information without wires. This realized the freedom of movement and enabled data transfer to different parts of the building, or city, or anywhere in the world. Based on the range in which communication takes place and on the mode of end users, the wireless networks can be classified into four: WPAN (Wireless Personal Area Network), WLAN (Wireless Local Area Network), WMAN (Wireless Metropolitan Area Network) and WWAN (Wireless Wide Area Network). Fig. 1.2 depicts the corresponding IEEE standards used in accordance with each type of wireless networks. Wireless networking standards like IEEE 802.11 (WLAN) and IEEE 802.16 (WMAN) typically focus on proving PC-to-PC or PC-to-ISP connectivity, over the range of a building or a metropolitan area, respectively. However, many applications will have shorter range requirements,
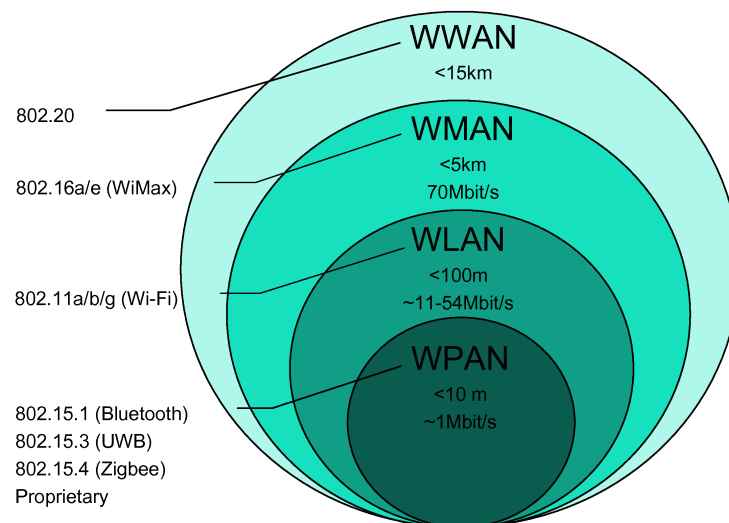
Fig. 1.2 Classification of the wireless networks

like connecting peripherals to mobile devices or PCs, without using wires etc. WPANs, which provide a wide variety of data rates, are a perfect fit for these applications.

The proliferation of wireless communication devices in our daily life shows no sign of stagnation. The ever-growing demand for higher quality media and faster content delivery drives the quest for higher data rates in the wireless communication networks. Even though the number of wireless applications continues to grow, bandwidth is still limited as in the days of Marconi. This limitation in available bandwidth has motivated the development of novel transmission techniques, out of which two that have gathered a lot of research interest in recent years is ultra-wideband (UWB) technologies and multiple-input multiple-output (MIMO). To meet the demand for higher data rate and capacity, the IEEE 802.15.3 task group employed Ultra Wide-Band (UWB) technique for WPAN communications. UWB radios take a different approach from 802.15.1 (Bluetooth) & 802.15.4 (ZigBee). Both the latter transmit signals over a long period using a small part of the spectrum, while UWB uses short pulses over a very large bandwidth. According to Shannon-Hartley theorem [148], a wide channel bandwidth can guarantee a good channel capacity, without invoking a high transmitted power.

Thus, UWB is able to provide high channel capacity for the wireless communication systems as it has an extremely wide bandwidth. Moreover, UWB offers a promising solution to the RF spectrum drought by providing the co-existence of new services with the current services, with minimal or no interference. On the other hand, MIMO technology established a breakthrough in the wireless communication systems by exploiting the multi-path scattering. It uses multiple transmitting and receiving antennas to increase the capacity and reliability of the communication systems, without invoking additional power or bandwidth. MIMO utilizes the multiplexing technique to improve the system transmission capacity by spreading the same total power over the antennas and thereby enhances the spectral efficiency. Moreover, the capacity scales linearly with the number of antennas used at the transmitter and receiver.

1.1   UWB Basics

UWB differs substantially from the conventional narrow band Radio Frequency (RF) and Spread Spectrum (SS) technologies because it uses extremely wide band of RF spectrum to communicate between transmitters and receivers. In doing so, UWB is able to transmit more data in a given period than the traditional technologies do. This makes UWB to offer several advantages such as large throughput, covertness, robustness to jamming and co-existence with current radio services.

1.1.1   History & Background

UWB is not a new technology; in fact its concept was initially employed by Marconi, in 1901, in his famous Transatlantic experiment using spark gap radio transmitters. However, the benefits of this large bandwidth were never considered at that time. Also, the communication world abandoned this wideband communications in favour of the narrow band or tuned communications. It is sixty years after Marconi the impulse radio technologies started being developed for Radar and military applications. However, this technology was restricted to such highly secure communications. Due to the advancement in microprocessing and fast switching in semiconductor technology, interest in the commercialization

of UWB has increased over the past several years. This made the developers
of UWB systems to pressurize the Federal Communications Commission (FCC)
to approve UWB for commercial use. As a result, in February 2002, the FCC
amended the Part 15 rules (governing the unlicensed radio devices) to include the
operation of UWB devices and approved the First Report and Order (R&O) for
commercial use of UWB technology under strict power emission limits for various
devices and countries [64]. Since then, UWB technology have advanced rapidly
as a promising high data rate wireless communication technology for various
applications. Although, all types of wireless services and devices, in India, fall
under the licensing authority of WPC (Wireless Planning and Coordination), they
haven't described any stringent frequency band limitations for UWB applications.
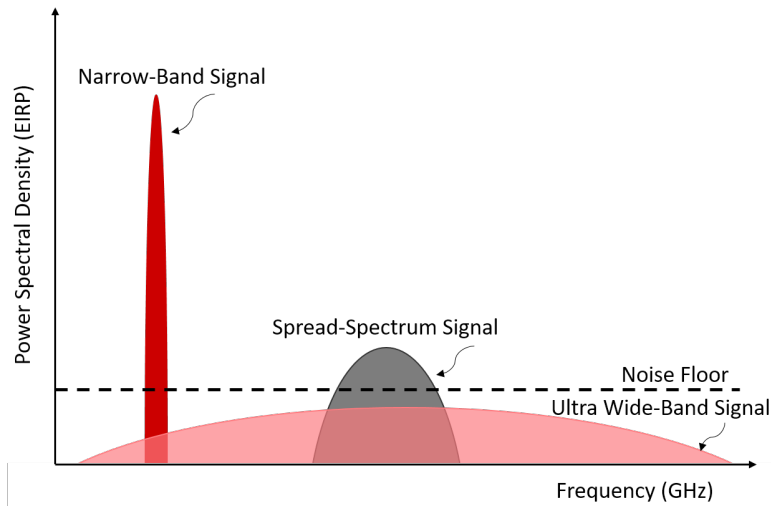
Fig. 1.3 Spectrum Utilization showing the co-existence of UWB signals with other
services

1.1.2 UWB Concepts

According to FCC, a UWB communication system is any radio system whose
spectrum occupies more than 20% of the center frequency, i.e.,its fractional
bandwidth $\left(\frac{2(f_H - f_L)}{f_H + f_L}\right)$ is at least 20%, or whose 10dB bandwidth $(f_H - f_L)$ is at
least 500 MHz. This radio system can co-exist with the current narrow band and
wideband services and therefore, its power spectral density is strictly limited by
relevant regulatory authorities. Fig. 1.3 illustrates the spectrum utilization of

UWB signal and conventional narrow band & SS signals [48]. UWB gleans the benefits of the high bit rate that it can handle due to its extremely wideband spectrum. According to Shannon-Hartley's theorem, the channel capacity C is given by,

$$C = BW * \log_2(1 + \frac{S}{R}),\tag{1.1}$$

where, BW is the bandwidth and $\frac{S}{R}$ is the Signal-to-Noise ratio (SNR). Equation 1.1 shows that the capacity (bit rate) is increased linearly with BW and logarithmically with $\frac{S}{R}$. Thus, the bit rate can be easily increased by increasing the BW, instead of the transmitter power. Range of operation of such systems are defined by the Friss-Transmission formula,

$$D \propto \sqrt{\frac{P_t}{P_r}},\tag{1.2}$$

where, D is the distance between transmitter & receiver, P_t is the transmitted power and P_r is the received power. Equation 1.1 & 1.2 together depicts the trade-off between bit rate (capacity) and range of operation (distance). Thus, for higher data rate lesser will be the achievable transmission distance, and vice versa. As a matter of fact, UWB is mainly used for high-bit rate short-range applications.

1.1.3   FCC Regulations & Emission Limits

On 14 February 2002, the FCC amended their Part 15 rules to open up an extremely large amount of bandwidth for the commercial development of UWB technology [64]. FCC defined the UWB bandwidth as "the frequency band bounded by the points that are 10dB below the highest radiated emission". Later, FCC placed operating restrictions for UWB in many countries in order to make the co-existing users unaffected by the UWB signals.

In USA, the FCC spectral mask specified 7.5 GHz of usable spectrum bandwidth between 3.1 GHz and 10.6 GHz for communication devices. FCC protected the existing users operating within this spectrum by limiting the power spectral density levels (EIRP) of UWB signals to -41.3 dBm/MHz or 75 nW/MHz, which is the same level as unintentional radiators such as television and computer
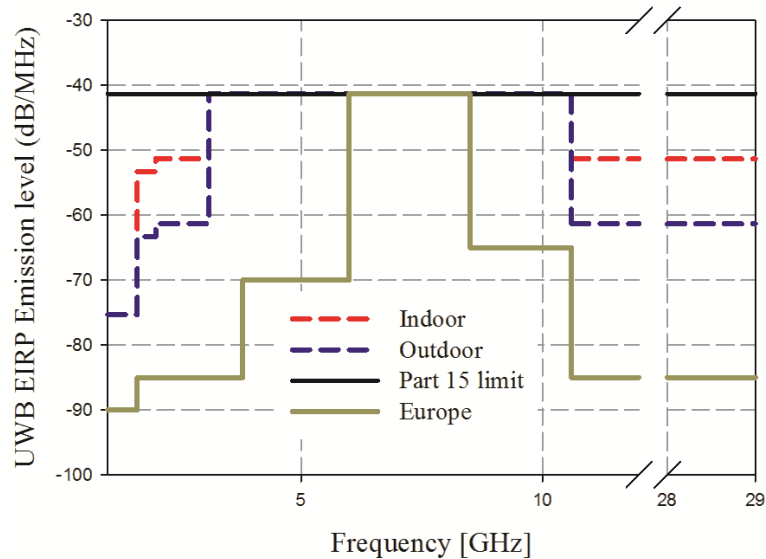
Fig. 1.4 FCC allocated spectral mask for UWB communications

monitors. Fig. 1.4 shows the spectral mask limitation of the power spectral density measured in a 1 MHz bandwidth at the output of an isotropic transmit antenna, for indoor and outdoor environments. The primary difference between indoor and outdoor operations is that the degree of attenuation required for the out-of-band region for outdoor operations will be higher compared to indoor operations. According to FCC, the indoor activities should be restricted to peer-to-peer operations inside buildings. In Europe, FCC provided a further wide frequency band from 1.6 to 10.6 GHz, but with a strict spectral mask than that specified for USA, as shown in Fig. 1.4.

Based on the present FCC regulations the UWB devices are categorized in to three: Communication, Imaging and Vehicular Radar. Both the indoor and outdoor communication devices fall under the communication section. Imaging deals with UWB-based through-wall imaging devices, whose operation are constrained to law enforcement and rescue teams. Whereas, vehicular radar deals with radar devices which are mounted on terrestrial transportation vehicles and are activated either while the vehicle are moving or while they are stationary. Table 1.1 summarizes the FCC emission limits for various UWB applications in each operating band.

Table 1.1 Emission limits in each operation band for different UWB applications

	Application		Operation Band (GHz)					
			0.96-1.6	1.6-1.99	1.99-3.1	3.1-10.6	10.6-22	22-29
EIRP **(dB/** **MHz)**	Communications	indoor	-75.3	-53.3	-51.3	-41.3	-51.3	-51.3
		outdoor	-75.3	-63.3	-61.3	-41.3	-61.3	-61.3
	Imaging		-53.3	-51.3	-41.3	-41.3	-41.3	-51.3
	Vehicular radar		-75.3	-63.3	-63.3	-63.3	-41.3	-41.3

1.1.4   UWB Standards & Transmission Schemes

IEEE established the 802.15.3a and 802.15.4a task groups to define a new physical layer concept for short-range high data rate WPAN and long-range low data rate WPAN applications, respectively. 802.15.3a is proposed to support a data rate of 110 Mbps with a distance of 10 meters. Whereas, the technical requirements for 802.15.4a include low data rate (>250 Kbps), low cost, low complexity and low power consumption (long battery-life). However, IEEE 802.15.3a has two competing proposals: Single-Band (SB) and Multi-Band (MB) approach. The SB approach is an Impulse Radio (IR)-based scheme, which is the original approach to UWB. This scheme uses very short duration pulses (typically of the order of several tens of picoseconds) that occupies a wide spectrum of several Gigahertz bandwidth, to convey informations. This pulse train can be directly transmitted without any carriers. Here, data is modulated using Pulse Amplitude Modulation (PAM) or Pulse Position Modulation (PPM) methods and for the multi-user access to the UWB channel two techniques are employed: Direct Sequence Spread Spectrum (DSSS) and Time Hopping Spread Spectrum (THSS) [207]. The UWB spectrum utilization in the case of SB approach, for both DSSS & THSS, are illustrated in Fig. 1.5.
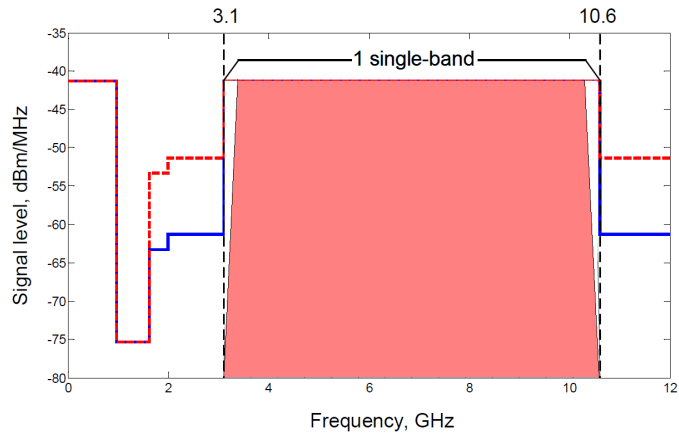
(a) Direct Sequence Spread Spectrum
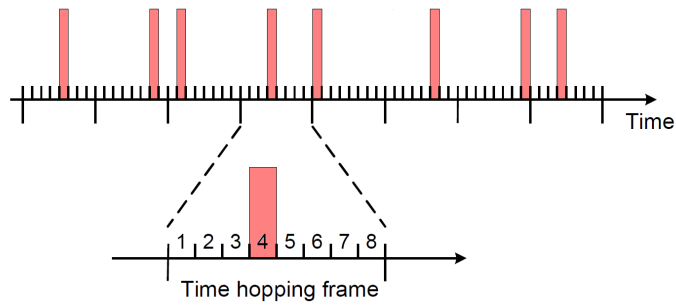
(b) Time-hopping Spread Spectrum

Fig. 1.5 Single-Band approach of the UWB spectrum
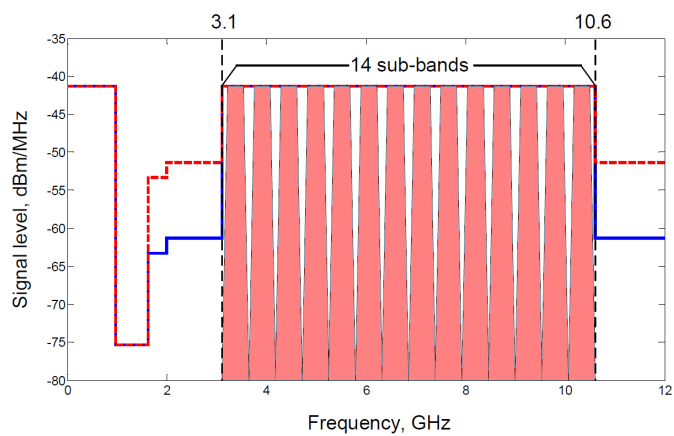
Fig. 1.6 Multi-Band approach of the UWB spectrum (Frequency-hopping)

Table 1.2 UWB advantages, disadvantages and applications

UWB property	Advantages	Disadvantages	Applications
Wide fractional bandwidth	High data rate communications, potential for gain-processing, Wall & ground penetration (low frequencies)	Interference to/from existing systems	High data rate WPAN, indoor localization Multiple access, low power stealthy communications
Very short pulse transmission	Direct resolvability of discrete multipath components, diversity gain	Large number of multipath propagation, long synchronization times	Low power combined communications and localization
Persistence of multipath reflections	Low power transmission, low fade margins	Scattering in angle of arrival	NLOS communications on ships and indoors
Carrier-less transmission	Hardware simplicity	Inapplicability of super-resolution beamforming	Smart sensor networks

The MB approach is a recent scheme, where the available band (3.1-10.6 GHz) is divided into several smaller and non-overlapping sub-bands with bandwidth not less than 500 MHz, to satisfy the FCC definition of UWB. Carrier-based modulation methods like BPSK, QPSK, OFDM etc. are used for the data modulation in this scheme and for multi-user access frequency hopping method is employed, as shown in Fig. 1.6.

The main advantage of SB approach is the simplicity in the transceiver structure, as no up- and down-mixers are needed. But in MB approach the implementation of up- & down-mixers and OFDM makes the transceiver design complicated. SB approach is very sensitive to multipath interference. But, better multipath resolution can be achieved by the discontinuous transmission of short pulses, whose pulse duration is shorter than the multipath delay. On the other

hand, the OFDM technique used for MB approach provides high spectral efficiency, inherent resilience to RF interference and robustness to multipath. Besides MB scheme has co-existence properties i.e., it can avoid transmission over the in-use bands, thus prevents the potential interference. To achieve this in SB scheme notch filters have to be employed, which may increase the system complexity and distort the received signal transmission. Table 1.2 summarizes the advantages and disadvantages for different UWB properties and their corresponding applications.

1.2 MIMO Principle

People's demand for faster data rate transmission seems endless and this have been the driving force behind the progress of modern wireless technologies. The application of diversity techniques using two or more antennas can enhance data rate & reliability of the communication systems, without invoking additional spectrum or transmit power in rich scattering environments. This multi-antenna systems with MIMO (Multiple-Input Multiple-Output) technology plays a pivotal role in providing a peak data rate of 1 Gbps with high spectrum efficiency (more bits per second per Hertz of bandwidth). MIMO is one of the smart antenna technology to improve the performance of communication systems.

1.2.1 History of MIMO Technology

MIMO finds its roots in the antenna diversity, a remarkable technological innovation, whose evolution started back in 1920s. The idea behind antenna diversity technique originated after the experiments conducted by Harold. H. Beverage & Harold. O. Peterson, who noticed entirely different received signal strengths from two radio broadcast stations located about a half mile apart [30]. They called this phenomenon as fading which was a result of the multipath propagation of radio waves. To overcome this fading they developed a diverse system in which the two different received signals were combined effectively to obtain improved signal quality [26, 72]. Due to the difficulty in implementation of dedicated and costly receivers for each antenna, F. A. Bartlett proposed a new technique in 1941, in which a single radio receiver is switched alternatively between two antennas for effectively presenting an average signal to the receiver, thus, providing

some immunity to fading [25]. Although antenna diversity was employed in large number of radio systems, it was limited to a technique used at receivers to encounter the impacts of multipath fading. However, the birth of MIMO technology changed the landscape for multi-antenna systems operating in multi-path channels. The primary ideas in this field was given by A. R. Kaye & D. A. George (1970), Branderburg & Wayner (1974) and by W, Van Ettan (1975, 1976). Later, Jack Winders & Jack Salz at Bell laboratories published several papers on beamforming related applications in the mid eighties (1984, 1986). The two researchers, Arogyaswami Paulraj and Thomas Kailath were the first to propose the concept of spatial multiplexing using MIMO, in 1993. However, the pioneer of MIMO technology were Gerard J. Foschini [65] and Gregory G. Raleigh [155], who configured the co-location of multiple antennas at one transmitter to improve the link throughput effectively (1996, 1998). This was a breakthrough for the proliferation of MIMO communication systems. Since then, MIMO technology have been implemented in various areas of communication.

1.2.2   Need for Multiple Antenna systems

Initially, the wireless communication systems were used for voice and small data rate transfer while most of the high data rate transfer were through wired communication systems. In the last few decades the landscape have changed with the need of high quality video communications and high speed data transfer among the wireless systems. As a result, numerous highly efficient wireless networking technologies have been developed and are widely deployed. Such wireless communication systems are likely to guarantee some attributes such as high data rate & good capacity (spectral efficiency), high Quality of Service (QoS), Low Bit Error Rate (BER), wide coverage range and low deployment, operation & maintenance costs. Assurance of all these requirements is very contentious by nature, particularly in Non-Line Of Sight (NLOS) propagation which have become common in wireless communication systems as a result of the massive introduction of radio communication in indoor and urban environments. This is because, in the case of NLOS propagation the signal is reflected along multiple paths, before finally being received at the receiver, and each of these rebounds can produce phase shifts, time delays, and distortions that can destructively

interfere with one another at the receiving antenna, as shown in Fig. 1.7. This detrimental impairment of transmitted signal is known as signal fading, one of the most crucial NLOS propagation phenomena.
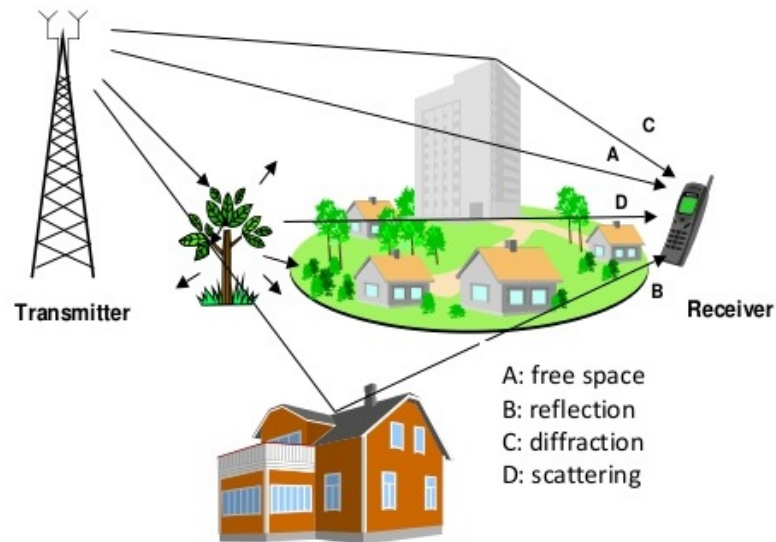
Fig. 1.7 Typical wireless propagation channel representation with random objects between Txr and Rxr

Basically, signal fading is the rapid fluctuations of received signal strength over short time intervals and/or travel distances. In a wireless communication system the data that is transferred from transmitter (Txr) to receiver (Rxr) through a propagation channel takes different paths on its way to the receiving end. Thus, the signal strength at the receiving end will vary according to the distance they travelled, as shown in the right side of the Fig. 1.8. This signal level variation is an after effect of the combination of three major factors, such as, Path loss, Shadowing and Multipath effect, which is illustrated well in Fig. 1.8.

- **Path Loss** : Basically path loss is the difference (in dB) between the transmitted power and received power. This difference is due to the reduction in power density of an electromagnetic wave or signal as it propagates through the environmental space between transmitter and receiver.Fig. 1.9 shows a typical block diagram representation of a wireless communication. As observed on the left side of Fig. 1.8, for path loss the signal power
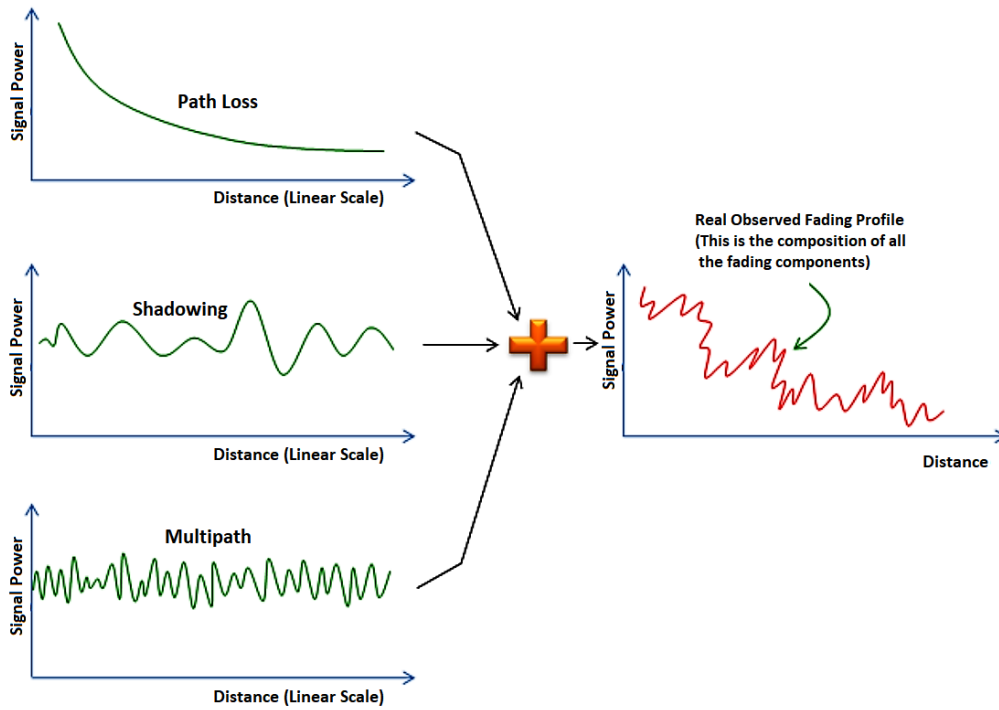
Fig. 1.8 Superposition of path loss, shadowing and multipath in the fading profile
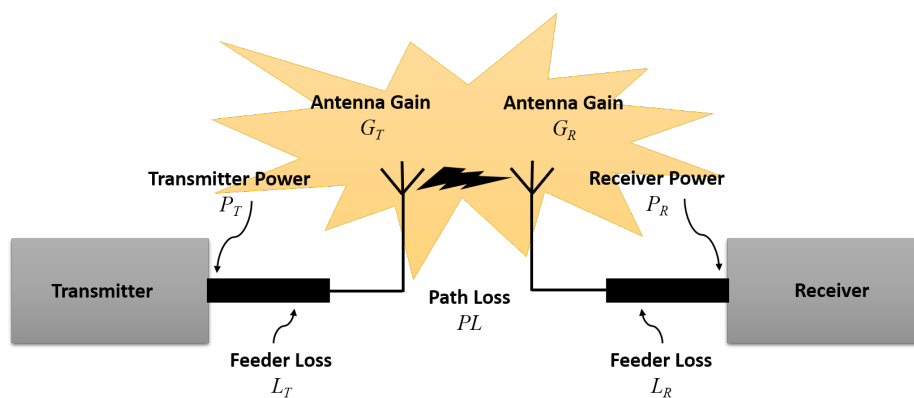
Fig. 1.9 A typical wireless link

gradually decreases with distance without much of fluctuations. This can be expressed empirically as [180],

$$PL = \frac{P_r(d_0)}{P_t} = k\left(\frac{d_0}{d}\right)^{\alpha}, \qquad (1.3)$$

where, α is the path loss exponent, P_T is the transmitted power, $P_R(d_0)$ is the received power at a distance d_0 (reference distance) from the transmitter, k is the transmission constant and d is the distance between Txr and Rxr. And finally path loss can be expressed in dB as,

$$PL(d) = \frac{P_R(d_0)}{P_T} = \overline{PL}(d_0) + 10\log\left(\frac{d}{d_0}\right)^{\alpha}, \qquad (1.4)$$

where, $\overline{PL}(d_0)$ is the mean pathloss in dB at distance d_0.

- **Shadowing** : In real life situation there would be lot of obstacles, such as buildings, hills, trees etc., present between Txr and Rxr. Due to the presence of these obstacles along the path of the signal propagation, some portions of the transmitted signal are lost through reflection, absorption, diffraction and/or scattering. This effect is known as shadowing, and the so called name came because the obstacles in the middle of Txr and Rxr castes a shadow on the Rxr antenna, if we assume Txr as a light source. So the net path loss can be expressed as

$$PL(d) = \frac{P_R(d_0)}{P_T} = \overline{PL}(d_0) + 10\log\left(\frac{d}{d_0}\right)^{\alpha} + \gamma, \qquad (1.5)$$

where, γ represents the effect of shadowing and is a normally (Gaussian) distributed random variable (in dB) with standard deviation σ. Both α and γ values are determined empirically. However, for free space α is kept as 2.

- **Multipath** : This type of fading occurs as the transmitted signal takes multiple paths to reach the receiver, due to the reflections from various objects present in the propagation environment. Each path is unique with distinct amplitude, phase and delay. These multiple replicas of transmitted

signal arrive at receiver with different time delays and are combined to reconstruct the original transmitted signal. This constructive and destructive combination of multipath signals at receiver causes sudden variation of signal power which may cause the degradation of SNR, resulting in a poor or fictional communication link between the Txr and Rxr.

Fig. 1.10 depicts the effect of these three factors on a transmitted signal. Generally, fading can be classified into two: Large-Scale (Slow) fading and Small-Scale (Fast) fading. The path loss and shadow fading comes under large-scale fading. It is the long term variation in the mean signal level caused by the mobile unit moving into the shadow of surrounding objects. So it is also known as slow fading. On
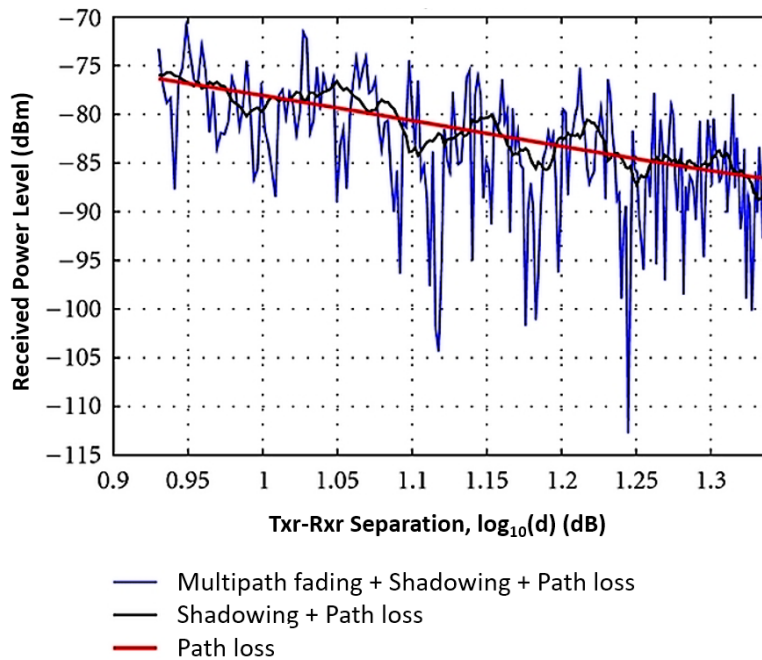
Fig. 1.10 Signal fading with distance

the other hand, small-scale fading is due to te multipath effect on the transmitted signal. This fading is concerned with the short term fluctuations in the signal amplitude caused by the local multipath. Thus the name fast fading.

Day-by-day the propagation environment is getting more complex and so do the number of propagation paths, that the transmitted signal have to take before reaching the receiver. This will increase the degree of signal fading and

thereby results in a poor communication system,which is a serious drawback for the modern era of wireless communication who are thirsty for high data rate and reliable communications. This raised the necessity to develop new wireless communication architecture that work well, not only in LOS (Line-Of-Sight) conditions but also in NLOS scenarios.

The conventional communication systems, where we have one antenna at the transmitter and one antenna at the receiver (Single-Input Single-Output, SISO), were not able to reduce the effects of multipath and interferences in NLOS scenarios. Thus, in 1998, Foschini and Grans [66] examined the possibility of using multiple-antennas or arrays to improve the reliability and capacity of communication systems by mitigating these vulnerable multipath fading problems. In a broader sense, multiple antenna systems are referred to the communication systems which consists of more than one antenna at the receiver (Single-Input Multiple-Output, SIMO) or at the transmitter (Multiple-Input Single-Output, MISO) or at both of them (Multiple-Input Multiple-Output, MIMO). Generally, we often refer SIMO (receiver diversity) and MISO (transmitter diversity) systems as the particular types of MIMO configurations. Fig. 1.11 illustrates the afore mentioned four types of antenna configurations. Out of all, MIMO systems shows commendable capacity performance and high data rate as the number of antennas increases, compared to the other multiple antenna systems. This is depicted in Fig. 1.12 which shows a linear increment in channel capacity for MIMO and a logarithmic increment for SIMO & MISO, as the numbers of antenna-elements are increased. Unlike the single-antenna systems (SISO), MIMO systems makes it possible to combat the detrimental multipath fading problem through appropriate coding technology and signal processing. Thus, MIMO takes the advantage of multipath propagation and improves the reliability and data throughput of communication systems, without sacrificing additional bandwidth or transmit power.

To see the benefits of MIMO, let us investigate the system performance of the MIMO compared with that of SISO, SIMO and MISO, for narrowband wireless communication systems operating with frequency-flat channels. Since the Signal-to-Noise power ratio (SNR) determines most of the system performance criteria such as, channel capacity, data rates, bit error rates etc., it is justifiable to investigate the SNR gain of the different multi-antenna configurations for a
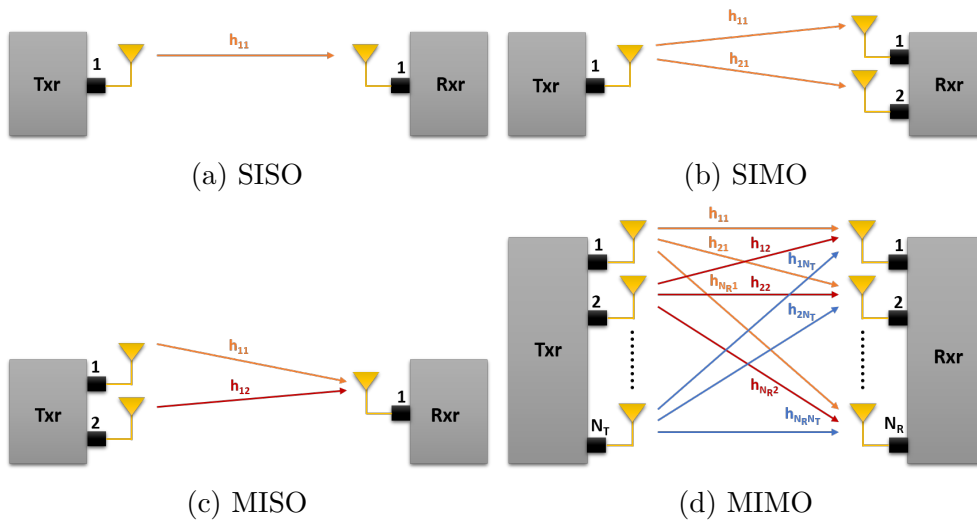
Fig. 1.11 Different antenna configurations of a communication system
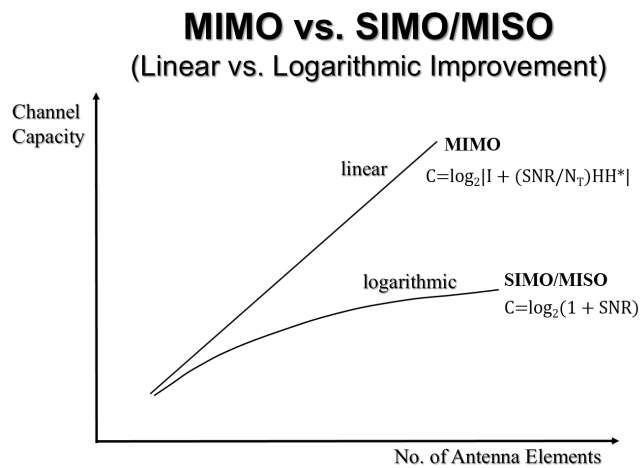
Fig. 1.12 Channel capacity comparison of MIMO & SIMO/MISO

valid comparison. In order to make the comparison fair, assume that the transmit power of the multi-antenna systems are same as that of the SISO.
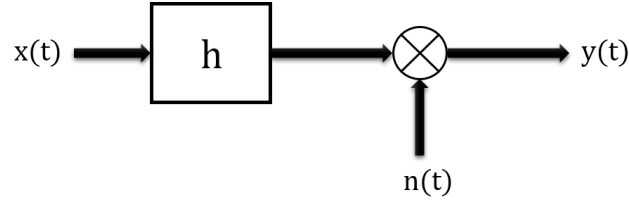
Fig. 1.13 Input-Output relationship of SISO

First, consider the case of single transmit antenna and single receive antenna (SISO), as depicted in Fig. 1.9. The input-output relationships of such a system is shown in Fig. 1.13 and can be formulated as

$$y(t) = h \ x(t) + n(t),$$ (1.6)

where, $x(t)$ & $y(t)$ are the transmitted and received signals, respectively. h is the channel response and $n(t)$ is the Additive White Gaussian Noise (AWGN) with zero mean and variance σ_N^2. The maximum possible data rate of such SISO systems are fundamentally limited by its channel capacity, which can be expressed as [174]

$$C = \log_2(1 + SNR); \quad for \ a \ bandwidth \ of \ 1Hz,$$ (1.7)

where, C is the channel capacity in bits/sec.

As seen from the above equation it is clear that the SNR plays a crucial role in the system performance. For the improvement of spectral efficiency multiple antennas are employed at transmitter or receiver ends or at both. Let, N_T and N_R be the number of antennas at transmitter side and receiver side, respectively.

For a SIMO case, where there is a single transmit antenna and N_R receiver antennas, the input-output relationship can be expressed as

$$y_i(t) = h_i \ x(t) + n_i(t),$$ (1.8)

where $i = 1, 2...N_R$ and h_i is the channel fading from transmitter to each receiver.

The Channel State Information (CSI) represents the state of a communication link from the transmitter to the receiver. It describes how a signal propagates

from the Txr to the Rxr and represents the combined effect of scattering fading and power decay with distance. If the Rxr does not have the CSI the received signals can be combined with an equal gain, like

$$y_{SIMO}(t) = \sum_{i=1}^{N_R} y_i(t) = \sum_{i=1}^{N_R} h_i \, x(t) + \sum_{i=1}^{N_R} n_i(t) \tag{1.9}$$

Then, the SNR of the combined signal is

$$SNR_{SIMO} = \frac{\mathbb{E}\left\{\left[\sum_{i=1}^{N_R} h_i \, x(t)\right]\left[\sum_{i=1}^{N_R} h_i \, x(t)\right]^*\right\}}{\mathbb{E}\left\{\left[\sum_{i=1}^{N_R} n_i(t)\right]\left[\sum_{i=1}^{N_R} n_i(t)\right]^*\right\}} = \frac{\sum_{i=1}^{N_R} \sigma_{h_i}^2}{N_R} \frac{\mathbb{E}\left[|x(t)|^2\right]}{\sigma_N^2}$$

$$= \frac{\sum_{i=1}^{N_R} \sigma_{h_i}^2}{N_R} SNR_T, \tag{1.10}$$

where, SNR_T denotes the SNR at the transmitter side. From equation 1.10, we can see that there is no gain in SNR if receiver does not know the CSI. On the other hand, if the receiver has the knowledge about CSI then the received signals can be combined using the maximum ratio combiner (MRC) as follows:

$$y_{SIMO}(t) = \sum_{i=1}^{N_R} h_i^* \, y_i(t) = \sum_{i=1}^{N_R} |h_i|^2 \, x(t) + \sum_{i=1}^{N_R} h_i^* \, n_i(t) \tag{1.11}$$

Thus the SNR gained is

$$SNR_{SIMO} = \frac{\mathbb{E}\left\{\left[\sum_{i=1}^{N_R} |h_i|^2 \, x(t)\right]\left[\sum_{i=1}^{N_R} |h_i|^2 \, x(t)\right]^*\right\}}{\mathbb{E}\left\{\left[\sum_{i=1}^{N_R} h_i^* \, n_i(t)\right]\left[\sum_{i=1}^{N_R} h_i^* \, n_i(t)\right]^*\right\}}$$

$$= \frac{2\sum_{i=1}^{N_R} \sigma_{h_i}^4 + \sum_{i_1=1}^{N_R} \sum_{i_2=1, i_2 \neq i_1}^{N_R} \sigma_{h_{i_1}}^2 \sigma_{h_{i_2}}^2}{\sum_{i=1}^{N_R} \sigma_{h_i}^2} \frac{\mathbb{E}\left[|x(t)|^2\right]}{\sigma_N^2}$$

$$= \left(\frac{\sum_{i_1=1}^{N_R} \sigma_{h_i}^4}{\sum_{i_1=1}^{N_R} \sigma_{h_i}^2} + \sum_{i_1=1}^{N_R} \sigma_{h_i}^2\right) SNR_T \tag{1.12}$$

In the third step of the derivation of above equation the property $\mathbb{E}\left[|h_i|^4\right]$ is replaced with $2\sigma_{h_i}^4$ as for complex Gaussian random variables [74, 94]. From the equation 1.12, it is clear that the SNR has increased exactly N_R fold (i.e., the SNR of SIMO is $(N_R + 1)$ times that of SISO) by using the MRC, when receiver knows CSI and all the links in SIMO have same fading power as that of SISO.

Next, consider MISO systems with N_T transmit antennas and single receive antenna. In this case the input-output relationship can be expressed as

$$y(t) = \sum_{i=1}^{N_T} h_i \; x_i(t) + n(t), \tag{1.13}$$

where, $i = 1, 2...N_T$ and h_i is the channel fading from each transmitter to the receiver. In this case also we make similar assumption as that of SIMO, except that $\mathbb{E}\left[|x_i(t)|^2\right] = \frac{\mathbb{E}[|x(t)|^2]}{N_T}$, where $\mathbb{E}[|x(t)|^2]$ is the transmitted signal power for the SISO case.

If the transmitter does not know the CSI, then the SNR achieved at receiver will be

$$SNR_{SIMO} = \frac{\mathbb{E}\left\{\left[\sum_{i=1}^{N_T} h_i \; x_i(t)\right]\left[\sum_{i=1}^{N_T} h_i \; x_i(t)\right]^*\right\}}{\mathbb{E}\{|n(t)|^2\}} = \frac{\sum_{i=1}^{N_T} \sigma_{h_i}^2}{N_T}\frac{\mathbb{E}\left[|x(t)|^2\right]}{\sigma_N^2}$$
$$= \frac{\sum_{i=1}^{N_T} \sigma_{h_i}^2}{N_T} SNR_T \tag{1.14}$$

It can be seen that there is no power gain at the receiver SNR.

On the other hand if the transmitter has CSI it will pre-process the transmitter for each transmit antenna so that some gain is achieved in the SNR at the receiver. As a part of the pre-processing let us assume that the transmitted signal of each transmit antenna is weighted by its channel fading as

$$x_i(t) \longrightarrow \frac{h_i^*}{\sqrt{\sum_{i=1}^{N_T} \sigma_{h_i}^2}} \; x_i(t) \tag{1.15}$$

Here, $\mathbb{E}\left[|x_i(t)|^2\right] = \mathbb{E}[|x(t)|^2]$ for the current situation. Then the overall transmitted power will be the same as that of SISO case and the received signal is given

by

$$y(t) = \frac{1}{\sqrt{\sum_{i=1}^{N_T} \sigma_{h_i}^2}} \sum_{i=1}^{N_T} h_i h_i^* x_i(t) + n(t) \tag{1.16}$$

Thus the received SNR for MISO is

$$SNR_{MISO} = \frac{\left(\frac{1}{\sum_{i=1}^{N_T} \sigma_{h_i}^2}\right) \mathbb{E}\left\{\left[\sum_{i=1}^{N_T} |h_i|^2 x_i(t)\right]\left[\sum_{i=1}^{N_T} |h_i|^2 x_i(t)\right]^*\right\}}{\mathbb{E}\{|n(t)|^2\}}$$

$$= \frac{\mathbb{E}\left[\sum_{i=1}^{N_T} |h_i|^4 |x_i(t)|^2\right] + \mathbb{E}\left\{\left[\sum_{i_1=1}^{N_T} |h_{i_1}|^2 x_{i_1}(t)\right]\left[\sum_{i_2=1,i_2\neq i_1}^{N_T} |h_{i_2}|^2 x_{i_2}(t)\right]^*\right\}}{\sigma_N^2 \sum_{i=1}^{N_T} \sigma_{h_i}^2}$$

$$\tag{1.17}$$

By properly manipulating the received signals one can improve the SNR of the communication system. One method is by adding up the received signal from different transmit antennas coherently (in-phase) and by allocating more power to the transmit antenna with better gain. This technique of aligning the transmit signal as needed is called beamforming. Two more methods are there, in order to analyse those two methods, let us assume two cases in the equation 1.17.

In the first case $x_{i_1}(t)$ & $x_{i_2}(t)$ are different steams of symbols for $i_1 \neq i_2$ and are mutually independent with zero mean. This corresponds to the case of multiplexing. Thus, equation 1.17 can be written as

$$SNR_{MISO} = \frac{2\sum_{i=1}^{N_T} \sigma_{h_i}^4 \mathbb{E}\left[|x_i(t)|^2\right]}{\sigma_N^2 \sum_{i=1}^{N_T} \sigma_{h_i}^2} = \frac{2\sum_{i=1}^{N_T} \sigma_{h_i}^4}{\sum_{i=1}^{N_T} \sigma_{h_i}^2} \frac{\mathbb{E}\left[|x_i(t)|^2\right]}{\sigma_N^2} = \frac{2\sum_{i=1}^{N_T} \sigma_{h_i}^4}{\sum_{i=1}^{N_T} \sigma_{h_i}^2} SNR_T \tag{1.18}$$

From the above equation it is clear that the received SNR is doubled as compared with the SISO case, considering that all the links have the same fading power as the SISO link. Moreover, in this case the data rate of the MISO is N_T-times that of the SISO.

For the second case, let $x_{i_1}(t) = x_{i_2}(t)$ for all i_1 &ß$_2$ and all are of zero mean. This corresponds to the case of diversity combining. Here, we have

$$
\begin{aligned}
SNR_{MISO} &= \frac{\mathbb{E}\left[\sum_{i=1}^{N_T}|h_i|^4|x_i(t)|^2\right] + \mathbb{E}\left\{\left[\sum_{i_1=1}^{N_T}|h_{i_1}|^2 x_{i_1}(t)\right]\left[\sum_{i_2=1,i_2\neq i_1}^{N_T}|h_{i_2}|^2 x_{i_2}(t)\right]^*\right\}}{\sigma_N^2 \sum_{i=1}^{N_T}\sigma_{h_i}^2} \\
&= \frac{\mathbb{E}\left[\sum_{i=1}^{N_T}|h_i|^4\right]\mathbb{E}\left[|x_i(t)|^2\right] + \mathbb{E}\left\{\left[\sum_{i_1=1}^{N_T}|h_{i_1}|^2\right]\left[\sum_{i_2=1,i_2\neq i_1}^{N_T}|h_{i_2}|^2\right]\right\}\mathbb{E}\left[|x_i(t)|^2\right]}{\sigma_N^2 \sum_{i=1}^{N_T}\sigma_{h_i}^2} \\
&= \frac{2\sum_{i=1}^{N_T}\sigma_{h_i}^4 + \sum_{i_1=1}^{N_T}\sum_{i_2=1,i_2\neq i_1}^{N_T}\sigma_{h_{i_1}}^2\sigma_{h_{i_2}}^2}{\sum_{i=1}^{N_T}\sigma_{h_i}^2}\frac{\mathbb{E}\left[|x_i(t)|^2\right]}{\sigma_N^2} \\
&= \left(\frac{\sum_{i_1=1}^{N_T}\sigma_{h_i}^4}{\sum_{i_1=1}^{N_T}\sigma_{h_i}^2} + \sum_{i_1=1}^{N_T}\sigma_{h_i}^2\right)SNR_T
\end{aligned}
$$

(1.19)

Thus, the result shows the same as for the SIMO case, i.e., the SNR is increased exactly N_T-fold, by using the pre-processing technique and if the transmitter knows CSI and all the links in MISO have same fading power as that for SISO. These three methods of signal manipulation are explained in detail in the coming section (Section 1.2.3).

In both the SIMO and MISO antenna configurations, the usage of multiple antennas at either Txr or Rxr increases the system performance, but with a limitation in number of antennas (refer Fig. 1.12). In order to overcome this limitation one has to use multiple antennas at both Txr & Rxr (MIMO).
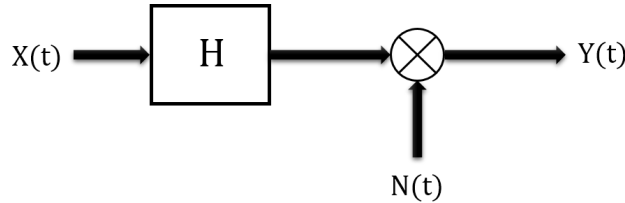
Fig. 1.14 Input-Output relationship of MIMO

For a MIMO case the input-output relationship can be schematically expressed as in Fig. 1.14 and can be formulated as

$$
Y(t) = H\ X(t) + N(t),
$$

(1.20)

where, $H \in C^{N_T \times N_R}$ is the channel matrix, where its entries have the magnitude and phase information of the propagation paths between the N_T transmitter ports and N_R receiver ports, $X(t) \in C^{N_T \times 1}$ are the transmitter symbols, $Y(t) \in C^{N_R \times 1}$ are the received symbols and $N(t \in C^{N_R \times 1})$ are the AWGN noise components. Notice that the channel matrix H is of the form

$$H = \begin{bmatrix} h_{11} & \ldots & h_{1N_T} \\ \vdots & \ddots & \vdots \\ h_{N_R 1} & \ldots & h_{N_R N_T} \end{bmatrix}$$

where, h_{ij} describes the channel coefficients between the jth transmit and i^{th} receive ports. If we are expressing H in the singular value decomposition form [75], then

$$H = U\Sigma V^*, \tag{1.21}$$

where, $U \in C^{N_R \times N_R}$ and $V \in C^{N_T \times N_T}$ are unitary; $\Sigma = [\sigma_{ij}]$ is an $(N_R \times N_T)$-dimensional non-negative and diagonal matrix ($\Sigma \in R^{N_R \times N_T}$) in the sense of $\sigma_{ij} = 0$ for all $i \neq j$. The properties of diagonal entries are $\sigma_{11} \geq \sigma_{22} \ldots \sigma_{N_{TR} N_{TR}} \geq 0$, where, $N_{TR} = min\{N_T, N_R\}$ is the rank of channel matrix H and the diagonal entries of Σ (i.e., $\sigma_{11}, \sigma_{22} \ldots \sigma_{N_{TR} N_{TR}}$) are the non-negative square roots of the eigen values of HH^*, the columns of U are eigen vectors of HH^* and the columns of V are the eigen vectors of H^*H. If the knowledge of CSI (i.e., H) is available at both the Txr and Rxr, the pre-processing and post-processing of the transmitted signal and receive signal, respectively, can be done in the following way.

$$\bar{X}(t) = V^*X(t), \ \bar{Y}(t) = U^*Y(t), \tag{1.22}$$

where, $\bar{X}(t)$ & $\bar{Y}(t)$ are the processed transmit and receive signals, respectively. Then

$$\bar{Y}(t) = \Sigma\bar{X}(t) + U^*N(t) \tag{1.23}$$

It is clear from the above equation that, the new MIMO channel is equivalent to N_{TR} independent channels each having the same bandwidth. By using spatial multiplexing data transmission rate can be increased N_{TR}-fold with the SISO

channel. The channel capacity of an instantaneous MIMO channel when the transmitter does not have the knowledge of CSI is given by

$$C = \log_2 \left| I + \frac{SNR}{N_T} HH^* \right|, \tag{1.24}$$

where, $I \in C^{N_R \times N_R}$ is the N_R-dimensional identity matrix. When the CSI is known to the receiver then equation 1.24 can be expressed as

$$C = \sum_{i=1}^{N_{TR}} \log_2 \left(1 + \frac{SNR}{N_T} \sigma_{ii}^2 \right) \tag{1.25}$$

Thus, from above equations we can see that the ergodic channel capacity of MIMO channel is increased N_{TR}-fold compared with the SISO channel. Thus, the MIMO technology can yield a considerable gain in the system performance compared with the SISO system.

1.2.3 MIMO Communication Techniques
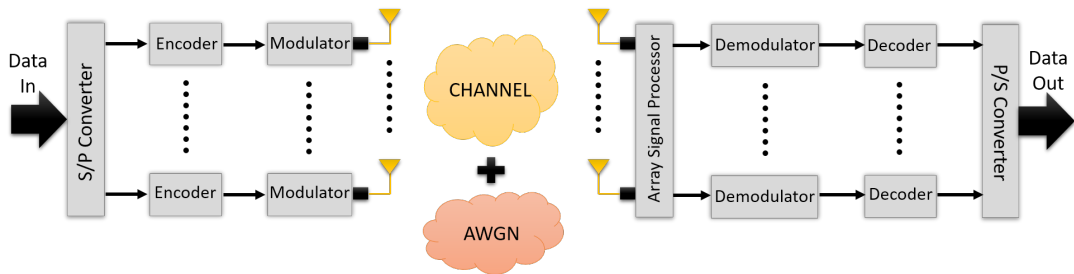
Fig. 1.15 A wireless communication system using MIMO technology

A block diagram of a typical MIMO based wireless communication system is shown in Fig. 1.15. As observed from the figure, multiple antennas are employed at both transmitter and receiver (MIMO). Here, the information streams from a particular information source are given to transmitter section where these data streams undergoes proper encoding and modulation and are then passed to the different antennas for transmission. These transmitted data streams are transferred to the receiver through a propagation channel, where the signal is got effected by some AWGN. Due to the presence of many obstacles in the propagation

environment the data streams undergoes multiple reflections, refractions etc. and takes multiple paths for their way to the receiver. Thus, each streams will have a unique signature for the channel path it takes, which can be distinguished at the receiver using adequate signal processing. These multiple data streams will be received by multiple antennas at the receiver and are demodulated and decoded in order to reproduce the original information data.

The MIMO communication system improves the performance of a wireless link by using some antenna techniques. Mainly, there are 3 flavours of antenna techniques with respect to how data is being transmitted across the given channel. These are:

1. Diversity

2. Spatial Multiplexing

3. Beam-forming

Diversity Technique

The principle of diversity technique is to send the same information across independent fading channels to combat fading i.e., it will provide the receiver with multiple versions of the same signal. When multiple uncorrelated copies of the same data are sent across independent fading channels, the amount of fade suffered by each copy of the data will be different. This guarantees that at-least one copy will suffer less fading compared to the rest of the copies. Thus, the chances of properly receiving the transmitted data increases. In effect, this reduces the signal degradation considerably, and effectively increases the link robustness by improving the reliability of the entire system. This also reduces the co-channel interference significantly. One can classify the existing diversity techniques into three categories:

- **Temporal Diversity** : This is also known as time diversity. Here, multiple copies of information are sent on different timeslots. This time slots are designed in such a way that the delay between the signal replicas should be greater than the Coherence Time (T_C) of the channel. Where, Coherence Time (T_C) is the statistical measure of the time duration over

which the channel impulse response is essentially invariant, and quantifies the similarity of the channel response at different times. This condition will produce uncorrelated data copies in uncorrelated channels over those time slots. In particular, time diversity uses error-correcting coding & interleaving techniques which breaks the channel memory into multiple chunks there by spreading and minimizing the effect of deep fade. But this technique consumes extra transmission time.

- **Frequency Diversity** : In this technique signal replicas are sent across different frequency bands. In order to create uncorrelated channels for transmission, each frequency bands should be separated by at-least the Coherence Bandwidth (B_C) of the channel. Where, Coherence Bandwidth (B_C) is the range of frequencies over which two frequency components have a strong potential for amplitude correlation. Thus, the level of fading experienced by each frequency bands are different and at-least one of the frequency bands will experience less amount of fade. Orthogonal Frequency-Division Multiplexing (OFDM) and Spread Spectrum uses this principle for data transmission. The main drawback of this technique is that it requires extra bandwidth for an effective data communication.

- **Antenna Diversity** : The main idea behind antenna diversity technique is to produce different replicas of the transmitted signal to the receiver by incorporating multiple antennas at the transmitter and/or receiver. This produces statistically independent signals from each antenna and when one or two of them fades, it is less likely that the other copies will be in deep fade simultaneously. Antenna diversity can be classified according to which physical mechanism is used to produce the uncorrelated signals from each antenna elements. Generally, there are 3 kinds of antenna diversity, which exploits the inherent Degrees of Freedom (DoF) of multipath propagation environment, however, are inherently interrelated:

  - Spatial Diversity

  - Polarization Diversity

  - Angle (Pattern) Diversity

Spatial diversity employs multiple antennas at transmitter and/or receiver, usually with same characteristics, that are physically spaced apart by a particular distance. Thus, the magnitude of the radiation pattern at each antenna port is essentially the same, but the phase patterns relative to a common co-ordinate system are such that the resultant radiation patterns of each antenna elements become orthogonal. In order to achieve statistically uncorrelated signals i.e., to experience a different fading pattern in the radio environment, a minimum distance is required between the antenna elements, which is determined by the fading environment through which the signal propagates.
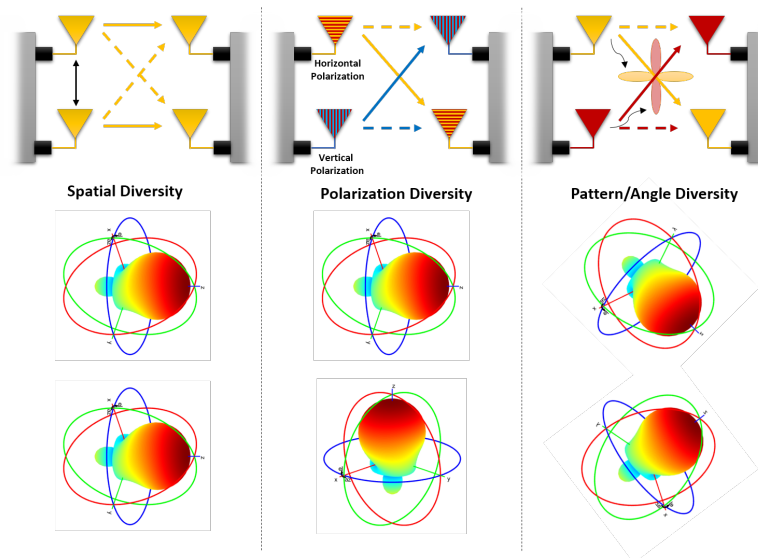
Fig. 1.16 Different antenna diversity techniques

Polarization diversity combines pairs of antennas with orthogonal polarizations (i.e., horizontal/vertical, ±slant 45°, left-hand/right-hand circular etc.) to radiate energy. This principle is based on the fact that the propagation characteristics of a wireless medium will not be same for differently polarized waves. Moreover, the reflections of the transmitted signal can undergo polarization changes depending on the medium through which they are travelling, thus, dispersing some of its energy to the other polarized signals. Due to this, a linearly polarized transmitted waves can come at the receiver end with an additional non-trivial orthogonal component. Thus,

by pairing two complementary polarizations, this technique can immunize a system from polarization mismatches that would otherwise cause a signal fade. Additionally, such diverse schemes has proven valuable at mobile and radio communication base stations since it is less susceptible to the near random orientations of transmitting antennas. The utilization of dual-polarized antenna (or multi-polarized antenna), in which the same antenna has two orthogonal components (co-polarized & cross-polarized), made this technique very popular since antenna installation space is minimized and mobile terminals can experience reliable communication in-spite of the angle of tilt of the handset.

Angle/Pattern diversity is an antenna diversity technique which imposes orthogonality by producing spatially disjoint radiation patterns. This is done by shaping the radiation patterns associated with different antenna elements. Usually, this technique consists of two or more antennas with different directive radiation patterns, that are physically separated by some distance. The radiation patterns of each antenna will be directed towards different directions, thus producing statistically independent replicas of the transmitted signal. Collectively, they are capable of discriminating a large portion of angle space and can provide a higher gain compared to a single omni-directional radiator. To generate pattern diversity, one can use: multi-mode antennas, where the antennas do not necessarily need to be separated by a physical distance; or external beam-forming networks (which will be discussed in the coming section).

All these three antenna diversity techniques and their corresponding radiation pattern appearances are depicted in Fig. 1.16. This classification is rather arbitrary and for most cases a combination of all these techniques may present on antenna diversity systems. This thesis mainly focuses on the design & development of antennas comprising these antenna diversity methods and its corresponding characteristic analysis.

In general, a MIMO communication system employing the diversity technique transmits the same information across different independent fading channels in order to reduce the probability that all the data copies undergo deep fade, simultaneously. As a result, the Symbol Error Rate (SER) of data transmission
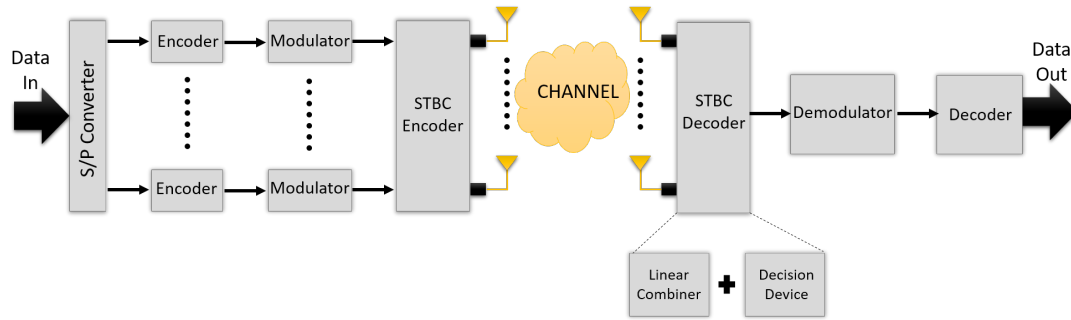
Fig. 1.17 Diversity based MIMO communication system

will be reduced considerably. The block diagram of such a diversity based MIMO system is shown in Fig. 1.17. As observed from the figure, the data to be transmitted undergoes the conventional ways of error-correction coding and modulation before it follows any diversity technique for transmission. Here, the diversity transmission and reception using Space-Time Coding (STC) is discussed (refer Fig. 1.17). STC ia a well-known diversity technique in which both the space and temporal diversity methods are being utilized in order to achieve the maximum gain and lowest error probability [196]. To do so, an STBC (Space-Time Block Coding) encoder sends multiple copies of data symbols from different antennas in different time slots. At the receiver, the multiple receiving antennas will receive these independently faded multiple data streams and loads it to the STBC decoder, where, it will undergo some linear combining and decision-making process. Followed by this the conventional demodulation and error-decoding procedures will take place to decode the original data bits. It is assumed that the CSI is known at the receiver and in most cases, it can be assumed as a perfect channel. But, in reality, CSI is obtained through channel estimation technique [165] or by some other methods [80].

In diversity method, it is less likely happened that all the data streams undergo deep fade, simultaneously. So these data streams are effectively combined (in the STBC decoder) using any of the following combining techniques:

- Switched Combining (SWC)

- Selection Combining (SC)

- Maximal Ratio Combining (MRC)

- Equal Gain Combining (EGC)

SWC method picks an antenna and uses it until the SNR falls below a threshold value. If the signal drops below the threshold, it switches to the next antenna that satisfies the threshold criteria. This method does not monitor all the branches, hence, it is cost effective as only one RF chain is needed at a time, but is less efficient as there is a possibility of a higher SNR branch goes unchecked. SWC is the only combining method that does not require the knowledge of CSI at the receiver. On the other hand, SC picks the signal branch with the highest SNR by monitoring all the branches simultaneously, and hence, it needs N_R RF chains [81]. MRC is a most widely adopted combining method, in which, the N_R signals are combined coherently at the receiver [222]. These signals are previously weighted with its complex conjugates, according to their SNR, in order to get a constructive combination. Thus, for MRC also N_R RF chains are needed for an effective combination. EGC method is a variant of MRC, where each signal chain is weighted with the same factor, irrespective of the signal amplitude. However, co-phasing of all signal is needed to avoid signal cancellation. MRC outperforms EGC, although it is easier and cheaper to implement than MRC. The main difficulty in MRC is the need of a perfect channel information estimation (both magnitude & phase), which is difficult to attain in practice.

Spatial Multiplexing (SM) Technique

According to Shannon's Channel Capacity theorem (refer equation 1.1) there is a limit on the capacity of a channel for a given bandwidth. The capacity is also limited by the SNR of the received signal. However, by using higher modulation scheme we can certainly increase the channel capacity, but for that we need to have high SNR. This trade off is difficult and expensive to be compromised. Therefore, it is necessary to look at other ways of improving the data throughput of the wireless link. Using Spatial Multiplexing (SM) one can effectively improve the link capacity and spectral efficiency. In this technique, multiple antennas are used at both Txr & Rxr to maximize the throughput of the system. Here, the data stream to be transmitted is multiplexed (or divided) among the several antenna branches to transmit via several independent channels. Thus, each spatial channel carries independent information and thereby increases the data

rate of the system under comparable SNR conditions. This can be compared to the Orthogonal Frequency-Division Multiple Access (OFDMA), where, different frequency sub-channels carry different parts of the modulated data.
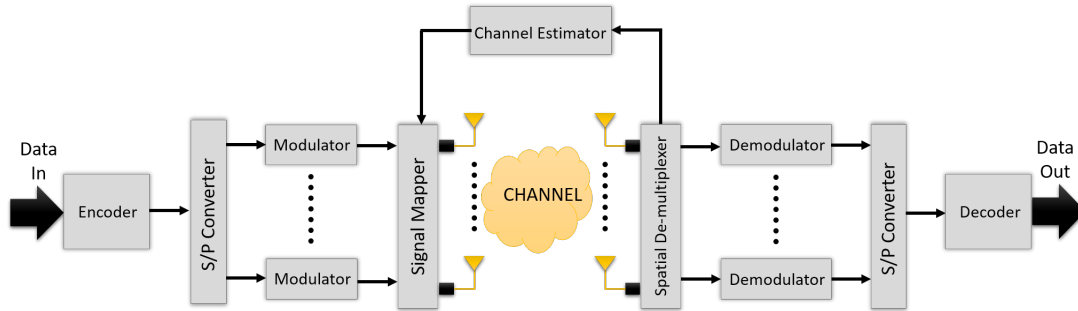
(a) Block diagram representation
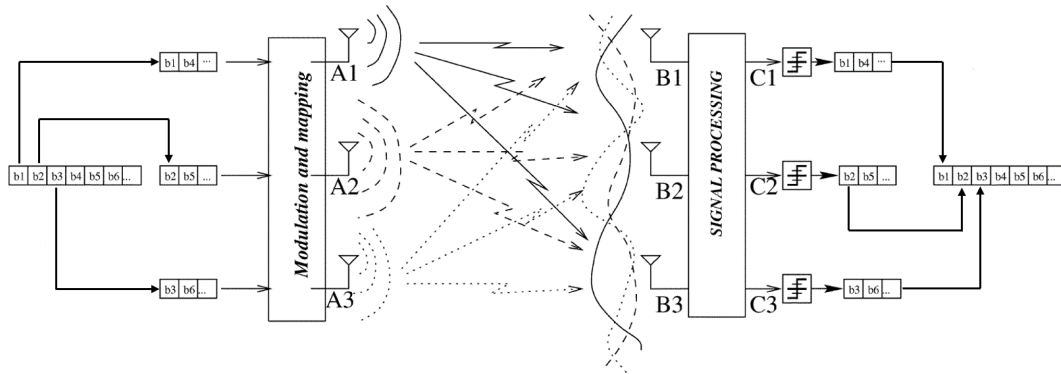
(b) Basic spatial multiplexing scheme [68]

Fig. 1.18 Spatial Multiplexing based MIMO communication system

Here, in SM, if the scattering by the environment is rich enough, several independent sub-channels are created in the same allocated bandwidth and these channels carry the different parts of the modulated data. Thus, a better multiplexing gain is attained at no additional cost on bandwidth and/or power. In a system with N_T transmit antennas and N_R receive antennas, often known as $N_T \times N_R$ spatial multiplexing system, the peak multiplexing gain is proportional to $min(N_T, N_R)$. This multiplexing gain in a MIMO configuration governs the overall capacity (data rate) of the system. A block diagram of such a SM based $N_T \times N_R$ MIMO communication system is shown in Fig. 1.18. As observed from the figure, the error encoded information bits are multiplexed (divided) into N_T-parallel data streams using a serial-to-parallel converter and are individually

modulated before transmitting it over different antennas. To recover the original data at the receiver it is necessary to perform some amount of signal processing. This is done by a SM decoder or Spatial demultiplexer. First, SM decoder will estimate the individual transfer characteristics (h_{ij}) to determine the channel transfer matrix. Once this has been estimated, the matrix [H] are produced and the transmitted data streams can be reconstructed by multiplying the receive vectors with the inverse of the transfer matrix ([H]$^{-1}$). These data streams are then demodulated individually and are combined appropriately to reconstruct the original information bits.

One can increase the link capacity by performing spatial multiplexing with and without the knowledge of CSI at the transmitter (i.e., closed-loop and open-loop, respectively). If CSI is not known to the Txr, the channel capacity increases linearly with the number of antennas, whereas, if the CSI is known to the Txr, the channel capacity can be further increased by some power allocation (using water-filling method) to the transmit antennas [39, 47].

Beamforming Technique

Beamforming is one of the advanced MIMO technique to enhance the throughput significantly. With the development of more adaptive systems and greater level of processing power it is possible to utilize this antenna beamforming technique to increase the coverage of transmitter. This enables directional signal transmission or reception without manually steering the antennas; and the antennas utilizing this technique is known as smart antennas. In this technique, several transmitters are set apart from one another, and they transmit same signal with different phase and delay. Here, a digital signal processor located at the receiver plays a crucial role by working in conjunction with antenna array to select the desire communication path. This enables the system to focus the radiation pattern in the desired direction and/or directions. The principle of beamforming is to weight the transmit signals in such a way that the receiver obtains a constructive superposition at different signal parts. For a feasible beamforming to happen, the knowledge of CSI is essential, both at the transmitter and receiver. At the receiver, based on the time delays of the impinging signals on the antenna elements, the digital signal processor computes the Direction-of-Arrival (DoA)

of the Signal-of-Interest (SoI) and it adjusts the gains & phases of the signal to produce a radiation pattern focusing on the SoI while tuning out the interferers (i.e., Signal-not-of Interest (SnoI)). This increases the SNR level at the receiver and will increase the area that can be covered by the transmitter.

(a) Switched Beam pattern coverage   (b) Adaptive Array approach
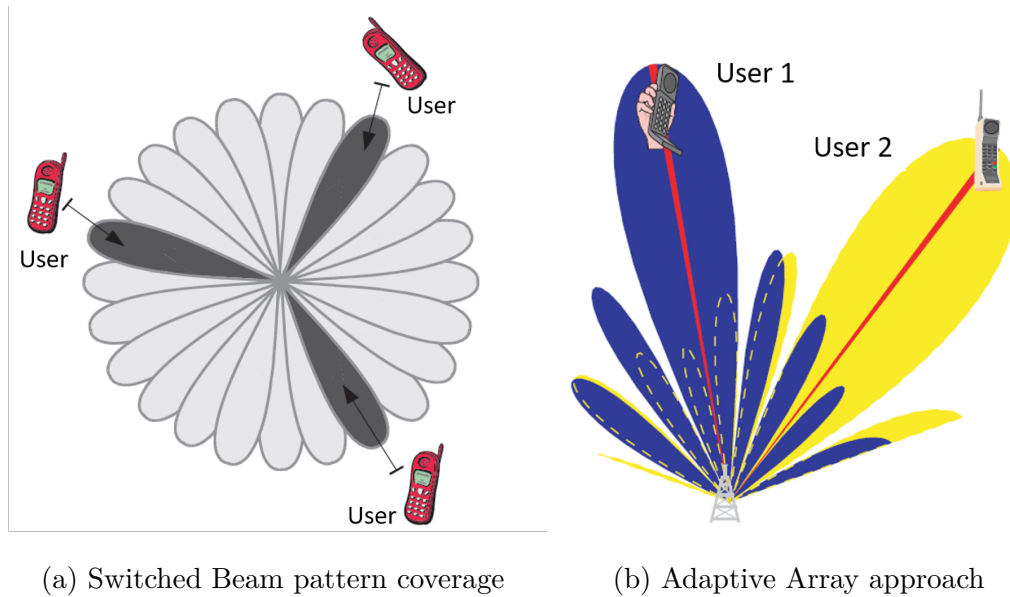
Fig. 1.19 Different smart antenna concepts [23]

This beamforming can be accomplished in a wireless communication system by utilizing two major configurations of smart antennas [164].

- Switched Beam Antennas

- Adaptive Array Approach

A switched beam method is the simplest smart antenna technique. It forms a finite number of fixed beams with an increased sensitivity in particular directions. Such an antenna system chooses one of the several predetermined fixed beams by detecting the signal strength and switches from one beam to another as the user moves throughout the sector, as shown in Fig. 1.19a. This method is based on a typical switching function and is able to select the beams that gives strongest received signals (with high SNR). Another way to realize the beam-switching is by phased array method. Here, by changing the phase differences of the signal fed to the antenna elements or received from them, the main beam can

be driven in different directions throughout the space. Thus, the switched beam system combines the pattern multiple antennas in such a way as to form narrow directional beams with greater spatial selectivity than can be achieved with conventional (single-element) approach.

Although, switched-beam method is simple and cost-effective, it lacks flexibility as only a limited number of fixed directions can be selected. Thus, there is a risk that the exact direction with highest SNR goes missing. Also, it does not fully reject the direction of SnoI or interference.

Adaptive antenna approach provide more degrees of freedom, since it can customize an appropriate radiation pattern in real time for each individual user. They can direct the main beam towards the SoI, while, suppressing the antenna patterns in the direction of interferers or SnoI, as illustrated in Fig. 1.19b. Adaptive arrays utilize sophisticated signal processing algorithms to continuously track the desired signals and interfering signals, and thereby dynamically adjusts the antenna patterns such that the main beam is in the direction of desired user and the nulls in the direction of interferers. Due to this accurate tracking and robust interference rejection capabilities multiple users can share the same conventional channel within the same cell. As a result, the capacity of the overall system will be enhanced effectively. Fig. 1.19b shows an adaptive antenna approach, where two users uses the same cell on the same conventional channel, simultaneously.
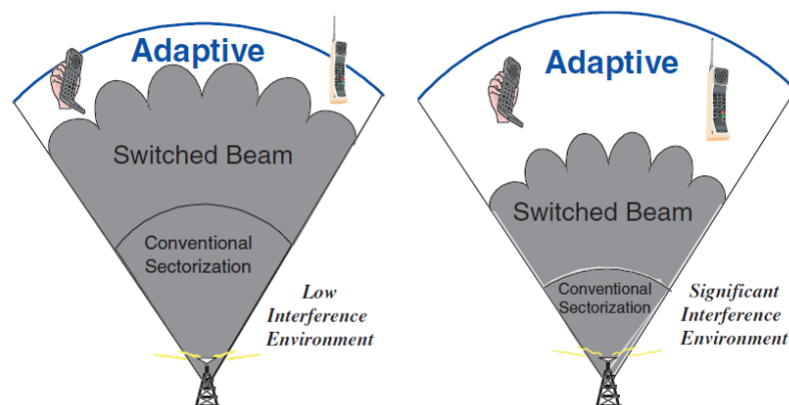
Fig. 1.20 Coverage patterns for Switched Beam & Adaptive Array approach [23]

Fig. 1.20 illustrates the relative coverage area for conventional sectorized, switched-beam and adaptive antenna systems. Both the switched beam and adaptive antenna technique provides significant gains over the conventional sectorized systems in the low-level interference scenario. However, for a high-level interference environment the interference rejection capability of the adaptive systems override the coverage area that either the conventional or switched beam systems can attain.

1.3   State-of-the-Art UWB-MIMO

The wireless communication is always an ever growing child which keeps on evolving with the advance technologies, standards and algorithms. This evolutionary race is the main motivation behind the entire research persons in the world to go ahead with new outcomes. The high data rate within a reliable wireless link is always the primary area of concern in the modern era of wireless communications. Day-by-day the people are becoming greedy and are in need of more-and-more data rate. Such a situation can be handled by using some more advanced technologies like UWB-MIMO, a combination of UWB & MIMO, [92].

We had already discussed the UWB systems and MIMO technologies in detail, in the previous sections. As is well-known, a UWB system as such is potential to increase the data transmission rate, because as per Shannon-Hartley theorem a wide channel bandwidth can guarantee a good channel capacity and high data rate. So there arise a question on the need of combining the UWB with MIMO, yet another potential technology which improves data rate & capacity of the wireless link. A simple answer to this question is that it is all due to the general greed of the people who needs even higher data rate and best quality of communication. But this is not the whole picture of the problem. UWB technology is mainly devoted for WPAN & WBAN communications, which will mostly occur in rich scattering indoor environments. Although, the UWB itself offers rich diversity due to its abundant multipath, the dense multipath propagation along with its transmit power limitation (by FCC) will make things difficult. An intelligent remedy for this problem is to exploit these scattering environments in such a way that it avoids the detrimental Inter Symbol Interference (ISI) to a great extent and improves the data rate and reliability of the communication link,

effectively. This can be accomplished by employing multiple antennas at both the transmitter and receiver side, which is termed as MIMO.

Generally, UWB systems are limited to short distance communications due to its very low transmission power limitation, allocated by FCC. Incorporating MIMO with the UWB extends the communication range as well as offers a reliable & robust wireless link. Moreover, the power limitations for UWB systems further limits the data transmission rate, which is not appreciable. Combining the MIMO technique into UWB provides a viable solution to this bottleneck problem [191]. By using STC (Space-Time Coding) technique in UWB systems, the power for a specific transmitted symbol can be strengthened, while keeping the overall transmitted power same as that of a single transmit antenna system, thus satisfying the FCC power regulation. And, if a beamforming technique is utilized, we can increase the signal power in a specific direction and may violate the FCC power spectral mask in that direction, but the power in all other directions will be the same as that without using the beamforming technique.

According to Edholm's law of data rate, within a couple of years several gigabits/second of indoor data rate will become a reality. Although, UWB itself provides an enormous bandwidth and thereby a rich time domain diversity, even more bandwidth will be required to fulfil the needs of near future. Therefore, if we are able to prove that the channel capacity of the UWB systems is directly proportional to the number of antennas employed at transmitter and/or receiver, data rate can also be increased further, without sacrificing additional bandwidth or power. This points out that the combination of UWB and MIMO will be a breakthrough in the modern wireless communication. Thus, the major benefits of a UWB-MIMO communication system can be summarized as, [36, 43], :

- Interference mitigation

- Higher data rate

- Improved link quality

- Extended coverage

- Reduced analogue hardware requirements

- Concurrent localization

1.4 Motivation & Scope of the Research

Wireless communication is one of the most vibrant areas in the communication field today. Although, it has been a topic of study since 1960s, the past few decades has seen a surge of research activities in this area. This is due to the demand for a robust and highly reliable wireless link, which can replace the conventional wired communication service, effectively. This can happen with the confluence of several factors like commendable data rate, good spectral efficiency (channel capacity), high Quality of Service (QoS), low Bit Error Rate (BER), low interference,wide coverage range and low deployment, operation & maintenance cost. The research community keeps-on contributing their efforts, in full-hand, to fulfil these requirements. Shannon-Hartley theorem made a brilliant breakthrough in the way communication theory was viewed in the early days and described the possibility for a high rate error-free digital data transmission over the communication channel with a specific bandwidth, in the presence of noise. According to this theorem, a wide channel bandwidth can guarantee a good channel capacity & high data rate, without invoking a higher transmitted power. This gave birth to the UWB systems which is a promising technology for many applications, due to its extremely wide bandwidth from 3.1-10.6 GHz (by FCC). However, its limitation in the power spectral density subsided the maximum possible data transmission rate and reduced the SNR level at the receiver, which deteriorated the communication in rich scattering environments. As a remedy to this problem researchers incorporated MIMO technology into UWB systems. It is a well known fact that MIMO mitigates the vulnerable multipath fading problem by taking advantage of the rich scattering environment. This helps to achieve a reliable high-rate error-free data transmission in a UWB communication system, even in the harsh wireless propagation environments. However, UWB-MIMO is still in its research infancy. This is because, the literature is scant of UWB-MIMO studies, as compared to the volumes of literature available for the narrowband MIMO research. Some researchers have considered the UWB channel measurements [95] and the full characterization of the spatial correlation of UWB channels [137] for multi antenna systems. But these studies only investigated the systems from either isolation or capacity perspective. Consequently, design of multi-antenna systems for UWB applications is extremely challenging especially

in low profile devices, where the size is a big constraint. In the context of such devices the size, bandwidth and inter-element isolation are so stringent that often efficiency and gain are sacrificed to fulfill the specifications. Thus, providing a UWB-MIMO system with low profile terminal devices having multiple antennas in it, which offers a good gain and efficiency by retaining low mutual coupling between the antenna elements in the entire operating band is a tough question to be addressed. Motivated by this, the thesis focuses on the design of compact & efficient UWB-MIMO antennas which provides high isolation between antenna elements. It aims at the development and detailed analysis of such novel antennas which is suitable for UWB applications.

1.5   Thesis Organization

This thesis presents an exhaustive study of the multiple-antenna systems devoted for UWB applications. This includes the design & development of such antennas, and also the detailed analysis to check the adaptability of those antennas for a UWB-MIMO communication system.

Chapter 1 brought forward the overall introduction to a UWB-MIMO technology. This chapter presented some basic trends in wireless communications, which lead to the invention of two leading technologies in wireless history : UWB and MIMO. Further, it explained about the basics of UWB systems and the principle behind the MIMO technology. Moreover, this chapter discussed the need for a combination of UWB & MIMO systems and its concern in the present wireless communication era.

Chapter 2 showcases the chronological history of both UWB & MIMO antennas. It also deals with a survey of the previous works done in the area of UWB-MIMO antennas, for understanding various approaches used in the past for achieving considerable isolation between antenna elements. This chapter also points out the novelty of the present work along with trending analysis techniques dedicated for UWB & MIMO systems.

Chapter 3 highlights the methods adopted to characterize the antennas employed in this thesis. These include the pre-fabrication studies, fabrication method, measurement facilities and different analysis strategies used for the antennas. In addition to the conventional frequency-domain parameters, the

transient transmission/reception characterization of antenna with the adequate time-domain parameters are also included in this chapter, to get knowledge on the pulse handling capability of the designed antennas. Moreover, the pulse correlation method of analysing the pattern stability of the antenna is detailed with corresponding spatial-domain parameters. To get a better understanding of the antennas in terms of its performance in a MIMO communication system, adequate figures-of-merits which projects the suitability of an antenna in such systems are also presented in this chapter. Further, this chapter witnesses the exploitation of Agilent SystemVue to evaluate the channel performance of communication system using the designed UWB-MIMO antennas.

Chapter 4 deals with the whereabouts of two novel compact coplanar antennas designed for UWB operation. Their optimized designs along with the conventional reflection/transmission coefficients and radiation characteristics are presented in this chapter. Also, the transient response of the antenna when subjected to an input pulse of specific standards and the corresponding time-domain analytic parameters are discussed in this section. The information regarding pattern stability analysis of the UWB antennas in spatial-domain are also included in this chapter. This section portrays both theoretical and experimental conclusions of the above mentioned analytic outcomes of the antennas.

Chapter 5 is the essence of this thesis, which discusses the several aspects of collocated multi-port UWB antenna for MIMO operation. Initially, it discusses the isolation mechanism or diversity technique adopted to lower the mutual coupling between the different antenna elements of a multi-port UWB antenna. This chapter includes the details of three different multi-port UWB antennas: two-port, three-port & four-port UWB-MIMO antennas. In addition to the conventional frequency-domain analysis, the transient response and the pulse correlated pattern analysis of the antennas to check the credibility of them in ultra-wideband operation is also showcased in this chapter. Further, this chapter presented various figures-of-merits portraying the MIMO/diversity performance of the antennas employed in this, along with their adequate comparison. All the experimental and theoretical investigations of the designed UWB-MIMO antennas are discussed in detail with appropriate validations.

Chapter 6 is an add-on to the chapter 5, as it portrays the channel performance evaluation & comparison of the various designed UWB-MIMO antennas with

respect to their channel behaviour. For the channel evaluation a two-stage Over The Air (OTA) method is utilized, where the radiation patterns obtained in a Single-Input Single-Output communication system can be used. This chapter introduces the exploitation of a new software named Agilent's SystemVue from Keysight Technologies as a channel emulator to create a real channel faded signal, for obtaining various MIMO channel parameters.

Chapter 7 summarizes the major findings came out of the study conducted on different antennas presented in the thesis and also shares some thoughts about the future scope of the work.

In the Appendix, details of a modified Bow-tie antenna designed for Digital Video Broadcasting-Handheld (DVB-H) applications and an open stub loaded high gain Asymmetric Coplanar Stripline (ACS) antenna compatible for IEEE802.11a, HIPERLAN2, HiSWANa, WiMAX (IEEE802.11e) & ISM 5.8 application bands are discussed.

Chapter 2

Literature Review

Ultra-WideBand (UWB) technology became very popular and gained a commendable interest during the early decades of the wireless communication era. The history of UWB antennas commenced with the introduction of various huge UWB antennas by Oliver Lodge in 1898, which includes spherical dipoles, square plate dipoles, triangular or bow-tie dipoles and bi-conical dipoles. Out of those, Lodge's bi-conical antenna, [129] that is shown in Fig. 2.1a, got used up in transmit-receive links in early days. After his inventions, different types of UWB antennas were developed in the coming years. P.S. Carter, in 1939, [35] rediscovered the Lodge's bi-conical antenna & conical monopole, to improve its broadband performance by incorporating a tapered feed (refer Fig. 2.1b). After that, in 1941 N. E. Lindenblad proposed the design of a coaxial horn [126], which became a well-known antenna for UWB performance during those periods. To improve its wideband performance Lindenblad implemented a continued impedance change in the antenna, by adopting the sleeve dipole design, as shown in Fig. 2.1c. Later, Lee Paulsen developed a similar antenna [113] and named it volcano smoke antenna (refer Fig. 2.1d), which found significant role as the cornerstone of television development. Investigations on this antenna pointed out that the bulging-monopole like structures yields an impedance bandwidth ratio of 5:1.

The development in the conventional UWB antennas continued with works of many researchers such as omni-directional and directional coaxial horn by L. N. Brillouin [29], bow-tie antenna which is originally proposed by Lodge and

later rediscovered by G. H. Brown & O. M. Wood Ward, inverted triangular dipole (diamond antenna) by R. W. Masters [141], elliptical monopole and dipole antennas by W. Stohr [185], vivaldi antenna (tapered slot antenna) by P. T. Gibson [69] etc.. These types of conventional UWB antennas found application in broadband communication areas, but are not very suitable for some high frequencies modern communication applications due to their bulky structures, manufacturing cost & integration difficulties. This made the researchers to invent some novel types of omni-directional UWB antennas from the principles of conventional UWB antennas, having small profile and wider operational bandwidth. They were mainly classified into two as : Planar & Printed UWB monopole antennas. Both of them succeeded in providing wider bandwidth and same radiation performance as that of the conventional UWB antennas, but with much smaller volumes.

The research on planar monopole antenna was initiated by G. Dubost & S. Zisler in 1976 [57], by replacing a conventional wire monopole with a planar monopole, which is located above a ground plane and usually fed using a coaxial probe. Some basic planar monopole antenna structures are depicted in Fig. 2.2. Agrawall et al [145] carried out a bandwidth comparison of these different planar monopoles such as, circular, elliptical, rectangular & trapezoidal monopoles and found that circular & elliptical monopoles exhibit much wider impedance bandwidth (circular: 1.17—12 GHz, elliptical: 1.21—13 GHz) than other geometries. Later, Evans et al [63] proposed that trapezoidal planar monopole structures were also capable of exhibiting good bandwidth ratio of 11:1. In addition to the basic geometries, Suh et al [172] presented a new interesting structure named as planar inverted cone antenna (PICA) which offers an impedance bandwidth ratio of 10:1 (Fig. 2.2d). Out of these various planar monopole structures, square monopole is the simplest one and is flexible in terms of its impedance matching, i.e., its impedance matching bandwidth can be varied by incorporating several techniques such as notching (Su et al [166]), bevelling (Peyrot-Solis et al [182]), double feeding (Antonino-Daviu [58]), trident-shaped feeding (Wong et al [102]) etc., as listed in Fig. 2.3.

These afore mentioned planar monopole UWB antenna need a perpendicular ground plane for their proper working which will be an inconvenience factor while dealing with the Monolithic Microwave Integrated Circuits (MMICs). For such

(a) Lodge's bi-conical antenna, [129]

(b) Carter's bi-conical antenna, [35]

(c) Lindenblad's coaxial horn, [126] (d) Volcano smoke antenna, [113]
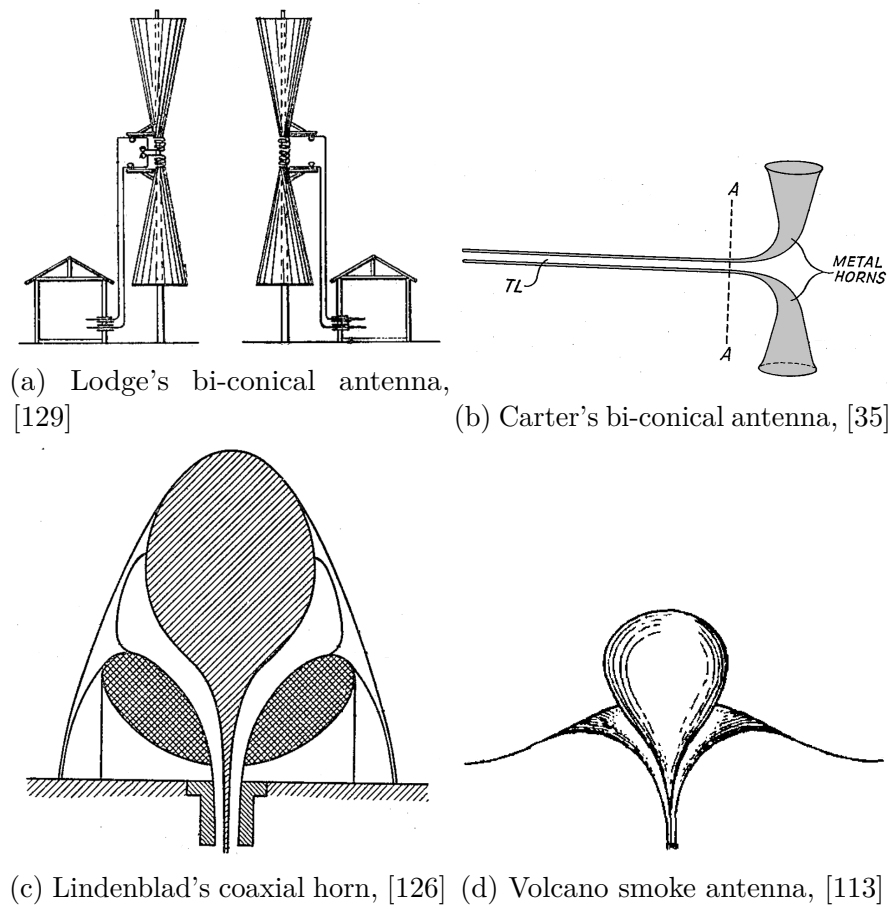
Fig. 2.1 Different conventional UWB antennas

(a) Circular   (b) Elliptical   (c) Trapezoidal   (d) PICA
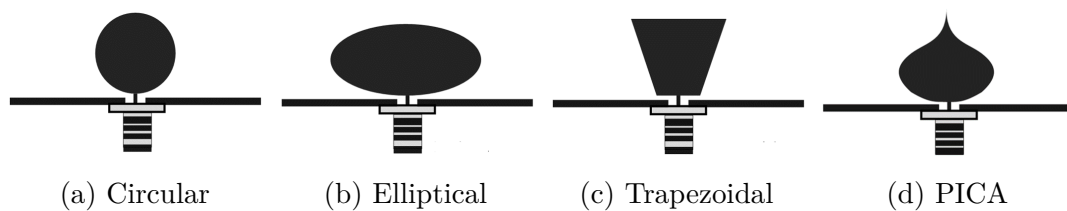
Fig. 2.2 Basic geometries of planar monopole antennas, [123]

portable wireless device applications these planar monopole structures seems to be bulkier and difficult to integrate. Moreover, introduction of source pulses in the UWB wireless communication systems, in 2003, made the antenna design considerations to effect significantly. At this point, the printed UWB monopole structure came into being, commonly with a monopole and a ground plane printed

(a) Square (b) Notching (c) Beveling

(d) Double feed (e) Trident-shaped
feed
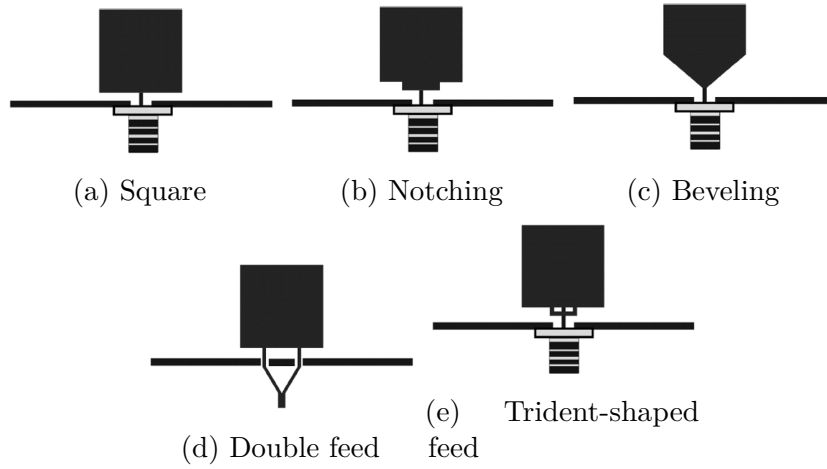
Fig. 2.3 Various wideband techniques, [123]

(a) Circular (b) Octagonal (c) Spline-shaped (d) U-shaped
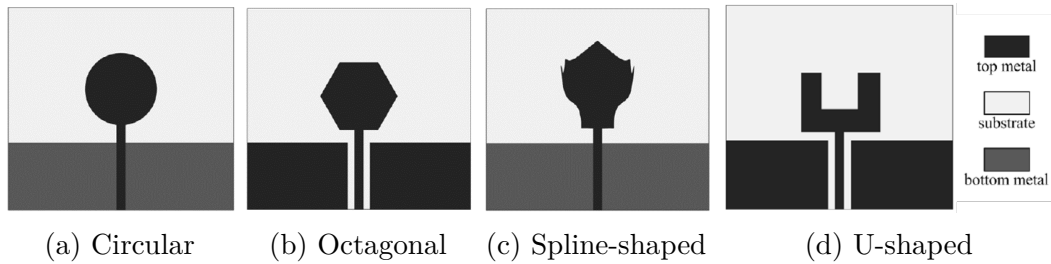
Fig. 2.4 Basic printed monopole structures, [123]

on the same or opposite side of a dielectric substrate, and having a microstrip or Coplanar Waveguide (CPW) feed-line to excite the monopole patch. Choi et al [171] were the first to introduce these types of printed monopole antenna with wideband characteristics, in 2004. Some printed monopole structures are depicted in Fig. 2.4. Out of all the representative structures, the printed circular monopole antenna [88] is the simplest and commonly used one, because of its satisfactory radiation performance and an impedance bandwidth ratio of 3.8:1 (2.69-10.6 GHz). However, other monopoles such as octagon monopole [61], spline-shaped monopoles [114], U-shaped monopole [85], Knight's helm shaped monopole [224] and two-step circular monopole [12] also performed well with considerable impedance and radiation characteristics.

Later, many ground modification techniques were also implemented in the UWB antennas for improving the radiation characteristics of the antenna [150,

211]. These include: cutting a notch at the ground plane (Huang et al. [76]) to improve the impedance bandwidth depending upon the size & position of notch, implementing saw-tooth truncated ground (Azim et al. [151]), employing rounded truncated ground plane (Melo et al. [56]). Trapeziform ground plane [211] was another interesting ground modification technique which helps the printed monopole antennas to achieve an impedance bandwidth similar to that of a discone antenna. Many other printed monopoles and feed structures with trapeziform ground were also studied at that time to improve the bandwidth performance further [87, 177, 210, 212].

Miniaturization came into being as a crucial factor in the antenna design as the wireless portable devices went smaller and smaller. One of the creative miniaturization approach is introduced by Sun et al [142], who produced a 40% size reduction in the overall area by simply making use of the structural symmetry. In this work they took only half of the symmetrical structure, relying on the principle that miniaturized half structures of the symmetrical planar monopoles can achieve similar bandwidth as the un-miniaturized full structures. In addition to this , incorporating staircase-shape either in the patch [62], or in the ground plane [106], or in both [173] to make the antenna size smaller and to improve the impedance matching bandwidth to comply with the FCC standards of UWB, became a common trend in those days.

Apparently, there came a usual tendency to make everything 'coplanar', i.e. ground and patch on the same side of the substrate, due to the advantages gained of being uni-planar. Some advantages of being coplanar over microstrip structures are: low dispersion & radiation loss, simple realization due to etching on one side, broadband performance as it does not need via holes for shunt and series elements etc.. An antenna can achieve this co-planarity by using either CPW or Co-Planar Strip (CPS) transmission line for feeding. The CPW transmission line was first proposed by Wen et al. [204]. It consist of a middle metallic strip on the surface of a dielectric substrate and two ground planes running adjacent & parallel to the strip on the same surface. Whereas, in a CPS transmission line only two metal strips will be there on the same surface of a dielectric substrate. This configuration was first analysed by A. E. Luna, [132], who experimentally verified the characteristics of co-planar strips. Both the CPW & CPS lines were capable of widening the impedance bandwidth of the antenna

effectively. Thus incorporating these co-planar feeding techniques for UWB antennas made them to achieve enhanced impedance bandwidth. Literature has abundant CPW-fed UWB antennas [19, 90, 147, 215], but is scant of CPS-fed antennas for UWB applications. Some available CPS-fed UWB structures are discussed in [116, 140, 218]. Apart from these two co-planar transmission lines there came another transmission line named as Asymmetric Co-planar Strip (ACS) line, in which the two metallic strips on the surface of a dielectric substrate will be of different size and may be of different structure. Sun et al [142] and Liu et al [219] used this feeding method to reduce the overall area of the UWB antenna as well as to improve the impedance bandwidth.

Like omni-directional UWB antennas, directional UWB antennas with high Gain performance were also found important to meet various applications. As a result, researchers found that using wide-slots and/or tuning stubs connected with the feed-line could realize the high gain directional property of a UWB antenna. This also improved the impedance bandwidth within a small profile. Jang et al. proposed two microstrip-fed rectangular wide-slot antennas in [83, 84], with a cross-shaped stub and a Π-shaped stub, respectively. The impedance bandwidth of these antennas could be tuned depending upon the length of the horizontal & vertical feed-lines as well as on the offset position of the feed-line. Later, researchers noted that the shape of the slot effects the antenna bandwidth more, than the shape of the tuning stubs. Subsequently, several wide-slot shapes other than the typical rectangular-slot were studied, such as tapered-slot [158], circular-slot [49], elliptical-slot [17] etc.. These wide-slot antennas provided much wider bandwidth than those with rectangular-slot. Some special geometries of printed slot antennas , other than the regular shapes mentioned above, were also introduced for UWB applications. These include a tapered-slot-fed annular-slot antenna [136], a semi-elliptic-slot antenna [70] etc..

Eventually, there came a need of rejecting some frequency bands, used by some existing narrow-band wireless services, which occupy the FCC specified UWB band (3.1-10.6 GHz). These include, IEEE802.11a WLAN (5.15-5.35 GHz), HIPERLAN/2 WLAN (5.725-5.825 GHz) and WiMAX (3.3-3.6 GHz). These existing wireless communication services may cause interference with the UWB systems. As a matter of fact, various UWB antennas with band-notched techniques have been introduced to survive from this electromagnetic interference.

Some existing band-notched techniques are: Embedding slot, Parasitic stubs, Band-stop transmission line and Hybrid techniques. Etching (or embedding) slots on the radiation patch or ground plane is the common and simplest way to reject particular frequency bands. By inserting V-shaped [101], inverted U-shaped [109], inverted Π-shaped [230], double L-shaped [86] slots or by using periodic structure slots [127, 188] on radiating element and/or ground plane, frequency-notched response can be achieved. Like embedding slot technique, placing parasitic stubs in the aperture area or nearby the radiating element (to form resonant structure) is also a common technique. Many such notched UWB antennas were studied like placing fractal tuning stub [130], sticking two arc stubs [40] etc.. Using a transmission line with bandstop characteristics to feed the UWB antenna, like the one discussed in [226] and [217], will also give a band-notch response without affecting the antenna radiation. Sometimes, it will be needed to reject more than one bands simultaneously, such as WLAN & WiMAX, WiMAX & HIPERLAN/2 etc.. In these cases different notched-band techniques have been used together, and were called as hybrid techniques, to realize the dual or triple band-rejection. Zhou et al. combined the embedding slot and parasitic stub band-rejection techniques to realize a dual-notched band on a annular ring UWB antenna, [223]. A triple band-notched UWB antenna was realized by Kim et al. [100], by incorporating a meander-shaped stub, two rectangular Complementary Split Ring Resonator (CSRR) on the feed-line and an inverted U-shaped slot in the center of the patch.

This thesis concentrates on the design and analysis of CPS-fed UWB antennas, which utilize the staircase-shaped structures to reduce the overall area as well as to enhance the impedance bandwidth. The core objective of this thesis is to incorporate MIMO technology into UWB systems and to investigate them thoroughly.

MIMO technology have their roots at the innovations regarding the antenna diversity techniques which started back in 1920s. But, the history of MIMO systems actually started when Jack Winters [208] proved the establishment of M-independent channels in the same bandwidth, if there are M-transmit & M-receive antennas. He also investigated the data rate limits that multiple-antenna system will have, while operating in a Rayleigh fading environment. The growth of the MIMO technology began after the pioneering works by two researchers:

Gerard J. Foschini [65] & Gregory G. Raleigh [155]. Former addressed the digital communication strategy in a Rayleigh fading environment when CSI is known to the receiver & unknown to the transmitter, and latter showed the improvement in the channel capacity with the number of multipath components or antennas at transmitter and/or receiver. They also showed that the co-location of multiple antennas at one transmitter/receiver is possible to effectively improve the throughput of the MIMO wireless link. These studies were a breakthrough for the MIMO communication and transformed them from an academic concept to a major component of modern wireless communication systems. MIMO technology is now consistently included in many sophisticated mobile wireless standards such as IEEE 802.11n, IEEE 802.11ac, IEEE 802.11ad, 3GPP LTE, WiMAX etc.. Although studies on various aspects of MIMO systems were conducted so far, the importance of proper antenna usage and its influence on MIMO systems were revealed by Waldschmidt et al. [33], in 2002.

Later, more focus was given in the designing of planar MIMO antennas as they are easier to mount at the terminals of the wireless communication systems. Researchers mainly concentrated on the co-location of two or more antenna elements to make the size of the antenna module compact, at the transmitter/receiver terminals. Fig. 2.5 shows some of such MIMO antennas, with their corresponding frequency range of operation.

Ko et al. introduced a two-port compact integrated antenna [103], with good isolation of 20 dB between the antenna elements, which can be utilized as a diversity antenna or as a duplexer to isolate receive and transmit signals. Here, two patch antennas were merged in combination with capacitive loading, as seen in Fig. 2.5a, to operate in 2.1-2.2 GHz frequency band.

Eventually, many papers showcased the different methods of isolating the closely-packed radiating elements of MIMO antennas. Etching slots on ground or modifying the ground plane were used in many MIMO antennas to reduce the mutual coupling between the antenna elements. Chiu et al isolated the two parallel PIFA elements by embedding slits on the ground plane, [41] (refer Fig. 2.5b). This antenna were capable of operating in 2.27-2.35 GHz band, with a good isolation of 20 dB between the antenna elements. Similarly, [11, 14, 144] embedded slots on the ground plane for better isolation between the antenna elements (refer Fig. 2.5c). Some MIMO antennas placed T-shaped & dual inverted

(a) 2.1–2.2 GHz, [103]

(b) 2.27–2.35 GHZ, [41]

(c) 1.8–2.9 GHz (WiFi & LTE), [14]

(d) 803–823 MHz & 2.22–2.9 GHz (LTE), [175]
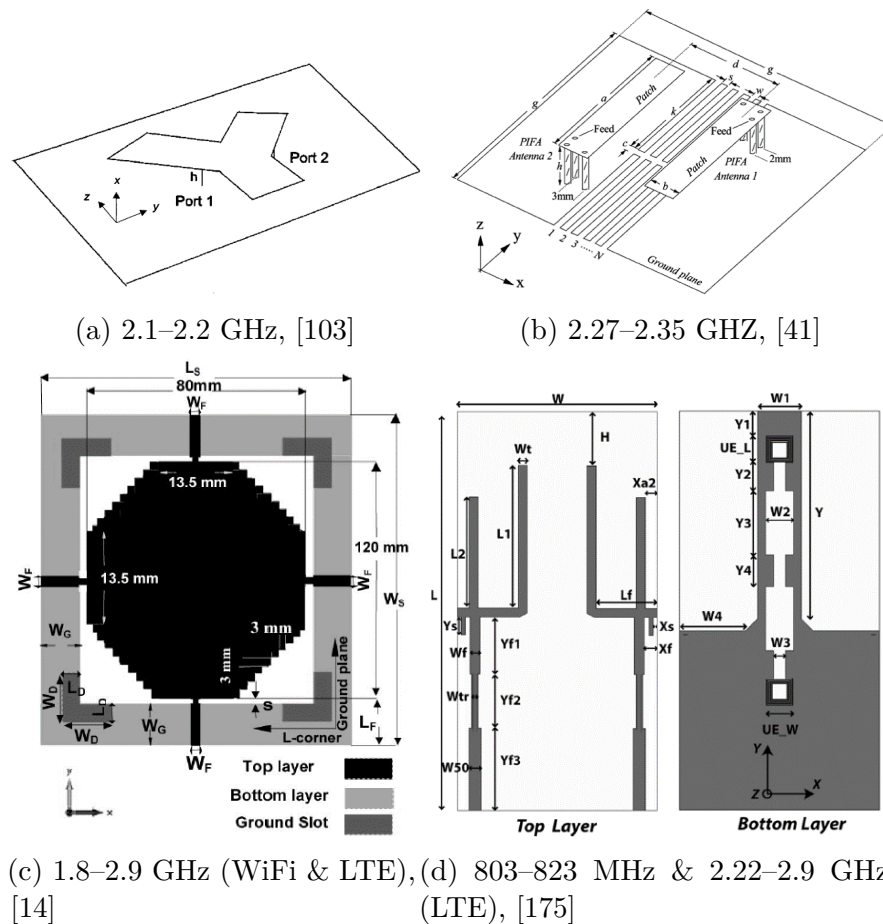
Fig. 2.5 Different planar MIMO antennas

L-shaped branches on the ground [53], or ground stubs [202] for better isolation. In [175], Defective Ground Structure (DGS) were utilized to isolate two 4-shaped antenna elements, as in Fig. 2.5d, which are capable of covering the two LTE bands (803-823 MHz & 2.440-2.9 GHz). Placing parasitic elements [10, 18] or neutralization line [24, 52] between antenna elements also reduces mutual coupling between them effectively.

Yet another method of reducing inter-element coupling is by making use of the spatial, polarization and/or pattern diversity techniques in the co-located MIMO antennas. Sánchez et al., in [131], utilized the polarization diversity along with EBG (Electromagnetic Band Gap) resonators to enhance the isolation between the two dual-band proximity coupled patch antenna. This made the antenna

to achieve an isolation of 55 dB at 2.1 GHz band and 40 dB at 2.4 GHz band. Later, a tri-port MIMO antenna, in [202], provided good pattern diversity for a MIMO system by using ground stubs and offered a wide band operation covering the WiMAX and 2.4 GHz WLAN application bands. Also, many 4-port MIMO antennas came up with arranging their antenna elements in differently polarized way to reduce the mutual coupling between them. These include: [209], in which four magneto-electric dipoles are arranged in a ring configuration to reduce the inter-element coupling, and [93, 124, 133, 162, 167], that realized the polarization diversity by arranging the antenna elements in a square-loop way to improve the isolation among the antenna elements. A few of these antennas also utilized the spatial separation between the radiating elements to gain better isolation among them.

Moreover, many multi-band MIMO antennas were studied to produce a single antenna, operating for various application areas such as WLAN, WiMAX, LTE, UMTS etc., simultaneously. A two-port MIMO antenna in [53] succeeded in producing a dual-band operation at UMTS (1.92-2.17 GHz) and 2.4 GHz WLAN bands. The MIMO antennas discussed in [10, 11, 144] were capable of performing dual-band operation by covering both the 2.4 GHz & 5.6 GHz WLAN. Likewise, [228] and [54] discussed MIMO antennas that can simultaneously operate in both domestic LTE700 & global LTE2600 bands. Apart from these dual-band antennas, one quad-band MIMO antenna was studied in [93], which has four F-shaped slot antennas operating in 2.28-2.66 GHz, 3.35-3.65 GHz, 5.07-5.3 GHz & 5.75-5.85 GHz, covering the WLAN as well as WiMAX application bands. Another hepta-band antenna covering GSM850/900/1800/1900/UMTS/LTE2300/2500 standards were configured as a two-port MIMO, in [24]. Literature also has MIMO antennas that are coplanar in nature, like [232] and [167], which utilized the CPW transmission line to feed the antenna elements. There are abundant volumes of such research articles available, which operates in the above mentioned application bands and perform good MIMO characteristics.

Recently, researchers found interest in merging the MIMO technology with the ever-green UWB systems. The keen interest behind the UWB-MIMO combo is due to the reduction in the bandwidth requirement if two or more antennas were placed (instead of one) at the transmitter and receiver. This will thereby increases the data rate and/or robustness of the UWB communication system. The early stages

of this research were solely focussed on the coding and channel characterization of the UWB-MIMO systems. In 2004, Enzo Baccarelli et al [20] anticipated the architecture of a transceiver by combining both multiple-antenna and pulse position modulation (PPM) IR UWB techniques and tested its performance in flat-faded application scenarios, typically in broadband 4G WLANs. The analysis on the channel capacity of a UWB-MIMO systems were found in [138, 178, 231]. These papers evaluated the improvement in the information rate and robustness of such systems. The first report on the space-time coding for a MIMO-UWB transmission was in [216], where they developed ST codes for an analog modulated multi-antenna UWB system with two transmitting and one receiving antennas. In [194], a spatial multiplexing coherent scheme for a 2×2 configured pulse based UWB-MIMO radio was discussed and experimentally investigated. A general multi-band OFDM coding frame work for UWB-MIMO systems was proposed in [179], where they combined the space-time frequency (STF) coding with the hopping multi-band OFDM modulation to exploit the available spatial & frequency diversities inherent in UWB environments. In addition to this, an approach of increasing the spatial/temporal diversity of a pulse-based UWB-MIMO system by selecting antennas across the data frame was introduced in [120], and was experimentally shown in [95].

UWB beamforming has gained much importance due to its ability of indoor localization within the UWB systems. Some reports on the UWB beamforming can be found in [77, 78, 159]. An experimental test-bed set-up, using optical delay lines, for studying the multiple-antenna beamforming over realistic UWB channels was discussed in [50]. An adaptive beamformer for ultra wideband wireless systems was discussed in [203], which shows that the signal bandwidth has little influence on the beamwidth and hence on the beam-focussing also. Moreover, the transient response of a uniform linear UWB array was experimentally investigated in [206], where it shows a good response without any sidelobes.

One of the crucial aspect of a UWB-MIMO study is the channel measurement and its characterization. Few important research works done on the channel measurement & characterization of a UWB-MIMO system were reported in [95, 137, 143]. Later, Thomas Kaiser et al, in [191], gave a brief overview of the available UWB-MIMO wireless technologies until then, which covered the channel capacity calculations, space-time coding (STC) and beamforming techniques. In

(a) 3.6–8.5 GHz, [154]

(b) 3.1-5 GHz, [170]

(c) 3.1–5.15 GHz, [227]
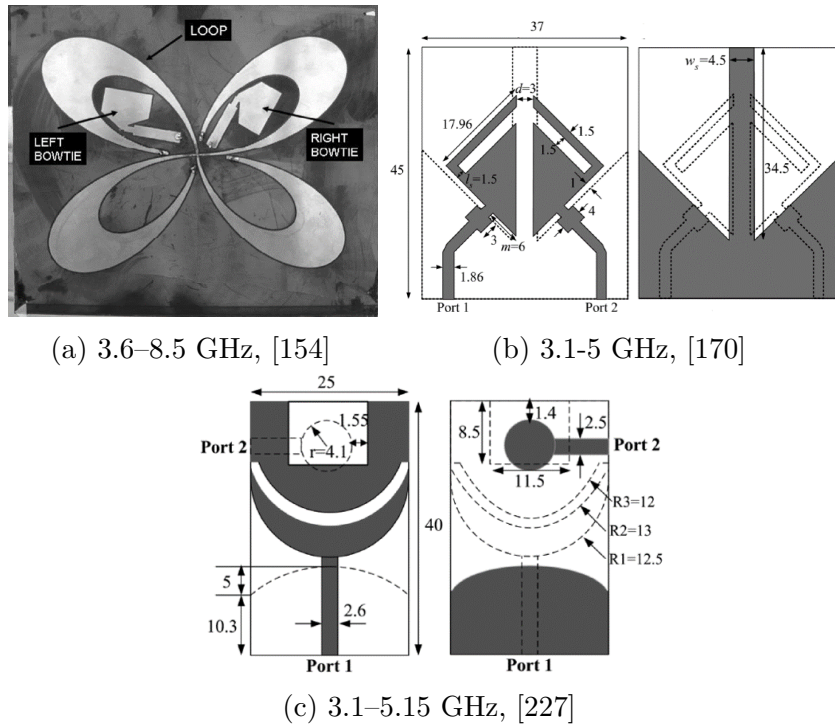
Fig. 2.6 Planar UWB-MIMO antennas designed at the beginning

[43], the system concepts , requirements & measurement set-ups for UWB-MIMO in home environment, in automotive environment and in public transport were discussed. This report also summarized the major benefits of incorporating MIMO technology into UWB systems.

Then came the days of co-located antenna designing for UWB-MIMO communication systems. Fig. 2.6 depicts some initial co-located planar MIMO antennas having UWB operation. A design of a vector antenna for a UWB-MIMO system operating in the frequency range of 3.6-8.5 GHz was discussed in [154]. The antenna consist of a center-fed loop antenna and two orthogonal bow-tie antennas that are in-plane with the loop antenna, as in Fig. 2.6a. Its channel capacity was also calculated in a rich scattering environment, resulting in a good spectral efficiency. Another UWB antenna with a combinational structure of two crossed exponentially tapered slots and a star-shaped clot, capable of operating in the FCC assigned band of 3.1-10.6 GHz was described in [89]. The transient response and polarization stability of the UWB antenna was also verified, and the possibility of that antenna to work in a MIMO configuration was also investigated in

[46]. However, the MIMO operation could be accomplished only in the frequency band from 2.4 GHz to 4.8 GHz.

In [192], a planar 2-port UWB diversity antenna which has a suspended square patch with a thick stem underneath, operating in 3.1-5.2 GHz band was proposed. It utilized both pattern diversity and partial polarization diversity to achieve an isolation of 13.5 dB within the operating band. Another planar 2—port UWB diversity antenna, having an overall volume of $37 \times 45 \times 0.8 mm^3$, with two notched triangular radiating elements on one side and a modifies ground on the other side was proposed in [170]. This antenna achieved an impedance bandwidth of 3.1-5 GHz (lower UWB band), and an isolation of 20 dB was obtained between the antenna elements because of a central vertical strip extension on the ground plane (see Fig. 2.6b).

A dual-orthogonal polarized antenna which is suited for polarimetric UWB radar and UWB-MIMO applications (for 3.1-10.6 GHz band) was presented in [9]. The antenna consist of two elliptically shaped dipoles, which are kept orthogonal to each other and encircled by a ground plane. For both polarizations a spatial separation of the feeding is obtained, as the feeding is placed on the outer side between the single ellipse and ground plane. Although, the radiation plane is of size $40 \times 40 mm^2$, with a minimum isolation of 20 dB between the antenna elements, it has the input impedance matching better than -6dB only.

In [226], a tree-like structure is extended from the ground plane to enhance the wideband isolation between the two elements in a $35 \times 40 mm^2$ UWB-MIMO antenna, with two radiating elements having shape similar to that in [170]. This antenna showed good impedance matching and better isolation (about 20 dB) across the band of 3.1-10.6 GHz.

In 2012, S. Zhang et al proposed a compact closely-packed 2-port UWB-MIMO antenna of sized $25 \times 40 mm^2$ (refer Fig. 2.6c), for USB dongle applications [227]. This antenna utilized both pattern & polarization diversities to enhance the isolation of 26 dB between the antenna elements, but was able to operate only in the lower UWB band (3.1-5.15 GHz). This paper reported various MIMO performance evaluation parameters such as Envelope Correlation Coefficient (ECC), diversity gain and multiplexing efficiency (these parameters will be explained in detail in Chapter 3). In the same year, another UWB-MIMO antenna for mobile devices with WLAN band-rejection was presented in [112].

This antenna has a printed folded monopole coupled with a parasitic inverted L-element to attain the UWB operation (3.1-10.6 GHz) and a parasitic meander line to improve the isolation (of 17 dB) between the two antenna elements. The antenna has a radiating area of size $13.5 \times 55mm^2$ and a ground plane of size $86.5 \times 55mm^2$.

In 2013, Liu et al [121] realized a 2-port UWB-MIMO antenna by simply placing two microstrip fed square monopole antenna orthogonal to each other. The overall area of the antenna is $26 \times 40mm^2$ with a common ground for both the antenna elements, and two long protruding stubs are added to ground plane to achieve an isolation of 15 dB between the antenna elements, in the operating band of 3.1-10.6 GHz. Later, Li et al. proposed a compact 2-element UWB-MIMO antenna [117], with an overall area of $27 \times 30mm^2$ only, which was smaller than most of the 2-port UWB-MIMO antennas available until then. The antenna has an impedance bandwidth of 3-11 GHz with two rejection bands at 3.30-3.7 GHz and 5.15-5.85 GHz. The antenna has a microstrip fed U-shaped patch and a rectangular metal strip, with two protruded ground parts to improve the input impedance and enhance the isolation for frequencies ≥ 4 GHz as it increases the distance between two feed ports. In the same year, Bybi et al. realized an uni-planar UWB-MIMO antenna with two CPW fed arc-shaped radiator elements placed orthogonal to each other, in [31]. This antenna (of size $50 \times 50mm^2$) has a 2:1 VSWR bandwidth of 2.76-10.75 GHz with a rejection band at 4.75-6.12 GHz and good transient response & diversity performance. This uni-planar configuration makes the antenna to be integrated easily with MMICs and have low dispersion & radiation loss. An inter-element isolation of 15 dB was achieved due to the presence of a diagonal strip between the ports in the ground plane.

In 2014, Yetisir et al. [60] presented a UWB-MIMO antenna having a collocated pair of dipole antennas, with an isolation of 40 dB between the elements. This high isolation was achieved by using orthogonal polarization arrangement with Resistive sheets (R-cards) placed between the antenna pair. Although, the antenna won good isolation among the radiating elements, it failed to lie on the FCC specified frequency range for UWB communication systems, as its operating range was from 700 MHz to 2.7 GHz. Moreover, the manufacturing of this MIMO antenna is a bit tedious due to the need of embedding R-cards for proper isolation. After the uni-planar MIMO antenna from Bybi et al., a compact

co-planar UWB diversity slot antenna was presented in [67] with a notched-band at 5.5 GHz. It consist of two CPW-fed staircase-shaped radiating elements for UWB operation, which were kept orthogonal to each other, and a decoupling rectangular stub placed at 45° between the two radiators to ensure high isolation. This antenna has a size of $48 \times 48mm^2$ and are capable of operating from 2.5 GHz to 12 GHz, with a band-notch from 5.1 GHz to 6 GHz, due to the presence of the Split Ring Resonator (SRR) slots on the radiator.

A butterfly antenna using genetic algorithm design optimization was presented in [13], which shows low correlation between the antenna elements and have high diversity gain. It used four arm-shaped self-grounded monopole radiators to achieve the UWB-MIMO operation and the array arrangement made the radiation pattern of the four antennas different with different polarizations. Then, one two-port UWB-MIMO antenna came up with dual band-notched operation at WiMAX (3.4-3.7 GHz) and WLAN (5.15-5.35 GHz & 5.725-5.825 GHz) over the UWB band (3.1-10.6 GHz), [189]. To reduce the mutual coupling between the radiating patches two decoupling structures were extended from the ground plane and shorted to the respective patches. To realize the notches, two extra branches were connected with these decoupling structures.

Mao et al., in [139], introduced a two-port UWB-MIMO antenna in which the radiator was shared by two antenna elements, to reduce the overall size of the structure. Moreover, etching a T-slot in the radiator & extending a stub on the ground made high isolation possible, and exciting the pentagonal radiator with perpendicular feeding structure realized dual polarization among the antenna elements, which again added isolation between them. This 2-port co-radiator UWB-MIMO antenna ($40 \times 40mm^2$) covered the FCC specified UWB band and can also be configured as a 4-port antenna with size $48 \times 48mm^2$. In the same year, a UWB-MIMO antenna utilizing two Quasi-Self-Complimentary (QSC) monopoles with an additional 2.4 GHz WLAN coverage was proposed in [219]. This antenna achieved an isolation of 20 dB between the antenna elements without using any other decoupling structures. The complementary and asymmetrical nature of the monopole benefited to obtain good isolation within the operating band of 2.19-11.07 GHz. Another UWB-MIMO antenna utilizing the QSC radiating structures is presented in [122], which was compact

than the one discussed above. For proper isolation, two rectangular slots were cut symmetrically on the ground plane between the antenna elements.

Another compact two-port UWB antenna of size $32 \times 32mm^2$ was discussed in [157], which placed the two open L-shaped slot antenna elements perpendicular to each other to obtain considerable isolation. In [156], a cross-configured directional UWB antenna for multi-directional pattern diversity was presented. It has a wide range of operation from 1.3 GHz to 20 GHz due to the asymmetric curve-shaped CPW fed directional antenna elements. The cross arrangement of the radiating elements were done in such a way that none of the antenna elements were in direct contact with each other and thereby achieved multi-direction pattern diversity characteristics.

A novel miniaturized two-layer Electromagnetic Band Gap (EBG) structures are utilized in [119] to reduce the mutual coupling between two UWB monopoles, operating in 3-6 GHz frequency band. This slit-patch EBG structure has two closely coupled arrays, one with linear conducted patches and other with slits on the ground plane.

Saleem et al., in [163], introduced an eight-element UWB-MIMO antenna with three distinct isolation mechanisms. The isolation mechanism consist of placing three types of structures: one closed-loop Frequency Selective Surface (FSS) for side-by-side element isolation, circular arcs for orthogonal element isolation and a set of four parallel strips that connect the circular arcs for isolation between antenna elements placed across each other. These structures provided 20 dB isolation over most of the desired UWB spectrum.

In 2015, Tripathi et al. used koch fractal UWB antennas to realize the multi-antenna operation, [176]. The antenna have four octagonal shaped fractal antennas placed in a square loop form to obtain better inter-element isolation of 17 dB within the 2-10.6 GHz band. In addition to that, this antenna possessed a notched-band at 5.15-5.85 GHz (WLAN) due to the presence of a C-shaped slot on the monopoles, and has an overall size of $45 \times 45mm^2$ only. In [183], a dual-polarized vivaldi antenna or tapered slot antenna with a wide bandwidth of 0.7-3.6 GHz was presented. Although it failed to possess FCC specified UWB operation, the configuration of the antenna is interesting and it gained a high isolation of 30 dB between the antenna elements. This dual-polarized configuration is achieved

by inserting two orthogonal vivaldi antennas in a cross-shaped form without a galvanic contact.

Kang et al. utilized two offset microstrip-fed antenna elements that are placed perpendicular to each other, to get a UWB-MIMO antenna with good isolation, [111]. Here, a parasitic T-shaped metal strip was placed between the radiating elements to further suppress the mutual coupling between them. And, for a rejection-band of 5.03-5.97 GHz from the operation band of 3.08-11.8 GHz, a pair of L-shaped slits were etched out from the ground plane.

In [37], Defective Ground Structure (DGS) were utilized to reduce inter-element coupling and improve impedance matching. A T-shaped slot and a line slot were etched out from the ground plane to get an isolation of 18dB within 3.1—10.6 GHz band. This two-port UWB-MIMO antenna has a very compact size of $22 \times 26mm^2$ and was smaller than most of the two-port UWB antennas available then. Inter-element isolation can also be attained by using neutralization lines between the antenna elements, like the one discussed in [229], which consist of two metal strips and a metal circular disc with a circular slot in it. This neutralization line created an isolation of 22 dB between the antenna elements, in 3.1-5 GHz operation range.

In [105], Stepped Impedance Resonator (SIR) principle is adopted to reduce the mutual coupling between the antenna elements. Using four SIRs a square-ring Defective Ground Structure (DGS) was formed and two microstrip-fed SIRs were placed on the other side of the substrate to realize a two-port UWB-MIMO antenna. In addition to this, a slot stub and a metallic stub were also combined with the DGS to obtain 20 dB isolation within the band of operation (3-12 GHz).

The method of placing the antenna elements orthogonal to each other, to attain polarization diversity for the multi-port UWB antenna have been used by many researchers, [15, 98, 193]. In [193], two identical elements, each of which has a planar radiator with microstrip fed over half size ground plane, were placed orthogonal to each other to get an isolation of 20 dB between the elements in 3.1-12.3 GHz band. In [15], again two identical UWB antennas were placed perpendicular to each other to attain considerable isolation. In this, a hybrid geometry (using half-circular ring and half-square ring) was used as an antenna element. Ground plane was curved & defected to improve bandwidth and an extended ground stub was also added to widen the bandwidth even more.

Similarly, in [98], to realize polarization diversity two antenna elements were kept orthogonal to each other, but with two different geometries. One was the typical microstrip-fed step rectangular monopole antenna and for the other a U-shaped slot was inserted in a step-rectangular monopole antenna. It also consists of a quarter-wave stub connected to the ground plane via pin diodes to introduce an on-demand WLAN band-rejection feature. Both the antenna elements operated in the 2-12 GHz frequency range with a 20 dB of inter-element isolation. An extension of this two-port UWB antenna to a four-element antenna was presented in [97].

Another QSC based UWB-MIMO antenna was discussed in [233], in which the antenna elements were kept orthogonal to each other and fed perpendicularly to obtain polarization diversity. The inherent decoupling ability of QSC structures and the orthogonal arrangement made an isolation of 20 dB possible in the 3-12 GHz frequency band. By etching a bent slit on the radiating element a WLAN notched-band was also realized.

Zhang et al. introduced a novel Asymmetric Co-planar Strip (ACS)-fed UWB-MIMO antenna, in [225], which composed of a radiator shared by two antenna elements to reduce the overall size of the antenna to $26 \times 26mm^2$. An I-shaped slot in the radiator and a metallic strip on the back broadened the bandwidth from 3.1 GHz to 10.6 GHz and improved the isolation to 15 dB within the whole operating bandwidth.

In 2016, Srivastava et al. [184] proposed a very compact four-element UWB antenna of size $42 \times 25mm^2$, which used stepped slot antennas as each radiating element for the UWB operation, having impedance bandwidth from 3.2 GHz to 12 GHz. The antenna elements were arranged in such a way that an inter-element isolation of 22 dB was achieved over the entire UWB spectrum, without the need of any decoupling network. Dhar et al. presented one Radio-Frequency (RF) amplifier-integrated UWB-MIMO antenna, in [51]. They co-designed a two-element semi-ring UWB-MIMO antenna with a commercially available UWB amplifier without the 50Ω interface impedance requirement, so that an improved wideband matching and total radiation efficiency can be achieved, over 1.8—5.5 GHz band.

In [82], a two-element non-planar 3-Dimensional (3D) UWB-MIMO antenna was realized by mounting the chamfered radiator patches in back-to-back or in

orthogonal (corner installation) configuration on a polystyrene block. Apart from this, a decoupling structure consisting of four C-shaped strips in between three vertical stubs were placed at the rear side of each antenna element, to reduce the inter-element coupling to about 20 dB within the UWB spectrum. Similarly, another non-planar 3D quad-element UWB-MIMO antenna was proposed in [27], in which four spline-shaped antenna elements were wrapped around a cuboid polystyrene block. To provide an isolation of 20 dB an inverted-L structure with an array of slotted Y-shaped FSSs were employed, and to retain the impedance matching over the entire band of 3.1—10.6 GHz a square spiral parasitic element was etched on the rear side.

A new method of isolating UWB antennas configured in a MIMO arrangement was introduced by Lin et al., in [125]. A carbon black film, which absorbs the electromagnetic signals, was coated on the feed-lines of two disc-shaped monopole UWB antennas to get an isolation of 15 dB in the 2.5-11 GHz band. No other decoupling structure were used in the afore mentioned UWB-MIMO antenna.

Liu et al. introduced a compact printed differential UWB-MIMO antenna with both notched-band and common mode suppression, in [128]. This was a quad-element antenna and each element consists of differential U-shaped microstrip feed-line on the bottom and a stepped-shaped slot on the top of the substrate. To obtain a rejection-band of 5.10-5.95 GHz from 2.95-10.8 GHz UWB spectrum, a half-wavelength resonant stub was embedded in the stepped-shaped slot. In addition to this, staged slots were embedded between the antenna elements to enhance the differential isolation to 15.5 dB.

Another UWB-MIMO antenna, in [99], utilized the CSRR unit to suppress the interference of RF currents flowing through its ground plane. The antenna was very compact ($23 \times 29mm^2$) and consists of two counter facing monopoles along with corresponding inverted-L stubs and one CSRR unit on the ground plane. These L-stubs and CSRR enables the tight packing of the antennas and good isolation, simultaneously. This antenna operates from 3 GHz to 12 GHz, thus covers the entire UWB spectrum, with an isolation of 15 dB and very low Envelope Correlation Coefficient (ECC).

This thesis deals with the design and analysis of compact UWB-MIMO antennas which are co-planar in nature and have commendable UWB and MIMO performances. For that, two novel, compact UWB antennas are proposed and

verified its operation in MIMO configuration. These two UWB antennas are co-planar in nature and is smaller than most of the co-planar UWB antennas available in the literature. Moreover, it covers the entire UWB spectrum that was allocated by FCC, and also have good transient responses within the spectrum. In this thesis, these antennas are co-located in different ways to get different MIMO configurations. In addition to this, simple decoupling methods are incorporated in the proposed UWB-MIMO antennas to get effective inter-element isolation, which include embedding parasitic strips and adopting spatial, polarization and/or pattern diversity methods. Chapter 4 & 5 details the entire antenna designs along with their decoupling strategies, frequency- & time-domain analysis and MIMO performance evaluation.

Chapter 3

Methodology

This chapter points-out the pre-fabrication studies, fabrication procedures and experimental analysis performed for characterizing the UWB-MIMO antennas discussed in the following chapters. The pre-fabrication studies like designing & optimizing the antennas are carried out using the CST Microwave Studio®[5]. Using this simulation software, the antennas are parametrically analysed to provide physical knowledge of their radiation behaviour and to optimize the designs to achieve the desired performance. The optimized antenna designs are then fabricated on microwave substrates by using Photo-lithographic process. After the fabrication of the antenna prototypes, its experimental analysis are carried out in the anechoic chamber using Vector Network Analyzer. Moreover, an in-depth study of the frequency-domain, time-domain & spatial-domain analysis and MIMO performance evaluation techniques, in concern with the UWB-MIMO antennas , are presented in this chapter. In addition to this, the Over The Air (OTA) performance analysis technique for multiple-antenna wireless communication systems are also explained in this chapter.

3.1   Pre-fabrication Studies

The designing and modelling of the proposed antennas are conducted using the 3D-ElectroMagnetic (EM) simulation software, CST (Computer Simulation Technology) STUDIO SUITE®. This 3D EM simulation software offers accurate & efficient computational solutions for electromagnetic design and analysis. It is

an user-friendly software and helps in the proper designing and optimization of devices operating in a wide range of frequencies. CST STUDIO SUITE®comprises many simulation modules. Out of all the CST MICROWAVE STUDIO®(CST MWS) module is used here, as it is a leading edge tool for fast and accurate analysis of high frequency devices such as antennas, filters, couplers, planar & multi-layer structures, and SI & EMC effects. This module gives a quick insight into the EM behaviour of the high frequency designs with its variety of available solver technologies. It consists of seven different solvers, out of which the transient solver (time-domain solver) is utilized for the antenna analysis in this thesis. The transient solver is a general purpose 3D EM simulator for examining the field propagation through a component or along the traces of a PCB, and also for delivering various frequency-domain results of planar or wideband antennas.

The first step in the antenna designing procedure is the construction of antenna geometries in the drawing plane of CST MWS. The antenna structure can be modelled by specifying the appropriate co-ordinates corresponding to the size of each component, along with their correct material assignations. The metal components in the antenna are assigned as copper with a finite thickness of 0.01mm and the dielectric substrates are assigned with appropriate materials either from the material library of CST MWS or by manually defining.

CST MWS has variety of in-built project templates corresponding to different application areas. The user can either select one of these templates so that the mesh size, mesh type, boundaries etc. can be assigned automatically, or defined manually.

For the studies in this thesis, planar antenna template is selected and specified the proper units, desired frequency range of operation, filed monitors required for the analysis and adequate solver. The solver used here is the time-domain solver as this thesis deals with ultra wideband antennas, and in this template the boundaries at all faces of the radiation box are set as 'open'. Appropriate ports are then assigned to excite each antenna elements, in the case of MIMO antennas. The CST MWS has the ability of multi-signal functionality for simultaneous or subsequent excitation of multiple ports, which is an essential feature for the MIMO antenna design.

After setting the solver parameters, the time-domain calculations are started. The antenna parameters like reflection & transmission coefficients, VSWR (Volt-

age Standing Wave Ratio), input impedances, radiation patterns, gains, current & field distributions etc. of each antenna elements can be obtained from the simulated results. The modeled antenna can then be optimized accordingly to meet the desired antenna parameters, by changing the dimensions, positions, materials etc. of the components. CST MWS can study the Electric Fields around the antenna geometry in the near/far field by inserting virtual probes at the problem space, which is essential for the transient analysis of the UWB antennas.

3.2 Antenna Prototype Fabrication

The microwave antenna prototypes must be fabricated on low-loss, thermally stable substrates with constant permittivity for the frequency range of operation. The antenna prototypes discussed in this thesis have been realized on FR4 Glass Epoxy, which is economic and easily available. The FR4 dielectric substrate used in this thesis has a dielectric constant of 4.3, loss tangent $(tan(\delta))$ of 0.02 and thickness of 1.6 mm.

The antenna structure are then fabricated on the selected dielectric substrate using the Photo-lithographic procedure. The first step in the fabrication process is to create a negative photo-mask corresponding to the antenna structure to be fabricated. Then, a single/double-sided copper clad FR4 substrate with suitable dimensions are cleaned properly using Acetone or Chloroform to remove the oxide coating or any impurities present on its surface. This coper clad is then dipped in a negative photo-resist, and dried using a high speed spinner to get a thin layer coating of the photo-resist on it. It is then exposed to UV-radiation fro two minutes, through the negative photo-mask. The photo-resist in the portions that are exposed to light will get hardened, and the unexposed photo-resist will get washed off when agitating the copper clad sheet in the developer solution for few minutes. This sheet will be rinsed with water and then treated with the Ferric Chloride ($FeCl_3$) solution to remove the unwanted copper portions. $FeCl_3$ dissolves the copper coating on the FR4 substrate except the parts underneath the hardened photo-resist layer. At last, the hardened photo-resist on the fabricated antenna prototype is removed by wiping it with Acetone solution.

3.3 Antenna Analysis

Generally, the antenna are characterized by analysing parameters like input impedance, gain, efficiency, radiation pattern, reflection & transmission coefficients and polarization properties [21]. For antennas with narrow band of operation, these parameters are analysed at the resonant/center frequency. But for antennas having wider bandwidth of operation these parameters are highly frequency dependent, so that the straight-forward evaluation of these electrical properties as function of frequency will not be sufficient to characterize their transient radiation behaviour. One proper approach is to conduct the transient analysis also, by modelling such antennas as an Linear Time-Invariant (LTI) system. Transient response analysis of an antenna can be performed either by direct time-domain measurements or by frequency-domain measurements followed by Fourier transformation. Measurements in time-domain can be faster than frequency-domain measurements as it uses very short pulses or step functions as driving voltage. However, frequency-domain measurements take advantage of high dynamic range with the standardized calibration of Network Analyzer, and is accurate like the direct time-domain measurements [205]. So in this thesis the frequency-domain way of analysing transient response is adopted.

In addition to these frequency-domain and transient analysis, the analysis in spatial-domain is also necessary to study the variation of antenna properties with respect to different directions around the antenna. This gives a clear picture of antenna's behaviour to its surroundings in space. Moreover, as the studies in this thesis are about co-located UWB-MIMO antennas, MIMO/diversity as well as the channel performance evaluations must also be considered. The diversity performance evaluation of a particular MIMO antenna gives an insight towards how the co-located antenna elements were correlated to each other during their individual performances. In order to have a keen knowledge about the effect of AUT on the channel capacity and the throughput of communication system, the channel performance must be evaluated systematically.

3.3.1 Antenna Measurement Facilities

All the radiation characteristic measurements of the proposed antennas are carried out using the test facilities available in the CREMA Lab, Department

of Electronics, CUSAT. These include Performance Network analyzer (PNA), Anechoic chamber, Automated turn-table assembly and power meter.

Network Analyzer

Network analyzer is the heart of all antenna measurements accomplished in this thesis. It is a versatile instrument used to characterize the antenna behaviour precisely, in terms of network scattering parameters or s-parameters. The Network Analyzer used for the studies in this thesis is the Agilent PNA (Performance Network Analyzer) E8362B [4]. This PNA provides the perfect combination of speed and precision for the demanding needs of high frequency, high-performance component test requirements. In addition to this, it have the right combination of fast sweep speeds, wide dynamic range, low trace noise and flexible connectivity. The key specifications of Agilent PNA E8362B Network Analyzer are:

- Frequency Range of 10 MHz to 20 GHz

- 123 dB of dynamic range at 20 GHz

- <0.006 dB of trace noise at 1 kHz IFBW

- <26 μsec/point measurement speed

- 32 measurement channels with up to 16,001 points per channel

- Supports TRM/LRM calibration for the most accurate on-wafer, in-fixture, and wave-guide measurements

Fig. 3.1a shows the Agilent PNA E8362B Network Analyzer used for the antenna measurements in this thesis. It has two ports, and prior to all the measurements these ports will be calibrated using the known standards (open, short & matched load) with appropriate calibration kit, over the desired frequency range. This is done to eradicate the losses or errors associated with the cables, connectors and other circuits used in the measurements.

Anechoic Chamber

Anechoic chamber is a big room (compared to the wavelength of operation) which simulate the free space environment required for the far field antenna

(a) Network Analyzer   (b) Anechoic chamber
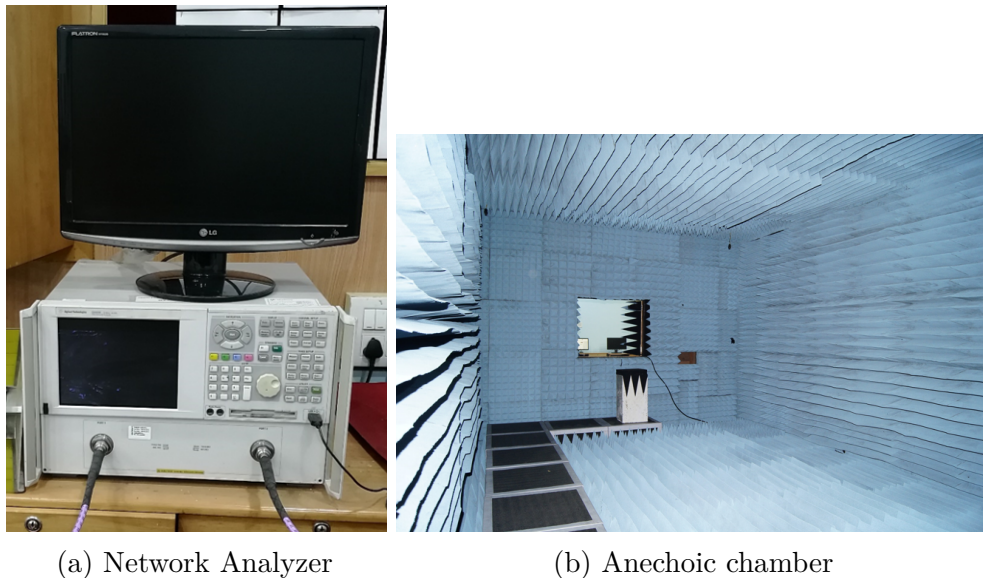
Fig. 3.1 Antenna Measurement Facilities of department of Electronics, Cochin University of Science of Technology

measurements. A photograph of the anechoic chamber available in the department is shown in Fig. 3.1b. This chamber can provide a 'quiet zone' and Antenna Under Test (AUT) is placed at this region. This quiet zone is achieved by spreading the walls, ceilings and floor with microwave absorbers made up of high quality, low density foam in pyramidal shape and impregnated with dielectrically/magentically lossy medium. Specifically, this pyramidal absorbers are carbon black impregnated Poly-Urethane foam. Its pyramidal shape gives geometrical impedance matching to the signals impinging on it and the carbon provides required attenuation for the waves incident on it. This chamber is surrounded by thin Aluminium sheets to shield it from the spurious EM interferences from outside. It is designed with an average reflectivity of -35 dB in the frequency range from 2 GHz to 18 GHz.

Automated turn-table assembly

An automated turn-table assembly placed in the anechoic chamber is used for plotting the radiation patterns of AUT. It consists of a stepper-motor driven rotating platform, where the AUT is mounted, and a micro-controller based antenna positioner interfaced with a Personal Computer (PC), for rotating the AUT. The PC controls the positioning and movement of AUT and synchronizes

the measurements through Network Analyzer. The AUT (on the turn-table) acts as a receiver. The transmitter is a standard wideband ($\approx$1–18 GHz) ridged Horn antenna and placed at the other end of the chamber. Both the AUT & standard Horn antenna will be connected to the PNA using low loss shielded cables. Moreover, to ease the measurement procedures a proprietary software, which is indigenously developed in the lab is also used. This software communicates with Network Analyzer using Standard Commands for Programmable Instruments (SCPI) and collects data at the ports through Ethernet communication. A serial connection using DB9 connector to the turn-table assembly controls the antenna rotation in a user-defined angle and direction.

3.3.2 Frequency-domain Analysis

The parameters that fall under the frequency-domain analysis of an antenna are reflection/transmission coefficients, VSWR, radiation pattern, gain and efficiency. In this section, these parameters and how they are measured for the studies in this thesis will be discussed in detail.

Reflection/Transmission Coefficient & VSWR

An antenna serves as an impedance matching device between a transmission line (coming from the transmitter) and the propagating medium (usually free space), within its operating frequency range. When there is an impedance mismatch between this transmission line and the antenna, a part of the incident energy will be reflected back to the source. A figure-of-merit to quantify this mismatch is called as Reflection Coefficient (Γ). It is the ratio of reflected voltage (current) to the incident voltage (current) and is same as the S_{11} if the antenna is connected to the port 1 of a two-port network. If the reflection coefficient is expressed in dB, it is termed as Return Loss (RL), i.e.,

$$RL = -20\log_{10}(|\Gamma|) = -20\log_{10}(|S_{11}|) \tag{3.1}$$

Thus, if the antenna and transmission line is perfectly matched ($\Gamma = 0$) $RL = \infty$ dB, i.e., no reflected power, and if it is not at all matched ($\Gamma = 1$) $RL = 0$ dB, i.e., all incident power is reflected back. These two conditions are ideal cases,

which are unrealistic. This antenna mismatch can also be quantified using another parameter termed as Voltage Standing Wave Ratio (VSWR). It is the ratio of maximum voltage (V_{max}) to minimum voltage (V_{min}) of the standing wave formed on the transmission line due to the presence of reflected power. This can be expressed as,

$$VSWR = \frac{V_{max}}{V_{min}} = \frac{1 + |\Gamma|}{1 - |\Gamma|} \tag{3.2}$$

A VSWR value of 2, which gives the return loss (RL) $\approx 10dB$ is considered as a tolerable limit for a matched antenna, [44].

A part of the incident power, that are not reflected back, will be transmitted to the propagation medium. The ratio of transmitted voltage (current) to the incident voltage (current) is termed as Transmission Coefficient (T) and is similar to S_{21} of a two-port network. Thus, the Insertion Loss (IL), often expressed in dB, can be formulated as,

$$IL = -20\log_{10}(|S_{21}|) \tag{3.3}$$

Prior to the measurement of these parameters the network analyzer must undergo a full-port calibration using the standard open, short, matched and thru loads, for the desired frequency range. To make sure that the reference plane is absolutely at 0° for all measurements in the desired frequency band, proper phase delay is introduced while calibrating, thus taking care of probable cable length variations. After that, the antenna is connected to the ports of the network analyzer. For a single-port antenna, either Port 1 or Port 2 of network analyzer need to be used for the measurement of S_{11} or S_{22}, respectively. But for a multi-port antenna, two ports of the corresponding antenna elements will be connected to the ports of network analyzer, and the remaining ports (if any) will be terminated with matched load, in the case of a two-port network. The magnitude and phase of the S-parameters (i.e., S_{11}, S_{21}, S_{12} & S_{22}) can then be measured directly from the network analyzer. Here, S_{11} & S_{22} indicate the return loss at the two ports of the antenna geometry and S_{21} & S_{12} indicate the isolation between the ports of the antenna. The 2:1 VSWR bandwidth of the antenna can also be checked, by pointing the markers on the return loss curves

where the value goes below the -10 dB level. By changing the trace format we can also collect the informations regarding VSWR, input impedance etc..

Radiation Pattern

The radiation pattern is a graphical representation of the spatial distribution of radiation from an antenna as a function of space co-ordinates. Usually, far-field patterns of the antenna are considered for the study, which are measured at a distance, $d > \frac{2D^2}{\lambda}$, where D is the largest dimension of the antenna and λ is the operating wavelength. Even though an antenna radiation pattern is assumed to be three-dimensional (3D), in its conventional way of measurement only the far-field patterns at the principal planes of the antenna are taken into consideration, due to the complexity in the experimental setup needed for a 3D pattern.
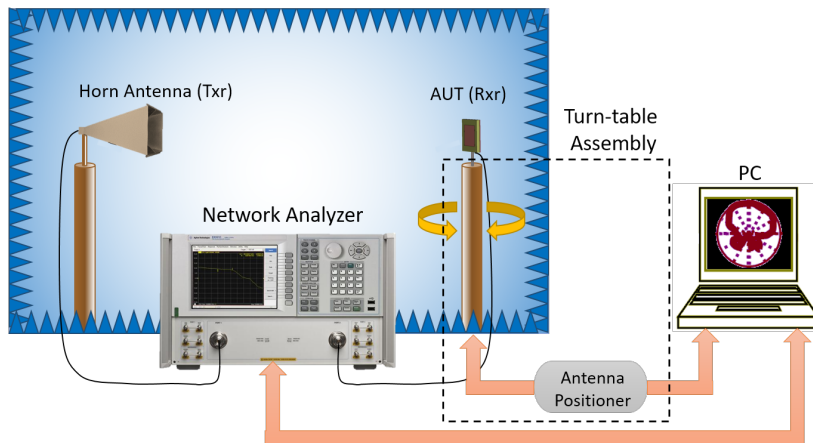
Fig. 3.2 Radiation pattern measurement set-up

The conventional way of radiation pattern measurement is carried out in an anechoic chamber, as depicted in Fig. 3.2, with the help of a network analyzer and the turn-table assembly. The AUT is mounted on the turn-table assembly, which is kept inside the quiet zone of the anechoic chamber as shown in Fig. 3.2, and is connected to the Port 2 of network analyzer with proper cabling. Here, for the pattern measurement, the AUT is operated in the receiving mode. Port 1 of the network analyzer is connected to a standard wideband ridged Horn antenna (1–18 GHz) and acting as a transmitter. This Horn antenna is kept at the far-field of AUT ($> \frac{2D^2}{\lambda}$), inside the anechoic chamber, and is fixed intact with the help

of an antenna holder mechanism. The AUT is then bore-sighted by adjusting their height, angle of reception and polarization. Thus, the network analyzer is set to measure S_{21} in the required frequency band and number of points. A Thru calibration is performed, which calibrates the $|S_{21}|$ data to 0 dB for every frequency point in the band. In order to exclude the counterfeit reflections from the neighborhood, which deteriorates the actual response, the time-domain gating feature of network analyzer is utilized with a gate-span slightly greater than the largest dimension of the AUT. Before commencing the measurement, the antenna positioner is set to home, which automatically sets the turn-table position at 0°. The in-house developed software in the PC then invokes the radiation pattern routine and measures the normalized $|S_{21}|$ data at the specified step-angles till it reaches the stop-angle, for the desired frequency points, all in one-take. Finally, the data can be saved in the PC at the specified location. Measurements are then repeated to get the patterns at other principal planes for both co-polar and cross-polar orientations of AUT and Horn, with proper gating.

Antenna Gain

One of the most important figure-of-merit that describes the performance of an antenna is its gain. The gain (G) of an antenna is defined as 'the ratio of power radiated by the antenna, in the direction of maximum radiation, to the power radiated by the reference antenna, in the same direction, when both are fed with same input power', [21]. If an isotropic radiator is taken as the reference antenna, gain is often expressed in dBi.

Generally, there are two basic methods to measure the gain of an antenna: Absolute-gain and Gain-transfer (Gain-comparison) measurement methods, [21]. The absolute-gain method is used to calibrate antennas that can then be used as standards for gain measurements, and it requires no prior knowledge of the gains of the antennas. Whereas, gain-transfer methods must be performed in conjunction with standard gain antennas (reference antennas) to determine the absolute gain of AUT. For the gain measurement in thesis, the gain-transfer method is adopted, using a wideband ridged horn antenna as the reference antenna, with known gain G_{ref} (dBi) and which operates in the same band as AUT. The experimental setup of this method is similar to that of a radiation
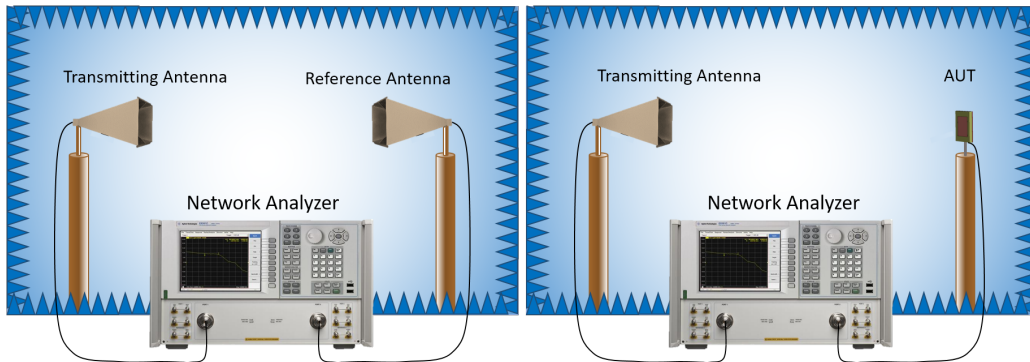
Fig. 3.3 Experimental setup for antenna gain measurement

pattern measurement. Initially, relative gain measurements are performed, which when compared with the known gain of the reference antenna, yield absolute gain of AUT.

This gain-transfer method requires two sets of measurements. An arbitrary antenna is connected to the port 1 (transmitter) and the reference antenna to the port 2 (receiver), of the network analyzer with required stimulated parameter in S_{21} mode. The antenna is bore-sighted and a Thru calibration is performed. This is saved in the analyzer and acts as the reference gain for AUT. In the second set, the reference antenna is replaced by the AUT and the transmission coefficient $|S_{21}|_{AUT}$ (dB) is recorded, which is the relative gain of AUT with respect to reference antenna. In both sets, the geometrical arrangement is maintained intact (other than replacing the antennas at receiver side) and the input power is managed to be same. Fig. 3.4 shows the two sets of gain-transfer measurement method. Finally, the absolute gain, G (dBi), can then be calculated as,

$$G = G_{ref} + |S_{21}|_{AUT}, \tag{3.4}$$

where, G_{ref} is the known gain of the reference antenna, in dBi, and $|S_{21}|_{AUT}$ is the relative gain of AUT, in dB.

Radiation Efficiency

According to IEEE, the antenna radiation efficiency is defined as the ratio of total power radiated by the antenna to the total power accepted by the antenna
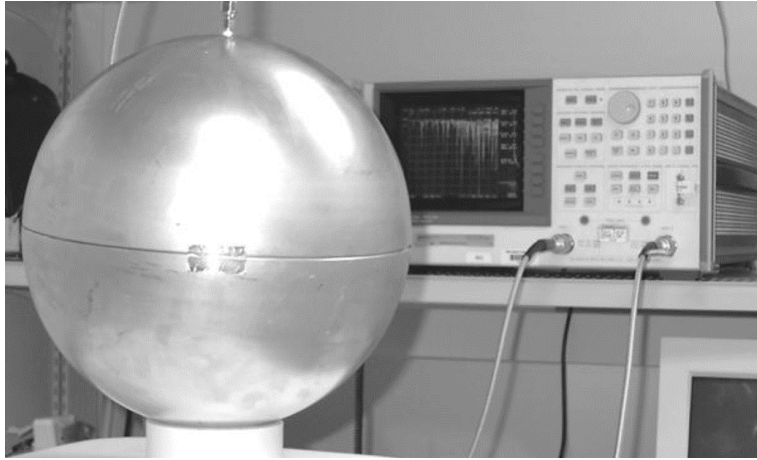
Fig. 3.4 Experimental setup for efficiency measurement, [Schantz, 2002]

at its input terminals, during radiation, [1]. A further acceptable definition of antenna efficiency would include reflected power, due to the mismatch at input terminals, as an explicit loss and define efficiency as the ratio of total power radiated by the antenna to the total power applied at it's input terminals (i.e. $\eta \equiv \frac{P_{rad}}{P_{in}}$). Schantz, in 2002, presented a method for evaluating the UWB antenna efficiency that explicitly include reflected power due to mismatch as a loss term, [168]. This method is a modification of the conventional Wheeler Cap method, which is being used to measure the radiation efficiency of narrow band antennas. Rather than restraining radiations from the antenna to a radiation sphere of radius $r \approx \frac{\lambda}{2\pi}$ (as in the narrow band approach), the modified Wheeler Cap method for UWB allows the antenna to radiate freely and then receive its own transmitted, reflected signal. Fig. 3.5 shows the efficiency measurement setup for such a Wheeler Cap approach.

The power budget for a transmitting antenna can be expressed in terms of power fractions, like, a fraction of the incident energy dissipated in losses ($l \equiv \frac{P_{loss}}{P_{in}}$), a fraction reflected back due to mismatch ($m \equiv \frac{P_{refl}}{P_{in}}$) and a fraction radiated ($\eta \equiv \frac{P_{rad}}{P_{in}}$). Thus, averaging over a suitable time interval and applying conservation of energy, yields:

$$l + m + \eta = 1 \tag{3.5}$$

The spherical shell (radiation sphere) enclosing the AUT enforces a near ideal time reversal of the transmitted signal. Thus, the antenna receives the reflected signal with negligible structural scattering, and the antenna mode scattering term is simply the mismatch fraction ($m = |S_{11-FS}|^2$). By the reciprocity principle, the transmit and receive efficiencies (η) are identical. The scattering coefficient inside the UWB Wheeler Cap can be expressed as,

$$
\begin{aligned}
|S_{11-WC}|^2 &= m + \eta^2 + \eta^2 m^1 + \eta^2 m^2 + \eta^2 m^3 ... \\
&= |S_{11-FS}|^2 + \eta^2 \sum_{n=0}^{\infty} |S_{11-FS}|^{2n} \\
&= |S_{11-FS}|^2 + \eta^2 \frac{1}{1 - |S_{11-FS}|^2}
\end{aligned}
\tag{3.6}
$$

Solving equation (3.6), radiation efficiency can be obtained as,

$$
\eta = \sqrt{(1 - |S_{11-FS}|^2)(|S_{11-WC}|^2 - |S_{11-FS}|^2)}
\tag{3.7}
$$

For measuring the radiation efficiencies of the antennas proposed in this thesis, a metallic chamber having diameter of about 40cm is used. Initially, the AUT is connected to the port 1 of the network analyzer and measures the return loss (S_{11-FS}), in the free space scenario. The AUT is then placed at the center of the oblate metallic chamber (Wheeler Cap) and measures the return loss (S_{11-WC}). The results in both the cases (i.e. free space and with Wheeler Cap) are saved in the network analyzer. Finally, by substituting the values for S_{11-FS} and S_{11-WC} in equation (3.7), the radiation efficiency of the AUT is calculated.

3.3.3 Time-domain Analysis

For UWB antennas, the conventional design parameters like reflection/transmission coefficient, gain, radiation pattern etc. become strongly frequency dependent, which complicates the analysis of the link budget via Friss transmission formula, [79]. Thus, a straight forward evaluation will not be sufficient to characterize the radiation properties of a UWB antenna. Therefore, proper methods must be considered to analyse the transient response of UWB antennas, as they are intended for remarkable pulse-handling capabilities. The transient analysis of
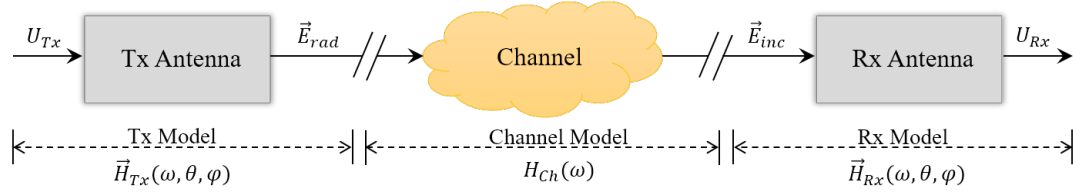
Fig. 3.5 System model of a UWB radio link

the antenna can be performed either by direct time-domain measurements or by a frequency-domain measurement followed by the Fourier Transformation. The time-domain measurements are much faster than the frequency-domain measurements as they uses very short pulses or step functions as driving voltage,[152]. The frequency-domain plus Fourier Transformation method is equally accurate as the direct time-domain way of transient analysis and also it take advantage of the high dynamic range and the standardized calibration of the network analyzer, [200, 205]. Also, the measurement can be done by making use of the existing test facilities available for narrow band antennas. This thesis follows the latter method, and for that the antenna is modelled as a Linear Time Invariant (LTI) system characterized by its spatio-temporal transfer function (gain and phase) & its associated impulse response [234].

Transient Transmission/Reception

Fig. 3.5 portrays a system model (LTI) to characterize a UWB radio link with two antennas in free space under the approximation of far-field and line-of-sight propagation [213, 214]. It consists of three blocks: the Transmit (Tx) antenna, the free space channel and the Receive (Rx) antenna. Each block is characterized by its transfer function $\vec{H}_{Tx}(\omega, \theta, \phi)$, $H_{Ch}(\omega)$ & $\vec{H}_{Rx}(\omega, \theta, \phi)$, and its associated impulse responses $\vec{h}_{Tx}(t, \theta, \phi)$, $h_{Ch}(t)$ & $\vec{h}_{Rx}(t, \theta, \phi)$, respectively. Thus, the free space transmission of the UWB system depicted in Fig. 3.6 can be expressed in frequency-domain as,

$$S_{21}(\omega) = \frac{U_{Rx}(\omega)}{U_{Tx}(\omega)} = \vec{H}_{Tx}(\omega, \theta, \phi) H_{Ch}(\omega) \vec{H}_{Rx}(\omega, \theta, \phi) \tag{3.8}$$

where,

$$H_{Ch}(\omega) = \frac{c}{2r\omega} e^{-j\omega r/c} \tag{3.9}$$

is the free space channel transfer function. $\vec{H}_{Tx}(\omega, \theta, \phi)$ is the transfer function that relates the transmitted signal $U_{Tx}(\omega)$ to the radiated electric field strength $\vec{E}_{rad}(\omega, r, \theta, \phi)$ at a certain distance r from the transmit (Tx) antenna (see equation (3.10)) and, $\vec{H}_{Rx}(\omega, \theta, \phi)$ is the transfer function that relates the received signal $U_{Rx}(\omega)$ to the incident electric field strength $\vec{E}_{inc}(\omega, \theta, \phi)$ at the receive (Rx) antenna (see equation (3.11)) [205].

$$\frac{\vec{E}_{rad}(\omega, r, \theta, \phi)}{\sqrt{Z_0}} = \frac{e^{-j\omega r/c}}{r} \vec{H}_{Tx}(\omega, \theta, \phi) \frac{U_{Tx}(\omega)}{\sqrt{Z_c}} \tag{3.10}$$

$$\frac{U_{Rx}(\omega)}{\sqrt{Z_c}} = \vec{H}_{Rx}(\omega, \theta, \phi) \frac{\vec{E}_{inc}(\omega, \theta, \phi)}{\sqrt{Z_0}} \tag{3.11}$$

Here, Z_c (assumed to be frequency independent) & Z_0 are the characteristic impedances of the Tx/Rx antenna ports and free-space, respectively. Likewise, the corresponding time-domain version of the equation (3.8) can be expressed as,

$$\frac{u_{Rx}(t)}{u_{Tx}(t)} = \vec{h}_{Tx}(t, \theta, \phi) * h_{Ch}(t) * \vec{h}_{Rx}(t, \theta, \phi) \tag{3.12}$$

And, equations (3.10) and (3.11) respectively becomes,

$$\frac{\vec{e}_{rad}(t, r, \theta, \phi)}{\sqrt{Z_0}} = \frac{1}{r}\delta\left(t - \frac{r}{c}\right) * \vec{h}_{Tx}(t, \theta, \phi) * \frac{u_{Tx}(t)}{\sqrt{Z_c}} \tag{3.13}$$

$$\frac{u_{Rx}(t)}{\sqrt{Z_c}} = \vec{h}_{Rx}(t, \theta, \phi) * \frac{\vec{e}_{inc}(t, \theta, \phi)}{\sqrt{Z_0}} \tag{3.14}$$

Here, the $\vec{h}(t, \theta, \phi)$ denotes the transient response corresponding to the transient transmission/reception, when the Tx antenna is excited with an impulse. Thus, by taking the inverse Fourier Transform of equations (3.10) & (3.11) the impulse responses of the antenna in transmission and receiving mode can be generated, respectively. The convolution with the Dirac-delta function $\delta\left(t - \frac{r}{c}\right)$, in equation (3.13), represents the time retardation due to the finite speed of light c. It is to be noted that, the antenna factors like transfer function & transient response are spatial vectors, which depends on the regarded direction of radiation (θ, ϕ) and the polarization vector properties (co- and cross-polarization) of the modeled

antenna. The relation between the receiving and transmitting mode of operation in frequency- & time-domain can be yielded by applying reciprocity theorem to the equations (3.13) & (3.14) [107] as,

$$\vec{H}_{Tx}(\omega, \theta, \phi) = \frac{j\omega}{2\pi c}\vec{H}_{Rx}(\omega, \theta, \phi) \tag{3.15}$$

$$\vec{h}_{Tx}(t, \theta, \phi) = \frac{1}{2\pi c}\ \frac{\partial}{\partial t}\vec{h}_{Rx}(t, \theta, \phi) \tag{3.16}$$

Equation (3.16) points out that transmit impulse response $\vec{h}_{Tx}(t, \theta, \phi)$ is directly proportional to the time derivative of the receive impulse response $\vec{h}_{Rx}(t, \theta, \phi)$. By substituting equation (3.16) in (3.13) and exchanging derivative function $(\frac{\partial}{\partial t})$ and convolution ($*$), the transient radiation (equation (3.13)) can be rewritten as,

$$\frac{\vec{e}_{rad}(t, r, \theta, \phi)}{\sqrt{Z_0}} = \frac{1}{2\pi rc}\delta\left(t - \frac{r}{c}\right) * \vec{h}_{Rx}(t, \theta, \phi) * \frac{\partial}{\partial t}\frac{u_{Tx}(t)}{\sqrt{Z_c}} \tag{3.17}$$

This represents the formulation for radiated fields of a Impulse Radiating Antenna (IRA) [32] and denotes the ideal antenna case with $\vec{h}_{Rx}(t, \theta, \phi) = \pm\delta(t)$ which radiates an electric field pulse that is proportional to the first-order time derivative of the input voltage pulse. This simply means that the ideal receiving antenna will have a Dirac-delta impulse response (i.e. independent of incident angle) which implies that the received voltage pulse will always have the same shape as the incident field pulse on the antenna. In the frequency-domain this corresponds to an antenna transfer function with a constant amplitude response and a linear phase response (or constant group delay).

Choice of Source Pulse

Generally, all the pulses which has a spectrum wider than 500 MHz and stipulated by FCC can be used as a source pulse for UWB transmission. However, the selection of proper source pulse with appropriate shape is a crucial design for UWB systems. Moreover, it is desirable for UWB signals to efficiently utilize the bandwidth and power allocated by FCC to maximize the received SNR under the stringent transmission power limitations.

The Gaussian monocycle has been the earliest proposal as the source pulse for UWB radar and communication systems [190]. But its Power Spectral Density (PSD) has direct current offset and for that reason it will not radiate effectively. Also, its PSD does not fall under the emission mask specified by FCC for any pulse width values chosen. One possible solution is to shift the centre frequency and adjust the bandwidth accordingly to meet these requirements. This can be accomplished by modulating the monocycle with a sinusoid to shift the centre frequency and by varying the pulse width. But, this modulation will increase the cost and complexity of the impulse radio system due to its carrier-less behaviour.

An effective method of pulse-shaping is by fine-tuning the higher-order derivatives of the Gaussian pulse. A family of differentiated Gaussian pulses which resemble sinusoids modulated by a Gaussian envelope $v_n(t)$ is broadly used as a source pulse for UWB systems due to its unique temporal and spectral properties.

$$v_n(t) = \frac{d^n}{d^n t}\Big[e^{-(\frac{t}{\tau})^2}\Big] \tag{3.18}$$

where, t denotes the time, τ is the time decay constant that determines the temporal width of the pulse and n is the order of differentiation. Fig. 3.6 showcases the Gaussian pulse with its family of derivatives (Rayleigh pulses) and their corresponding PSD plots. As noticed from the figure, the Rayleigh pulses up to the third order are not getting fit in to the FCC spectral mask, mainly those peaking at lower UWB frequencies. It is also to be noted that, the energy (peaks of PSD) moves to higher frequencies as the order of derivative increases. Hence, by choosing the suitable order and pulse width one can find a pulse which falls under the FCC spectral mask and this can be used as a source pulse for the UWB radio link. Some higher-order Rayleigh pulses like, 4th-order Rayleigh pulse with $67ps < \tau < 76ps$ and 5th-order Rayleigh pulse with $67ps < \tau < 76ps$ can match the UWB band directly [38]. For the pulse distortion analysis in this thesis, the 4th-order Rayleigh pulse, whose PSD peaks at $\approx 6GHz$, is chosen as the source pulse ($u_{Tx}(t)$) and is expressed by,

$$u_{Tx}(t) = v_4(t) = \Big[\frac{16}{\tau^8}(t-1)^4 \; - \; \frac{48}{\tau^6}(t-1)^2 \; + \; \frac{12}{\tau^2}\Big]e^{-\left(\frac{t-1}{\tau}\right)^2} \tag{3.19}$$
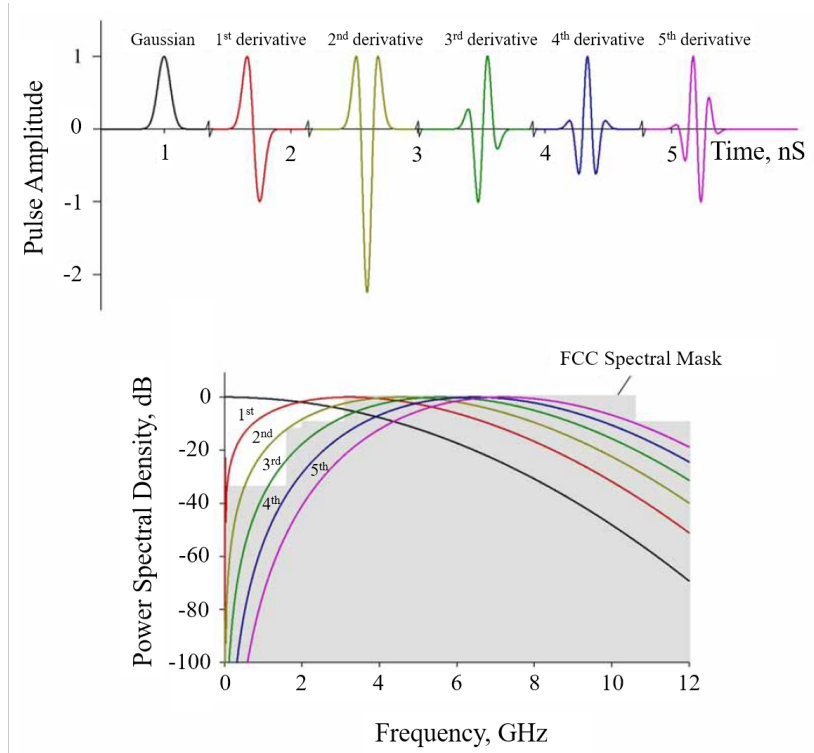
Fig. 3.6 Gaussian Pulse and its derivatives in time domain, and their PSDs

Implementation in CST

For the transient response analysis of the UWB antennas studied in this thesis the virtual probe feature of CST is utilized. Fig. 3.7 shows the virtual probe arrangement adopted for the time-domain study of an antenna in this thesis. As noticed from the figure, the probes are arranged in the two principal planes of an antenna at a distance (r) according to the AUT's far-field range. The probe-orientation (vertical or horizontal) and the gap between each probes are selected with respect to the orientation of AUT and the required data-resolution, respectively.

Here, probes are placed at a distance of $r = 15cm$ and the antenna is excited with an input pulse $u_{Tx}(t)$ whose frequency spectrum covers the antenna's bandwidth and conforms the FCC spectral mask. For the analysis in this thesis the 4th derivative of Gaussian pulse is chosen as the input pulse given by equation (3.19) and with $\tau = 67ps$. The radiated electric field pulses $\vec{e}_{rad}(t, r, \theta, \phi)$ are then
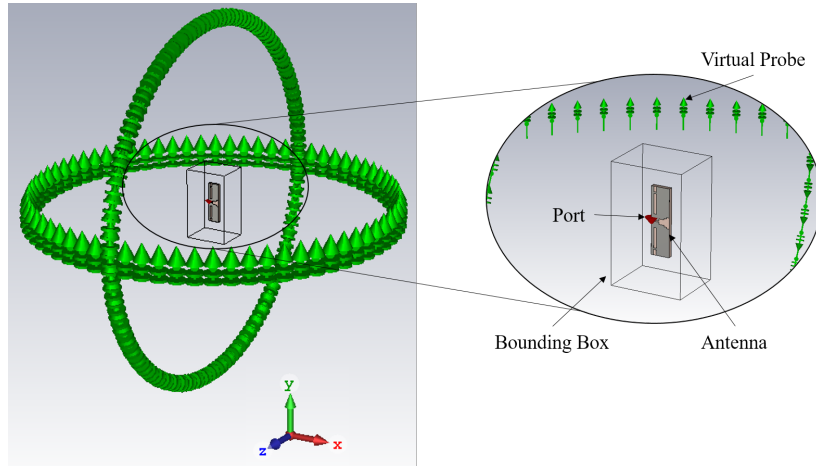
Fig. 3.7 Virtual probe arrangement in CST Microwave studio

probed directly over a wide range of angles in the two principal planes using the virtual probes, as in Fig. 3.7. After taking the Fourier Transform of $u_{Tx}(t)$ & $\vec{e}_{rad}(t, r, \theta, \phi)$, and using equation (3.10) the transfer function $\vec{H}_{Rx}(\omega, \theta, \phi)$ is deduced. The impulse response $\vec{h}_{Tx}(t, \theta, \phi)$ can be calculated from this transfer function by simply taking its Inverse Fast Fourier Transform (IFFT).

Realistic Approach

In reality, the transfer functions of both the Transmitting and Receiving antennas can be deduced from simply measuring the S_{21} in frequency-domain. By using two identical horn antennas oriented for bore-sight transmission/reception and considering equation (3.8), the following expressions for corresponding transfer functions can be derived, as

$$H_{Tx}(\omega, \theta, \phi) = \sqrt{\frac{j\omega}{c} \frac{S_{21}(\omega, \theta, \phi)}{H_{Ch}(\omega)}} \qquad (3.20)$$

$$H_{Rx}(\omega, \theta, \phi) = \sqrt{\frac{c}{j\omega} \frac{S_{21}(\omega, \theta, \phi)}{H_{Ch}(\omega)}} \qquad (3.21)$$

where, $H_{Ch}(\omega)$ is given by equation (3.9). This characterizes the reference antenna (Txr antenna) and thus, by replacing the Rxr antenna with AUT, its transfer
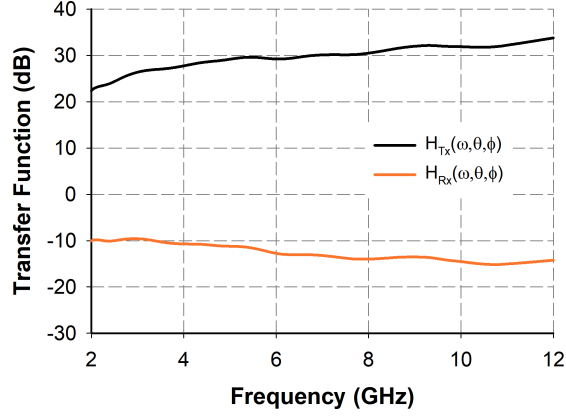
(a) Transmitting & receiving Transfer Functions
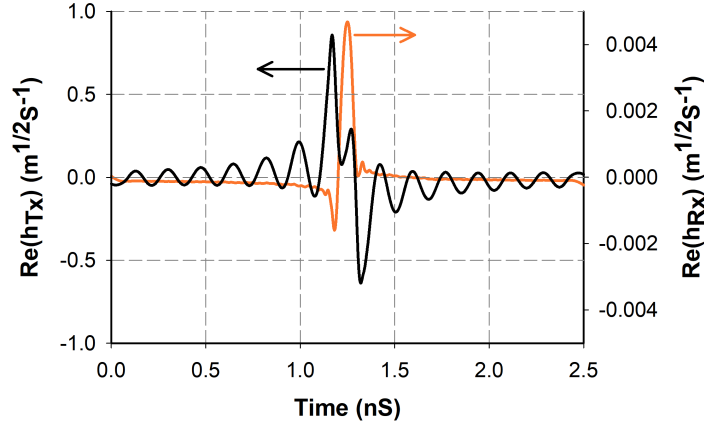
(b) Transmitting & receiving Impulse Responses

Fig. 3.8 Measured characteristics of wideband horn antenna

function $(H_{AUT}(\omega, \theta, \phi))$ for multiple orientation can be expressed as

$$H_{AUT}(\omega, \theta, \phi) = \frac{S_{21}(\omega, \theta, \phi)}{H_{Tx}(\omega, \theta, \phi)H_{Ch}(\omega)} \tag{3.22}$$

The phase of transmission coefficient S_{21} should be unwrapped properly in order to get appropriate physical results. In this thesis the Txr and Rxr antennas are kept at a distance of $r = 15cm$ and appropriate calibrations are carried out to eliminate the dispersive effects of connecting cables.

The impulse responses ($\vec{h}_{Tx}(t, \theta, \phi)$ & $\vec{h}_{Rx}(t, \theta, \phi)$) can be easily deduced from their corresponding transfer functions by taking their Inverse Fast Fourier Transform (IFFT), but with adequate zero-padding and forming conjugate frequency response S_{21}^* [213]. Specifically, before taking IFFT the conjugate of the zero-padded data is reflected to the negative frequencies to get a spectrum which is symmetric around DC, to conform to a real signal spectrum. Thus, IFFT of this resulting double sided spectrum gives a real impulse waveform.

Fig. 3.8 shows the measurement results of two identical wideband antennas at transmitting and receiving sides. The measured transfer function is depicted in Fig. 3.8a and the corresponding impulse response is shown in Fig. 3.8b, which denotes they are different from each other by a derivative function.

UWB Antenna Quality Measures

The antenna model of Fig. (3.5) enables the study of dispersive effects due to a particular antenna structure, radiation outcome of arbitrary input waveforms and also influences of frequency-dependent matching and losses. Therefore, the quality measures of the efficiency of a dispersive UWB AUT can be derived directly from the transient response of the AUT. Mainly there are two important aspects to be considered: the antenna's ability to effectively transmit and receive power and the distorting influence on the waveform to be transmitted or received [205]. These measures are accomplished with the help of some frequency-domain and/or time-domain parameters, discussed below. For the sake of simplicity co-polarization is considered for all the formulations.

- **Frequency-domain parameters** The effective Continuous-Wave (CW) gain pattern G_{eff} can be calculated from the transfer function [213] as

$$
\begin{aligned}
G_{eff}(\omega, \theta, \phi) &= \frac{2\omega}{c} |\vec{H}_{Rx}(\omega, \theta, \phi)|^2 \\
&= \frac{2c}{\omega} |\vec{H}_{Tx}(\omega, \theta, \phi)|^2
\end{aligned}
\tag{3.23}
$$

The IEEE standard gain G of the antenna, which excludes mismatch losses, can be easily derived from the G_{eff} using the antenna's input reflection

coefficient $S_{11}(\omega)$ [205] as

$$G(\omega, \theta, \phi) = \frac{G_{eff}(\omega, \theta, \phi)}{1 - |S_{11}(\omega)|^2} \tag{3.24}$$

In order to quantify the measures of distortion in frequency-domain, the antenna's transfer function is denoted as $H(\omega) = |H(\omega)|e^{j\phi(\omega)}$, with the magnitude $|H(\omega)|$ in meters and the phase angle $\phi(\omega)$ in radians. Thus, the group delay $\tau_g(\omega)$ of a transfer function is defined as

$$\tau_g(\omega) = -\frac{d\phi(\omega)}{d\omega} = -\frac{d\phi(f)}{2\pi df} \tag{3.25}$$

where, $\phi(f)$ is the frequency dependent of the received signal. The delay that may encountered by a portion of the spectral energy at a given ω (angular frequency), during its transmission through a filter is termed as the group delay. For minimal distortion, the group delay should be constant within the frequency band of interest, i.e.,the phase should increase linearly with frequency.

- **Time-domain parameters** The way in which an antenna effects on the pulse distortion can also be investigated in time-domain by analyzing the envelope of the transient response. This envelope localizes the distribution of energy versus time and is a direct measure of the dispersion of antenna [201, 205]. The envelope of the analytical response defined in the frequency domain [149] can be expressed as,

$$H_n^+(\omega) = \begin{cases} 2H_n(\omega) & \text{for } \omega > 0 \\ 0 & \text{for } \omega \leq 0 \end{cases} \tag{3.26}$$

The Fourier transform of (3.26) gives the complex analytical response h_n^+ in time-domain and the real valued antenna transient response is given by

$$h_n(t) = \Re\{h_n^+(t)\} \tag{3.27}$$

According to equation (3.14), the peak output voltage from an incident wave depends on the peak value $p(\theta, \phi)$ of the antenna's transient response

and is given by,

$$p(\theta, \phi) = \max_t |h_n^+(t, \theta, \phi)| \tag{3.28}$$

The envelope width gives the measure of linear distortion of an antenna and is defined as the Full Width Half Maximum (FWHM) of the magnitude of the transient response envelope:

$$\tau_{FWHM}(\theta, \phi) = \tau_{0.5}(\theta, \phi) = t_2|_{|h_n^+(t_2,\theta,\phi)|=p/2} - t_1|_{|h_n^+(t_1,\theta,\phi)|=p/2,\ t_1<t_2} \tag{3.29}$$

The time until the envelope has fallen from the peak value $p(\theta, \phi)$ below a fraction α of the main peak (i.e., $\alpha p(\theta, \phi)$) is defined as the duration of ringing, τ_r and is calculated as

$$\tau_{r=\alpha}(\theta, \phi) = t_\alpha|_{h_n^+(t_\alpha,\theta,\phi)=\alpha p(\theta,\phi)} - t_p|_{h_n^+(t_p,\theta,\phi)=p(\theta,\phi),\ t_p<t_\alpha} \tag{3.30}$$

The lower bound for α is selected according to the noise floor of the antenna measurement. For the comparison of ringing of antennas with different gains under the constraint of constant noise floor, the α is chosen to be equal to 0.22 (-13 dB).

- **Pulse-distortion analysis: Fidelity** The pulse distortions introduced by an antenna along different orientations can be analysed from its spatio-temporal impulse response. In the case of UWB systems, the receivers are based on pulse energy detection or correlation of received pulse with a template waveform stored in the receiver. The received pulse $u_o(t)$ can be obtained by convolving the impulse response $\vec{h}_n(t, \theta, \phi)$ with the input pulse $u_i(t)$:

$$u_o(t) = \vec{h}_n(t, \theta, \phi) * u_i(t) \tag{3.31}$$

Therefore, we need to examine the pulse distortion by calculating the fidelity factor [110]. This factor measures the faithfulness of a system to reproduce the time shape of the input signal and thereby quantifies the pulse handling capability of an antenna. Thus, the fidelity between $u_i(t)$ and $u_o(t)$ is

formulated as,

$$F(\theta, \phi) = \max \frac{\int_{-\infty}^{+\infty} u_i(t).u_o(t-\tau)dt}{\sqrt{\int_{-\infty}^{+\infty} |u_i(t)^2|dt. \int_{-\infty}^{+\infty} |u_o(t)^2|dt}} \tag{3.32}$$

where, τ is the delay which can be varied to maximize the numerator. Fidelity F yields the maximum of the cross-correlation function between two waveforms and compares its shapes only, not amplitudes. The F reaches unity as the shape of both waveforms are exactly same, which denotes a distortion-less pulse from the antenna. The measurement of F is conducted for different spatial orientations of the antenna [134].

3.3.4   Spatial-domain Analysis

Spatial-domain analysis of an antenna yields the knowledge of its radiation properties with respect to the surrounding directions. Some parameters under this analysis helps to characterize and quantify the performance of UWB antennas. By combining the concepts of pulse fidelity, time-domain correlation patterns and frequency-domain correlation patterns, the concept of frequency domain correlation patterns and a figure-of-merit called Pattern Stability Factor (PSF) are derived to characterize the pattern stability of wideband antennas [55]. Usually, an antenna is represented by a single transfer function in the UWB system design and optimization schemes. However, this will not be the case for modern UWB antennas as they are complicated in design and hence their transfer function depends on the direction. Therefore, for the proper system design and optimization it is necessary to select a single transfer function (corresponding to a single reference direction) from those corresponding to infinite number of directions. Fortunately, the frequency-domain correlation pattern will guide us to select the best transfer function for a given antenna in a given application, which is based on pulse correlation concepts but conducted in frequency-domain.

The frequency-domain correlation pattern portrays the relationship between radiation in a reference direction to radiation in all other directions of interest, over a specified bandwidth. The selection of this reference direction of an antenna is so crucial in the analysis in order to get accurate outcomes. Whereas, the

PSF quantifies the overall pattern stability of a wideband antenna, for a specific bandwidth and a range of directions. This quantitative measure is useful to

- to compare the pattern stability performance of different antennas quantitatively

- to examine the effect of ground-plane modifications, packaging, integration of antennas with cases etc. [104]

- to assess the pattern stability improvement methods [16]

- to define the pattern stability bandwidth

Frequency-domain Correlation Pattern

The frequency-domain correlation pattern $C(\vec{R})$ represents how the radiated waveform in a reference direction $\vec{R}$ is correlated to all other directions of interest $\vec{r}$ on average and is formulated as

$$C(\vec{R}) = \frac{\int\limits_{\Omega} F^2(\vec{R}, \vec{r})ds}{\int\limits_{\Omega} ds} \tag{3.33}$$

where, $F^2(\vec{R}, \vec{r})$ denotes the relationship between radiated fields between two directions, Ω is the range of operating directions of the antenna and integration is with respect to the direction of interest $\vec{r}$. The factor $F^2(\vec{R}, \vec{r})$ is defined in frequency-domain as

$$F^2(\vec{R}, \vec{r}) = \frac{\left| \int\limits_{BW} E(\vec{r}, f)E^*(\vec{R}, f)df \right|^2}{\int\limits_{BW} \left| E(\vec{r}, f) \right|^2 df \int\limits_{BW} \left| E(\vec{R}, f) \right|^2 df} \tag{3.34}$$

where, $E(\vec{r}, f)$ is the radiated electric-field in frequency domain, $*$ stands for complex conjugate and BW is the bandwidth of interest. If the antenna has a spherical coverage, then Ω is a sphere and therefore it will be a double integration over a solid angle of 4π. If the coverage is limited to a plane (i.e., azimuthal or

elevation), then it will be a line integral. As noted from the equation (3.33), $C(\vec{R})$ reaches its maximum value of unity when $F^2(\vec{R}, \vec{r}) = 1$ in all directions. This is an ideal condition in which the antenna has an extremely stable pattern throughout the operating bandwidth and is difficult to achieve in practice. Practically, a direction $\vec{R}$ in which $C(\vec{R})$ is maximized will be searched, and is selected as the best direction for optimization. This unique direction along which $C(\vec{R})$ is maximum is the direction that is best correlated to all other directions on average. Therefore, the transfer function in this direction will be the best one to represent the given UWB antenna.

Pattern Stability Factor (PSF)

For an ideal antenna $F^2(\vec{R}, \vec{r}) = 1$ for all $\vec{R}$ and $\vec{r}$, and $C(\vec{R}) = 1$ for all reference directions $\vec{R}$. By taking these observations into consideration, a single figure-of-merit is defined to quantify the overall pattern stability performance of an antenna. This figure-of-merit is named as Pattern Stability Factor (PSF) and is defined for a given frequency band as

$$PSF = \frac{\displaystyle\int_{\Omega} C(\vec{R}) ds}{\displaystyle\int_{\Omega} ds} \tag{3.35}$$

where, Ω is same as before, i.e., the range of operating directions of the antenna, but the integration is now with respect to the reference direction $\vec{R}$. Thus, for an ideal antenna with extremely stable pattern the PSF is unity. For a UWB antenna with considerably good all-round performance, PSF > 0.95 will be desirable. Selection of Ω solely depends on the direction of interest for a given application. Only single integrals are required for all calculations if the directions of interest are limited to one plane. The PSF bandwidth of a given antenna is given by

$$\lim_{BW \to 0} F^2(\vec{R}, \vec{r}) = 1 \tag{3.36}$$

This implies that, within a sufficiently narrow bandwidth any antenna will give almost perfectly stable patterns. As the operating bandwidth is increased, the

PSF tends to deteriorate from its ideal conditions. Therefore, it is logical to describe an antenna bandwidth based on its pattern stability performance.

Theoretical and Experimental Implementation

For the theoretical calculation of PSF [55], initially the range of direction of interest is discretized accordingly, and in these discrete directions the frequency-domain radiated electric field values are detected at a fixed distance in the far field over the operating bandwidth. The detection of radiated electric field $E(\vec{r}, f)$ is performed by using the virtual probe facility available in CST. These probes are oriented and arranged according to the plane of interest, at a fixed distance as shown in Fig. 3.7. These electric field values are then substituted in (3.34) to calculate $F^2(\vec{R}, \vec{r})$ for all pairs of discrete directions. Subsequently, from (3.33) and (3.35) the frequency-domain correlation patterns and PSF are calculated, respectively.

The PSF calculation can also be performed using experimental data, simply by substituting the amplitude and phase of measured radiation patterns in (3.34) just like theoretical data. Here, the absolute field strength is not required rather a scaled or normalized pattern is sufficient. For antennas with stable phase centers, the phase values in (3.34) will be cancelled out and hence only amplitude (scalar) measurements are sufficient. Alternatively, the PSF can also be determined by measuring the transmission between two identical antennas. In this case, one antenna is kept stationary and the other antenna is rotated around the fixed one, and the transmission coefficient S_{21} is measured using the vector network analyzer. This measured S_{21} is then substituted for electric field values $E(\vec{r}, f)$ in (3.34) and thereby the PSF is calculated.

3.3.5   MIMO/Diversity Performance Evaluation

According to the SNR level, a multiple-antenna system can be operated in diversity or multiplexing schemes in a rich scattering environment. When SNR level is low the antenna diversity technique is used to increase the reliability of a wireless communication link, by transmitting uncorrelated signals and thereby reducing the chances of deep signal fading. Whereas for high SNR level spatial multiplexing technique is employed to achieve maximum data rate, which creates

several uncorrelated channels by taking the advantage of channel fading. The conventional antenna performance metrics and parameters such as impedance bandwidth, radiation pattern, gain, efficiency etc. will not be sufficient for the complete characterization of a multiple-antenna system. There are some figures-of-merit which governs the MIMO/diversity performance of such systems. These parameters helps to gain knowledge about the suitability of a given multi-port antenna for an effective MIMO system. This is accomplished by analysing the impact of individual antenna-element performance on to the functioning of other subsequent elements. Some main figures-of merit used for the MIMO/diversity performance evaluation in this thesis are discussed below.

Correlation Coefficient

Correlation coefficient is a measure that describes how well the transmitted/received signals from different ports are independent to each other in a multi-element system. This parameter can be evaluated in three forms: complex, envelope and power correlation coefficients. Usually, envelope correlation coefficient (ρ_{ij}^e) is preferred to evaluate MIMO/diversity capabilities of a multi-antenna system. Under the assumption that the received signals have a Rayleigh distributed envelope and randomly distributed phase [135], the ρ_{ij}^e is related to the complex correlation coefficient (ρ_{ij}^c) by

$$\rho_{ij}^e = |\rho_{ij}^c|^2 \tag{3.37}$$

The ρ_{ij}^e varies from zero to one, and for a good MIMO/diversity performance its value should be low, which is a great challenge in low-profile end-terminals due to their space constraints. However, low correlation can be made possible by reducing the mutual coupling between the antenna-elements using any of the isolating techniques: spatial, polarization, angle and/or structural separation.

The common trend of spatial diversity technique follows the rule of allowing at least a half wavelength separation between antenna elements. This ensures the envelope correlation to be less than or equal to 0.5, which is fair enough to produce high diversity gain between the antenna-elements. Assuming that all the multipath components lie in the horizontal plane, Clarke [42] formulated the normalized correlation coefficient of the signal envelopes at the terminals of two

vertical monopole antennas separated by a distance of d, on the mobile receiving vehicle which is travelling through an isotropically scattered field, as

$$\rho_{ij} \cong J_0^2 \left(\frac{2\pi d}{\lambda} \right) \tag{3.38}$$

where J_0 is the Bessel function of the first kind with order zero and λ is the wavelength. This expression is valid for a uniform angle of arrival in azimuth plane and identically polarized receiving antennas with omnidirectional nature that co-polarized with the incoming wave. However, (3.38) shows higher values than in reality (mainly for smaller d) as it does not consider the mutual coupling factor between the antenna-elements.

Practically, an antenna designer will try to design a multi-antenna system with minimal coupling between the ports while meeting the input matching requirements. This implies that the signal correlation should be low as possible (ideally zero) for a fair MIMO/diversity performance. The conventional way of computing the envelope correlation for a two-antenna system is given by [198]

$$\rho_{12}^e = \frac{\left| \iint\limits_{4\pi} \left[\vec{F}_1(\theta,\phi) \ * \ \vec{F}_2(\theta,\phi) \right] d\Omega \right|^2}{\iint\limits_{4\pi} \left| \vec{F}_1(\theta,\phi) \right|^2 d\Omega \iint\limits_{4\pi} \left| \vec{F}_2(\theta,\phi) \right|^2 d\Omega} \tag{3.39}$$

where, (θ,ϕ) are the elevation and azimuthal angles, $\vec{F}_i(\theta,\phi)$ is the far-field radiation pattern of the antenna system when i^{th} port is excited and Ω is the solid angle. Here, * denotes the Hermitian product. The above expression is hold true for an isotropic environment with balanced polarizations. However, computing envelope correlation coefficient in this way is a cumbersome process, whether it is done experimentally and/or numerically, as it needs to know the three-dimensional radiation patterns from all the ports. Later, Ko et al. [103] experimentally showed that the diversity system performance can also be determined from mutual coupling or direct envelope correlation measurements. Following this, Blanch et.al. [161] formulated a way to compute the envelope

correlation from the S-parameter characterisation of the antenna system:

$$\rho_{ij}^e = |\rho_{ij}^c|^2 = \left| \frac{S_{ii}^* S_{ij} + S_{ji}^* S_{jj}}{\sqrt{\left(1 - (|S_{ii}|^2 + |S_{ji}|^2)\right)\left(1 - (|S_{jj}|^2 + |S_{ij}|^2)\right)}} \right|^2 \quad (3.40)$$

where, ρ_{ij}^e is the envelope correlation coefficient between i^{th} and j^{th} ports of a multi-antenna system. Thus, for a N-port antenna system, (3.40) can be generalized as

$$\rho_{ij}^e = |\rho_{ij}^c|^2 = \left| \frac{\sum_{n=1}^N S_{in}^* S_{nj}}{\sqrt{\prod_{k=i,j}\left(1 - \sum_{n=1}^N S_{kn}^* S_{nk}\right)}} \right|^2 \quad (3.41)$$

for $i, j = 1, 2, 3, ...N$ (N= no.of antenna elements). This approach has the advantage that it does not require a tedious computation nor any three-dimensional radiation patterns of the antennas and provides a clear knowledge about the effects of mutual coupling and input match on the diversity performance of the antenna system. However, this expression holds true for a diversity system in a uniform multipath environment with loss-less antennas having high radiation efficiencies, which is practically not possible. Therefore, calculating signal correlation through this method suffer poor accuracy if the radiation efficiencies of the antennas are low and correlation of losses is not included in the calculation. This uncertainty can be avoided by incorporating the radiation efficiencies and worst cases for the correlation of losses into the expression for complex correlation as [73],

$$|\rho_{ij}^c|_{guaranteed} = |\rho_{ij}^c| + \rho_{loss} \quad (3.42)$$

where,

$$|\rho_{ij}^c| = \left| \frac{S_{ii}^* S_{ij} + S_{ji}^* S_{jj}}{\sqrt{\left(1 - (|S_{ii}|^2 + |S_{ji}|^2)\right)\left(1 - (|S_{jj}|^2 + |S_{ij}|^2)\right)}\eta_{rad_i}\eta_{rad_j}} \right| \quad (3.43)$$

$$\rho_{loss} = \sqrt{\left(\frac{1}{\eta_{rad_i}} - 1\right)\left(\frac{1}{\eta_{rad_j}} - 1\right)} \quad (3.44)$$

Here, η_{rad_i} & η_{rad_j} represents the radiation efficiencies of ith & j^{th} antenna elements, respectively. For N-port antenna systems, equations (3.43) & (3.44) can be generalised as,

$$|\rho_{ij}^c| = \left| \frac{\sum_{n=1}^{N} S_{in}^* S_{nj}}{\sqrt{\prod_{k=i,j} \left(1 - \sum_{n=1}^{N} S_{kn}^* S_{nk}\right) \prod_{m=1}^{N} \eta_{rad_m}}} \right|^2 \tag{3.45}$$

$$\rho_{loss} = \sqrt{\prod_{k=1}^{N} \left(\frac{1}{\eta_{rad_k}} - 1 \right)} \tag{3.46}$$

for $i, j = 1, 2, 3...N$. Thus, for a Rayleigh-fading channel the envelope correlation coefficient is given by

$$|\rho_{ij}^e|_{guaranteed} = |\rho_{ij}^c|_{guaranteed}^2 \tag{3.47}$$

which is the worst case of signal correlation by considering the losses & efficiency, and the actual values of signal correlation is sure to lie below the level created by (3.47). Moreover, antenna systems with an envelope correlation coefficient less than 0.5 are recognized to provide significant diversity performance, [198].

Mean Effective Gain (MEG)

A power imbalance in the multiple channels of a multi-antenna system will cause significant diversity loss, which is due to the poor antenna efficiency. This mismatch is a crucial factor to be considered while designing a diversity system and can be quantified by calculating the Mean Effective Gain (MEG) of an antenna. MEG can be termed as a single parameter which describes the impact of an antenna on the link budget of a communication system. It is a statistical measure of how deterministic an antenna in a stochastic channel. The concept of MEG was introduced by Taga [187], who defined it as the average power received by an AUT in the propagation channel of interest to the sum of the average powers that would be received in that same environment by two isotropic antennas (vertically and horizontally polarised). Thus, the MEG of the ith antenna element is the ratio of the mean received power (P_{rec}) to the total mean incident power

(P_{inc}) at that element and can be formulated as

$$MEG_i = \frac{P_{rec}}{P_{inc}}$$
$$= \oint \left(\frac{XPR \, G_{\theta i}(\Omega)P_\theta(\Omega) + G_{\phi i}(\Omega)P_\phi(\Omega)}{1 + XPR} \right) d\Omega \qquad (3.48)$$

where Ω is the solid angle & $d\Omega = sin\theta \, d\theta \, d\phi$, $G_{\theta i}(\Omega)$ & $G_{\phi i}(\Omega)$ are the θ and ϕ components of the realized active power gain pattern of ith antenna element, and $P_\theta(\Omega)$ & $P_\phi(\Omega)$ are the θ and ϕ components of the angular density functions of incident power. XPR represents the cross-polarization power and is formulated as

$$XPR = \frac{P_\theta(\Omega)}{P_\phi(\Omega)} \qquad (3.49)$$

For a uniform propagation environment, where $XPR = 1$ and $P_\theta(\Omega) = P_\phi(\Omega)$ $= \frac{1}{4\pi}$, equation (3.48) can be simplified as

$$MEG_i = \frac{\eta_{tot_i}}{2} \qquad (3.50)$$

with η_{tot_i} being the total efficiency of the $i^t h$ antenna element and is calculated by taking the product of antenna mismatch efficiency (η_{mis_i}) and radiation efficiency (η_{rad_i}) as

$$\eta_{tot_i} = \eta_{mis_i} \, \eta_{rad_i} \qquad (3.51)$$

The radiation efficiency is calculated by using the Schantz's method of efficiency evaluation, discussed in 3.3.2, in transmit mode by exciting the ith antenna element and terminating all other ports with matched load of 50Ω. Therefore, the mismatch efficiency is given by, [91]

$$\eta_{mis_i} = 1 - \sum_{j=1}^{N} |S_{ij}|^2 \qquad (3.52)$$

with N as the total number of ports. For an optimal diversity performance, the signals received from the antennas must satisfy the criteria of, [103, 198],

$$\frac{MEG_i}{MEG_j} \cong 1 \qquad (3.53)$$

In order to ensure that the average power received by any two antenna elements is nearly equal, the ratio of MEG between those two antenna elements should have a value close to unity.

Diversity Gain

Employing diversity technique in a multi-antenna system is a potential way to combat channel fading. Different diversity techniques, as discussed under subsection 1.2.3, can be used to enhance the overall link reliability of the system by receiving multiple replicas of the transmitted streams at the receiver, through different channel paths. This guarantees that at-least one copy of the transmitted signal will suffer less fading as compared to the other copies and provides uncorrelated signals at the receiver. Therefore, a proper combination of the signals at receiver using appropriate combining techniques will provide higher SNR levels resulting better signal reception.

The diversity gain (DG) is a figure-of-merit to quantify the diversity performance of a communication system and is the slope of error probability in a received SNR curve. DG represents the increment in the received SNR of the combined signals within the diversity antenna system as compared to the SNR of a single reference antenna (SISO system), at a given Symbol Error Rate (SER) probability. In other words, DG is the comparison between a combined Cumulative Distribution Function (CDF) and a reference CDF at a certain level of CDF. Depending upon the selection of the reference antenna DG can be defined in three ways: apparent Diversity Gain (DG), Effective Diversity Gain (EDG) & Actual Diversity Gain (ADG), [197].

In apparent diversity gain the best branch of a multi-antenna system with strongest SNR level is selected as the reference antenna, at a certain signal probability. Therefore, the comparison of the combined signal level and reference signal level can be formulated as, [195]

$$DG = \frac{(\gamma_c/\Gamma_c)}{(\gamma/\Gamma)_{BestBranch}}\Big|P_{\gamma_c} = 1\% \ or \ 50\% \qquad (3.54)$$

where γ_c & γ are the instantaneous SNR and Γ_c & Γ are the mean SNR of the combined signal & best-branch signal (reference antenna), respectively. Equation (3.54) holds true for a probability P_{γ_c}, typically of the value 1% or 50%.

However, the performance of this branch gets affected by the presence of other branches and will decrease its efficiency due to the effect of mutual coupling. Therefore, another reference antenna with 100% efficiency in free space is taken into consideration, and introduced another metric named Effective Diversity Gain (EDG), as

$$EDG = \frac{(\gamma_c/\Gamma_c)}{(\gamma/\Gamma)_{BestBranch}} \eta_{BestBranch} \Big| P_{\gamma_c} \tag{3.55}$$

where $\eta_{BestBranch}$ is the total efficiency of the best branch (branch with 100% efficiency) and it considers the losses due to mismatch, material properties and mutual coupling in the diversity performance calculations.

The diversity combined signal can also be related to an existing single antenna solution which is to be replaced by the diversity antenna implementation under test, in the same propagation environment and at a certain level of CDF. This can be termed as Actual Diversity Gain (ADG) and is formulated as

$$EDG = \frac{(\gamma_c/\Gamma_c)}{(\gamma/\Gamma)_{SingleAntennaSolution}} \Big| P_{\gamma_c} \tag{3.56}$$

This metric shows the actual effectiveness of replacing a single-antenna system with multiple antennas and thus finds crucial role in the practical implementation of diversity in mobile devices. Fig. 3.9 depicts performance of various diversity metrics at different CDF levels. In ideal case, the maximum diversity gain for two uncorrelated antennas with 100% efficiency using selection combiner is taken to be 10dB with probability level of 1%, where the radio link reliability is 99%. If the two branches of a diversity system are correlated to each other due to the lack of cross-polar discrimination at the receiving terminal, the diversity gain will be reduced resulting in poor MIMO performances. Hence, it is clear that the correlation coefficient must kept low enough to keep the diversity still effective. The effect of envelope correlation coefficient (ρ^e) on diversity gain in [135] points that, as long as ρ^e is less than 0.7, the degradation of the diversity gain can be related to ρ^e by a factor DF, which is defined as [220]

$$DF = \sqrt{1 - \rho^e} \tag{3.57}$$
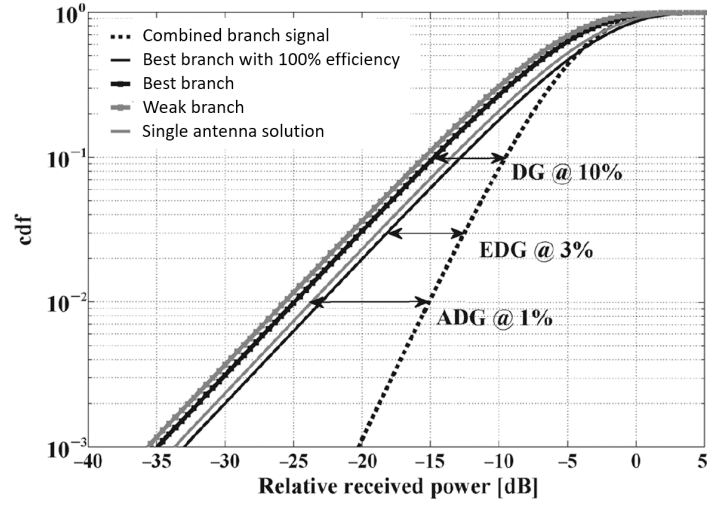
Fig. 3.9 Diversity performance of DG, EDG & ADG

Moreover, to attain high diversity gain the signal power levels from the antennas in a diversity system must not be too different. To illustrate this the ratio of antenna branch power is analysed by using the MEGs of the antenna and is formulated as (for two branches i & j)

$$k = min\left(\frac{MEG_i}{MEG_j}, \frac{MEG_j}{MEG_i}\right) \tag{3.58}$$

Thus, the diversity gain (DG) of a multi-antenna system can be expressed as

$$DG = DG_0 \cdot DF \cdot k \tag{3.59}$$

where, DG_0 is the diversity gain in ideal case. DG_0 calculated using two ideal lossless antennas with 100% efficiency and zero correlation, for a radio link of 99% reliability is found to be 10dB in the case of selection combining.

Multiplexing Efficiency

Multiplexing efficiency (η_{mux}) is a simple and intuitive power-based metric for the Spatial Multiplexing (SM) mode of operation in MIMO systems, which gives an approximate closed-form expression to have an insight to the performance impact

of non-ideal behaviour of multiple antennas [153]. It is defined as the loss of power efficiency of a non-ideal MIMO antenna system to achieve the same performance as that of an ideal antenna system with 100% efficiency and zero correlation between antennas, in the same propagation channel. In another way it is a generalization of the single antenna total efficiency to the case of a multi-antenna implementation. Assuming a high SNR performance, the closed-form expression of η_{mux} for a two-element MIMO antenna in the case of a reference propagation channel with uniform 3D Angular Power Spectrum (APS) is given by

$$\eta_{mux} = \sqrt{\eta_{tot_1}\eta_{tot_2}(1 - |\rho^c|^2)} \tag{3.60}$$

where, η_{tot_1} & η_{tot_2} are the total efficiencies of the two antenna-elements, and $|\rho^c|$ denotes the magnitude of complex correlation between them. The geometric mean of efficiencies ($\sqrt{\eta_{tot_1}\eta_{tot_2}}$) gives the impact of efficiency imbalance, while the term $\sqrt{(1 - |\rho^c|^2)}$ represents influence of power loss due to correlation in the performance of MIMO antennas. For N-element MIMO antenna (3.60) can be generalized as [118]

$$\eta_{mux} = \sqrt[N]{\prod_{i=1}^{N} \eta_{tot_i}} \ \det(R) \tag{3.61}$$

where, η_{tot_i} stands for the total efficiency of ith antenna-element and R is the normalized correlation matrix of the MIMO antenna, where R_{ij} is the complex correlation coefficient between i^{th} and j^{th} antenna-element. The geometric mean term is intuitive in that the overall efficiency of MIMO antenna should come in between the efficiencies of the constituent antennas, and the correlation induced term points out that as the correlation between the ports increases the condition number of R also get increased, which in turn decreases $\det(R)$.

Due to the unique features of η_{mux}, it is perfect for figuring out the capability of a MIMO terminal antenna in a realistic user scenario [160].

3.3.6   Channel Performance Evaluation

MIMO technology outcomes many drawbacks of SISO communication by exploiting the rich multipath channel. The major challenge for a MIMO antenna is how to create a repeatable scenario which accurately reflects its radiation performance

in a realistic wireless propagation environment. Even though the diversity performance of a multi-antenna system can be evaluated by using different isolation & correlation studies, for the complete investigation of a MIMO antenna behaviour in a propagation channel Over The Air (OTA) test is necessary.

Numerous studies on different methods of MIMO OTA testing were conducted by European Cooperation in Science and Technology (COST) 2100 [6], Cellular Telecommunication and Internet Association (CTIA) [2] and Third Generation Partnership Project (3GPP) RAN WG4 [3]. The different methods for MIMO OTA, adopted by the afore mentioned organizations, fall under four major categories: the multi-probe anechoic chamber method, the reverberation chamber method, the two-stage method and the two channel anechoic chamber method. These methods vary in the way they reproduce a specific MIMO channel model. In this thesis, the two-stage method of OTA testing is followed to evaluate the performance of designed UWB-MIMO antennas in a propagation channel.

The two-stage MIMO OTA method follows simpler procedures as compared to the other methods for OTA testing. It is based on the fact that the three-dimensional far-field radiation pattern of a MIMO antenna can fully capture the effect of mutual coupling between the antenna-elements. As the name indicates, this method consists of two stages of operation:

1. Measuring the far-field radiation pattern of MIMO antenna inside an anechoic chamber, in the conventional way (SISO OTA method).

2. Convolving the measured radiation pattern with the desired channel model by using a MIMO channel emulator to produce the real channel faded signal.

In the first stage, the existing SISO OTA anechoic chamber is utilized for the 3-D far-field radiation pattern measurements of a multi-antenna system. The multi-element AUT is placed inside an anechoic chamber, which is set up as described in 3GPP TS 34.114 [10], and the 3-D radiation pattern of individual antenna element is measured in the conventional SISO way of pattern measurement. For the accurate evaluation, both the magnitude and phase informations of the radiation patterns, at different ϕ & θ angles, are necessary. In the second stage, the measured 3-D far-field radiation patterns were convolved with desired channel model using a commercial channel emulator, to emulate the integrated channel.
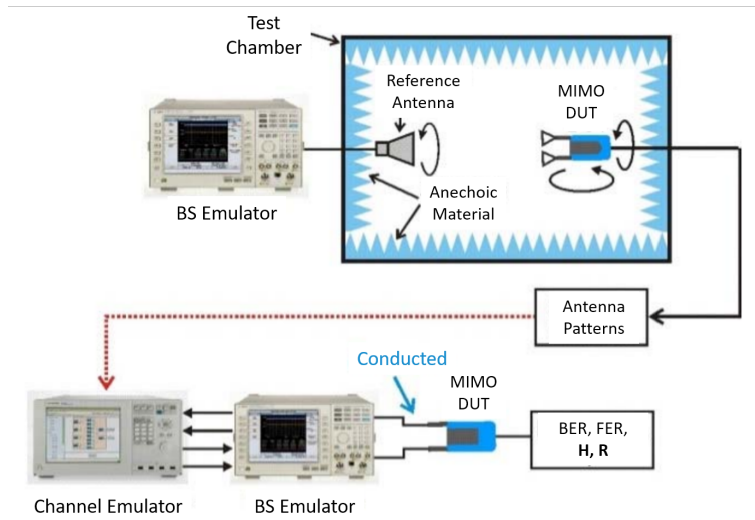
Fig. 3.10 Two-stage MIMO OTA testing method (TR 37.976 [8])

Thus, a real channel faded signal is produced after the convolution, from which the channel capacity and throughput performance of the MIMO AUT can be evaluated. The MIMO OTA testing based on the afore mentioned two-stage method is illustrated in the Fig. 3.10. As observed from the figure, the measured radiation pattern of the MIMO AUT from the anechoic chamber is loaded to a commercial MIMO channel emulator, which emulates an integrated channel model incorporating multi-antenna impact as well as multipath channel effect [8]. From this, the end-to-end throughput and channel capacity of the wireless link due to the implementation of MIMO AUT can be evaluated. In this thesis, the radiation patterns of the designed UWB-MIMO antennas are convolved with correlation-based and WINNER-II channel models in the Agilent SystemVUE by Keysight Technologies to obtain the OTA performances.

The main advantages of adopting two-stage method for MIMO OTA testing are:

- Reuses the existing SISO OTA anechoic chamber for pattern measurements making it highly cost-effective

- Requires only a two-channel emulator regardless of the channel model complexity

- Can be scaled to higher-order MIMO testing due to fewer instruments necessity as compared to the multi-probe methods

- The channel models are accurate and flexible, as it can altered in accordance with the desired operating environment such as indoor, outdoor, high or low Doppler spread, high or low delay spread etc..

3.4   Chapter Summary

This chapter portrayed the different methodologies adopted for the investigation of various antennas mentioned in this thesis. It briefly explained the procedures followed for the optimization and fabrication of the designed antennas. Moreover, the concept behind different analysis methods required for a UWB-MIMO antenna and its theoretical & practical implementation are also discussed in this chapter. Apart from the conventional ways of analysis used for narrow band antennas, necessary time-domain & spatial-domain analytic methods for wideband antennas are also included. In addition to this, different MIMO quality measures in terms of its isolation and diversity performance as well as the effectiveness of a MIMO antenna in a channel are also discussed.

Chapter 4

Compact Coplanar UWB antennas

The rapid progress in the field of wireless communication demanded the need of low profile mobile devices which uses tiny built-in antennas at the wireless terminals. For the ease of integration and to attain low dispersive responses within the wide frequency band, one should opt coplanar-fed radiating elements for the design of an antenna, [19, 90, 147, 215]. This triggered me to design UWB band antennas employing co-planar feed.

Compact UWB antennas are found to be used in many small profile communication gadgets for different applications. This chapter portrays the details and characteristics of two novel compact UWB antennas that are coplanar in nature and are suitable for low profile wireless terminals. Out of the two UWB antennas, first one is a Co-Planar Stripline (CPS) fed antenna whereas the second antenna is fed by an Asymmetric Co-planar Stripline (ACS). Both the antennas utilized the staircase-shaped slots on the radiators to attain the wide frequency range of operation. The detailed geometrical descriptions of the optimized antennas and the effect of different parameters on the antenna radiation characteristics, which helped to optimize the structure for the desired range of frequency band, are illustrated in this chapter. The surface current distributions along with the corresponding radiation patterns are also studied in detail. The analysis of the antennas based on various conventional frequency-domain parameters are interpreted. Also, the transient response of the antenna when subjected to an

input pulse of specific standards and the corresponding time-domain analytic parameters are discussed. Moreover, the information regarding pattern stability analysis of the UWB antennas in spatial-domain are also included in this chapter. Further, the performance of both UWB structures are then experimentally verified using the fabricated antennas.

4.1 The CPS-fed UWB antenna

This section deals with a co-planar stripline (CPS) fed antenna for UWB applications. Co-planar feeding technology requires only one side processing of the substrate, because both radiating elements and ground planes are on the same side of the substrate. This increases the fringing of the fields in the antenna which causes the possibility of achieving wider impedance bandwidth for those antennas. Moreover, fabrication and integration process of co-planar antennas are much easier as compared to that of microstrip fed antennas.

(a) Geometry   (b) Simulated reflection coefficient
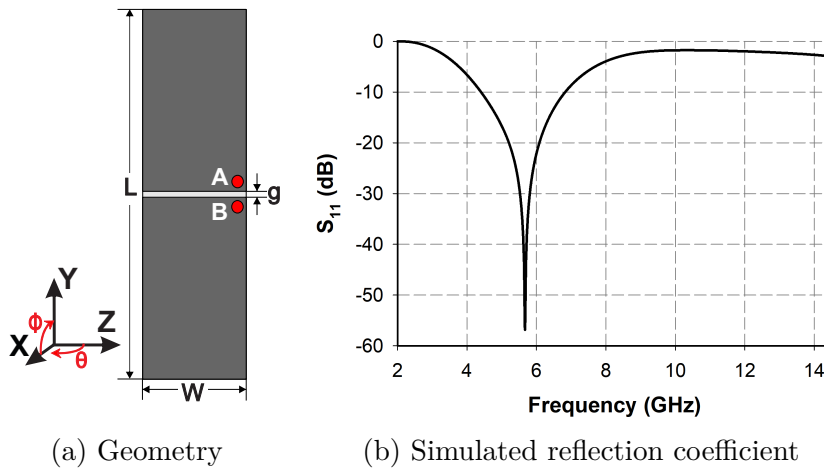
Fig. 4.1 Geometry and reflection coefficient of the CPS-fed dipole antenna; L=25mm, W=7mm, g=0.4mm

By taking all these factors into consideration, a CPS fed antenna is etched on a FR-4 substrate of relative permittivity (ϵ_r) 4.3, loss tangent ($tan(\delta)$) 0.02 and thickness (h) of 1.588mm. The geometry of the antenna is shown in Fig. 4.1a. The points 'A' & 'B' (red dots) corresponds to the location of feeding points (inner

Table 4.1 Geometric dimensions of the three stages of staircase-shape formation (values in mm)

Stage 1		Stage 2		Stage 3	
Parameter	Values	Parameter	Values	Parameter	Values
F_1	1.8	F_1	0.5	F_1	0.5
W_1	1	W_1	1	W_1	1
		F_2	1.3	F_2	0.5
		W_2	1	W_2	1
				F_3	0.8
				W_3	2

and outer conductors of coaxial cable used to feed this antenna, respectively). It has two radiating rectangular patches of size $12.3mm \times 7mm$, separated by a gap (g) of 0.4mm. The antenna is very compact with an overall size of $L = 25mm \times W = 7mm$. This antenna acts as a normal dipole with coplanar feed and radiates at 5.6 GHz with a 2:1 VSWR bandwidth of 2.5 GHz, as shown in Fig. 4.1b. Although this antenna has good impedance bandwidth, our aim is to design an antenna which can be used for the UWB radio systems. For that the 10 dB impedance bandwidth must be in range from 3.1 GHz to 10.6 GHz.

In order to attain further bandwidth, the technique of etching stepped-slots on the radiating patch is utilized on the afore mentioned CPS-fed dipole antenna in Fig. 4.1a. These slots on radiating patch are seen in the shape of steps of a staircase, which can thus be termed as staircase-shaped slots. These staircase-shaped slots can merge different resonance to achieve wider bandwidth in the structure, and increases the degree of freedom with which the resonances could be controlled compared to the antenna with curved slot. Thus, for a geometry which has space constraints staircase-shaped slots are well suited for wide bandwidth operation than a curved slot. Wide bandwidth realization with step-slot is well explained in [173] and [71], where former employed staircase-shape on radiating patch as well as on ground plane of their antenna, while the latter etched the stepped-slot on the ground plane only. Both the above
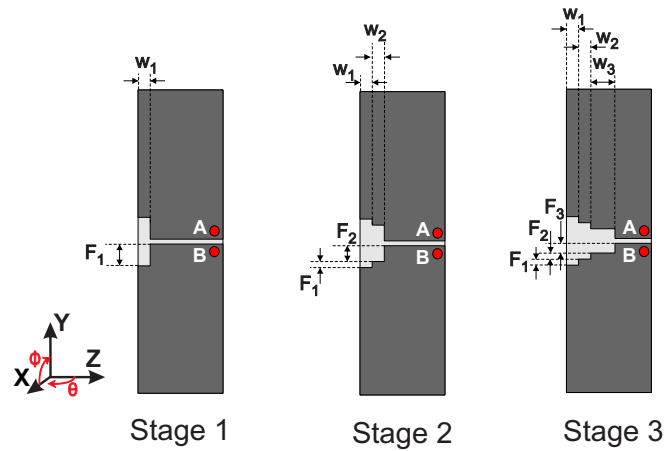
(a) Stages of staircase-shape on the geometry of the antenna
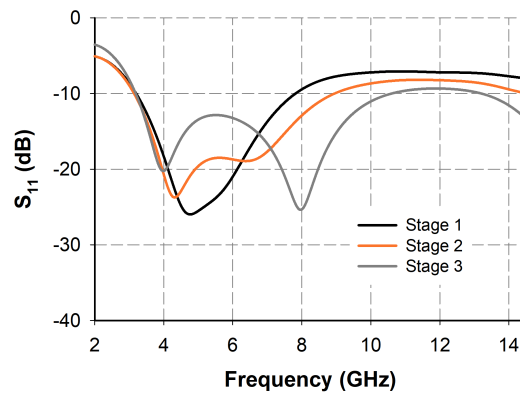
(b) Simulated reflection coefficient

Fig. 4.2 Geometric evolution of the staircase-shape and its corresponding simulated reflection coefficient; refer Table 4.1 for dimensions of the respective stages

antennas are microstrip in nature and it is very difficult to align the radiating patch and ground plane properly during manufacturing, to obtain the results. For the current antenna design,the coplanar geometry is selected for the ease of fabrication. The introduction of staircase-shape is carried out in three stages on the dipole antenna, as shown in Fig. 4.2a. Fig. 4.2b shows the reflection coefficient corresponding to the three stages. It is clear from the figure that the staircase-shape increases the bandwidth by introducing new resonances, and

merging it in an adequate way. Different values for the staircase-shaped slots are tried using the CST Microwave studio to attain the required 2:1 VSWR bandwidth for UWB operation. The dimensions of the steps at each stages of evolution are listed in Table 4.1 and the optimized dimensions of the slot are obtained at Stage 3. The addition of each step increases the bandwidth of resonant curve further. However, the bandwidth obtained after the third stage of staircase-shape, which created two resonances at 4 GHz and 8 GHz, is not sufficient for UWB operation.

(a) Geometry   (b) Simulated reflection coefficient
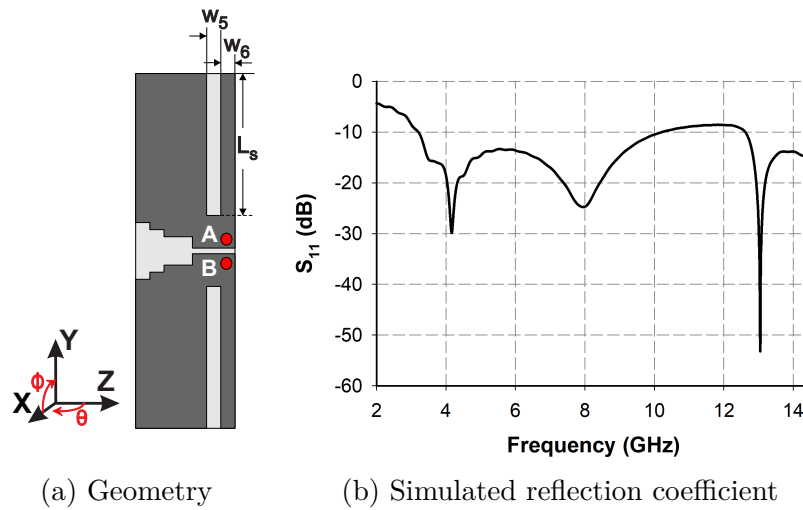
Fig. 4.3 Geometry and reflection coefficient of the slit loaded antenna; L_s=10mm, W_5=1mm, W_6=1mm

Adding a horizontal slit of size $L_s = 10mm \times W_5 = 1mm$ at the bottom line of antenna, as shown in Fig. 4.3a, created an additional resonance at 13 GHz with high impedance matching. This is shown in the reflection coefficient plot of the slit-loaded antenna in Fig. 4.3b. This additional resonance is due to the new current path formed along the slit edge. But the resonance at 13 GHz does not contribute to the 2:1 VSWR bandwidth required for a UWB antenna. Thus, somehow this resonance is needed to be shifted so as to widen the entire bandwidth. This can be accomplished by adjusting the current path along the slit edge. A short across the slit will create a current loop and provides the possibility of shifting the higher resonance at 13 GHz to some lower frequency region, so as to achieve the required UWB bandwidth. After trying various short

(a) Geometry   (b) Simulated reflection coefficient
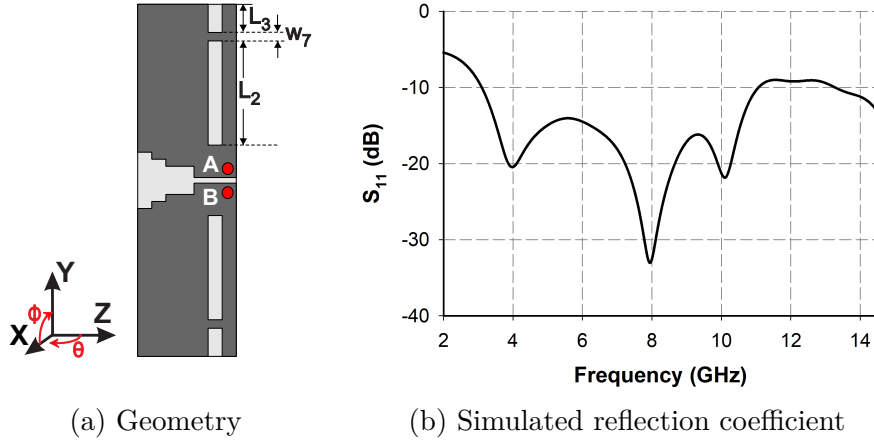
Fig. 4.4 Geometry and reflection coefficient of the antenna with metal strip short across the slit; L_3=2mm, L_2=7.4mm, W_7=0.6mm

positions and short dimensions it is found that a metal strip short (vertical metal strip) of size $W_7 = 0.6mm \times W_5 = 1mm$ at L_2=7.4mm realizes the required resonance shift. This metal strip position shifted the resonance at 13 GHz to 10 GHz and thus, helped to achieve the required bandwidth of 3.1 - 10.6 GHz for UWB radio communication systems. The modified geometry is shown in Fig. 4.4a and the corresponding reflection coefficient of the short loaded antenna is plotted in Fig. 4.4b. Also, by moving the position of this short to and fro, one can control the occurrence of higher resonance which is created due to the presence of horizontal slit. This is because, the current path length along the loop changes with the short position.

In order to study the influence of metal strip short on the performance of antenna, it is moved through the slit, from its outer end to the inner corner, thereby changing the length L_2. The corresponding change in reflection coefficient is plotted in Fig 4.5a. To study the effect of one parameter all the other parameters are kept intact. As discussed above, the position of the metal strip short (i.e., the length L_2) is responsible for the shift of higher order resonance (third resonance) to a desired frequency point. This is because, the resonance moves to higher frequency points as the position of the short strip is moved inwards through the horizontal slit, as seen in Fig 4.5a. It is because of the change in the current path length along the slot corresponding to L_2, caused by the change in strip position.

(a) Effect of L_2 (b) Effect of W_5
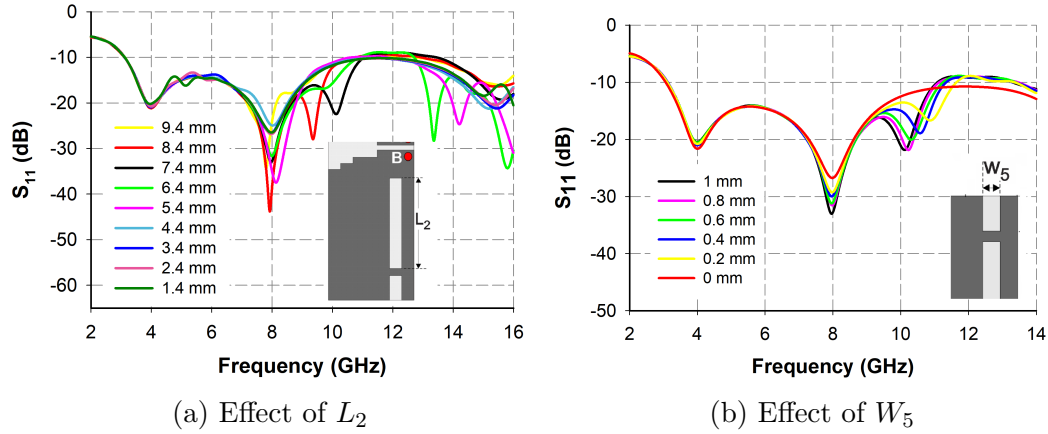
Fig. 4.5 Change in reflection coefficient as L_2 & W_5 are varied

An optimized position of $L_2 = 7.4$ mm is selected to conform with the required bandwidth for UWB operation.

Another important parameter in this UWB antenna is the horizontal strip width (W_5) which creates a higher resonance and gives a fine tuning for that resonance. Fig 4.5b depicts the effect of W_5 on the reflection coefficient of the antenna and it is clear from the figure that W_5 give only a fine tuning of the higher resonance, while L_2 produces abrupt shift of the resonance (see Fig 4.5a). As the value of W_5 decreases there results a small shrinkage for the current path length causing a fine shifting of higher order resonance to upper frequencies and a narrow impedance variation causing the matching of second resonance to decline. Also, if the width (W_5) is zero the higher resonance vanishes, as observed from the Fig 4.5b. Thus, the width W_5 is optimized to be 1 mm for this antenna to attain the desired resonances with adequate impedance matching.

The Fig. 4.6 depicts the optimized geometry of CPS fed UWB antenna (UWB-I) and the corresponding parameters are listed in the Table 4.2. This whole structure is etched out on a FR-4 glass epoxy substrate with relative permittivity $\epsilon_r = 4.3$, loss tangent $\tan(\delta) = 0.02$ and thickness $h = 1.588$ mm. The overall size of the antenna is $0.25\lambda_0 \times 0.07\lambda_0$ at 3.1 GHz, which is very compact as compared to the other available coplanar UWB antennas, [90, 142, 173, 219]. Thus, the coalesced resonances of the staircase-shaped radiator along with the modified slit, realizes the wide bandwidth of the antenna that covers the UWB
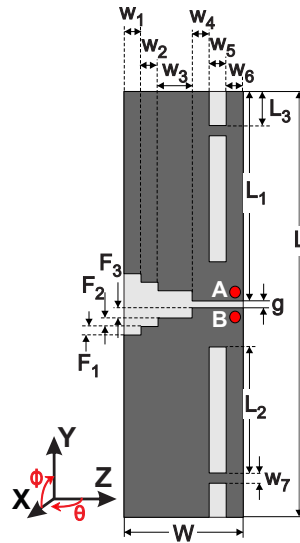
Fig. 4.6 Geometry of the CPS-fed UWB antenna (UWB-I); refer Table 4.2 for dimensions
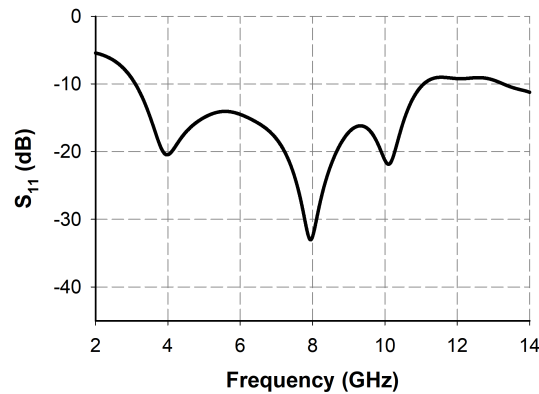
Fig. 4.7 Simulated reflection coefficient of the CPS-fed UWB antenna (UWB-I); dimensions as in Table 4.2

frequency range specified by FCC. The reflection coefficient of the optimized UWB-I is shown in Fig 4.7. The antenna offers a 2:1 VSWR bandwidth of the order of 114% (from 3 GHz to 11 GHz), satisfying the frequency range needed for UWB radio systems as per the FCC guidelines. This wide bandwidth is a result of the combination of three different resonances at 4 GHz, 8 GHz & 10 GHz. The planes corresponding to $\phi = 0°$ (X-Z) & $\theta = 90°$ (X-Y) represents the

Table 4.2 Geometric parameters of UWB-I (in mm)

Parameters	L	W	L_1	L_2	L_3	F_1	F_2	F_3
Values	25	7	12.3	7.4	2	0.5	0.5	0.8
Parameters	W_1	W_2	W_3	W_4	W_5	W_6	W_7	g
Values	1	1	2	1	1	1	0.6	0.4

two principal planes of the antenna. The symmetry of the antenna with respect to the feeding point ensured exact symmetry of antenna currents with respect to $\phi = 0°$ plane, irrespective of frequencies. Here, the balanced antenna prototype is fed directly by a 3.5 mm coaxial connector to make the wideband measurements simpler. The coaxial connector is modeled in the simulations and verified that the imbalance current on inner and outer conductors of the coaxial connector is sufficiently small. Thus the unbalanced feeding does not degrade the expected balanced antenna performance significantly [115].
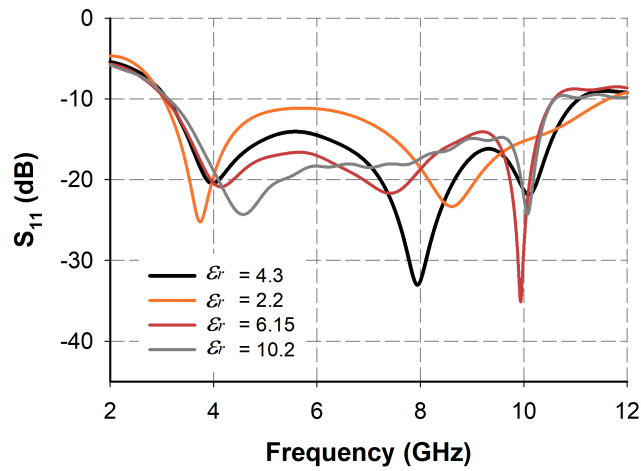
Fig. 4.8 Reflection coefficient of the antenna computed on different ϵ_r; Dimensions of each antenna are as in Table 4.3

The change in geometrical parameters of the CPS-fed UWB antenna (UWB-I) when it is etched on different substrates with different ϵ_r and h are summarized in

Table 4.3. The corresponding reflection coefficient of each antenna with varying ϵ_r and h are compared in Fig. 4.8. Simulation studies on the radiation characteristics of the antenna have been carried out for three different substrates and in all cases the antenna succeeded in achieving the required bandwidth for UWB operation.

(a) 4 GHz   (b) 8 GHz   (c) 10 GHz
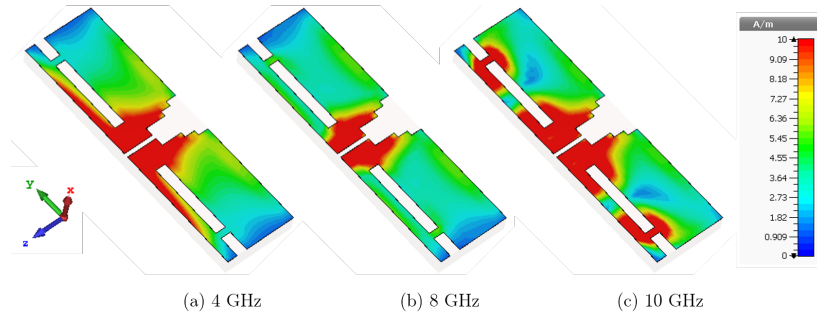
Fig. 4.9 Surface current distribution of UWB-I ; Dimensions as in Table 4.2

(a) 4 GHz   (b) 8 GHz

(c) 10 GHz
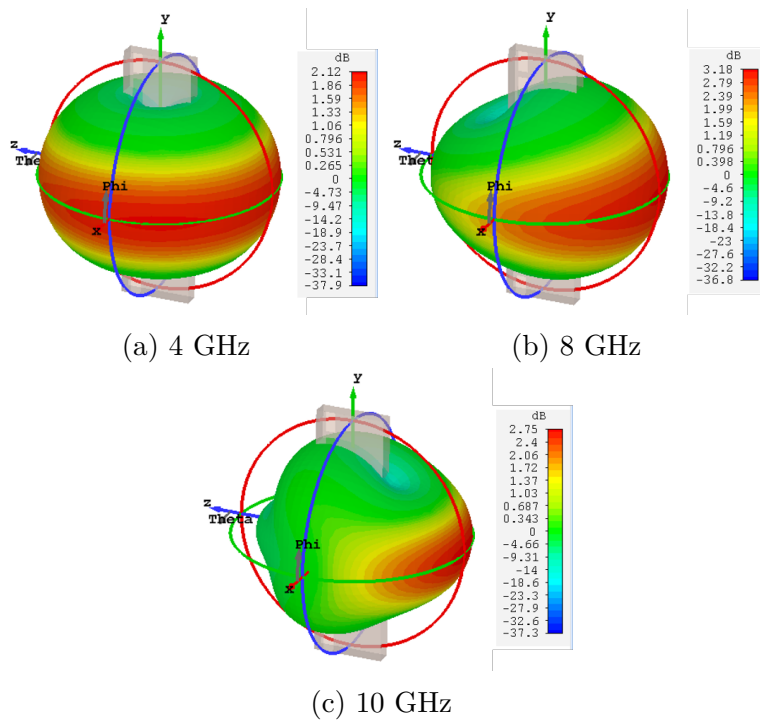
Fig. 4.10 Simulated 3D Radiation pattern of UWB-I; Dimensions as in Table 4.2

The reflection coefficient of an antenna can only represent the antenna's behaviour as a lumped load at the end of a feeding line. The detailed electromag-

Table 4.3 Geometric parameters of UWB antenna on different substrates (in mm)

Substrate: FR-4, ϵ_r=4.3, h=1.588mm							
Parameters	L	W	L_1	L_2	L_3	F_1	F_2	F_3
Values	25	7	12.3	7.4	2	0.5	0.5	0.8
Parameters	W_1	W_2	W_3	W_4	W_5	W_6	W_7	g
Values	1	1	2	1	1	1	0.6	0.4
Substrate: Rogers RT5880, ϵ_r=2.2, h=1.57mm							
Parameters	L	W	L_1	L_2	L_3	F_1	F_2	F_3
Values	30	8.4	14.76	8.8	2.4	0.6	0.6	0.96
Parameters	W_1	W_2	W_3	W_4	W_5	W_6	W_7	g
Values	1.2	1.2	2.4	1.2	1.2	1.2	0.72	0.48
Substrate: Rogers RO3006, ϵ_r=6.15, h=1.28mm							
Parameters	L	W	L_1	L_2	L_3	F_1	F_2	F_3
Values	22.5	6.3	11.07	6.3	2.16	0.45	0.45	0.72
Parameters	W_1	W_2	W_3	W_4	W_5	W_6	W_7	g
Values	0.9	0.9	1.8	0.9	0.9	0.9	0.54	0.36
Substrate: Rogers RT6010, ϵ_r=10.2, h=0.635mm							
Parameters	L	W	L_1	L_2	L_3	F_1	F_2	F_3
Values	20	5.6	9.84	5.6	1.92	0.4	0.4	0.64
Parameters	W_1	W_2	W_3	W_4	W_5	W_6	W_7	g
Values	0.8	0.8	1.6	0.8	0.8	0.8	0.48	0.32

netic behaviour of an antenna can be unveiled by inspecting the surface current distributions and the radiation patterns.

The simulated surface current distributions of the UWB-I corresponding to three resonant frequencies are portrayed in Fig. 4.9. It is clear from the figure that the first resonance, i.e., 4 GHz is due to the half wavelength ($\lambda/2$) variation of current along the length (L) of the structure. At this frequency the current is mainly focused around the steps-slots as well as along the bottom line of the antenna, and thus both contributes the electromagnetic radiation at that frequency. The surface current distribution of second resonance (8 GHz) reveals the importance of staircase-shaped slots in the antenna, as the current is highly concentrated on the steps. It was observed from Fig. 4.2 that, the resonance at 8 GHz is due to the addition of step-slots to the radiator and thus they determine the resonant behaviour of the antenna at 8 GHz. From Fig. 4.3 and Fig. 4.4 it is clear that the resonance at 10 GHz is due to the addition of horizontal slit and vertical strip on the antenna. This is confirmed after analysing the surface current distribution at 10 GHz, as the current is concentrated mainly along the slit corner and around the vertical strip, which in turn becomes the cause for radiation at that frequency.

Fig. 4.10 shows the simulated three-dimensional (3D) radiation pattern of the antenna at 4 GHz, 8 GHz and 10 GHz. At 4 GHz the pattern is found to be omni-directional, which is due to the dipole mode of excitation. The pattern is partially omni-directional at 8 GHz and goes slightly directive at 10 GHz. These slight directive patterns at higher frequency regions are due to the action of slit and the shorted strip, which changes the current distribution from the way it would be for its fundamental mode of operation.

4.1.1   Experimental Results

The prototype of UWB-I is shown in Fig. 4.11, which is fabricated as per the optimized dimensions desribed in Table .4.2. The radiation performance of the fabricated UWB-I is then verified experimentally with the help of Network Analyzer and anechoic chamber.

Fig. 4.12 depicts the measured reflection coefficient of the antenna along with its simulated result. It shows a broad impedance bandwidth from 3 GHz to
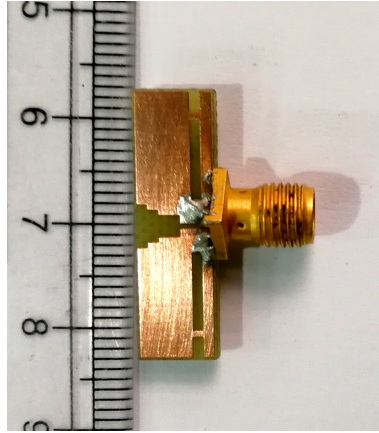
Fig. 4.11 Fabricated UWB-I; Dimensions as in Table 4.2
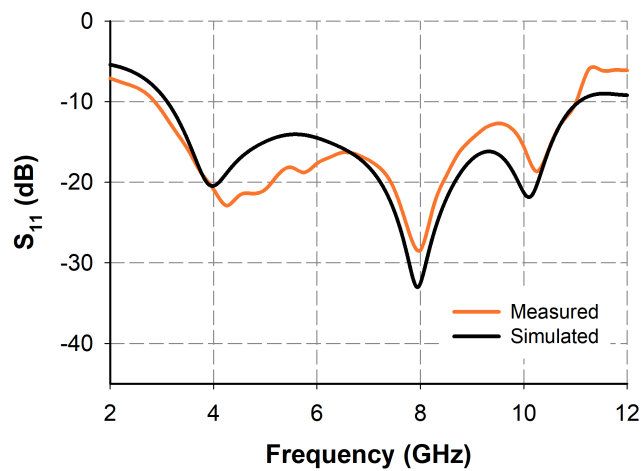
Fig. 4.12 Measured and simulated reflection coefficient of UWB-I; Dimensions as in Table 4.2

11 GHz for $S_{11} < -10dB$ and compares well with the simulated results. The slight discrepancies are the result of mechanical tolerances due to the connector soldering, which are not accounted in the simulation.

The normalized 2-Dimensional (2D) radiation patterns of UWB-I for three different frequencies in the operating band are sketched in Fig. 4.13, at two principal planes (X-Z: $\phi = 0°$ & X-Y: $\theta = 90°$ Plane). The planes at which the patterns were measured are pictured on the antenna geometry and depicted in the top of Fig 4.13. Here, E_ϕ and E_θ represents the ϕ and θ components of the

Table 4.4 Polarization Isolation of UWB-I (values in dB); Dimensions as in Table 4.2

Freq. (GHz)	$\phi = 0°$ (X-Z) Plane	$\theta = 90°$ (X-Y) Plane
4	30.38 dB	37.85 dB
8	32.67 dB	38.47 dB
10	33.6 dB	34.30 dB

E-field pattern along the plane of interest, respectively. It is observed that the polarization of UWB-I is along Y direction, and for the antenna oriented as in Fig. 4.6 E_ϕ represents the co-polarization & E_θ denotes the cross-polarization component of its field pattern. Both the co-polarization and cross-polarization patterns are compared for the simulated and measured results in the frequency band of interest. The patterns in the lower UWB band are found to be omni-directional, whereas in the higher UWB band, the pattern goes slightly directional. However, the antenna exhibited stable radiation patterns throughout the 3.1-10.6 GHz frequency band.

Polarization purity and polarization stability are two vital factors that need to be considered in the case of antennas operating for UWB-MIMO communication systems. Polarization purity of an antenna is defined as the ratio of desired polarization component to its undesired component, and denotes how purely the antenna's polarization is oriented to one direction. It can be calculated by taking the difference of power levels (in dB) of ϕ and θ components along the plane of interest and in the direction of propagation, for a single frequency. Table 4.4 summarizes the radiated power level differences of UWB-I for different frequencies in respective planes. It is clear from the table that the isolation stood above 30 dB along $\phi = 0°$ plane and above 34 dB along $\theta = 90°$ plane. Thus, the polarization purity between ϕ and θ components in both planes of interest are excellent for UWB-I in-spite of its small size.

Stable polarization across the frequency band of interest contributes to attain a well-defined pulse response by minimizing positioning accuracy errors. The polarization differences for different frequencies, in Table 4.4, shows that the proposed antenna has stable polarization through out the operating band, as the

(a) At $\phi = 0°$ (X-Z) Plane

(b) At $\theta = 90°$ (X-Y) Plane
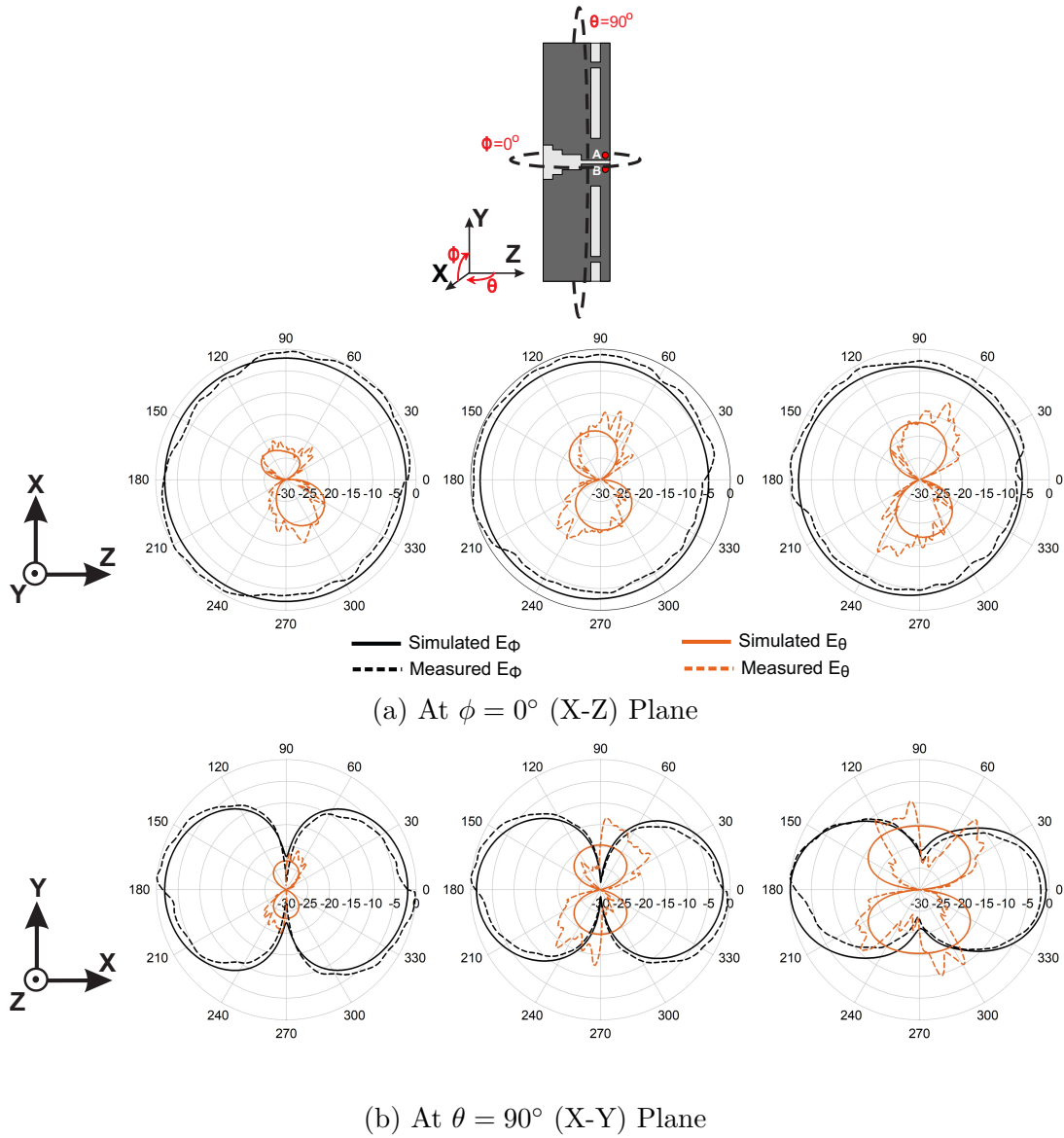
Fig. 4.13 2D Radiation Pattern of UWB-I for 4 GHz, 8 GHz & 10 GHz; Dimensions as in Table 4.2

polarization isolation level doesn't differ much while the frequency of operation varies. This study confirmed the good pulse-handling capability of UWB-I in favour for various UWB applications.

The measured gain of the antenna, by Gain Comparison Method and measured radiation efficiency using Schantz's Wheeler Cap method are illustrated in
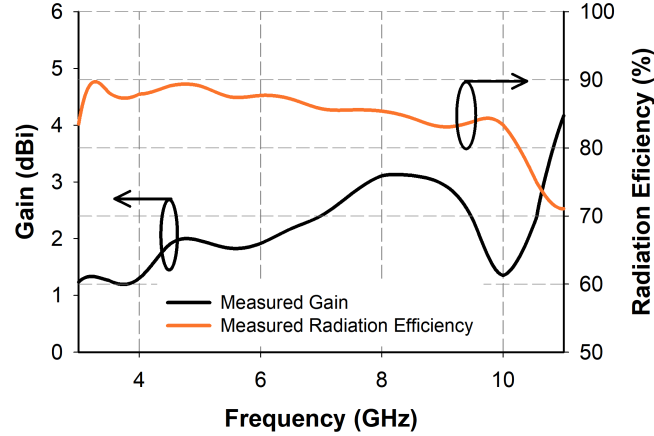
Fig. 4.14 Measured gain and radiation efficiency of UWB-I; Dimensions as in Table 4.2

Fig. 4.14. As observed from figure, the antenna exhibits stable gain across the 3.1-10.6 GHz band with a peak gain of 3.1 dBi at 8.5 GHz. The antenna has an average gain of 2.15 dBi and radiation efficiency >74% in the UWB band of interest.

4.2 The ACS-fed UWB antenna

This section deals with the study of an Asymmetric Coplanar Strip (ACS) fed UWB antenna. The ACS is a modification of the slot line in which the width of both the lateral strips will not be of same size and shape. The ACS feeding method is well known for its freedom to select feed dimensions based on the circuit requirements as well as for the antenna miniaturization. Thus, ACS can be effectively utilized for the design of compact un-iplanar antennas, and here in this thesis it is used for the design of a compact coplanar UWB antenna.

The design of the antenna started with a simple ACS fed dipole, as shown in Fig. 4.15a, which consist of two lateral strips of $L \times W_1$ and $L_a \times W_8$, separated by a gap of g. The dimensions of the antenna are included in the caption of respective figures. These asymmetric strips are etched on an FR-4 substrate of size $L = 25mm \times W = 10mm$ with relative permittivity ϵ_r of 4.3, loss tangent $tan(\delta)$ of 0.02 and thickness h of 1.588mm. The points 'A' & 'B' (red dots) in the

(a) Geometry   (b) Simulated reflection coefficient
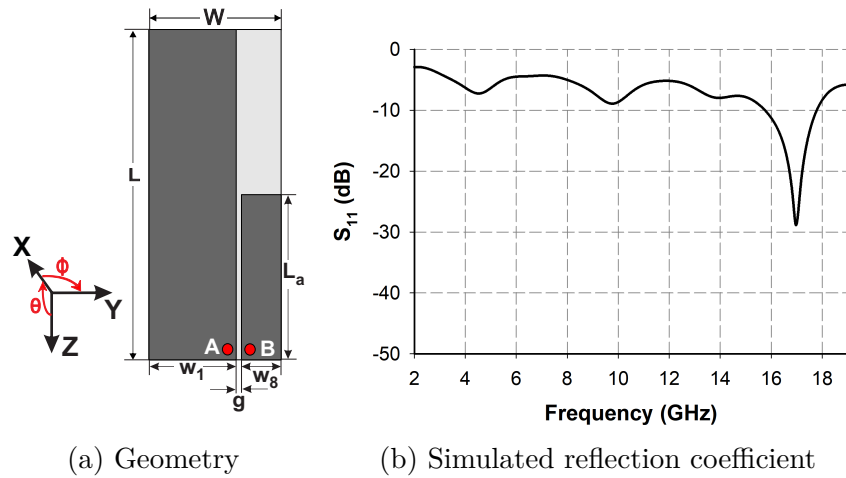
Fig. 4.15 Geometry and reflection coefficient of the asymmetric coplanar fed dipole antenna; L=25mm, W=10mm, W_1=6.6mm, W_8=3mm, L_a=12.5mm, g=0.4mm

geometry corresponds location of the feeding points. The reflection coefficient of the antenna is plotted in Fig. 4.15b, which shows a well matched resonance at 17 GHz.

(a) Geometry   (b) Simulated reflection coefficient
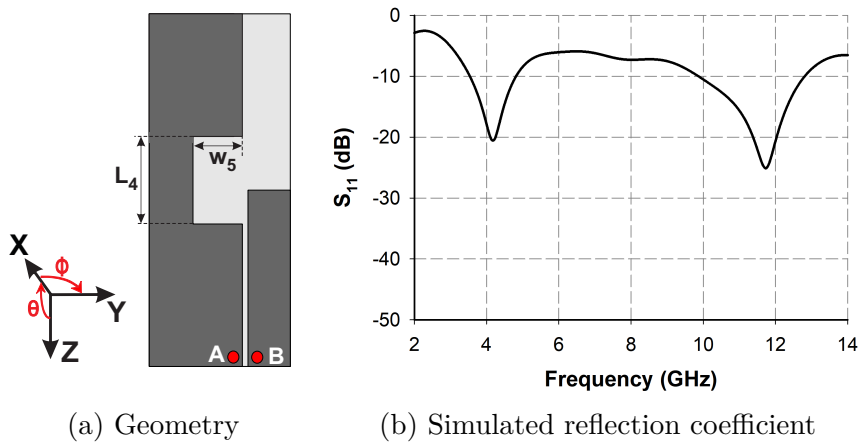
Fig. 4.16 Geometry and reflection coefficient of the slot loaded ACS-fed antenna antenna; L_4=6.2mm, W_5=2.9mm

In order to realize wider bandwidth a slot of size $L_4 \times W_5$ is etched out from the larger strip, as seen in Fig. 4.16a. Fig. 4.16b denotes that this slot

(a) Geometry

(b) Simulated reflection coefficient
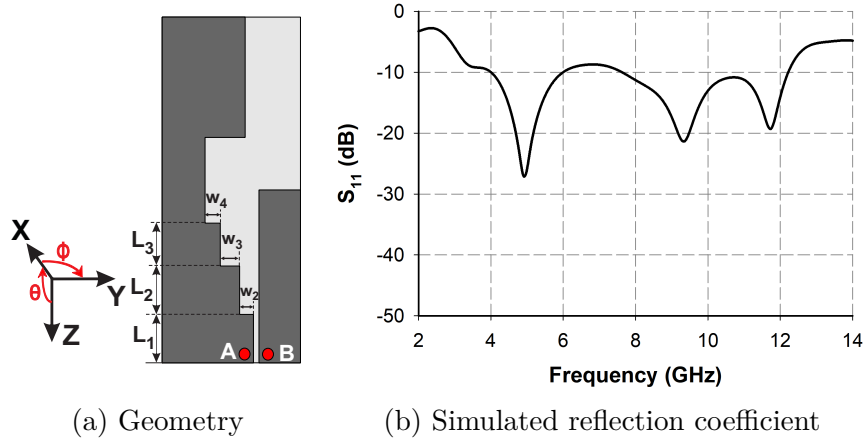
Fig. 4.17 Geometry and reflection coefficient of the ACS-fed antenna with staircase-shaped slots; L_1=3.5mm, L_2=3.5mm, L_3=3.1mm, W_2=1mm, W_3=1.4mm, W_4=1.1mm,

created two resonance at 4.2 GHz and 11.7 GHz, due to the change in current distribution occurred across the slot placed area. The excitation of resonances by inserting slots on ground plane of a Coplanar Waveguide (CPW) fed antenna was well explained by Sujith et al, in [186]. Also, the creation of two resonances using asymmetric slots on ground plane was discussed in [199]. Sujith et al claims that a resonance is created if and only if the discontinuity is created along the propagation path of the transmission line. The principle behind the geometry of Fig. 4.16a and its resonances in Fig. 4.16b follows that of [186], which concludes that the slot helps to radiate electromagnetic energy at both 4.2 GHz and 11.7 GHz. However, the antenna in Fig. 4.16a failed to cover the 3.1-10.6 GHz bandwidth for UWB applications.

In order to increase the 2:1 VSWR bandwidth a staircase-shaped slot of three consecutive steps is etched out along the propagation path, as shown in Fig. 4.17a. This will enhance the electromagnetic propagation and thus creates three resonances at 4.89 GHz, 9.36 GHz and 11.7 GHz, as seen in Fig. 4.17b. Although, this antenna widened the bandwidth it failed to cover the needed lower UWB band (from 3.1 GHz). To increase the impedance matching of the resonance step-slots are created on the upper left corner of the antenna, as shown in Fig. 4.18a. Fig. 4.18b shows that these step slots improved the impedance

(a) Geometry

(b) Simulated reflection coefficient
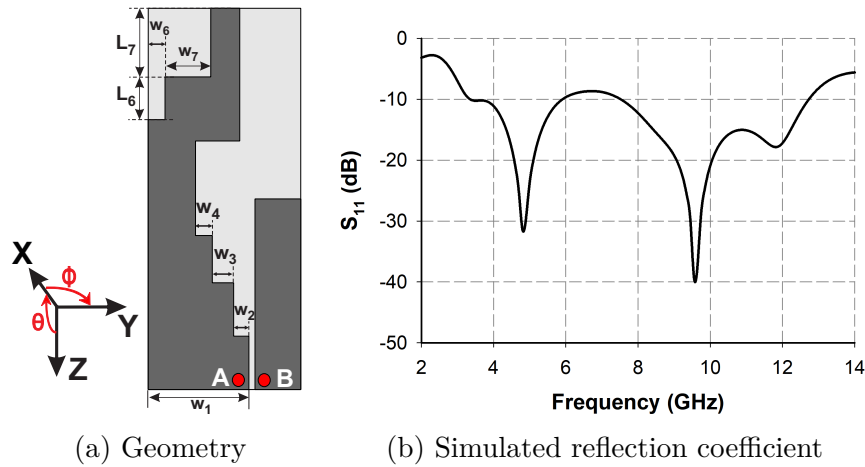
Fig. 4.18 Geometry and reflection coefficient of the ACS-fed antenna with additional step-slots; L_7=4.5mm, L_6=2.8mm, W_6=1.1mm, W_7=3mm

matching of the resonances as they intensified the electromagnetic propagation at those frequencies.

(a) Geometry

(b) Simulated reflection coefficient
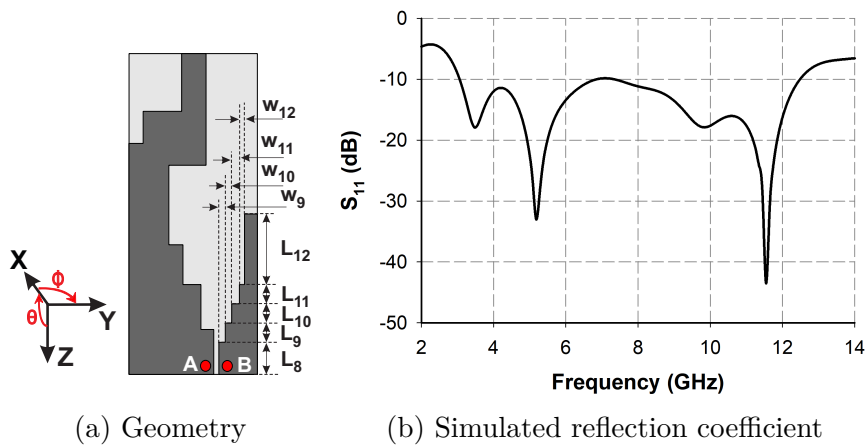
Fig. 4.19 Geometry and reflection coefficient of the ACS-fed antenna with staircase-shaped slots on smaller strip; Dimensions in Table 4.5

To attain the entire UWB band of 3.1-10.6 GHz bandwidth staircase-shaped slots are placed on the smaller strip (right strip) as shown in Fig. 4.19a. This created a resonance at lower frequency at 3.5 GHz, thus realised the required 2:1

Table 4.5 Dimensions of the staircase-shaped slot in Fig. 4.19a; Values in mm

Parameter	Values	Parameter	Values	Parameter	Values
L_8	2.5	L_9	1.5	L_{10}	1.5
L_{11}	1.5	L_{12}	5.5	W_9	0.5
W_{10}	0.5	W_{11}	0.6	W_{12}	0.4

VSWR bandwidth for UWB applications. The reflection coefficient of the antenna depicted in Fig. 4.19b shows that the antenna achieved the UWB bandwidth requirement. All the dimensions of the staircase-shaped slot is listed in Table 4.5.

Although, large number of parameters define the overall geometry of the antenna in Fig. 4.19a, three of them have great influence on the UWB performance, and their size variation brings noticeable changes in the antenna response. The three parameters which are taken for study are W_X $(= W_1 - (W_2 + W_3 + W_4))$, L_7 and L_{12}, which are shown in the inset of Fig 4.20. Fig 4.20a shows the effect on reflection coefficient of the antenna while changing the size of W_X. The portion of antenna which denotes W_X is given in the inset of Fig 4.20a. It is observed from the figure that, while W_X is increased from 1.1mm to 5.1 mm the resonance at 11.5 GHz is got shifted to higher frequencies due to the change in the effective electrical length caused by the change in inductance at that point. A close look on the resonance curve shows that the change in W_X also changes the impedance matching of the resonances in the entire bandwidth, mainly of second resonance at 5.2 GHz. So the width W_X need to be selected carefully to attain the required impedance bandwidth. It is seen from the figure that, when W_X is taken as 3.1mm antenna possessed a 2:1 VSWR bandwidth from 3 GHz to 12.45 GHz, which is thus taken as the optimized value for W_X for the UWB operation.

Another important parameter needed to be analysed is the L_7, which has noticeable effect on the higher two resonances at 9.7 GHz and 11.5 GHz (of Fig. 4.19b) . The change in the reflection coefficient as L_7 is varied from 2.5mm to 6.5mm is plotted in Fig 4.20b. It is observed from the figure that a change in L_7 changes the position of the resonances in higher UWB band due to the variation in the inductance value over that region. This makes the resonances of the higher UWB band to be merged differently, resulting a change in their

(a) Effect of W_X

(b) Effect of L_7

(c) Effect of L_{12}
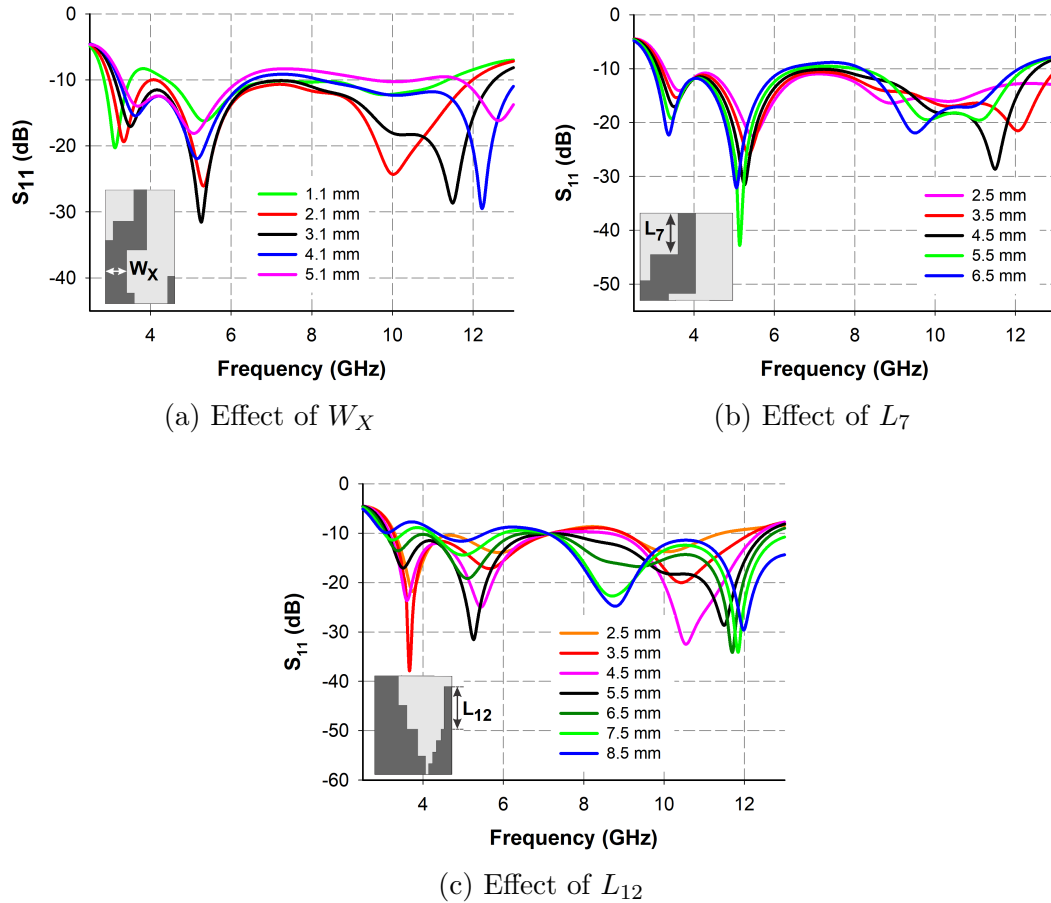
Fig. 4.20 Change in reflection coefficient as W_X, L_7 & L_{12} are varied; Dimensions as in Table 4.6

bandwidth. The reflection coefficient for L_7=4.5mm shows the better results as compared to other curves in Fig 4.20b. Thus, L_7=4.5mm is taken as the optimized value for the current UWB antenna design.

The length L_{12} is a predominant parameter for this UWB antenna as it has effect on all the antenna resonances. Fig 4.20c shows the change in reflection coefficient of the antenna as the length L_{12} is changed from 2.5mm to 8.5mm. This L_{12} contributes electromagnetic propagation in every frequencies and, this length combined with the staircase-shaped slot near to it has great effect on the resonances at lower UWB band, as noticed in Fig. 4.19b. This parameter need to be optimised wisely by considering both lower as well as higher UWB bands,

as it has significant effect on both. It is obvious that as length L_{12} varies the inductance of the strip changes apparently, thus changing the effective electrical length of the antenna. At lower UWB band this change makes a significant variation in their impedance matching causing the antenna to lose their 2:1 VSWR bandwidth for UWB application. At higher UWB band this change of inductance causes the frequencies of the higher harmonics to be unevenly shifted. This makes some resonances to be spaced apart across the spectrum andreduces the chances of effective overlapping between them. As a result the impedance matching becomes worse in these frequency ranges. After a rigorous parametric analysis the value of L_{12} is optimized to be 5.5mm for better UWB operation.
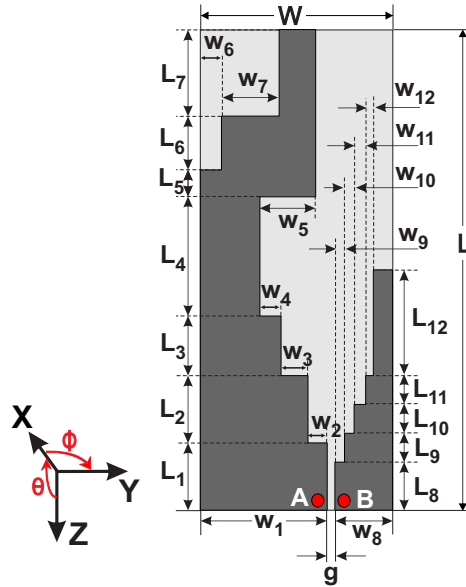
Fig. 4.21 Geometry of the ACS-fed UWB antenna (UWB-II); refer Table 4.6 for dimensions

The optimized geometry of the ACS fed UWB antenna (UWB-II) is shown in Fig. 4.21 and the corresponding parameters are listed in Table 4.8. This antenna is very compact and is etched out on the front side of a $L = 25mm \times W = 10mm$ FR-4 glass epoxy substrate with relative permittivity $\epsilon_r = 4.3$, loss tangent $\tan(\delta) = 0.02$ and thickness $h = 1.588$ mm. The planes corresponding to $\theta = 90°$ (X-Y) & $\phi = 0°$ (X-Z) represents the two principal planes of the antenna for all measurements. The antenna is found to be polarized along Z-axis. The

Table 4.6 Geometric parameters of UWB-II (in mm)

Parameter	Value	Parameter	Value	Parameter	Value
L_1	3.5	L_9	1.5	W_5	2.9
L_2	3.5	L_{10}	1.5	W_6	1.1
L_3	3.1	L_{11}	1.5	W_7	3
L_4	6.2	L_{12}	5.5	W_8	3
L_5	1.4	W_1	6.6	W_9	0.5
L_6	2.8	W_2	1	W_{10}	0.5
L_7	4.5	W_3	1.4	W_{11}	0.6
L_8	2.5	W_4	1.1	W_{12}	0.4
L	25	W	10	g	0.4
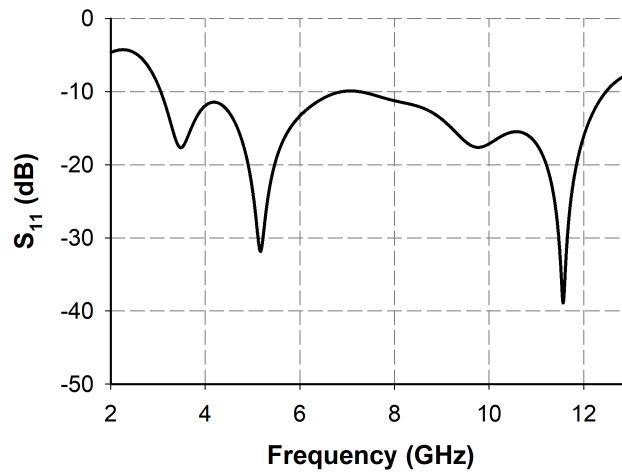
Fig. 4.22 Simulated reflection coefficient of UWB-II Dimensions as in Table 4.6;

simulated reflection coefficient of the optimized UWB-II is plotted in Fig. 4.22. The simulated -10dB bandwidth appears to span a wide frequency range from 3 GHz to 12.45 GHz thus offers a fractional bandwidth of 135% (from 3 GHz to 12.45 GHz), which satisfies the FCC specified frequency range for UWB radio

systems. This broad bandwidth is a result of the combination of four different resonances at 3.5 GHz, 5.2 GHz, 9.7 GHz & 11.5 GHz.

(a) 3.5 GHz   (b) 5.2 GHz   (c) 9.7 GHz   (d) 11.5 GHz
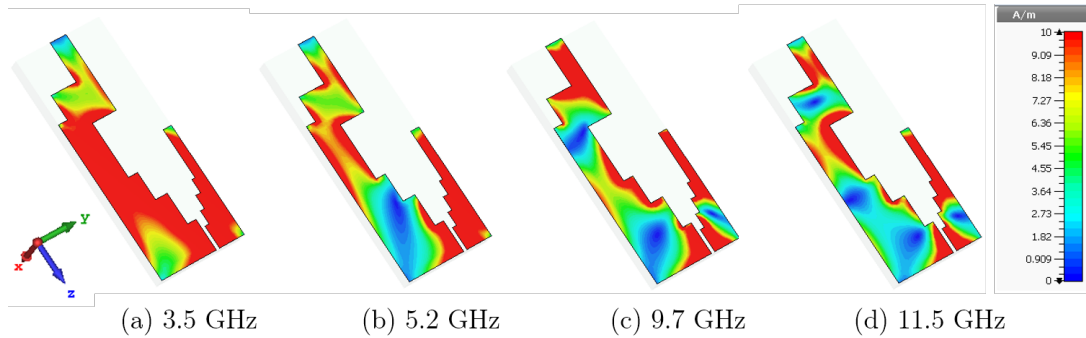
Fig. 4.23 Surface current distribution of UWB-I; Dimensions as in Table 4.6

(a) 3.5 GHz   (b) 5.2 GHz

(c) 9.7 GHz   (d) 11.5 GHz
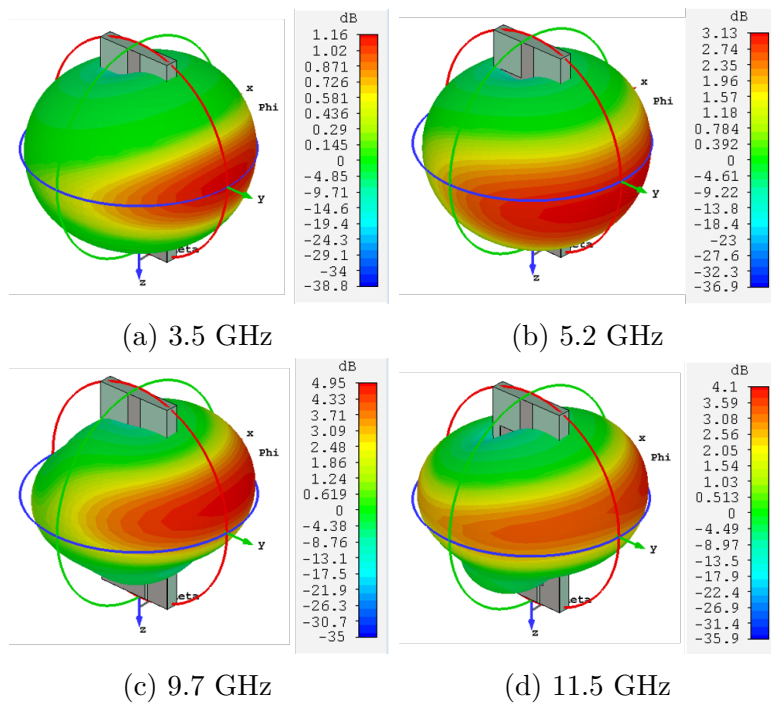
Fig. 4.24 Simulated 3D Radiation pattern of UWB-II; Dimensions as in Table 4.6

In order to examine the electromagnetic behaviour of the antenna, its surface current distributions and corresponding 3D radiation patterns at the resonant frequencies are plotted in Fig 4.23 and Fig 4.24, respectively. It is observed from the Fig 4.23a that the staircase-shaped slots on the larger strip as well as on the

smaller strip contributes the electromagnetic radiation at 3.5 GHz. At 5.2 GHz smaller strip have larger influence along with the corners of the step-slots at the upper part of the antenna, as shown in Fig 4.23b. It is noticed from Fig 4.23 that for 9.7 GHz and 11.5 GHz the upper strip length L_7 has significant contribution to the radiation at those frequencies. In addition to this, the staircase-shaped slots corresponding to the length $L_3 + L_4$ shows significant radiation at 9.7 GHz and length corresponding to L_4 & width W_5 contributes the resonance at 11.5 GHz. As discussed earlier, the length L_{12} of smaller strip has remarkable hand in all the resonances of the antenna and this is confirmed by analysing it in the antenna's surface current distribution of Fig 4.23, which shows its contribution for every resonances. The 3D radiation patterns, in Fig 4.24, shows that the UWB-II has partial omni-directional behaviour at 3.5 GHz and has slightly directional radiation behaviour towards the Y-axis for 5.2 GHz, 9.7 GHz and 11.5 GHz. The directive behaviour of radiation patterns are due to the asymmetric nature of the antenna. It is clear from figure that the pattern is directive towards the Y-direction of the antenna.

4.2.1 Experimental Results

A prototype of the UWB-II of Fig. 4.21, with the dimensions in Table 4.8, is fabricated and practically verified its performance. A photograph of the fabricated antenna is depicted in Fig. 4.25.

A comparison of the simulated reflection coefficient with the measured result of UWB-II is portrayed in Fig. 4.26. The measured reflection coefficient compares well with the simulated one and offers a 2:1 VSWR bandwidth from 3 GHz to 12.85 GHz, with a fractional bandwidth of 140%, covering the entire 3.1-10.6 GHz frequency band for a UWB communication system.

The normalized simulated and measured two-dimensional radiation patterns of UWB-II at two principal planes (X-Z : $\phi = 0°$ & X-Y : $\theta = 90°$) are plotted in Fig. 4.27 for 3.5 GHz, 5.2 GHz, 9.7 GHz and 11.5 GHz. Here, E_ϕ and E_θ represents the ϕ and θ components of the E-field pattern along the plane of interest, respectively. The polarization of UWB-II is found be along Z-axis and for the antenna oriented as in Fig 4.21, E_θ represents the co-polarization & E_ϕ denotes the cross-polarization components of the field pattern. Both the
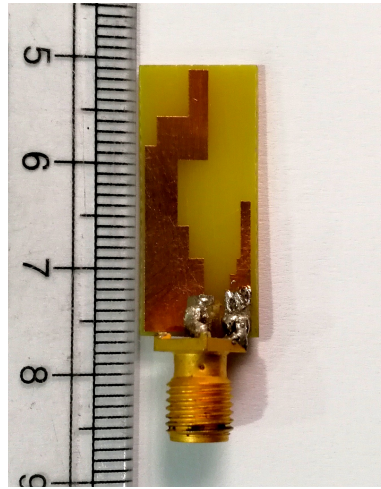
Fig. 4.25 Fabricated UWB-II; Dimensions as in Table 4.6
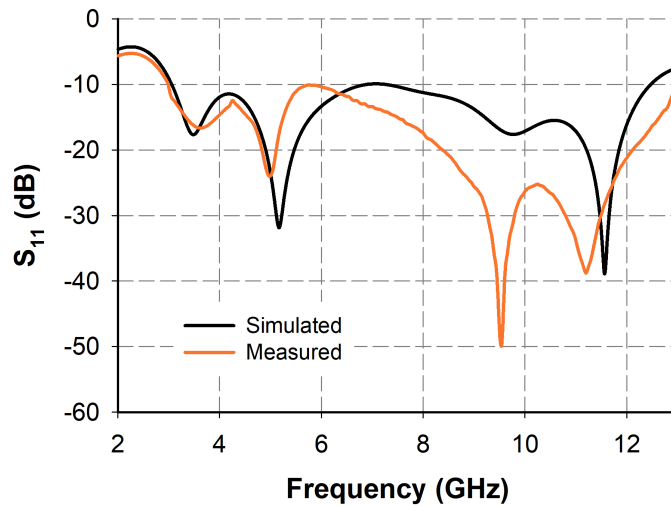
Fig. 4.26 Measured and simulated reflection coefficient of UWB-II; Dimensions as in Table 4.6

co-polarization and cross-polarization patterns for four different frequencies: 3.5 GHz, 5.2 GHz, 9.7 GHz & 11.5 GHz are plotted. The simulated and measured patterns conforms well with each other in the operation band. The planes at which the patterns were measured are pictured on the antenna geometry and depicted in the top of Fig 4.27. At 3.5 GHz the patterns are partially omni-directional whereas, for higher frequencies (5.2, 9.7 & 11.5 GHz) the pattern

(a) At $\phi = 0°$ (X-Z) Plane

(b) At $\theta = 90°$ (X-Y) Plane
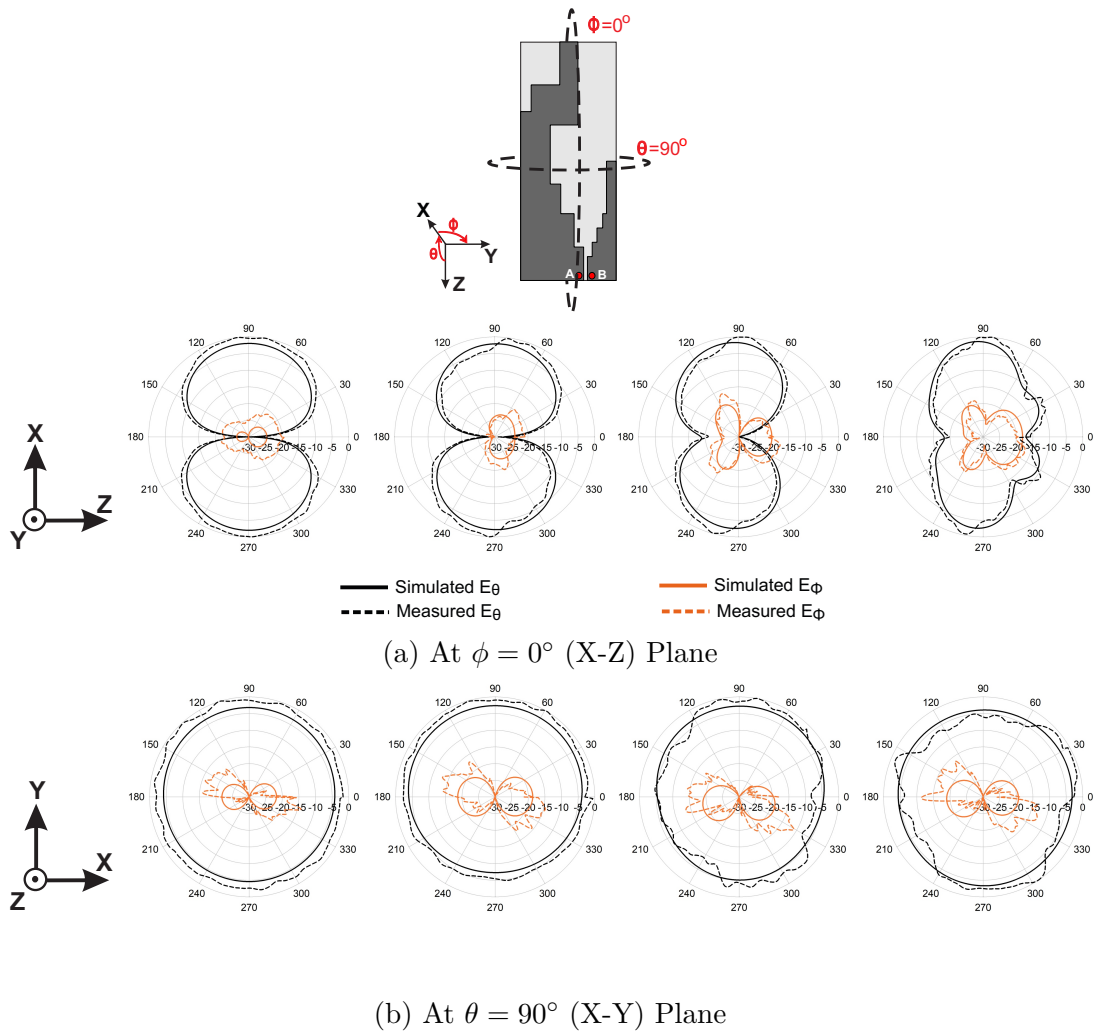
Fig. 4.27 2D Radiation Pattern of UWB-II for 3.5 GHz, 5.2 GHz, 9.7 GHz & 11.5 GHz; Dimensions as in Table 4.6

goes slightly directive towards the 90° as a result of the structural asymmetry. However, the radiation patterns are stable throughout the band of operation for UWB communication systems.

By analysing the θ and ϕ components of the field pattern in Fig. 4.27, the polarization isolation of the UWB-II are calculated and is summarized in Table 4.7, which shows the power differences (in dB) of ϕ and θ components along the two principle planes and in the direction of propagation, for different frequencies. It is clear from the table that the isolation stood above 31 dB along $\phi = 0°$ plane

Table 4.7 Polarization Isolation of UWB-II (values in dB); Dimensions as in Table 4.2

Freq. (GHz)	$\phi = 0°$ (X-Z) Plane	$\theta = 90°$ (X-Y) Plane
3.5	-36.06 dB	-24.68 dB
5.2	-34.5 dB	-21.97 dB
9.7	-33.67 dB	-21.86 dB
11.5	-31.84 dB	-21.9 dB

and above 21 dB along $\theta = 90°$ plane. Thus, it is clear that the UWB-II offers a better polarization purity throughout the band of interest in-spite of its small size. The polarization differences for different frequencies, in Table 4.7, shows that the proposed antenna has stable polarization through out the operating band, as the polarization isolation level doesn't differ much while the frequency of operation varies. This study confirmed the well-defined pulse transmission capability of UWB-II for UWB communication systems.
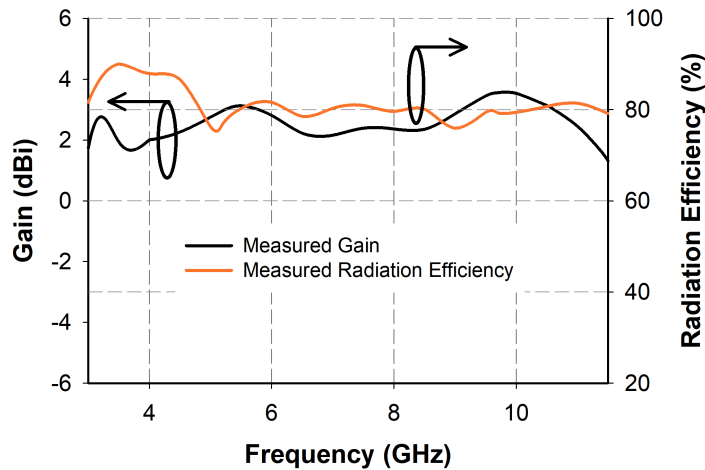
Fig. 4.28 Measured gain and radiation efficiency of UWB-II; Dimensions as in Table 4.6

Fig. 4.28 illustrates the measured gain and radiation efficiency of UWB-II The antenna exhibits stable gain across the 3.1-10.6 GHz band with a peak gain

of 3.5 dBi at 9.7 GHz. The antenna has an average gain of 2.6 dBi and radiation efficiency >75.9% in the UWB band of interest.

4.3 Time-domain Analysis

In this section the transfer properties of the UWB antennas discussed in the above sections are investigated and compared. Although the antennas were matched properly, they may behave differently when non-sinusoidal waveforms are transmitted/received, and hence this transient studies are very important for UWB antennas. The analysis setup and the underlying theory followed for the study are discussed in Section 3.3.3. For measurement & simulation setup both the receiving antenna & CST virtual probes are kept at a distance of 20 cm in far-field from the transmitting antenna, respectively. The studies are performed in the azimuthal($\phi = 0°$ plane for UWB-I & $\theta = 90°$ plane for UWB-II) and elevation plane($\theta = 90°$ plane for UWB-I & $\phi = 0°$ plane for UWB-II) of the antennas.

4.3.1 Transfer Function

The magnitude of the simulated transfer function $\vec{H}_{Rx}(\omega, \theta, \phi)$ of both UWB antennas at their azimuth as well as elevation plane in the frequency band of interest are depicted in Fig 4.29. The magnitude of transfer function for UWB-I is symmetrical around 180° for all frequencies. The Fig. 4.29a shows the transfer function of UWB-I along its azimuthal ($\phi = 0°$) and elevation ($\theta = 90°$) plane. Along azimuthal plane, the intensity of transfer function is uniform for lower frequency range ($\approx$ from 3 GHz to 6 GHz), for all θ angles. This is due to the omni-directional radiation pattern of the antenna for these frequencies. It was observed from Fig 4.13 that the radiation pattern of UWB-I goes slightly directive towards 180° for higher frequencies. This is got reflected on its transfer function, showing maximum values for the angles about 180° and minimum values about 0°. In the elevation plane of UWB-I antenna, the transfer function has maximum intensity for 0° and 180° of ϕ angles whereas, poor transfer function for 90° and 270°, throughout the 3.1-10.6 GHz frequency band. This corresponds to the

(a) UWB-I
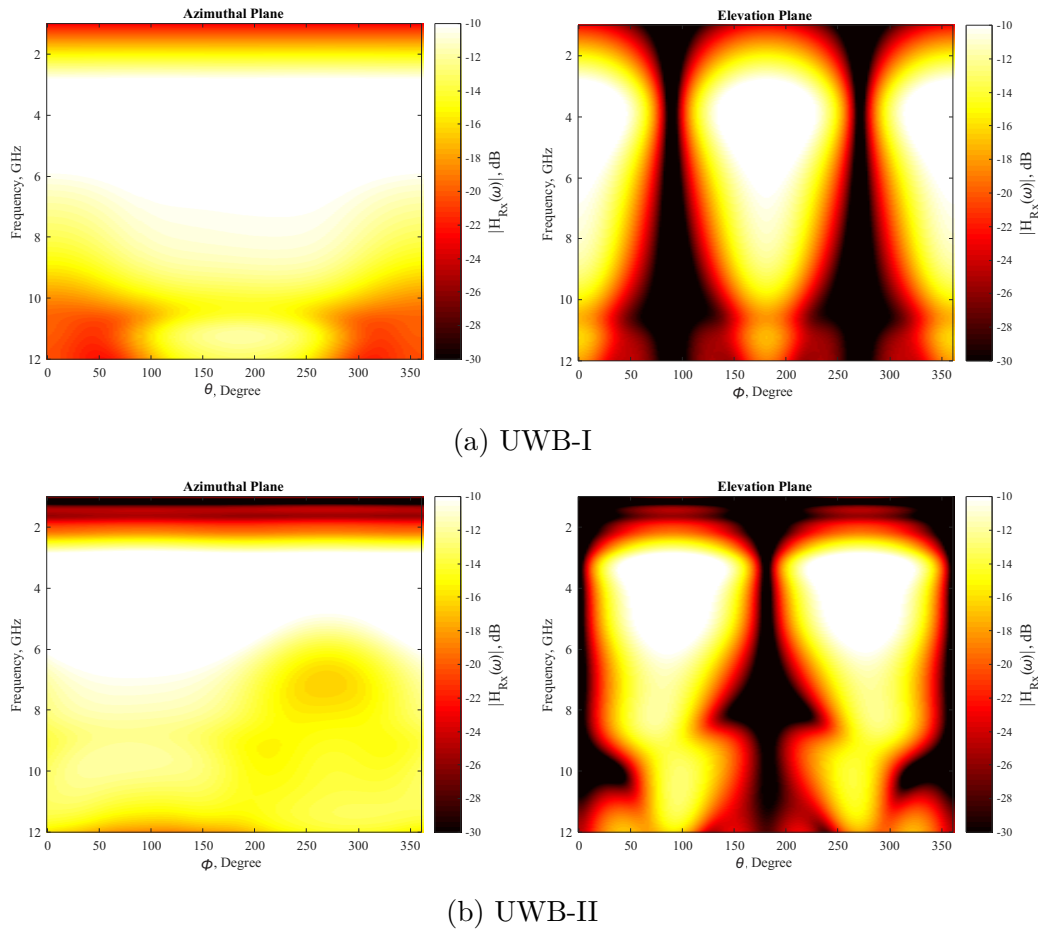
(b) UWB-II

Fig. 4.29 Simulated transfer function in the azimuthal and elevation plane

sharp nulls in the radiation pattern of UWB-I 90° and 270°, along its elevation plane.

The simulated magnitude of transfer function of UWB-II is plotted in Fig. 4.29b, for different angles and different frequencies. For UWB-II, the magnitude of transfer function along azimuthal plane ($\theta = 90°$ plane) has maximum intensity for angles about 90° compared to the other angles, mainly in higher UWB band. However, the transfer function has a kind of uniform amplitude for lower frequencies (upto 5 GHz), due to their partial omni-directional behaviour. Whereas, in elevation plane ($\phi = 0°$ plane) the transfer function has abrupt magnitude fall at 0° and 180°, corresponding to the radiation pattern nulls of the antenna.

(a) UWB-I

(b) UWB-II
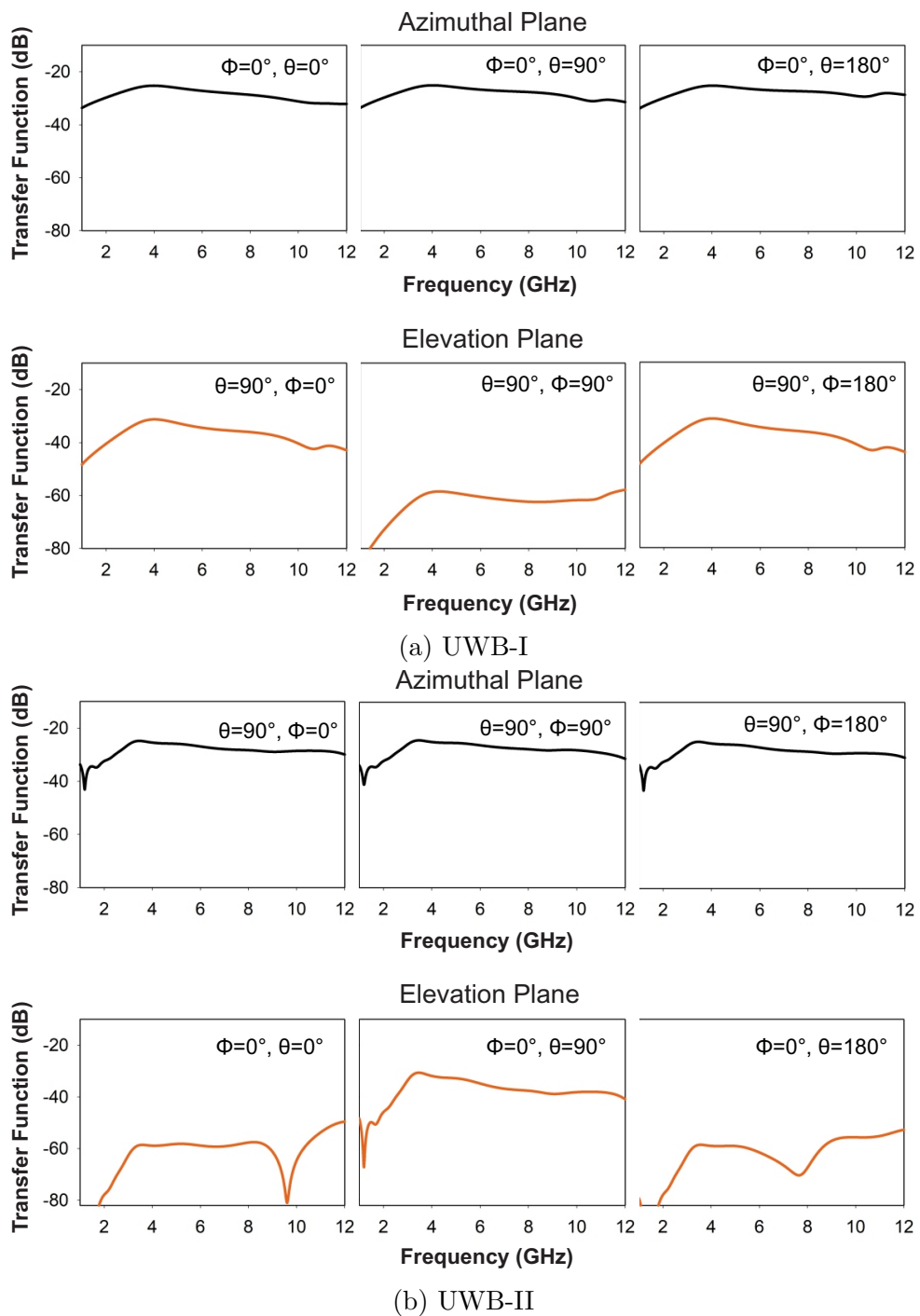
Fig. 4.30 Measured transfer function in the azimuthal and elevation plane

The corresponding measured transfer functions at two principle planes of both UWB antennas are depicted in Fig 4.30. The intensity variations in magnitude of transfer function agrees well with the simulations across both azimuthal and elevation angles and frequencies. Only the magnitude variations at angles 0°, 90° and 180° are shown for convenience. The measured transfer function of UWB-I along its azimuthal and elevation plane is depicted in Fig 4.30a. It is observed from the figure that, along azimuthal plane the magnitude of transfer function is similar for the three angles, whereas along elevation plane ($\theta = 90°$) the transfer function goes below 60dB at $\phi = 90°$. This abrupt magnitude fall at 90° is due to the sharp nulls of radiation pattern.

Similarly, the measured transfer function of UWB-II along both the principle planes are plotted in Fig 4.30a. It is observed from the figure that for the frequency range of operation from 3.1 GHz to 10.6 GHz, transfer function is flat in most of the cases, which denotes good transient response for the antenna. For UWB-II the transfer function along azimuthal plane have similar characteristics for all the three angles. While along elevation plane($\phi = 0°$) there are abrupt magnitude falls <60dB for $\theta = 0°$ and $\theta = 180°$ corresponding to the pattern nulls, compared to that of other angles.

4.3.2 Impulse Response

From the complex values of simulated transfer function the impulse response of the antennas are derived and its real values are plotted in Fig 4.31. It is observed from the respective figures that both the antennas have sharp and well formed impulse responses at all angular regions, except for those angles in elevation plane where the magnitude of transfer function have sharp nulls. For UWB-I the sharp nulls are at 90° & 270° (refer Fig 4.31a) and for UWB-II nulls are present at 180° & 0° (refer Fig 4.31b). The impulse responses from the measured values of transfer function are depicted in Fig 4.32. It is observed from the figure that the amplitude of impulse responses has variation along the elevation plane of both the antennas. The amplitude of the impulse response is minimum for θ=90°, ϕ=90° for UWB-I, as seen in Fig 4.32a and for UWB-II it has minimum values for ϕ=0°, θ=0° & ϕ=0°, θ=180°, as shown in Fig 4.32b, which corresponds to their pattern nulls. The measured values of impulse responses conforms well

(a) UWB-I

(b) UWB-II
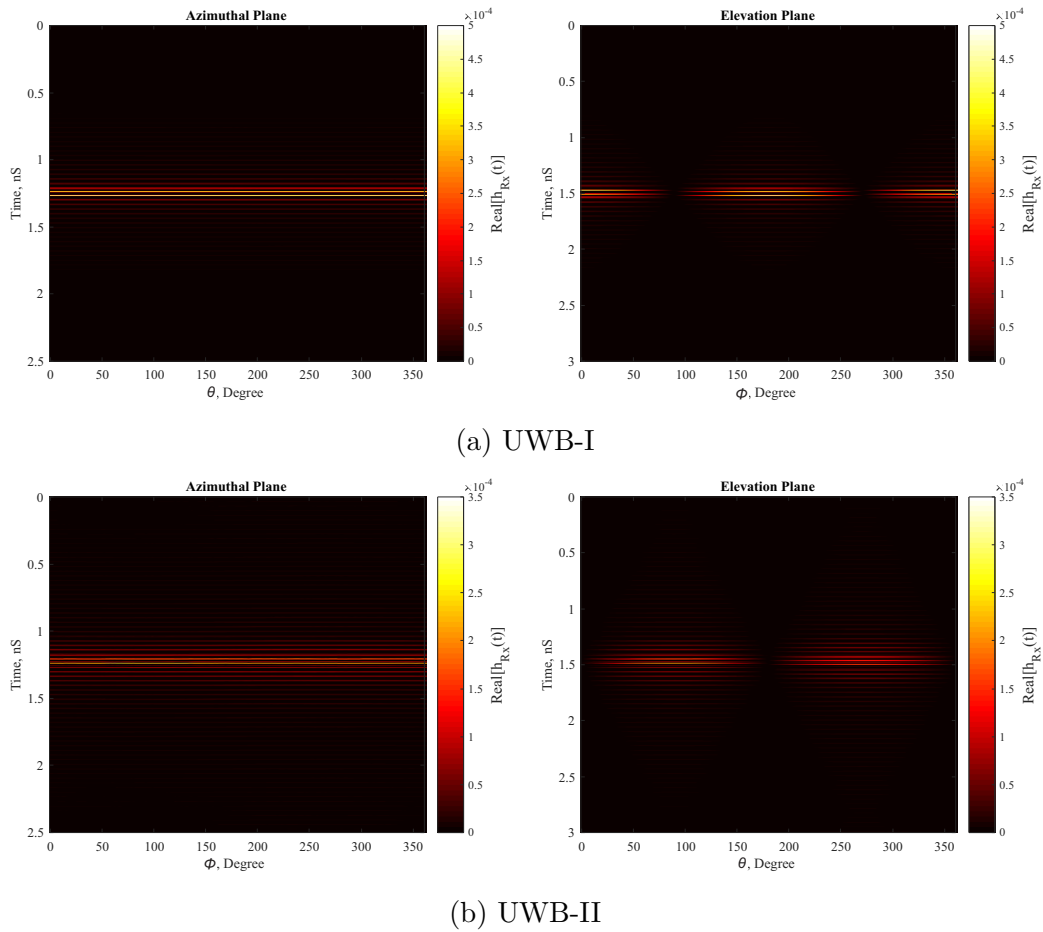
Fig. 4.31 Simulated impulse response in the azimuthal and elevation plane

with those of simulated one across both azimuthal and elevation angles in the frequency band of interest.

4.3.3 Quality Measures of UWB antennas

The simulated and measured transfer properties are quantified with the help of certain quality measures, as discussed in Section 3.3.3. One of the crucial parameters to quantify the transfer properties of a UWB antenna is the group delay, which can be measured using two identical antennas oriented Side-to-Side or Face-to-Face. The results of group delay measurements of both UWB-I and UWB-II are plotted in Fig 4.33a and Fig 4.33b, respectively. The arrangement of

(a) UWB-I
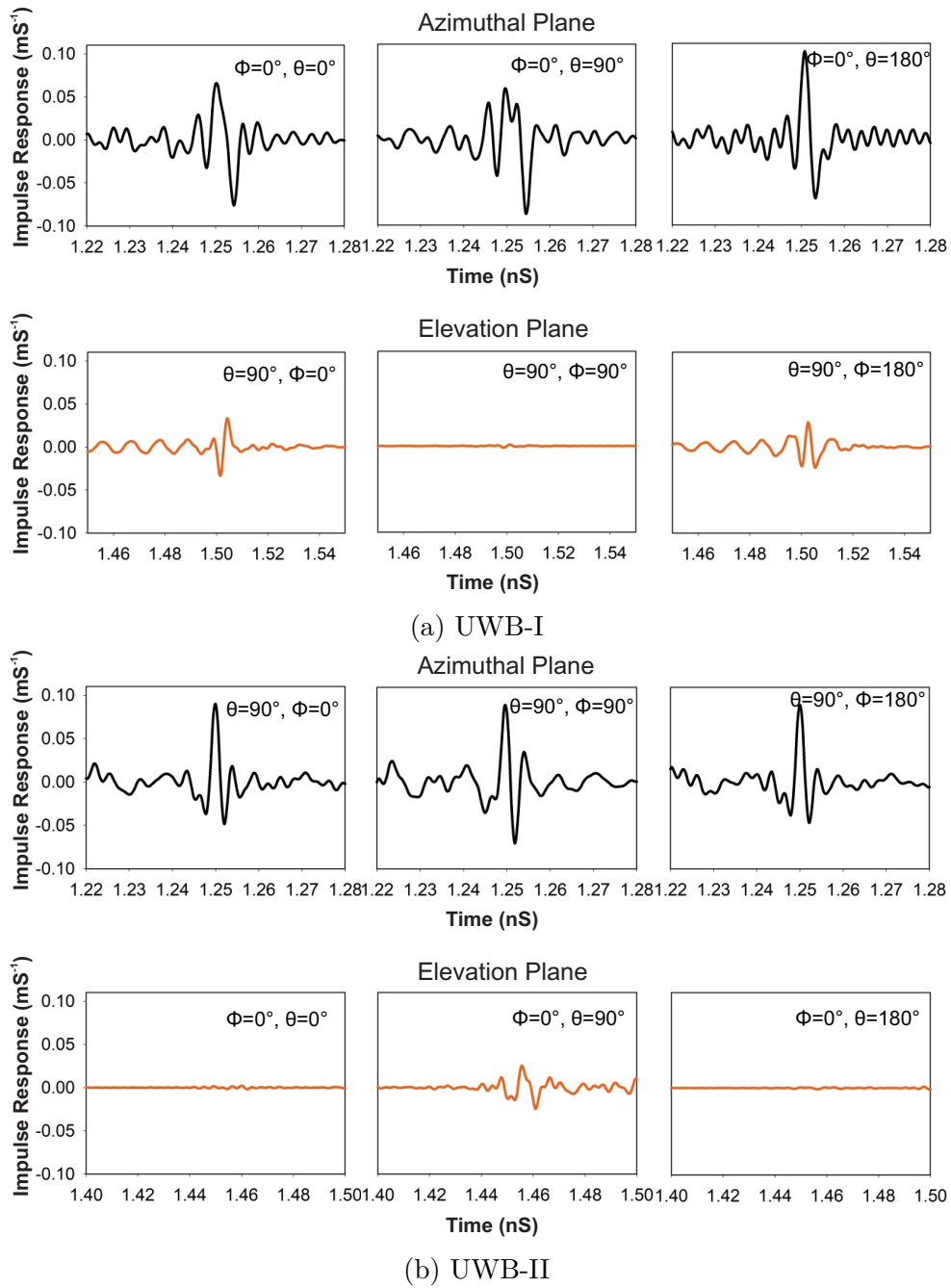
(b) UWB-II

Fig. 4.32 Measured impulse response in the azimuthal and elevation plane

identical antennas for both Face-to-Face & Side-to-Side orientations of UWB-I and
UWB-II are shown on top of the corresponding graphs, in Fig 4.33a and Fig 4.33b,
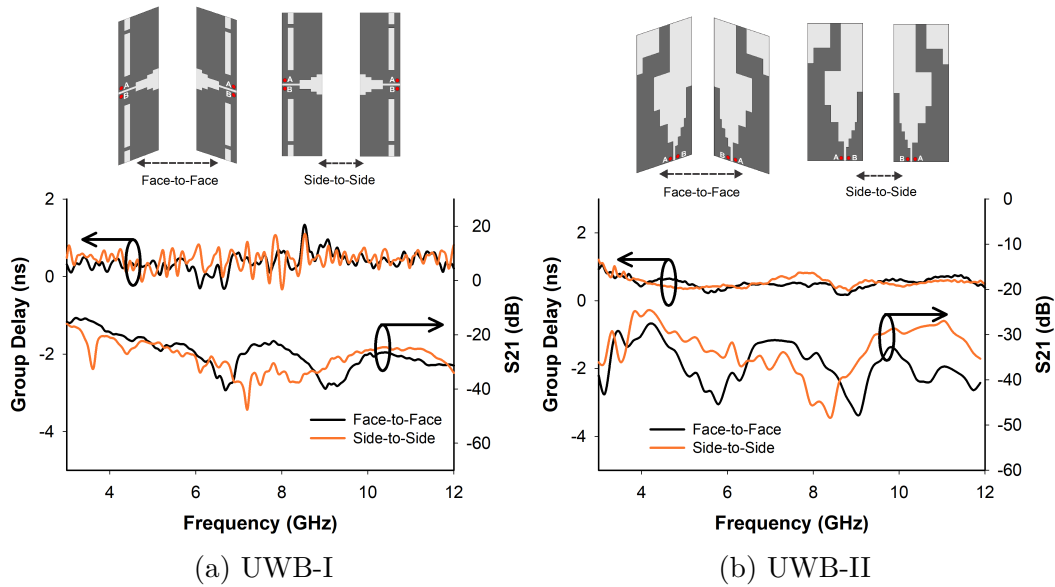
Fig. 4.33 Measured group delay of both UWB antennas

respectively. For the case of an ideal lossless transmission, the group delay will be flat denoting a linear variation of phase with frequency. In addition to the group delay, corresponding values of S_{21} for the afore mentioned orientations are also included in the respective figures. The group delay of UWB-I shows a variation ≤ 0.1nS and that of UWB-II has a variation ≤ 0.8nS throughout the UWB bandwidth of 3.1-10.6 GHz. Thus, for both the antennas the measured group delays are within the tolerable range of ± 1nS, showing a linear change of phase with frequency.

The Table 4.8 summarizes the values of FWHM, ringing and fidelity factor of both UWB antennas, calculated from the simulated and measured transient responses across their azimuth and elevation planes. These factors gives an idea about the dispersive behaviour of the UWB antennas. It is clear from the table that both antennas have narrow FWHM and low ringing, which manifests high fidelity factor for their respective planes. This shows that the antennas gives only tolerable distortions to the pulses that are transmitted through them. The measured and simulated values conformed well with each other in the azimuthal plane than in elevation plane, as the antennas have partially omni-directional patterns in that plane.

Table 4.8 FWHM, Ringing and Fidelity of UWB antennas

		Angle (θ or ϕ)	FWHM (pS)		Ringing (pS)		Fidelity (%)	
			Sim.	Meas.	Sim.	Meas.	Sim.	Meas.
UWB - I	Azimuthal	0°	190.9	175	136.4	130	90.39	95.7
		90°	177.2	185	122.7	141	96.04	93.62
		180°	190.9	180	136.4	128	93.38	95.5
	Elevation	0°	150	175	149	125	85.78	96.9
		90°	191.2	180	135.3	136	90.4	95.4
		180°	150	210	149	155	85.78	87.9
UWB - II	Azimuthal	0°	176.2	165	121.9	135	90.74	96.9
		90°	170.6	175	108.4	125	96.27	98.1
		180°	176.1	170	121.9	127	91.06	97.8
	Elevation	0°	149.1	190	338.8	150	88.2	90.7
		90°	176.2	175	121.9	130	90.7	93.9
		180°	135.5	175	284.5	125	79.97	86.75

4.4 Spatial-domain Analysis

The analysis of an antenna in its spatial-domain will gives a clear picture of the fluctuations in the radiation properties around the antenna. This analysis can be performed by calculating the correlation patterns and Pattern Stability Factor (PSF) of the antenna at its respective planes, in the directions of interests, as discussed in section 3.3.4.

In this section investigations carried out in the spatial-domain for both UWB-I and UWB-II are explained in detail, with their simulated as well as measured results. For simulations, the frequency-domain radiated electric field values around the antennas are probed out using the virtual probes in CST, kept at

(a) UWB-I   (b) UWB-II
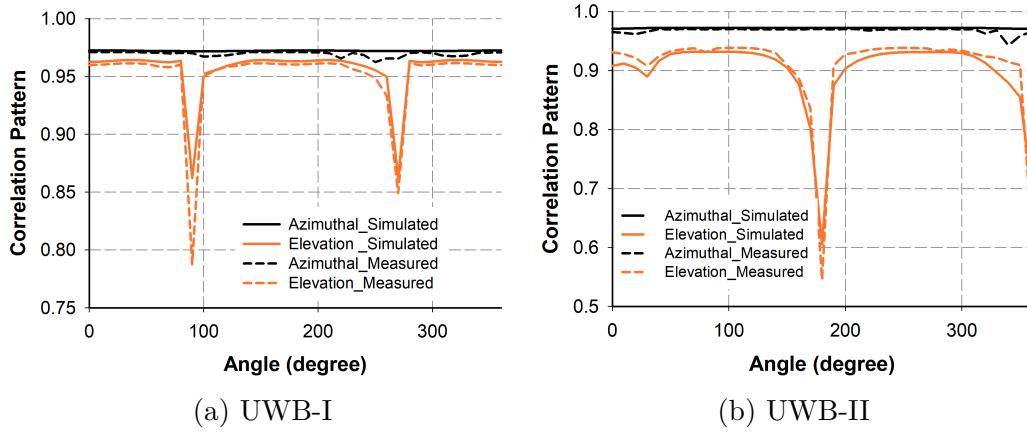
Fig. 4.34 Simulated and measured frequency domain correlation pattern of UWB antennas

Table 4.9 PSF Values for 3.1 - 10.6 GHz band

	$\phi = 0°$ **(X-Z) Plane**		$\theta = 90°$ **(X-Y) Plane**	
	Sim.	Meas.	Sim.	Meas.
UWB-I	0.9722	0.9612	0.9565	0.9342
UWB-II	0.9721	0.9680	0.8985	0.9071

a distance of R in far-field with a separation of 10° between them. While for experimental part, the S_{21} between the AUT & a horn antenna is measured at 10° intervals around the AUT with a radius of R (refer section 3.3.4). For both UWB antennas, the probes are kept at a distance of $R = 20$ cm from their centers and the respective E-field (or S_{21}) values at azimuthal & elevation planes are detected. To identify the best reference direction for system design, the correlation patterns of these two antennas are determined using the afore mentioned input data, over the azimuth & elevation plane in the frequency range of 3.1–10.6 GHz, and the results are shown in Fig. 4.34. From the correlation patterns the corresponding PSF values are calculated and are listed in Table 4.9 . This gives an idea of the degree of stability the antennas possess in their band of operation. For an ideal antenna the PSF values will be equal to unity and PSF>0.9 is taken as a desirable value for a good all-round performing antenna.

In the case of UWB-I, the correlation pattern over azimuth plane (here, X-Z plane) is constant, throughout the 3.1 - 10.6 GHz band, as they are more correlated with all directions on average. Also, in this plane the antenna shows high values for correlation pattern in all the directions concerned. However, in elevation plane (here, X-Y plane) the correlation pattern shows dips in the direction of 90° and 270°, which are due to the presence of nulls in the radiation pattern at those directions. This indicates that the reference directions in all the range, other than at these two points at its elevation plane, are the best to use. The PSF values of UWB-I in Table 4.9 at both azimuth and elevation plane points out an excellent degree of stability for the antenna, as the values are > 0.93 in the 3.1 - 10.6 GHz frequency band. The PSF value goes a little down in its elevation plane because of the poor correlation in the patterns at 90° and 270°. But the overall stability stands up to the mark in both planes over the band of interest. Moreover, both the simulated and measured results conform very well with each other in the operation band.

For UWB-II, the correlation pattern in azimuth plane (X-Y plane) appears distorted between 0° - 40°, while remains constant in rest of the band with fairly good correlation for all other directions. For the case of this antenna also, the correlation pattern in its elevation plane (X-Z Plane) shows dips in the direction of 180° and 360° due to the presence of nulls, which denotes the directions with less performance level. The PSF values in Table 4.9 at both azimuth & elevation plane are > 0.907 in the band of interest showing a desirable level of stable performance for UWB-II.

4.5   Chapter Summary

In this chapter, the characteristics of two coplanar UWB antennas are studied. Both the antennas utilized the step shaped resonators for attaining the wide bandwidth to cover the required frequency band for a UWB radio communication system. The radiation pattern of both UWB antennas goes slightly directive in their higher frequencies. They offered stable gain and good radiation efficiency across the entire band of interest. The transfer properties of the antennas are also investigated in this chapter. This study gave an idea about the pulse handling capability of these UWB antennas. The intensity of transfer function is reduced

corresponding to the low radiation points around the antennas and the radiation got reflected in the corresponding impulse responses as a dispersion. FWHM & ringing quantified the dispersion and fidelity gives the cross-correlation between transmitted and received pulses. The summarized values of quality measures reveals that both UWB antennas have minimum FWHM, ringing and reasonably good fidelity throughout their operation bandwidth. This verifies the good pulse handling capability of the antennas. In addition to this, the spatial-domain characteristics of both UWB antennas are also discussed in this chapter. The frequency-domain correlation patterns of both antennas helped to select the best reference directions for them which have better transfer properties. Also, the PSF values revealed that the antennas have good pattern stability over the entire UWB bandwidth.

Chapter 5

Coplanar Multi-port antennas for UWB-MIMO Communication

The demand for high data rate and good channel capacity is always the primary area of concern in the modern era of wireless communication systems. The race for such a communication system lead to the invention of Multiple-Input Multiple-Output (MIMO) technology, which utilizes the diversity or spatial multiplexing technique to improve the reliability or data rate of the communication systems by mitigating the vulnerable multipath fading problem, where signals may combine destructively at the receiver. This goal is achieved either by transmitting multiple replicas of information over the different antennas or by spreading the same total transmit power over the antennas to improve spectral efficiency. Research on MIMO antennas had been started many years ago, and tremendous works focusing on WLAN and WiMAX standards are there in the literature.

According to Shannon-Hartley theorem, a wide channel bandwidth can guarantee a good channel capacity, without invoking a high transmitted power. UWB antennas are a good choice for this, which has been expanding rapidly as a promising technology for many applications such as ground penetrating radars, location tracking, data communication, Body Area Networks (BAN) etc.., since FCC had specified 3.1 – 10.6 GHz as the frequency band for UWB Radio systems. It transmits data in short pulses and is devoted mainly to short range applications due to the limitations of the power spectral density of -41.3 dBm/MHz within the UWB band. One of the biggest advantages of UWB is the immunity against

fading effects. However, owing to the limitations in the power spectral density, the data transmission rate of UWB gets limited and the SNR at the receiver becomes low, which deteriorates the performance of UWB systems. Researches show that incorporating MIMO technique with UWB provides a viable solution to this bottleneck. This will help to achieve data rates more than 1 Gb/s for wireless communications. This chapter discusses about such UWB-MIMO antennas, which are coplanar in nature and the different antenna elements are co-located on to a single substrate. One of the challenging task for such antennas are to employ diversity technique in the co-located geometry, by maintaining low mutual coupling between the antenna elements as well as keeping the overall size compact, in the wide bandwidth.

This chapter investigates the performance of three different MIMO antennas, designed using the combinations of two coplanar UWB antennas, discussed in the previous chapter. The isolation mechanism and the antenna-element arrangement are made in such a way that the overall size of the co-located antenna is very less. The isolation mechanisms adopted in the respective geometries to attain minimal inter-element coupling are also discussed. The surface current distributions on the antennas together with their radiation characteristics for the different resonant frequencies are analysed in detail. The performances of fabricated antennas are then experimentally verified and are found to be in agreement with the simulated results. In addition to this, the transfer properties and spatial-domain characteristics of the antennas are investigated as they are bound to work in UWB communication environment. Moreover, the MIMO/Diversity performance of the antennas are also evaluated by computing the required figures-of-merit governing the suitability of antennas for MIMO applications.

5.1   The Two-port UWB-MIMO antenna

For a two-port MIMO antenna configuration it is required to integrate two antenna elements on a single substrate. This thesis discusses about the design and development of MIMO antenna systems for UWB applications, and hence the antenna elements must perform well in the 3.1-10.6 GHz operating band for UWB communication systems, as per FCC regulations. Therefore, the UWB antennas investigated in Chapter 4 are used as the antenna-elements for to accomplish a

(a) Face-to-Face configuration   (b) Side-to-Side configuration

(c) Back-to-Back configuration
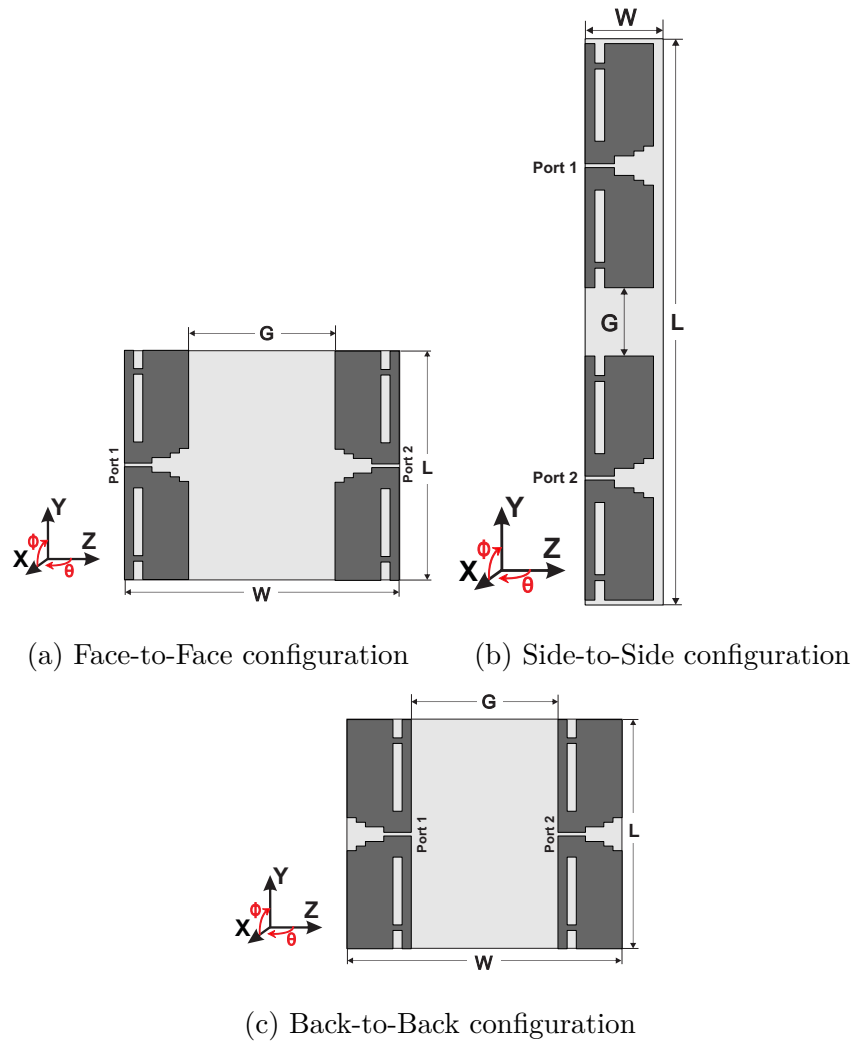
Fig. 5.1 Three different UWB-MIMO configurations

two-port UWB-MIMO antenna. These two elements must be isolated properly to have seamless antenna performances. This isolation can be achieved either by proper arrangement of antenna-elements and/or by placing decoupling structures in between them. The UWB-I antenna, discussed in Section 4.1, is configured in three different ways to obtain the UWB-MIMO operation, as shown in Fig. 5.1. The dimensions of antenna elements are same as that of the optimized dimensions of UWB-I, enlisted in the Table 4.2. In the Face-to-Face configuration, the two UWB-I are placed facing each other and separated by a distance of $G = 16$mm, as shown in Fig. 5.1a. The overall size of this configuration is 25mm $\times$

(a) Face-to-Face configuration

(b) Side-to-Side configuration

(c) Back-to-Back configuration
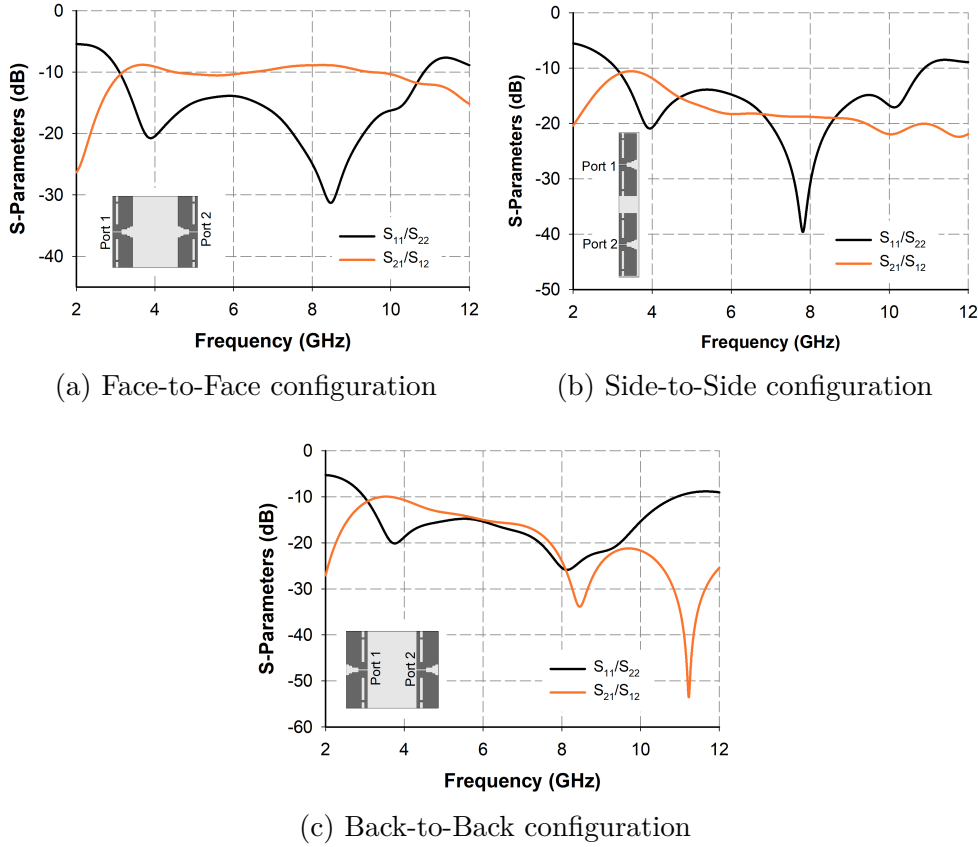
Fig. 5.2 Simulated s-parameters of three antenna configurations

30mm ($= L \times W$) which is etched on a FR-4 substrate of relative permittivity $\epsilon_r = 4.3$, loss tangent $tan(\delta)$=0.02 and thickness h=1.588 mm. The same FR-4 material is used for all the UWB-MIMO antennas in this chapter. In Side-to-Side configuration, the UWB-I elements are arranged adjacent to each other with a separation of G=7mm, as shown in Fig. 5.1b. For this case the overall size became 57mm $\times$ 8mm ($= L \times W$). In the third configuration (Back-to-Back), the UWB-I antennas are kept back to each other separated by a distance of $G =$ 16mm, as shown in Fig. 5.1c. The overall size of this configuration is same as that for Face-to-Face arrangement. Fig. 5.2a, 5.2b & 5.2c illustrate the simulated S-parameters corresponding to the three antenna-elements configurations, which are shown in the inset of figures. The S_{11} curves in the figures show that all the configurations succeeded in achieving the UWB frequency band of 3.1-10.6

GHz. It is to be noted that for a good MIMO antenna performance an isolation of atleast 20 dB is required between the antenna elements. From Fig. 5.2a it is clear that, for Face-to-Face configuration the magnitude of transmission coefficient $|S_{21}| \cong 10$ dB in the entire UWB band, which is due to the strong mutual coupling between the two antennas. This corresponds to the low isolation between the antenna elements. For Side-to-Side configuration the $|S_{21}|$ goes above 15 dB after 4.5 GHz till 9-9.5 GHz, and after that isolation is enhanced as $|S_{21}|$ goes beyond 20 dB (refer Fig. 5.2b). Whereas, when the two UWB antennas are connected Back-to-Back, the $|S_{21}|$ goes above 20dB for frequencies greater
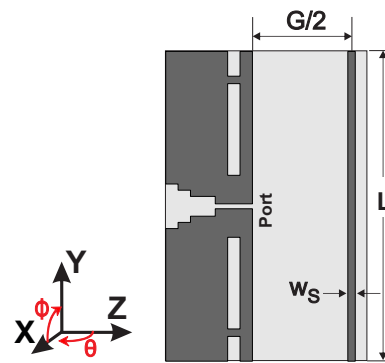
(a) UWB-I with isolation strip
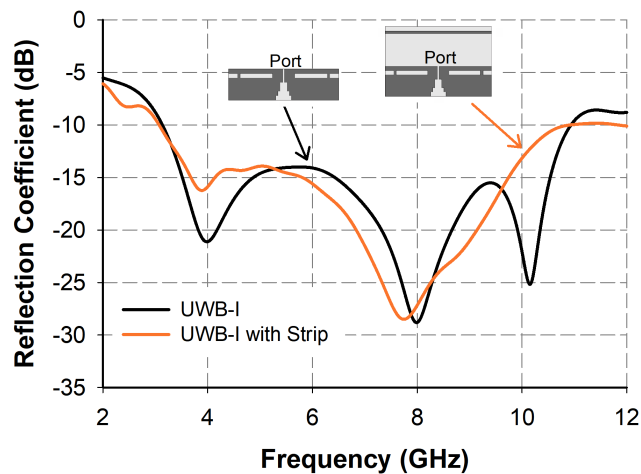
(b) Reflection coefficient of UWB-I with & without strip

Fig. 5.3 Simulated s-parameters UWB-I with and without isolation strip; L=25mm, W_S=0.4mm & G=16mm

than 7.5 GHz, which guarantees a good isolation between the antennas for those frequencies. But here also, the mutual coupling of the antennas is strong in the lower UWB band. This high mutual coupling is due to the fact that the port-to-port distance is $< 0.5\lambda_0$ for frequencies between 3.1-7.5 GHz, where λ_0 is the free space wavelength at the resonant frequency. However, it can be resolved by the use of a proper decoupling method in the MIMO antenna. Although, both the Side-to-Side and Back-to-Back configurations are found to have considerable isolations in higher UWB band, the possibilities of enhancing the isolation in lower UWB band within a small profile is more in Face-to-Face arrangement of UWB-I.

In order to enhance the inter-element isolation in lower frequency band, a metal strip can be added in between the antenna-elements as a decoupling structure,[112], between them. To check whether the addition of this strip will deteriorate the impedance matching performance of UWB antennas, the reflection coefficient of a single UWB-I is simulated by placing a metal strip of width W_S=0.4mm and length=25mm (=L) at a distance of 7.8mm from the port of UWB-I. The placement of metal strip is shown in Fig. 5.3a and corresponding reflection coefficient is plotted in Fig. 5.3b. It is clear from the figure that, the strip deteriorates the reflection performance of the antenna slightly, but the impedance matching is still lower than -10dB within the UWB band. Thus, in the Back-to-Back configured UWB-MIMO antenna (Fig. 5.1c) a metal strip of size $L \times W_S$ is added as an isolation element between the two UWB antennas. The antenna configuration of the two-port UWB-MIMO antenna with isolation strip is shown in Fig. 5.4, where the metal strip is kept at half the way from port 1 to port 2.

A comparison of the reflection and transmission coefficients of the 2-port UWB MIMO antenna with and without the metal strip is depicted in Fig. 5.5. From the figure it is clear that the reflector effectively decreases the coupling between the two antenna elements and thus drags the isolation level to stand below -20dB in the 3.1-7.5 GHz band. So, the presence of reflector together with the Back-to-Back configuration of the antenna elements helped the proposed MIMO antenna to get an enhanced isolation level of -20dB throughout the band of operation. In addition to this, the two-port antenna with isolation structure
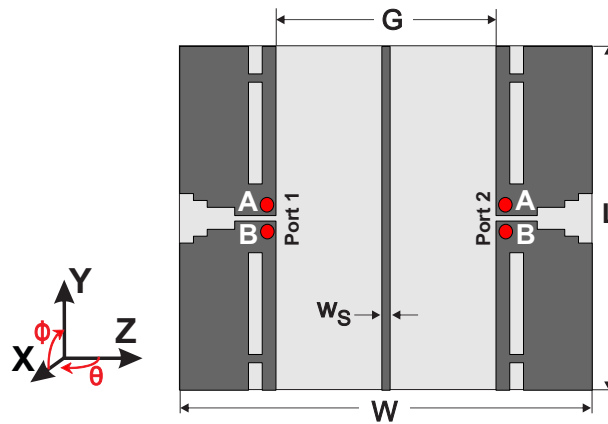
Fig. 5.4 Geometry of two-port UWB-MIMO antenna; $L = 25$mm, $W = 30$mm, $G = 16$mm, $W_S = 0.4$mm
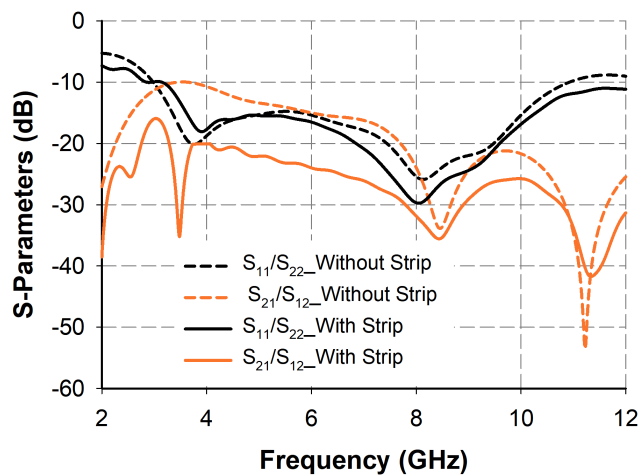
Fig. 5.5 Simulated S-parameters of two-port UWB-MIMO antenna with and without strip; $L = 25$mm, $W = 30$mm, $G = 16$mm, $W_S = 0.4$mm

offered a 2:1 VSWR impedance bandwidth from 3.1 GHz to 11 GHz, satisfying the frequency range needed for UWB radio systems as per the FCC strategies.

Parametric studies are conducted to investigate the influence of some important parameters on the reflection and transmission characteristics of the two-port MIMO antenna and thus to optimize their values. The effect of variation of the distance between the two ports (G) and the width of the isolator strip (W_S)

(a) Reflection coefficient (S_{11}/S_{22})   (b) Transmission coefficient (S_{21}/S_{12})
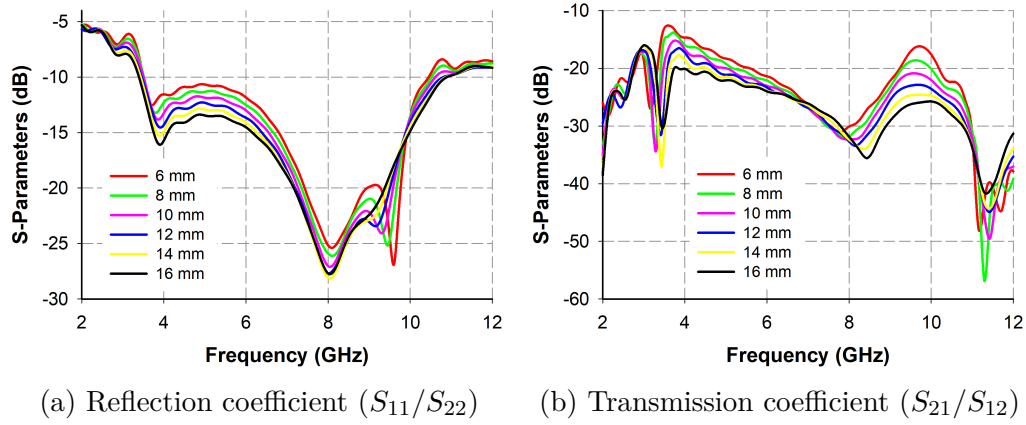
Fig. 5.6 Change in S-parameters with G, the separation between two antennas; $L = 25$mm, $W = 30$mm, $W_S = 0.4$mm

(a) Reflection coefficient (S_{11}/S_{22})   (b) Transmission coefficient (S_{21}/S_{12})
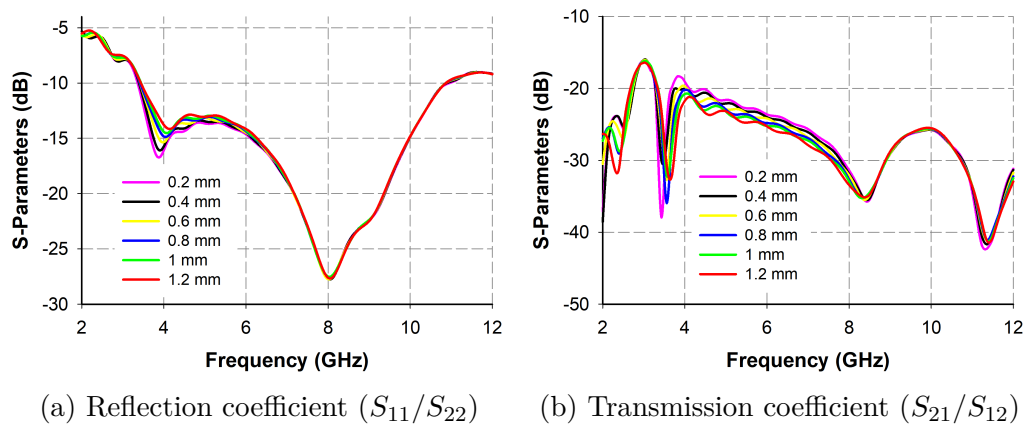
Fig. 5.7 Change in s-parameters as W_S is varied; $L = 25$mm, $W = 30$mm, $G = 16$mm

on the antenna impedance performance are carried out. In both the cases all other parameters, except the parameter under investigation, are kept same. The effect of the distance G on the impedance matching and the isolation is depicted in Fig. 5.6a & 5.6b, respectively. From Fig. 5.6a, it is observed that when the distance G between two ports is increased the reflection coefficient of the antenna is improved. That means, the impedance matching can be improved by tuning G. This is due to the fact that, as the two antenna-elements get closer, one element will affect the performance of other adversely. This happens because of the re-

radiations from the other passive antenna-element when it is closer to any active element. Fig. 5.6b shows that, the mutual coupling between the two antenna elements can be further reduced by increasing G. This is because, as G increases, the port-to-port distance between two antenna-elements also increases, which will help the antenna to satisfy the condition of separation $\geq 0.5\lambda_0$ between the two ports, where λ_0 is the free-space wavelength of the antenna at the frequency of interest. This adequate separation will produce considerable isolation between the two elements. However, due to the space constraints an optimum value of G=16 mm is considered for the present antenna design.

Fig. 5.7a & 5.7b illustrates the influence of the isolator strip width (W_S) on reflection and transmission coefficients, respectively. Initially, the strip width (W_S) is set at 0.2 mm and then increased up to 1.2 mm, this change in W_S has got effect in the frequencies between 3.1 – 7.5 GHz only. Fig. 5.7a & 5.7b points out an inverse relationship between the impedance matching and the isolation level of the proposed antenna. That is, as W_S increases, the impedance matching decreases while the isolation between the two antennas increases. By considering both the impedance and isolation requirements, an optimum value of W_S=0.4 mm is selected for the final antenna design. For this value of W_S, the antenna possess a 2:1 VSWR bandwidth of 3.1 -11 GHz and an isolation of greater than 20 dB throughout that bandwidth.

The optimized dimensions of the two-port UWB-MIMO antenna shown in Fig. 5.4 are $L = 25$mm, $W = 30$mm, $G = 16$mm and $W_S = 0.4$mm. Both the antenna elements along with the metal strip are printed on one side of a FR-4 substrate with a relative permittivity (ϵ_r) of 4.3, loss tangent ($tan(\delta)$) of 0.02 and thickness (h) of 1.588 mm. The overall size of this two-port MIMO antenna is $0.25\lambda_0 \times 0.3\lambda_0$ (where, λ_0 is the free-space wavelength at 3.1 GHz), which is very compact and smaller than most of the coplanar two-port UWB-MIMO antennas reports in the literature. The planes corresponding to $\phi = 0°$ (X-Z) & $\theta = 90°$ (X-Y) represents the two principal planes for all far-field measurements of the antenna. The connections of outer and inner conductors of the coaxial connectors to the individual antenna-elements are denoted in the figure as 'A' and 'B' (red dots), respectively.

The reflection coefficient of an antenna can only represent the antenna's behaviour as a lumped load at the end of a feeding line. The detailed electro-

(a) Two-port antenna without isolation strip

(b) Two-port antenna with isolation strip
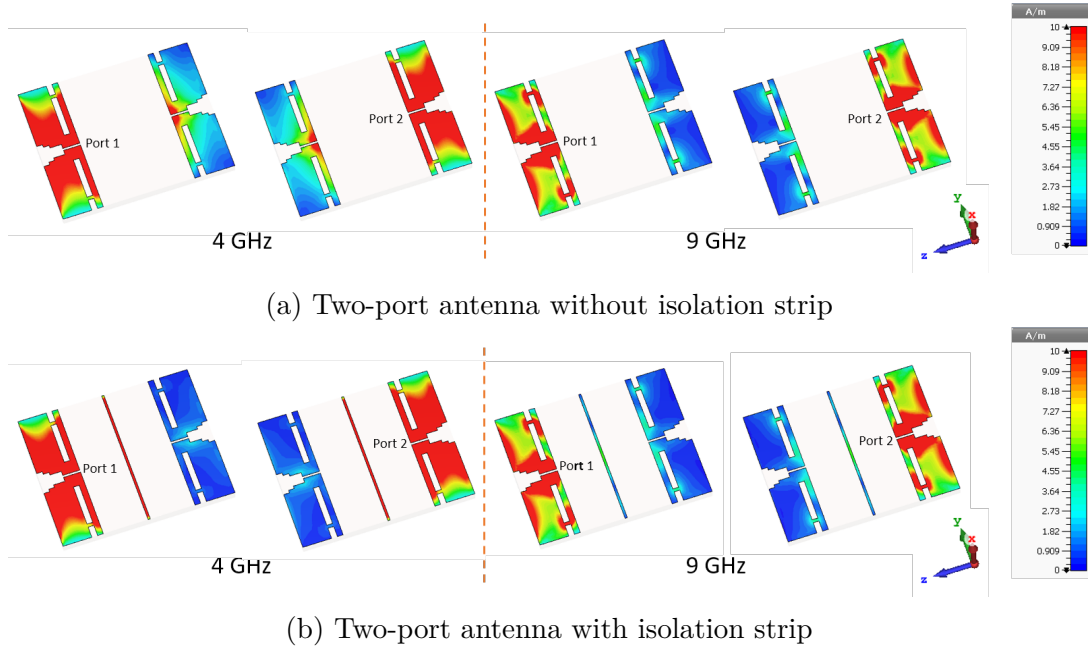
Fig. 5.8 Surface current distribution at 4 GHz & 9 GHz for each port excitation (other port is passive); $L = 25$mm, $W = 30$mm, $G = 16$mm, $W_S = 0.4$mm

magnetic behaviour of an antenna can be unveiled by inspecting the surface current distributions in the antenna structure by exciting only one port at a time. The mutual coupling between closely packed antennas is due to the large flow of surface current from the excited port to the other ports. With the help of decoupling structures this migration of surface current can be blocked or attenuated, and hence can reduce the mutual coupling. Here for the two-port antenna, a simple metal strip is used for the isolation purpose and its effect on the surface current distribution is shown in Fig. 5.8, at 4 GHz and 9 GHz. Fig. 5.8a depicts the current distribution for port 1 & 2 excitations, when there is no isolation strip between the antenna elements and Fig. 5.8b portrays the change in current distribution while the isolation strip is added to the structure. It is inferred from the Fig. 5.8a that the two-port antenna have large inter-element coupling in the lower UWB band (at 4 GHz) and less coupling in its higher frequency band (at 9 GHz). The low coupling at the higher frequencies are due to its Back-to-Back configuration, resulting in adequate port-to-port distance between the antenna elements. On placing the isolation strip the current distribution for

the lower frequencies (4 GHz) are changed, as shown in Fig. 5.8b. The invasion of surface current on to the other port is reduced tremendously because of the presence of isolation strip. Whereas, distribution at higher frequencies (9 GHz) remained same as the strip has no effect on those frequencies. Thus, the metal strip acts as an isolator for lower frequencies and has great influence on the antenna's surface current distribution. But, for higher frequencies its decoupling behaviour degrades slowly and its influence on surface current also decreases. However, mutual coupling will not be increased for those frequencies because of the configuration of antenna elements.

It is a well known fact that, a metal conductor placed at a distance of $0.10\lambda_g$ to $0.25\lambda_g$ away from the feeding point will act as a reflector and produces high directive gain in the direction of propagation [22], where λ_g is the guided wavelength of the antenna at resonant frequency. If it is $\geq 0.25\lambda_g$ also, this metal conductor shows reflective nature, but will have destructive interference which causes the directive gain of the antenna to fall off. Thus in the current case of two-port UWB-MIMO antenna, the conductor strip present in between its antenna-elements can be termed as a reflector for the frequencies between 3.1 GHz to 7.5 GHz. Also, this parasitic conductor strip is about 5% longer than the resonant length of antenna elements for 3.1-7.5 GHz, which is yet another metric for a parasitic element to become a reflector. The behaviour of the metal strip as a reflector can be confirmed with the analysis of 3-D radiation pattern of two-port antenna. Fig. 5.9 shows the simulated 3D radiation pattern of both MIMO antennas with and without metal strip, at 4 GHz & 9 GHz for each port excitation. On comparing Fig. 5.9a & 5.9b it is clear that the pattern goes directive when the isolation strip is placed between the antenna elements. Also, the front-to-back (F/B) ratio at the antenna-element is increased for the antenna with strip, with a change in peak gain from 3.9 dB to 4.95 dB for 4 GHz. This confirms the reflective nature of the metal strip at 4GHz. However, the metal strip does not retain its reflective behaviour at higher frequencies (9 GHz), as the pattern remained unchanged with slight change in gain. To establish the behaviour of metal strip as a reflector, the peak gain of the antennas are simulated and plotted against frequency in Fig. 5.10. It is noticed from the figure that the gain of two-port antenna with isolation strip is increased for frequencies between 3.1 and 7.5 GHz as compared to that of antenna without strip. This points

(a) Two-port antenna without isolation strip

(b) Two-port antenna without isolation strip
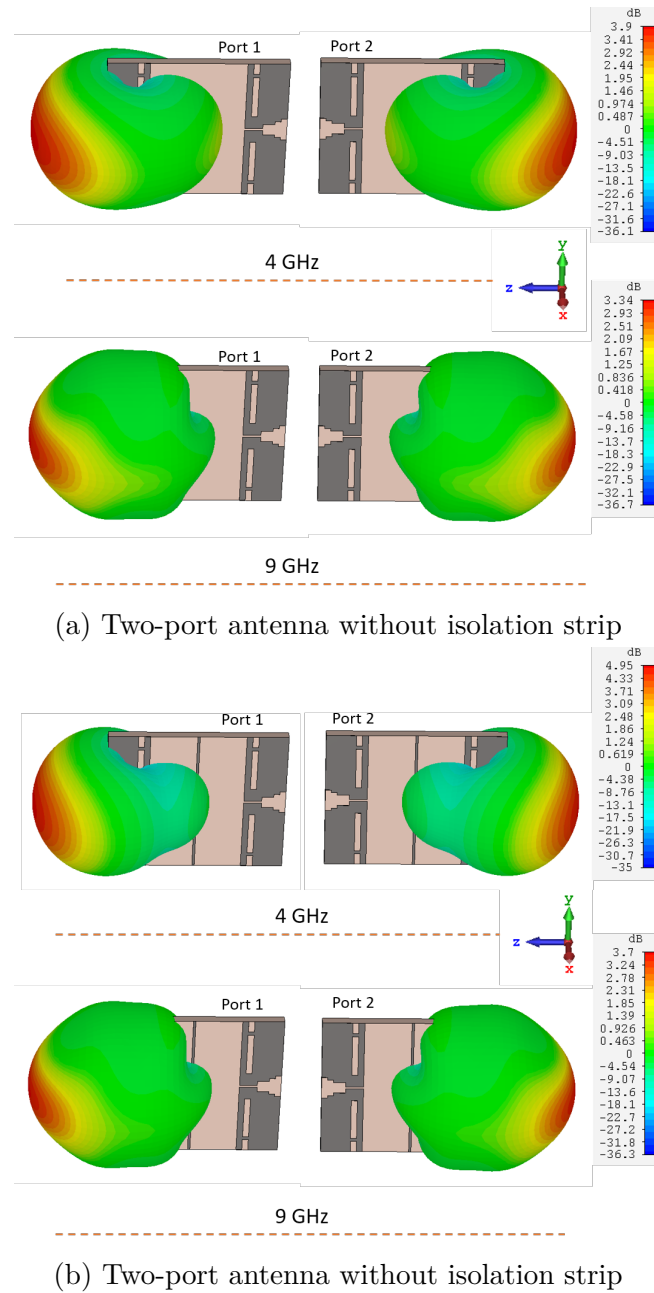
Fig. 5.9 Simulated 3D radiation pattern at 4 GHz & 9 GHz for each port excitation; $L = 25$mm, $W = 30$mm, $G = 16$mm, $W_S = 0.4$mm

out the range of operation of the isolation strip and its behaviour as a reflector. Moreover, the radiation patterns of the two ports are 180° out-of phase with each other, thus achieving angle diversity within the two-port antenna structure.
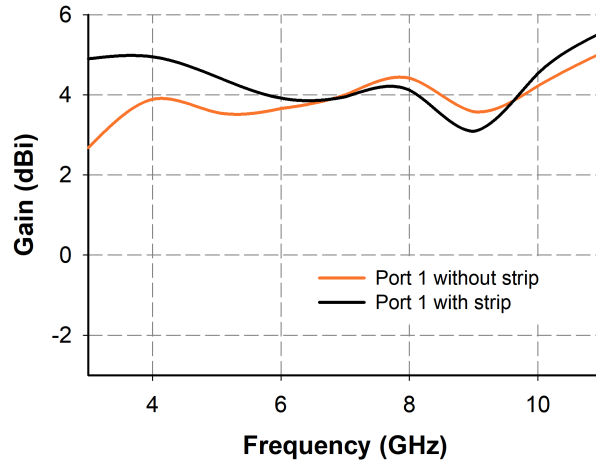
Fig. 5.10 Simulated Gain of two-port UWB-MIMO antenna with and without strip; $L = 25$mm, $W = 30$mm, $G = 16$mm, $W_S = 0.4$mm

5.1.1 Experimental Results

A prototype of the two-port UWB-MIMO antenna is shown in Fig. 5.11 which is fabricated using the optimized dimensions of antenna as in Fig. 5.4. The radiation characteristics of the antenna is then measured, and for the analysis of one port all the other ports are terminated with matched load.
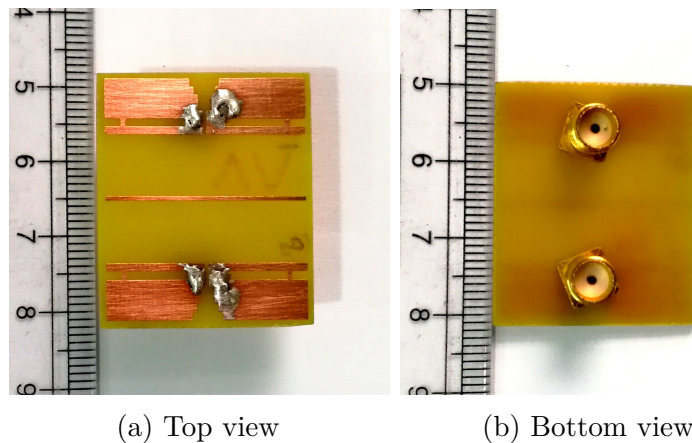
(a) Top view   (b) Bottom view

Fig. 5.11 Prototype of the two-port UWB-MIMO antenna; $L = 25$mm, $W = 30$mm, $G = 16$mm, $W_S = 0.4$mm

(a) Without isolation strip

(b) With isolation strip
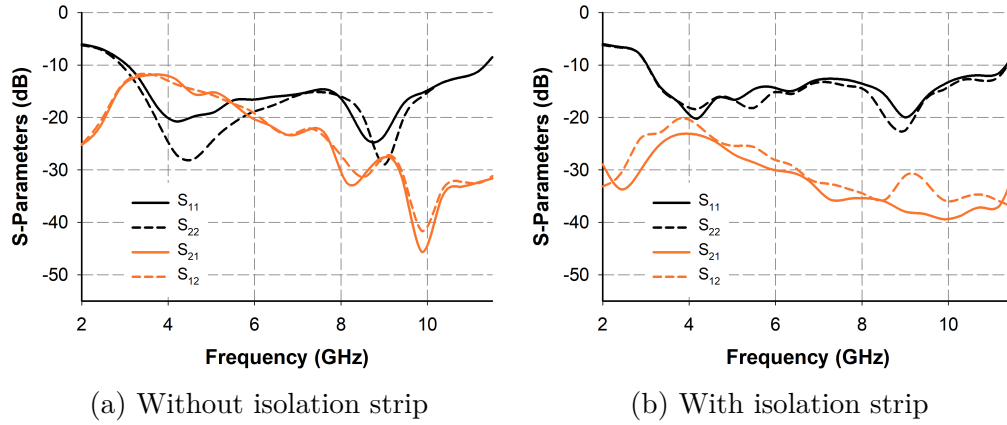
Fig. 5.12 Measured s-parameters of the two-port UWB-MIMO antenna with and without strip; $L = 25$mm, $W = 30$mm, $G = 16$mm, $W_S = 0.4$mm

The measured S-parameters of the two-port antenna with and without the decoupling strip are compared and is depicted in Fig. 5.12. The enhancement in isolation for the antenna with decoupling strip is observed in the figure (refer Fig. 5.12b). The measured reflection coefficients of Fig. 5.12b show that the optimized antenna has a 2:1 VSWR bandwidth from 3.1 to 11.3 GHz for both the ports, thus satisfying the impedance matching requirements for UWB systems specified by FCC. It is also noticed from the figure that, the antenna posses an excellent isolation throughout the UWB band with a minimum and maximum isolation of 22 dB and 41 dB, respectively, which makes them suitable for UWB-MIMO operation. The simulated and measured results are in good agreement with each other and the slight discrepancies are due to their fabrication tolerances.

The Fig. 5.13 shows the simulated and measured radiation patterns of two-port UWB-MIMO antenna for both port excitation (Ant1 & Ant2), at 4 & 9 GHz over $\phi = 0°$ (X-Z) plane & $\theta = 90°$ (X-Y) plane. Here, E_ϕ and E_θ represents the ϕ and θ components of the E-field pattern along a particular plane, respectively. On comparing the patterns of Ant1 and Ant2 at $\phi = 0°$ plane, it is clear that the antenna possess angle diversity in its radiation patterns as they are appeared to be spatially shifted by 180°. The polarization isolation values of the two-port antenna is summarized in Table 5.1, for two principle planes of the antenna and for two different frequencies. The polarization purity of an antenna element is calculated by taking the difference of power levels (in dB) of ϕ and θ

components along the plane of interest and in the direction of propagation, for a single frequency. It is observed from the table that the polarisation isolation of both antenna-elements stood above 23 dB along $\phi = 0°$ plane and above 20 dB along $\theta = 90°$ plane, in the UWB region. On comparing the power level

(a) At $\phi = 0°$ (X-Z) Plane

(b) At $\theta = 90°$ (X-Y) Plane
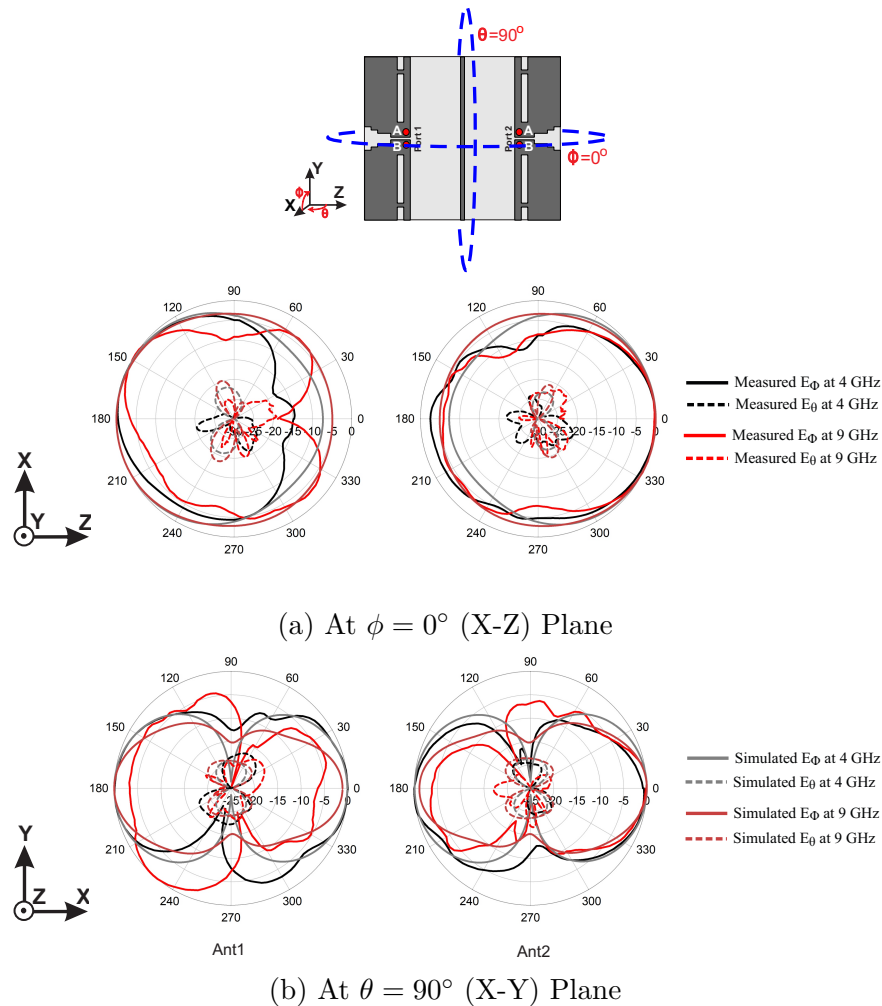
Fig. 5.13 2D Radiation Pattern of two-port UWB MIMO antenna for 4 GHz & 9 GHz; $L = 25$mm, $W = 30$mm, $G = 16$mm, $W_S = 0.4$mm

differences along a plane of a single antenna-element for different frequencies, it is found that, the values doesn't differ much showing the polarization stability of the antenna for a frequency band of interest. Thus, the two-port UWB-MIMO antenna attained excellent polarization purity and have stable polarizations in

Table 5.1 Polarization Isolation of two-port antenna (values in dB); $L = 25$mm, $W = 30$mm, $G = 16$mm, $W_S = 0.4$mm

Freq.	$\phi = 0°$ (X-Z) Plane		$\theta = 90°$ (X-Y) Plane	
	Ant1	Ant2	Ant1	Ant2
4 GHz	23.63	24.13	22.94	25.25
9 GHz	27.73	23.13	20.34	21.22

the 3.1-10.6 GHz band of UWB operation, which contributes a well defined pulse response across the frequency band.

(a) Gain
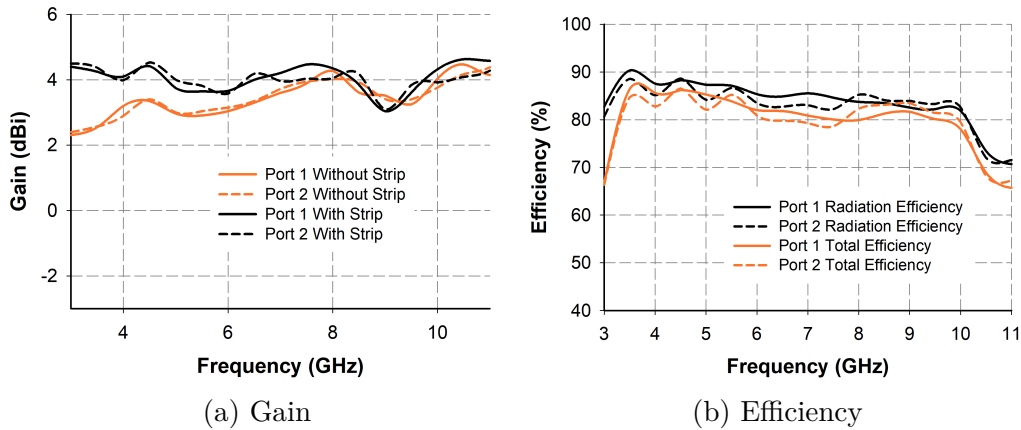
(b) Efficiency

Fig. 5.14 Measured gain and efficiency for each elements of two-port UWB-MIMO antenna; $L = 25$mm, $W = 30$mm, $G = 16$mm, $W_S = 0.4$mm

A comparison of the measured peak gain of the two-port antenna with and without reflector, for both port excitation, is depicted in Fig. 5.14a. The increase in peak gain for lower UWB band (3.1 - 7.5 GHz), for the antenna with isolation strip, is seen in the figure. The antenna with strip showed an increase in gain of 1 dBi at 4 GHz as compared to the gain of antenna without strip. Thus, the two-port UWB-MIMO antenna with isolation strip exhibits a stable gain across the 3.1-10.6 GHz band with an average gain of 4.1 dBi for both the ports. The radiation efficiency (η_{rad}) of the 2-port UWB MIMO antenna is measured using the Schantz's Wheeler Cap method, with one port excited and the other port is matched with 50Ω load. From radiation efficiency, the total efficiency (η_{tot}) is

calculated and both are plotted against frequency in Fig. 5.14b. It is understood from the figure that the antenna elements have a good impedance matching and high isolation, because the discrepancies in η_{rad} and η_{tot} are less. The two-port antenna offers an average radiation efficiency better than 83% in theUWB band of operation, for both the ports.

5.2 The Three-port UWB-MIMO antenna

In a three-port MIMO antenna there will be three antenna-elements co-located on to single piece of substrate and are isolated to each other for their seamless performance. Here, in this thesis the two UWB antennas discussed in Chapter 4 are utilized as the antenna-elements to make a three-port UWB-MIMO antenna.

We have seen a two-port UWB-MIMO antenna in the previous section of this chapter (Section 5.1), using two UWB-I antennas and an isolation strip between them. To make a three-port UWB-MIMO antenna the isolation strip of two-port antenna is replaced with another UWB antenna (i.e., the third antenna-element). Here, the UWB-II of chapter 4 is used as the third antenna-element. The antenna configuration of such a three-element UWB-MIMO antenna is shown in Fig. 5.15a and its corresponding simulated S-parameters are plotted in Fig. 5.15b. The optimized dimensions of UWB-I and UWB-II (listed in Table 4.2 and Table 4.8, respectively) are taken for the designing of antenna-elements. The space between Ant1 (port1) and Ant2 (port2) are kept as G=16mm itself, as for two-port antenna. The third-element Ant3 (port3) is placed between them, at a distance of $w_1 = w_2$=3mm from Ant1 and Ant2, as shown in Fig. 5.15a. Thus, the overall size of the three-port antenna remained same as that of two-port (25mm×30mm).

The simulated S-parameters plot in Fig. 5.15b shows the reflection (S_{11}, S_{22} & S_{33}) and transmission (S_{21}, S_{31} & S_{23}) coefficients of the three port UWB-MIMO antenna. The isolation between Ant1 & Ant2 (S_{21}) is excellent at higher UWB band because of sufficient port-to-port distance between them. However, the isolation of them at lower frequency band is more than 15 dB, which is a fairly good score, due to the presence of conducting patches of Ant3 between Ant1 & Ant2. The radiation pattern of Ant3 (UWB-II) is found to be directive towards the smaller conducting patch of it (here, towards port2 in the three-port antenna), as discussed in Chapter 4 (Section 4.2). This made the isolation between Ant2 &

(a) Antenna geometry
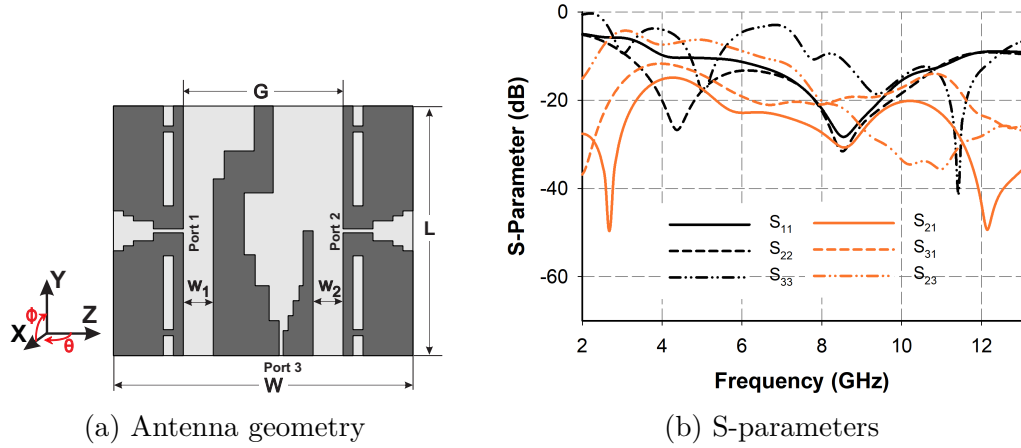
(b) S-parameters

Fig. 5.15 Design of a three-port antenna and its simulated s-parameters; $L = 25$mm, $W = 30$mm, $G = 16$mm, $w_1 = w_2 = 3$mm

Ant3 (S_{23}) so poor of about 5 dB in the UWB band, which is not at all acceptable for a MIMO performance. The mutual coupling between Ant1 & Ant3 is also large due to the insufficient spacing between them, thus having an isolation (S_{31}) of 10 dB only. The presence of large conducting patch of Ant3 deteriorated the impedance curve of Ant1 (S_{11}) due to the electromagnetic coupling between them, as shown in Fig. 5.15a. Thus, it failed to cover the required bandwidth for UWB systems. However, Ant2 (S_{22}) managed to have good impedance coverage favourable for the UWB systems. Due to the lack of enough space between the antenna elements the 2:1 VSWR impedance bandwidth of Ant3 (S_{33}) is also very poor.

In order to overcome these drawbacks of inter-element spacing, the G (spacing between Ant1 & Ant2) of three-port antenna is increased to 31mm and the modified geometry is depicted in Fig. 5.16a. Thus, the overall size of the antenna became L=25mm$\times W$=45mm, with $w_1 = w_2$=10.5mm. The simulated reflection (S_{11}, S_{22} & S_{33}) and transmission (S_{21}, S_{31} & S_{23}) coefficients of the modified structure are shown in Fig. 5.16b. It is observed from the figure that all the antenna-elements covered the required impedance bandwidth for UWB operation, because of the adequate spatial separation between them. This three-port MIMO antenna has a good isolation of 20 dB between Ant1 & Ant2 (S_{21}) as they are spatially well-separated. The isolation enhancement in most of the UWB band

(a) Antenna geometry
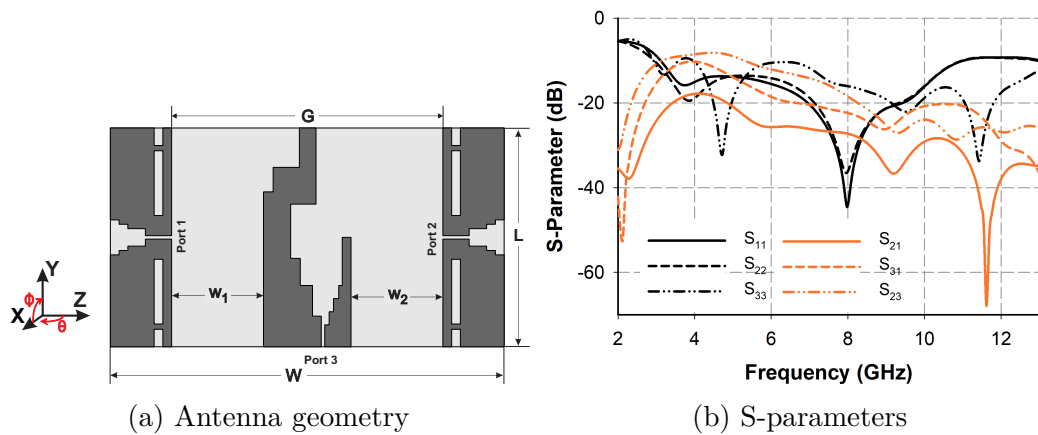
(b) S-parameters

Fig. 5.16 Design of a three-port antenna with increased separation and its simulated s-parameters; $L = 25$mm, $W = 45$mm, $G = 31$mm, $w_1 = w_2 = 10.5$mm

(4.5-10.6 GHz) is due to their enough port-to-port distance, which is greater than $0.5\lambda_0$. Whereas, the improvement in isolation for lower frequencies from 3.1 GHz to 4.5 GHz is due to the presence of conducting patches between Ant1 & Ant2, which attenuates the coupling between them. But, the antenna exhibits poor
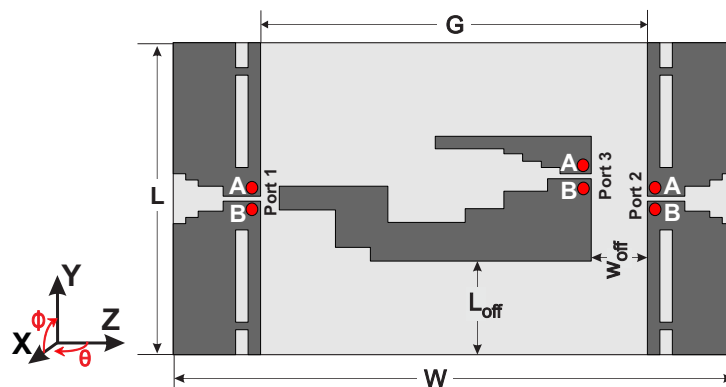
Fig. 5.17 Geometry of three-port UWB-MIMO antenna; $L = 25$mm, $W = 45$mm, $G = 31$mm, $L_{off} = 7.5$mm, $W_{off} = 4.5$mm

isolation between Ant3 & 2 (S_{23}) and Ant1 & 3 (S_{31}), of the order of 9 dB and 11 dB, mainly in the lower UWB band. This is due to the polarization dependency of Ant3 on Ant1 & Ant2. This drawback can be vanquished by increasing the
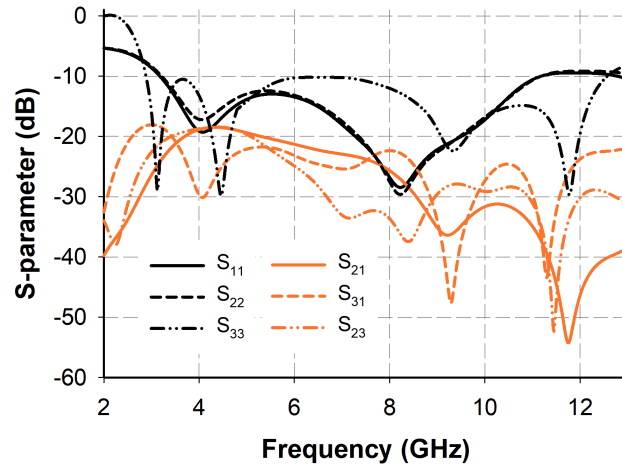
Fig. 5.18 Simulated s-parameters of the three-port UWB-MIMO antenna; $L = 25$mm, $W = 45$mm, $G = 31$mm, $L_{off} = 7.5$mm, $W_{off} = 4.5$mm

G further, but this is not advisable for the design of compact MIMO antennas. Another solution to this problem is to make the third element in a different polarization from Ant1 & Ant2. This can be accomplished by placing UWB-II (Ant3) in such a way that its polarization becomes orthogonal to that of Ant1 & 2, as shown in Fig. 5.17.

Here, the overall dimension $L \times W$ of three-port antenna and separation between Ant1 & 2 G is kept same as before as, 25mm × 45mm and 31mm, respectively. The third antenna element, Ant3 (UWB-II) is placed at an offset of $W_{off} = 4.5$mm from Ant2 and $L_{off} = 7.5$mm from the bottom of the antenna, as shown in Fig. 5.17. The simulated s-parameters of the three-port structure is plotted in Fig. 5.18. It is clear from the reflection coefficients (S_{11}, S_{22} & S_{33}) that all the antenna elements covered the 2:1 VSWR bandwidth from 3.1 to 10.6 GHz for UWB communication systems. The isolation between all the elements (S_{21}, S_{31} & S_{23}) stood above 20 dB throughout the operation bandwidth. Thus, this configuration helped to attain good UWB-MIMO impedance performance and the optimized values of the antenna are $L = 25$mm, $W = 45$mm, $G = 31$mm, $L_{off} = 7.5$mm, $W_{off} = 4.5$mm. The red dots 'A' and 'B' in Fig. 5.17 represents the outer and inner conductors of the coaxial connector used to feed the antenna, respectively. Ant 1 & Ant 2 are excited in its normal dipole mode and are

polarised along Y direction, while Ant 3 has a polarisation along -Z direction. All the three antenna elements are printed on the same side of a FR-4 substrate with relative permittivity ϵ_r of 4.3, loss tangent $tan(\delta)$ of 0.02 and thickness h of 1.588 mm. The planes corresponding to $\phi = 0°$ (X-Z) & $\theta = 90°$ (X-Y) represents the two principal planes for the three-port UWB-MIMO antenna for all far-field measurements.
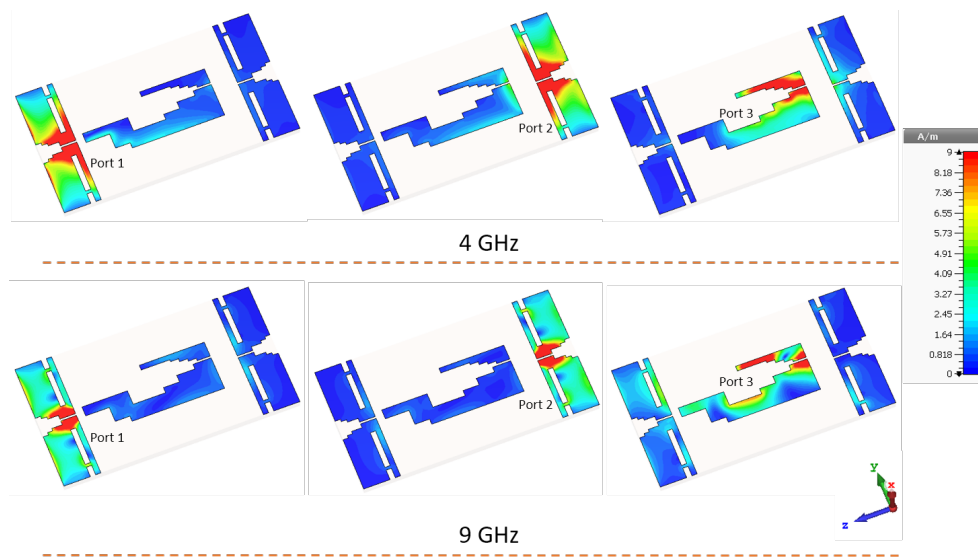
Fig. 5.19 Surface current distribution at 4.5 GHz & 8.5 GHz for each port excitation; $L = 25$mm, $W = 45$mm, $G = 31$mm, $L_{off} = 7.5$mm, $W_{off} = 4.5$mm

The enormous flow of surface current from the excited port to other ports is the main cause behind mutual coupling between adjacent antenna elements and hence poor isolation between them. Fig. 5.19 illustrates the simulated current distribution of three-port antenna, at 4 GHz & 9 GHz for the excitation of each port. It is observed from the figure that the flow of current from one port to other ports is reduced significantly and hence prevented the coupling of electromagnetic energy among the elements. In this three-port UWB MIMO antenna this surface current migration is controlled by incorporating three MIMO antenna diversity techniques : spatial, polarization and angle diversity.

The back-to-back arrangement of Ant1 & Ant2 with a spatial separation of G=31mm to attain the port-to-port distance of greater than $0.5\lambda_0$ for 4.5-10.6 GHz frequency band, is the spatial diversity in this MIMO antenna. The
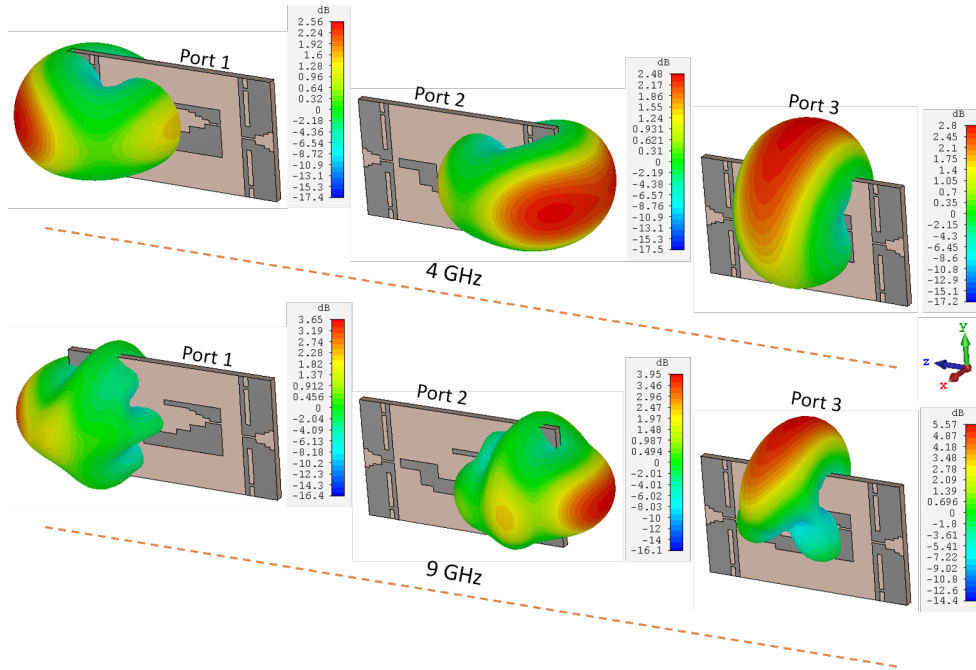
Fig. 5.20 Simulated 3D radiation pattern at 3.9 GHz & 9.3 GHz for each port excitation; $L = 25$mm, $W = 45$mm, $G = 31$mm, $L_{off} = 7.5$mm, $W_{off} = 4.5$mm

placement of Ant3 in orthogonal to Ant1 & Ant2, thus making the polarization of Ant3 along -Z direction and that of Ant1 & 2 along Y direction is the realization of polarization diversity in the antenna structure. The back-to back configuration of Ant1 & 2 and the presence of conducting patches of Ant3 between them , made the radiation pattern of Ant1 and Ant2 to be directive to 180° and 0° in the $\phi = 0°$ plane, respectively. This can be seen in the simulated 3D radiation pattern of three-port UWB-MIMO antenna in Fig. 5.20. Figure shows the pattern orientation of each antenna elements for the respective port excitation, for 3.9 GHz and 9.3 GHz. Moreover, the field pattern of Ant3 is slightly directive towards the 90° in the $\theta = 90°$ plane, due to the radiation behaviour of UWB-II. Thus, the three-port antenna attained angle diversity within its structure by having the patterns of three antenna elements to three different directions, as seen in Fig. 5.20.

(a) Top view   (b) Bottom view
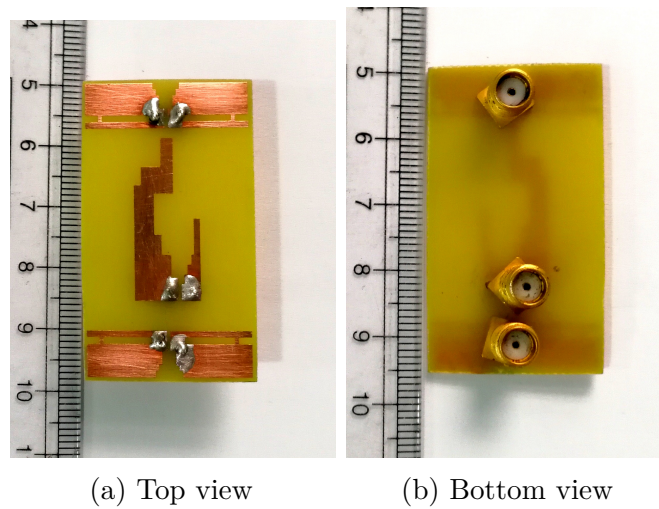
Fig. 5.21 Prototype of the three-port UWB-MIMO antenna; $L = 25$mm, $W = 45$mm, $G = 31$mm, $L_{off} = 7.5$mm, $W_{off} = 4.5$mm
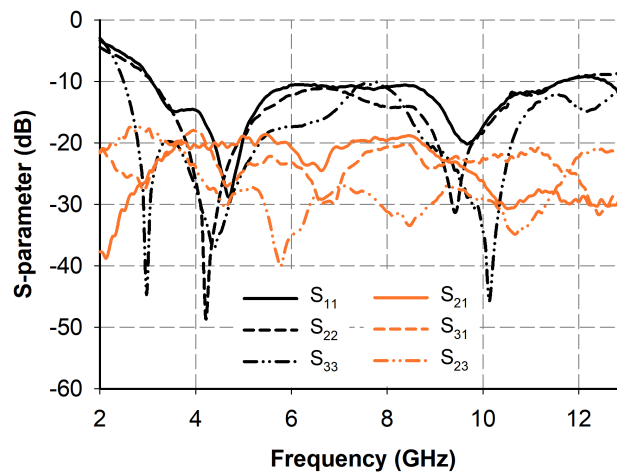
Fig. 5.22 Measured S-parameters of the three-port UWB-MIMO antenna; $L = 25$mm, $W = 45$mm, $G = 31$mm, $L_{off} = 7.5$mm, $W_{off} = 4.5$mm

5.2.1 Experimental Results

The three-port antenna in Fig. 5.17 is fabricated with the optimized dimensions and is verified practically for its radiation performances. A photograph of the fabricated structure is shown in Fig. 5.21. All the measurements for one port of

the antenna are conducted by terminating the other ports by matched load of 50Ω.

The measured S-parameters of the three-port antenna is shown in Fig. 5.22. It is observed from the figure that, the antenna exhibits a 2:1 VSWR impedance bandwidth from 3.1 to 11.3 GHz for all ports, thus covering the required bandwidth for UWB operation. This three-element antenna offers an isolation above 19.5 dB, 19 dB and 20 dB between Ant1 & 2 (S_{21}), Ant1 & 3 (S_{31}) and Ant3 & 2 (S_{23}) in the UWB band, respectively.

Fig. 5.23 shows the measured radiation patterns of three-port UWB-MIMO antenna for all the port excitation, at 4 GHz and 9 GHz over $\phi = 0°$ (X-Z) plane and $\theta = 90°$ plane. The planes at which measurements are taken are drawn on the antenna geometry and is shown above the plots of radiation patterns (see Fig. 5.23). On comparing the patterns it is found that Ant1 and Ant2 is directed towards 180° and 0° in the $\phi = 0°$ plane, respectively. While pattern of Ant3 is directed towards the 90° in the $\theta = 90°$ plane. This confirms the presence of angle diversity in the three-port antenna structure, due to its tri-directional radiation pattern. The polarization isolation of all antenna-elements in the three-port

Table 5.2 Polarization Isolation of three-port antenna (values in dB); $L = 25$mm, $W = 45$mm, $G = 31$mm, $L_{off} = 7.5$mm, $W_{off} = 4.5$mm

Freq.	$\phi = 0°$ (X-Z) Plane			$\theta = 90°$ (X-Y) Plane		
	Ant1	Ant2	Ant3	Ant1	Ant2	Ant3
4 GHz	24.78	21.54	-27.9	21.76	26.33	-27.06
9 GHz	20.14	20.52	-20.3	19.86	22	-20.47

antenna is summarized in Table 5.2, for $\phi = 0°$ & $\theta = 90°$ planes at two different frequencies. It is noticed from the table that the polarization isolation for Ant1 is >19 dB, Ant2 is >20 dB and Ant3 is >20 dB in both the planes. This shows that the antenna has good polarization purity between ϕ and θ field components, for a particular antenna element. It is noticed that the isolation values for Ant3 are negative as compared to that of Ant1 and Ant2. This is because in both planes the ϕ component is dominant over θ component for Ant1 and Ant2, whereas θ component is dominant for Ant3. Thus the field components are complement to

(a) At $\phi = 0°$ (X-Z) Plane

(b) At $\theta = 90°$ (X-Y) Plane
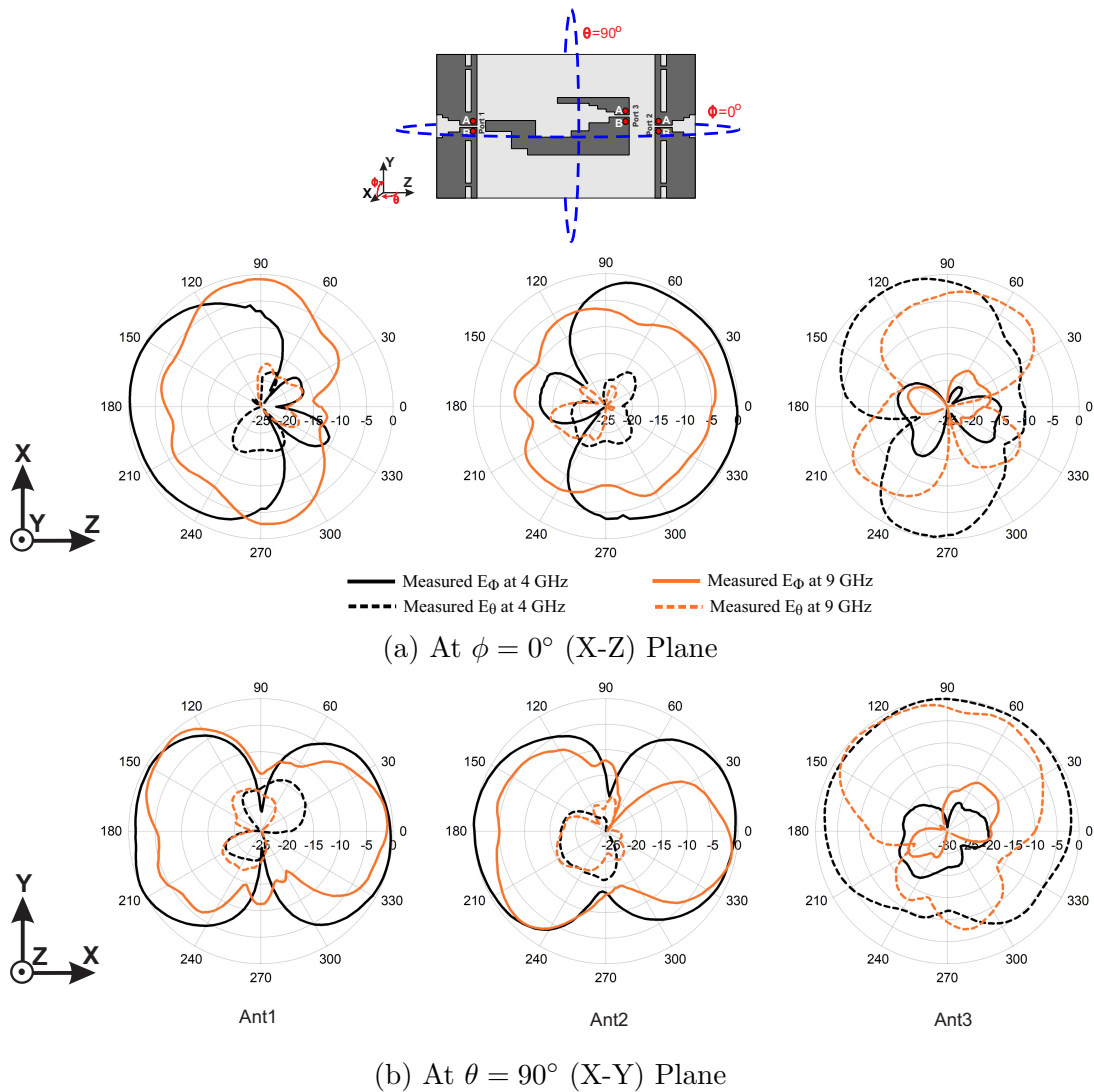
Fig. 5.23 2D Radiation Pattern of three-port UWB-MIMO antenna for 4 GHz & 9 GHz; $L = 25$mm, $W = 45$mm, $G = 31$mm, $L_{off} = 7.5$mm, $W_{off} = 4.5$mm

each other for Ant1 & 2 and Ant3 in both the planes. This shows that Ant3 is orthogonally polarized from that of Ant1 (and Ant2), which fulfils the polarization diversity in the antenna. In addition to this, the power level differences of single antenna-element along a particular plane shows only considerable variations for different frequencies. Thus, the antenna gained polarization stability which is required for good pulse handling capability.
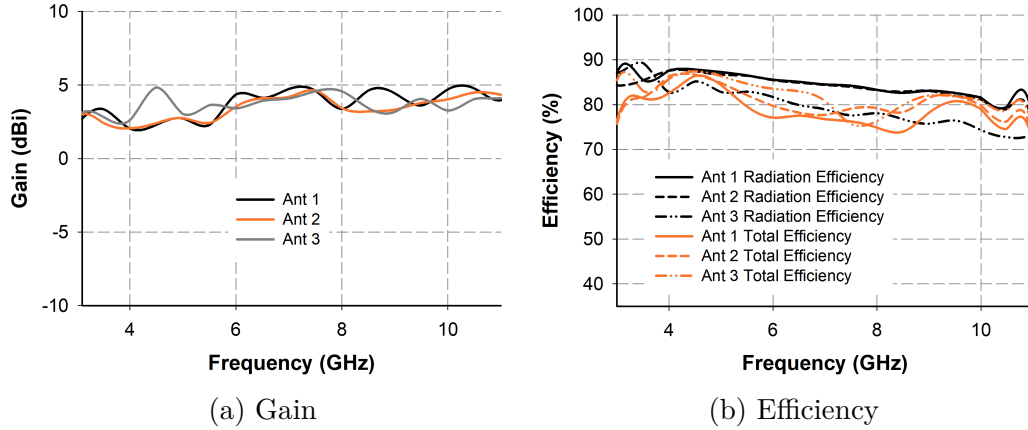
(a) Gain   (b) Efficiency

Fig. 5.24 Measured gain and efficiency of the each elements of three-port UWB-MIMO antenna; $L = 25$mm, $W = 45$mm, $G = 31$mm, $L_{off} = 7.5$mm, $W_{off} = 4.5$mm

The peak gain of the antenna across the operating band, measured according to the gain comparison method, is shown in Fig. 5.24a. The antenna exhibits stable gains across the UWB band, which makes it suitable for practical UWB applications. The radiation efficiency (η_{rad}) of each antenna element is measured using the Schantz's Wheeler Cap method and the corresponding total efficiency (η_{tot}) is calculated from η_{rad} and both are plotted in Fig. 5.24b. The antenna exhibits an average gain of 3.65 dBi, 3.35 dBi & 3.64 dBi for Ant1, Ant2 & Ant3 and radiation efficiency better than 72% across the UWB band, respectively

5.3   The Four-port UWB-MIMO antenna

To realize a four-port UWB-MIMO antenna four UWB antennas need to be co-located on to a single piece of substrate, with adequate inter-element isolations. In this thesis, four UWB-I antennas are utilized to accomplish the quad-element antenna. The dimensions for antenna-elements are taken as in Table 4.2. Here, two antenna-elements are arranged in the back-to-back configuration along Z-direction (as in two-port UWB-MIMO antenna), while the other two antenna-elements are in back-to-back to each other along Y-direction. The spatial separation (G) between antenna elements along the axis is kept as 29mm in order to isolate

those elements properly and also to have the sufficient space needed for the other two antenna-elements. The arrangements of four UWB-I elements Ant1,

(a) Antenna geometry

(b) S-parameters
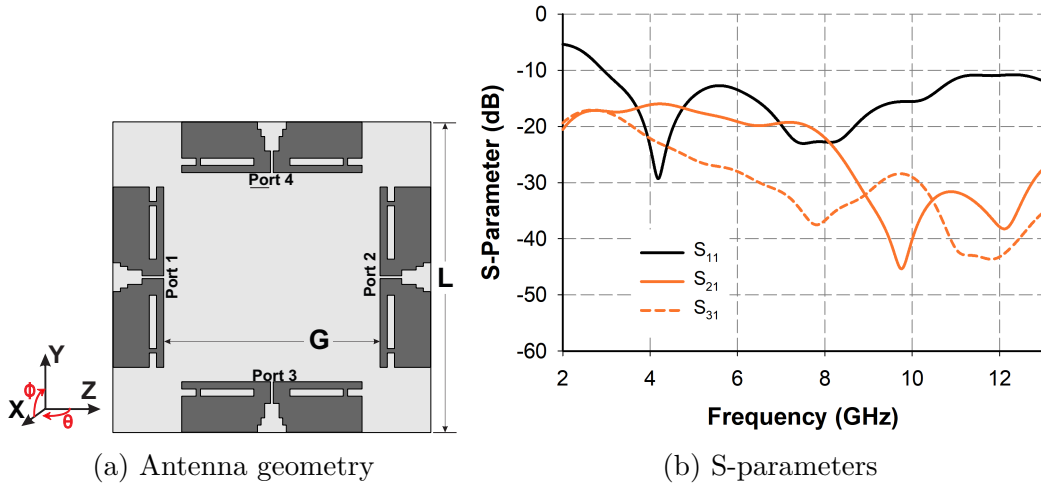
Fig. 5.25 A four-element UWB-MIMO antenna with $L = 43$mm, $G = 29$mm

Ant2, Ant3 & Ant4, corresponding to the port 1, port 2, port 3 & port 4, on to a substrate of $43mm \times 43mm$ is shown in Fig. 5.25a. Ant3 & Ant4 are placed adjacent to Ant1 & Ant2, in an orthogonal way to attain polarization of Ant1 & Ant2 along Y-direction and that of Ant3 & Ant4 along Z-direction. The simulated S-parameters of the four-port antenna are shown in Fig. 5.25b. Here, only the curves of S_{11}, S_{21} & S_{31} are plotted because of the structural symmetry. Due to this symmetry, it is verified and found that $S_{11}=S_{22}=S_{33}=S_{44}$, $S_{21}=S_{43}$ & $S_{31}=S_{41}=S_{32}=S_{42}$. It is noticed from the figure that the 2:1 VSWR impedance bandwidth of the antenna-elements covers the required 3.1-10.6 GHz frequency bandwidth for UWB operation with an excellent isolation better than 20 dB between Ant1 & Ant3 (S_{31}). This high isolation is due to the orthogonal polarization of Ant1 & Ant3. But, the isolation between Ant1 & Ant2 (S_{21}) is less than 20 dB for the lower UWB band, whereas in higher band they show excellent isolation. This low isolation in lower band is due to the high mutual coupling between Ant1 & Ant2 because of the insufficient port-to-port distance ($<0.5\lambda_0$). This will be the same case for Ant3 & Ant4, since $S_{21}=S_{43}$.

This high mutual coupling can be reduced by placing a reflector of $25mm \times 0.4mm$ between the antenna-elements, as done for the case of two-port UWB-

MIMO antenna. Since this problem lies for both S_{21} (Ant1 & 2) and S_{43} (Ant3 & 4) two reflectors must be added into the structure. Thus the reflector appears to be in the shape of a cross $(+)$ at the middle of the antenna structure. The
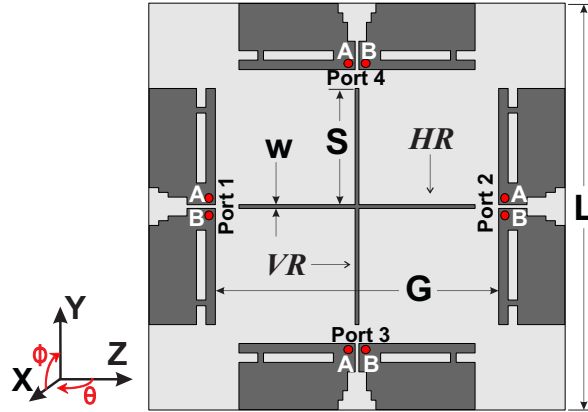
Fig. 5.26 Geometry of four-port UWB-MIMO antenna; $L = 43$mm, $G = 29$mm, $W = 0.4$mm, $S = 12.3$mm
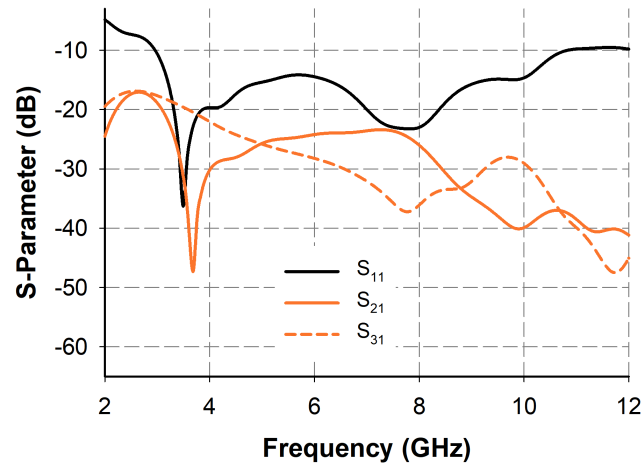
Fig. 5.27 Simulated s-parameters of quad-element UWB-MIMO antenna; $L = 43$mm, $G = 29$mm, $W = 0.4$mm, $S = 12.3$mm

modified four-port antenna with cross-shaped reflector is shown in Fig. 5.26. As seen from the geometry, this reflector has two parts: Vertical Reflector (VR) and Horizontal Reflector (HR). The VR helps in the isolation between Ant1 & Ant3 whereas, HR favours Ant3 & Ant4 to be isolated. The simulated S-parameters

of the four-port antenna with cross-reflector is shown in Fig. 5.27. It is observed from the figure that, the mutual coupling between Ant1 & Ant2 is reduced at lower UWB band also, as the isolation curve S_{21} between elements 1 & 2 went down keeping the isolation to be better than 25 dB in the whole UWB band. The S_{31} remained same, as the reflector does not influence the mutual coupling between Ant1 & Ant3. Thus, the antenna geometry in Fig. 5.26 is a good candidate for a 4×4 UWB-MIMO communication system. The optimized dimensions of the antenna are L=43mm, G=29mm, S=12.3mm, W=0.4mm. The four antenna elements and the cross-shaped decoupler is printed on the front side of a $0.43\lambda_0 \times 0.43\lambda_0 \times 0.016\lambda_0$ (at 3.1 GHz) FR-4 substrate with relative permittivity ϵ_r of 4.3 and loss tangent $tan(\delta)$ of 0.02. The connections of outer (A) and inner (B) conductors of the coaxial connectors to the corresponding antenna-elements are denoted in the figure in red dots. The two principal planes of the four-port antenna are defined at $\phi = 0°$ (X-Z) plane and $\theta = 90°$ (X-Y) plane for all far-field measurements.
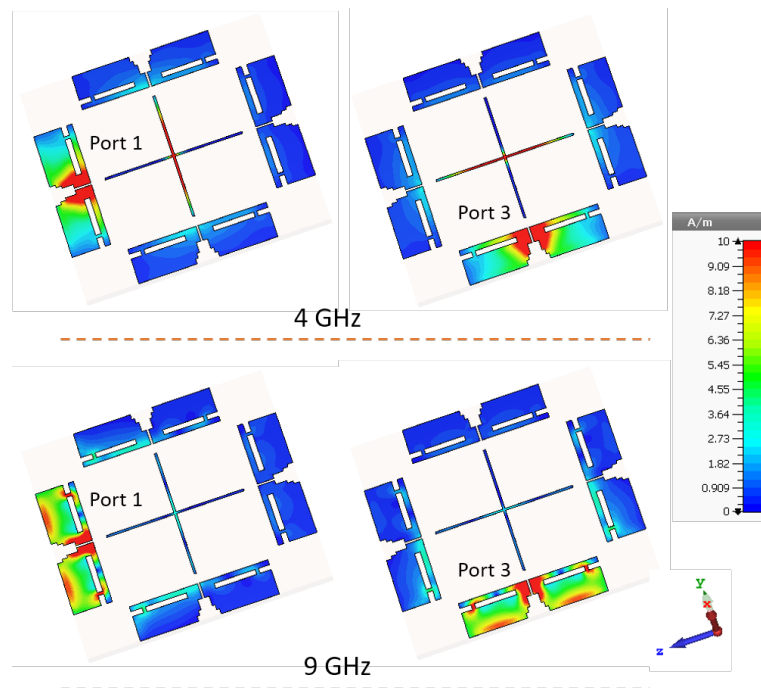
Fig. 5.28 Surface current distribution at 4.8 GHz & 9.6 GHz for excitation of port 1 and port 3; $L = 43$mm, $G = 29$mm, $W = 0.4$mm, $S = 12.3$mm

Thus, in the optimized geometry of four-port UWB-MIMO antenna, the following three physical mechanisms work together to expedite the high isolation between the antenna elements.

1. The antenna elements Ant1 and Ant2 are arranged in a back-to-back configuration, separated by a distance of G, along the Z-axis. Similarly, Ant3 and Ant4 are configured back-to-back along the Y-axis. Thus the antenna elements along the axes are physically separated from one another which helps to attain spatial diversity within the geometry, which enabled high isolation between them. However, this mechanism fails to work for 3-5 GHz, as the port-to-port distance (G) at this frequency range is less than $0.5\lambda_0$. So, mutual coupling will be greater for these frequencies.

2. To reduce the mutual coupling for 3-5 GHz, a cross-shaped reflector is placed at the center of the antenna, which is a combination of two reflectors: V R & HR. This acts as an isolating structure for antenna elements for 3-5 GHz. We know that the inter-element coupling mainly occurs due to the transfer of surface current from the excited port to the other ports. So, the surface current distribution of the antenna for 4 GHz & 9 GHz, when port 1 & 3 are individually excited, are shown in Fig. 5.28. It is observed from the figure that, VR attenuates the migration of surface current between Ant1 and Ant2 only, while HR attenuates that of Ant3 and Ant4. This is because, the current vectors in the HR get cancelled out when Ant1 or Ant2 is excited. This is shown in the Fig. 5.29, which is the vector current
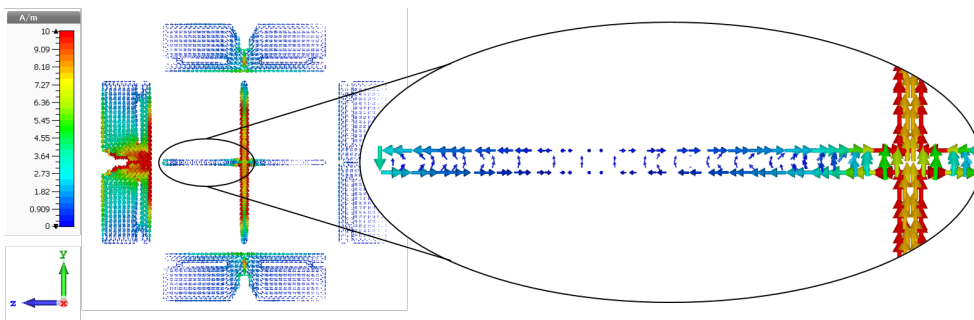
Fig. 5.29 Vector surface current distribution on four-port UWB-MIMO antenna for excitation of port1 at 4.5 GHz; $L = 43$mm, $G = 29$mm, $W = 0.4$mm, $S = 12.3$mm

distribution at 4.5 GHz while exciting the Ant1. It is noted that the current vectors on the edges of HR is opposite to each other, which will be cancelled out thus making that reflector to be inactive. Similarly, VR has no effect when Ant3 or Ant4 is excited. Thus we can say that VR & HR serve as reflectors for Ant1 & 2 and Ant3 & 4, respectively. This concept is derived from the fact that, a properly spaced (0.10-0.25λ_g, where λ_g is the guided wavelength at resonant frequency) metal conductor with same length or slightly greater than that of the driven element will act as a reflector [22]. Here, the VR and HR individually is made 5% longer than the resonant length (for 3.1-5 GHz) of the antenna elements. Fig. 5.28 points out that the influence of the cross-shaped reflector on surface current distribution, and so on the isolation, is significant for 4.8 GHz and negligible for 9.6 GHz, denoting its operation as a reflector for lower frequencies.

3. The Ant3 (or Ant4) is orthogonal to Ant1 (or Ant2), as shown in Fig. 5.26. This makes the Ant1 & Ant2 to be polarized along Y-direction and Ant3 & Ant4 to be polarized along Z-direction, which reduces the mutual coupling between adjacent elements (Ant1 & 3) throughout the UWB band since each antenna-element has a stable polarization across their operation bandwidth. This denotes the polarization diversity of the UWB-MIMO antenna.

Basically, each antenna element of the quad-element structure has an omni-directional coverage for lower UWB band and slightly directional coverage for higher frequencies, in the $\phi = 0°$ plane. But, due to the presence of cross-shaped reflector in the middle of antenna structure, each antenna elements exhibit directional radiation pattern in the entire UWB band. For the lower frequencies, VR points the main beam of Ant1 & 2 along the negative and the positive Z-axis, respectively. While, HR directs the main beam of Ant3 & 4 along the negative and the positive Y-axis, respectively. Hence, the quad-element antenna can realize the angle diversity in its radiation patterns, for the whole UWB bandwidth. Fig. 5.30 shows the simulated 3D radiation patterns for all ports at 4 & 9.5 GHz. The figure clearly depicts the angle diversity between the ports, as all the patterns of antenna elements are directed to four different direction, for their respective frequencies.
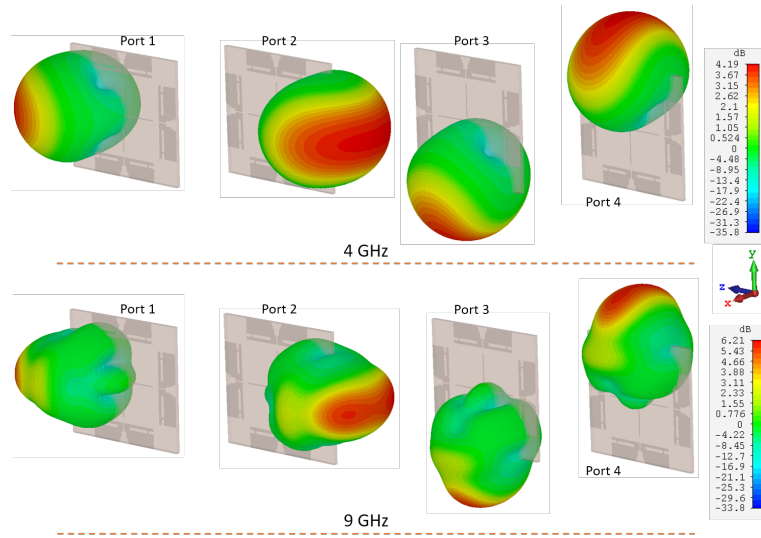
Fig. 5.30 Simulated 3D radiation pattern at 4 GHz & 9.5 GHz for each port excitation; $L = 43$mm, $G = 29$mm, $W = 0.4$mm, $S = 12.3$mm

Thus, the four-port UWB MIMO antenna attained a good inter-element isolation over the entire operation band because of the spatial separation of the elements along with the presence of cross-shaped reflector (for oppositely placed antenna-elements) as well as the orthogonal polarization of adjacent antenna elements.

5.3.1   Experimental Results

The quad-element antenna in Fig. 5.26 is fabricated with the optimized dimensions and is validated experimentally for its performances. A photograph of the fabricated structure is shown in Fig. 5.31. All the measurements for one port of the antenna are conducted by terminating the other ports by 50Ω matched load.

The measured and simulated s-parameters of the four-port antenna are shown in Fig. 5.32. It is observed from the figure that, the antenna exhibits a 2:1 VSWR impedance bandwidth from 3.1 to 11 GHz for all ports with a fractional bandwidth of 114%, thus covering the required bandwidth for UWB operation. This quad-element antenna offers an isolation above 20 dB between both oppositely and adjacently placed antenna elements, throughout the bandwidth of operation. The simulated and measured results agree well with each other in the band of interest.

(a) Top view   (b) Bottom view
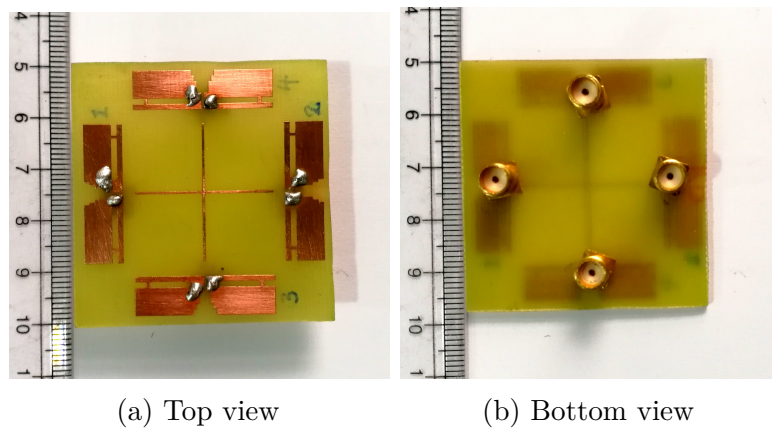
Fig. 5.31 Prototype of the four-port UWB-MIMO antenna; $L = 43$mm, $G = 29$mm, $W = 0.4$mm, $S = 12.3$mm
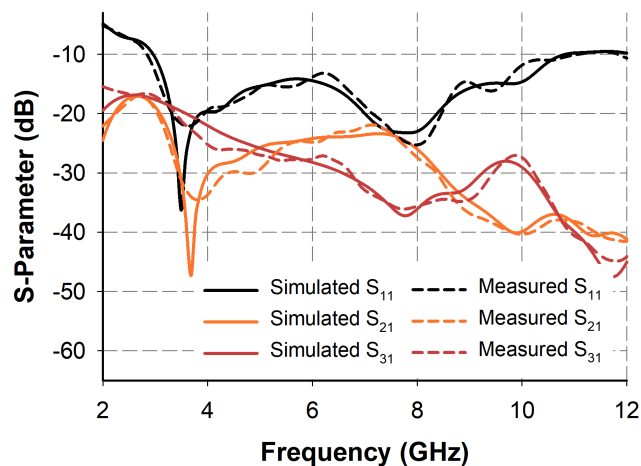
Fig. 5.32 Measured s-parameters of the four-port UWB-MIMO antenna; $L = 43$mm, $G = 29$mm, $W = 0.4$mm, $S = 12.3$mm

Fig. 5.33 shows the measured and simulated radiation patterns of four-port UWB-MIMO antenna for all the port excitation, at 4 GHz and 9 GHz over $\phi = 0°$ (X-Z) plane and $\theta = 90°$ plane. The planes at which measurements are taken are drawn on the antenna geometry and is shown above the plots of radiation patterns (see Fig. 5.33). On comparing the patterns it is found that Ant1 and Ant2 are directed towards 180° and 0° in the $\phi = 0°$ plane, respectively. While patterns of Ant3 and Ant4 are directed towards 270° and 90° in the $\theta = 90°$

(a) At $\phi = 0°$ (X-Z) Plane
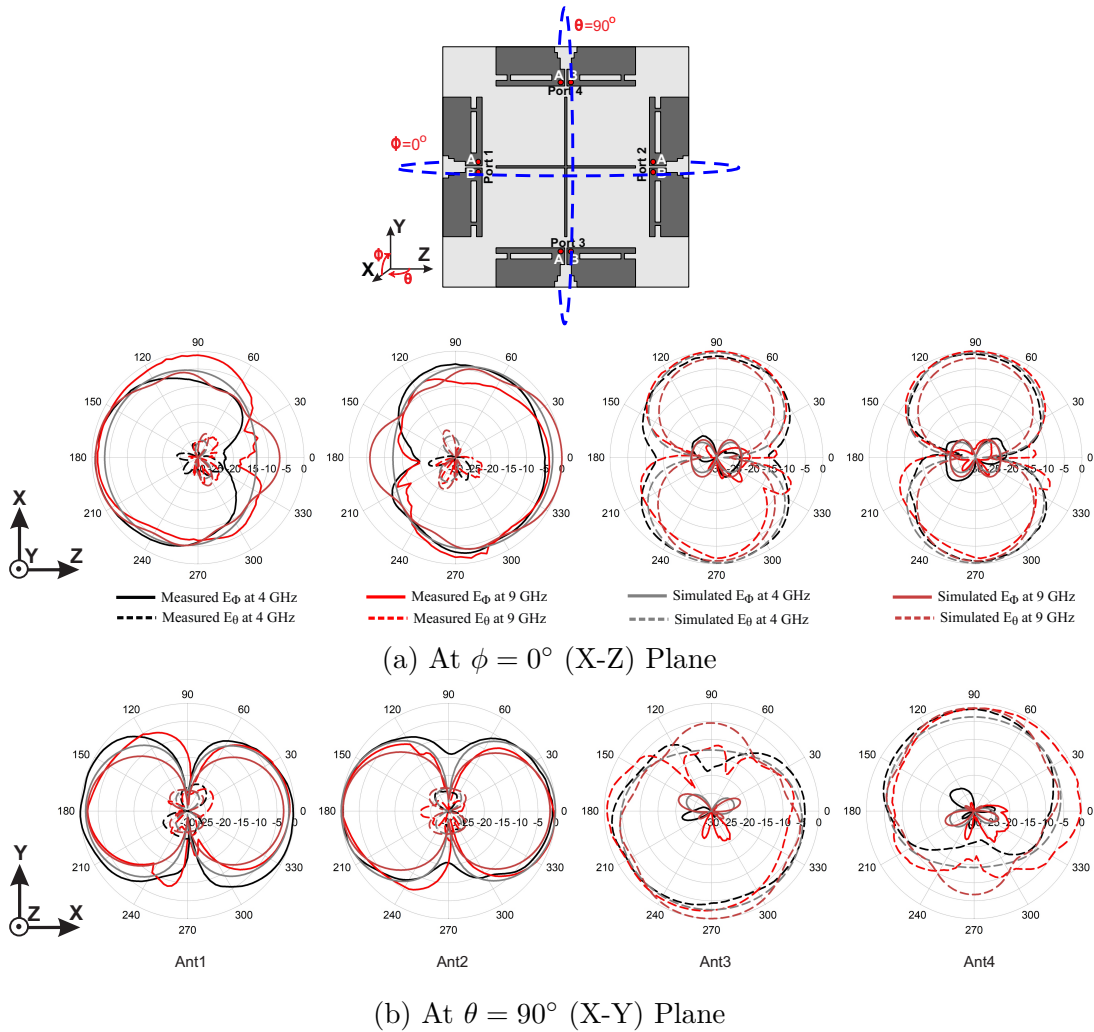
(b) At $\theta = 90°$ (X-Y) Plane

Fig. 5.33 2D Radiation Pattern of quad-element UWB-MIMO antenna for 4 GHz & 9 GHz; $L = 43$mm, $G = 29$mm, $W = 0.4$mm, $S = 12.3$mm

Table 5.3 Polarization Isolation of four-port antenna (values in dB); $L = 43$mm, $G = 29$mm, $W = 0.4$mm, $S = 12.3$mm

Freq.	$\phi = 0°$ **(X-Z) Plane**				$\theta = 90°$ **(X-Y) Plane**			
	Ant1	Ant2	Ant3	Ant4	Ant1	Ant2	Ant3	Ant4
4 GHz	23.2	23.22	-28.98	-35.7	28.56	30.16	-38.5	-26.55
9 GHz	25.92	22.62	-29.56	-30.3	23.59	25.66	-36.97	-28.45

plane, respectively. This confirms the presence of angle diversity in the four-port antenna structure, due to its directional radiation patterns to four different directions. The polarization isolation of all antenna-elements in the four-port antenna is summarized in Table 5.3, for $\phi = 0°$ & $\theta = 90°$ planes at two different frequencies. It is noticed from the table that the polarization isolation for Ant1 is >23 dB, Ant2 is >22 dB, Ant3 is >28 dB and Ant4 is >26 dB in both the planes. This shows that the antenna has good polarization purity between ϕ and θ field components, for a particular antenna element. It is noticed that the isolation values for Ant3 and Ant4 are negative as compared to that of Ant1 and Ant2. This is because in both planes the ϕ component is dominant over θ component for Ant1 and Ant2, whereas θ component is dominant for Ant3 and Ant4. Thus the field components are in complement to each other for Ant1 & 2 and Ant3 & 4 in both the planes. This shows that Ant3 & 4 are orthogonally polarized from that of Ant1 & 2, which fulfils the polarization diversity in the four-port antenna. In addition to this, the power level differences of single antenna-element along a particular plane shows negligible variations for different frequencies. Thus, the antenna has excellent polarization stability in the operation band which is required for good pulse handling capability.
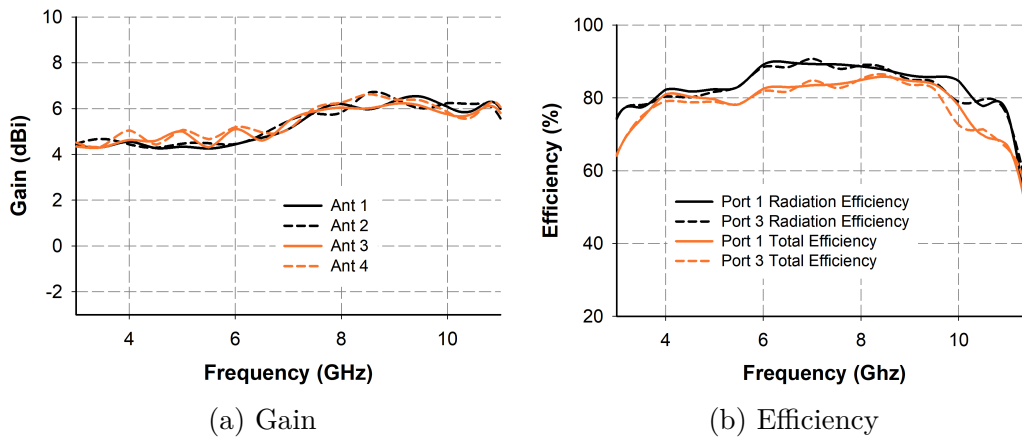
(a) Gain   (b) Efficiency

Fig. 5.34 Measured gain and efficiency of the each elements of four-port UWB-MIMO antenna; $L = 43$mm, $G = 29$mm, $W = 0.4$mm, $S = 12.3$mm

The gain of each antenna element, measured using the Gain Comparison Method, is depicted in Fig. 5.34a. As observed from the figure, the antenna

offers a stable gain with a peak gain of 6.7 dBi at 8.5 GHz with a variations less than 2.2 dBi, within the UWB. The radiation efficiency (η_{rad}) of the Ant1 & 3, measured using Schantz's Wheeler Cap Method, is shown in Fig. 5.34b, which reveals that the efficiency is better than 80% in the UWB spectrum, with a peak efficiency of 91% at 7 GHz. From η_{rad}, the total efficiency (η_{tot}) is calculated, and is included in Fig. 5.34b. The similarity between η_{rad} and η_{tot} confirms the perfect matching of the antenna.

5.4   Time-domain Analysis

In this section the transfer properties of the three UWB-MIMO antennas discussed in the above sections are investigated and compared. Although the antenna-elements were matched properly they may behave differently when non-sinusoidal waveforms are transmitted/received, and hence this transient studies are very important for antennas operating in UWB frequency band. The analysis setup and underlying theory for the study are followed as discussed in Section 3.3.3. For measurement & simulation setup, both the receiving antenna & CST virtual probes are kept at a distance of 20 cm in far-field from the transmitting antenna,where, the minimum distance for far-field (in the case of four-port antenna) calculated at 3.1 GHz is 7.6 cm. Here, for the measurement of one port, all the other ports are terminated with a matched load of 50Ω. The studies are performed in the azimuthal($\phi = 0°$ plane) and elevation plane($\theta = 90°$ plane) of the MIMO antennas.

5.4.1   Transfer Function

The magnitude of the simulated transfer function $\vec{H}_{Rx}(\omega, \theta, \phi)$ of the three UWB-MIMO antennas at their azimuth and elevation plane in the frequency band of interest are depicted in Fig 5.35 and Fig. 5.36, respectively. Fig. 5.35a shows the simulated transfer function of Ant1 & Ant2 in the two-port UWB-MIMO antenna for azimuthal plane. Its is observed from the figure that, for the case of Ant1, the intensity of transfer function is high between 100° and 250° compared to other angles, which conforms to the radiation pattern maximum at 180°. A similar behaviour is observed throughout the UWB range.

(a) two-port UWB-MIMO antenna

(b) three-port UWB-MIMO antenna

(c) four-port UWB-MIMO antenna
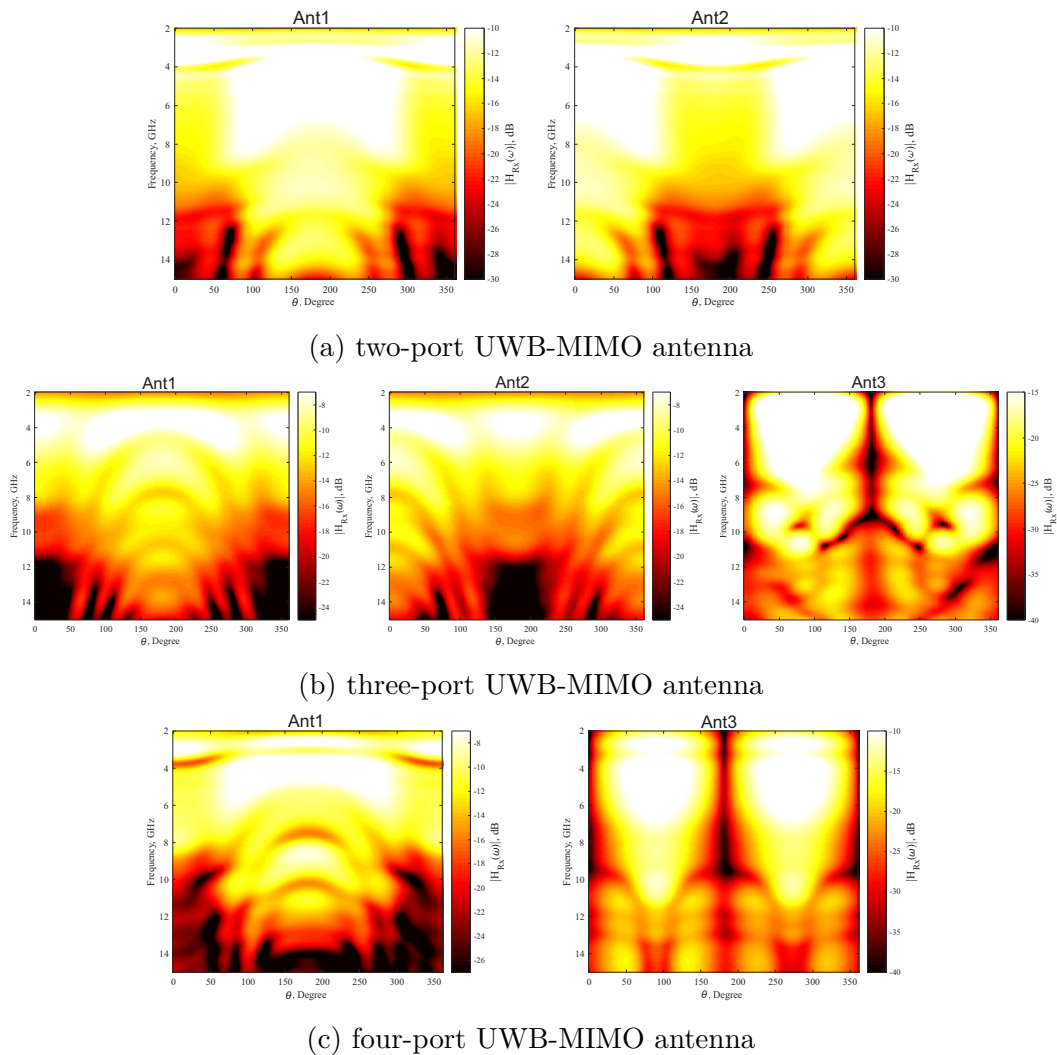
Fig. 5.35 Simulated transfer function in the azimuthal plane for three UWB-MIMO antennas

Similarly, for Ant2, the intensity is maximum between 285° and 75° compared to other angles which is due to the radiation pattern maximum at 0°. It is noticed that due to the symmetry of two-port antenna structure the transfer functions are similar for the two antenna elements, apart from the direction maximum of respective radiation patterns. The plot indicates a 180° shift in their intensity variation for Ant1 and Ant2, because of the 180° spatial shift of their radiation patterns. Fig. 5.35b is the transfer function plot in azimuthal plane for the three-port UWB-MIMO antenna. In this case, both Ant1 and

Ant2 have similar transfer functions except their direction of maximum intensity. That means, the only difference between the transfer functions of Ant1 and Ant2 are, one (Ant1) have maximum value between 100° and 250° whereas the other (Ant2) have high values between 285° and 75°. But Ant3 have a different transfer function plot compared to Ant1 and Ant2, because of the utilization of a different antenna-element and an orthogonal polarization from the other two. Here, Ant3 have a sharp nulls at 180° and 360° and has maximum intensity for other angles, as shown in the third plot of Fig. 5.35b. For the case of four-port UWB-MIMO
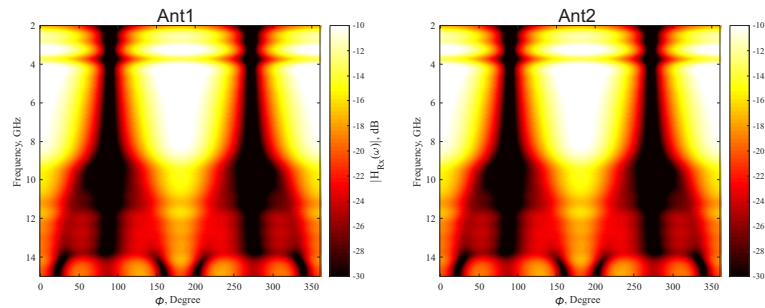
(a) two-port UWB-MIMO antenna
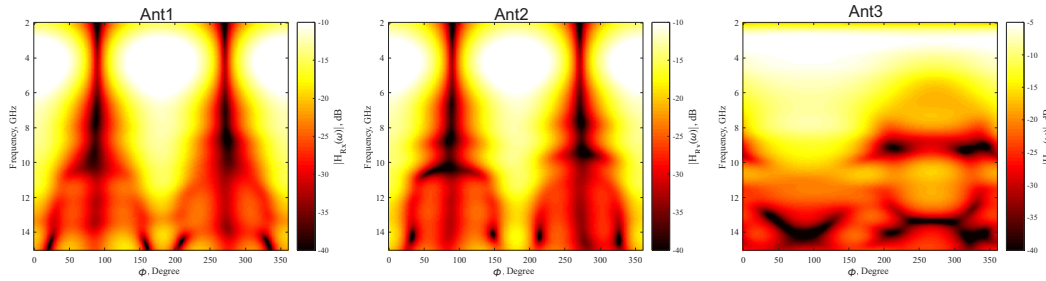
(b) three-port UWB-MIMO antenna
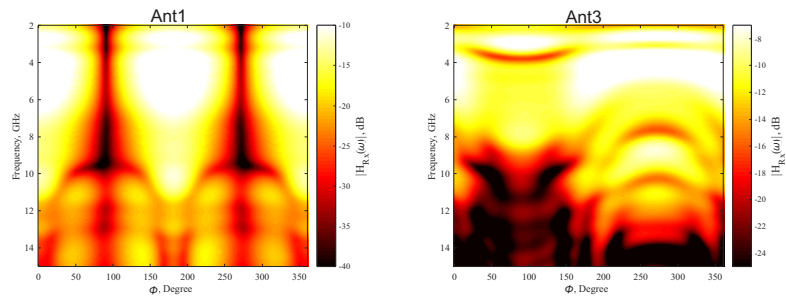
(c) four-port UWB-MIMO antenna

Fig. 5.36 Simulated transfer function in the elevation plane for three UWB-MIMO antennas

antenna, shown in Fig. 5.35c, the transfer functions of only Ant1 and Ant3 are plotted because of the structural symmetry. Here, it is noticed that the transfer function is maximum between 100° and 250° compared to other angles for Ant1, while for Ant3 maximum is about 90° and 270° and have sharp nulls at 180° and 360°. This is due to the polarization difference between Ant1 and Ant3 in the MIMO antenna structure. Ant2 and Ant4 of quad-element MIMO antenna have similar transfer function as that of Ant1 and Ant3, respectively. Only difference will be Ant2 have intensity maximum at a range of angles which are 180° space shifted with that of Ant1; similarly for Ant4 and Ant3.

Fig. 5.36 shows the corresponding transfer function of three UWB-MIMO antennas in its elevation plane. For two-port antenna, both Ant1 and Ant2 have sharp nulls at 90° & 270° corresponding to their radiation pattern nulls, as shown in Fig. 5.36a. Similarly, the transfer functions of Ant1 and Ant2 along elevation plane of three-port antenna are similar, whereas that of Ant3 is entirely different due to the orthogonal polarization of Ant3 with respect to Ant1 & Ant2, as seen in Fig. 5.36b. Ant3 have maximum intensity about 90° and have minimum values at 270°. Fig. 5.36c depicts the magnitude of transfer function for the four-port antenna along its elevation plane, which showed only the cases of Ant1 and Ant3 due to the antenna structural symmetry. Here, it is seen that Ant1 have sharp nulls at 90° & 270° corresponding to their radiation pattern nulls while Ant3 have maximum of transfer function about 270° and minimum about 90°.

The corresponding measured transfer functions of all the three MIMO antennas along azimuthal and elevation plane are plotted in Fig. 5.37 and Fig. 5.38, respectively. The intensity variations in magnitude of transfer function agrees well with the simulations across both azimuthal and elevation angles, and frequencies. Only the magnitude variations at angles 0°, 90° & 180° are shown for convenience. In the case of azimuthal plane, the magnitude of transfer function of two-port antenna is maximum at $\theta = 180°$ and minimum at $\theta = 0°$ for Ant1, whereas magnitude is maximum at $\theta = 0°$ and minimum at $\theta = 180°$ for Ant2, as shown in Fig. 5.37a. Similarly, for three port antenna, magnitude of transfer function is maximum at $\theta = 180°$ for Ant1 and at $\theta = 0°$ for Ant2. In the case of Ant3, transfer function goes higher at $\theta = 90°$, as seen in Fig. 5.37b. The Fig. 5.37c shows the measured transfer function of four-port antenna, in which that of Ant1 and Ant4 are plotted at $\theta = 0°$, 90° & 180°. Ant1 has maximum amplitude

(a) two-port UWB-MIMO antenna

(b) three-port UWB-MIMO antenna

(c) four-port UWB-MIMO antenna
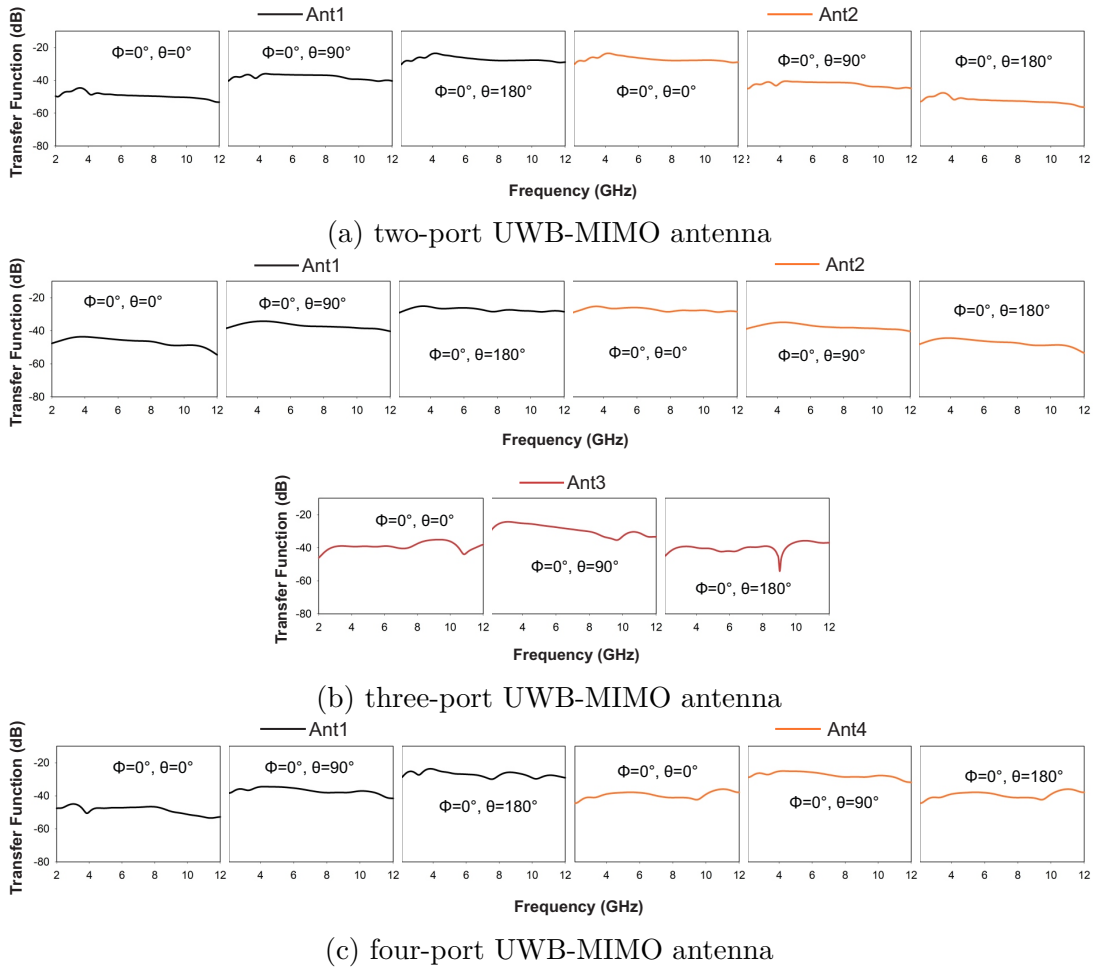
Fig. 5.37 Measured transfer function in the azimuthal plane for three UWB-MIMO antennas

at $\theta = 180°$ and Ant4 has maximum at $\theta = 90°$. These measured intensity variations of UWB-MIMO antennas goes in accordance with the simulated plots, in Fig. 5.35. Fig. 5.38 shows the magnitude of measured transfer function along the elevation plane of the antenna elements of respective UWB-MIMO antennas.

5.4.2   Impulse Response

From the complex values of simulated transfer function the impulse response of the antennas are derived and its real values are plotted. Fig. 5.39 shows the

(a) two-port UWB-MIMO antenna

(b) three-port UWB-MIMO antenna

(c) four-port UWB-MIMO antenna
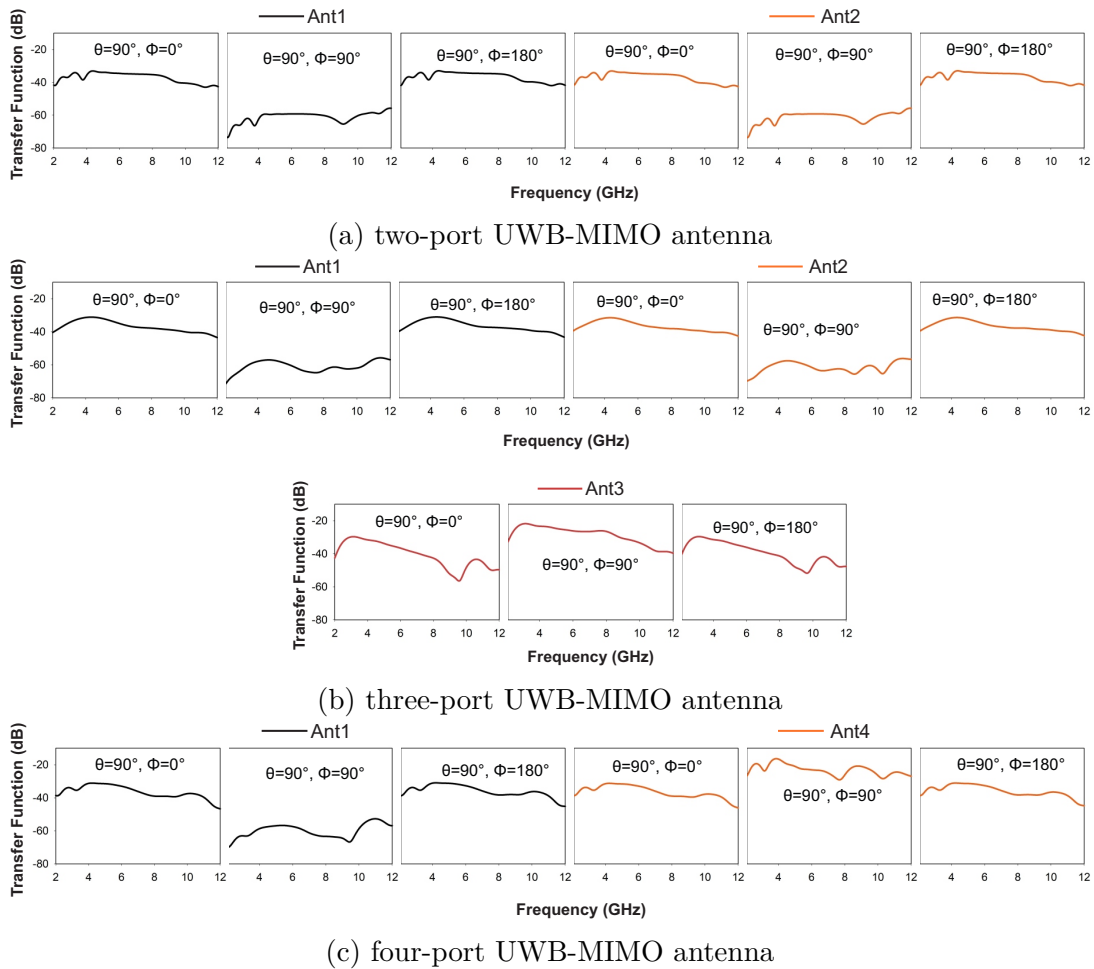
Fig. 5.38 Measured transfer function in the elevation plane for three UWB-MIMO antennas

simulated impulse response of three UWB-MIMO antennas along azimuthal plane and Fig.5.40 shows that along elevation plane. Along the azimuthal plane, the Ant1 of two-port system have sharp impulse response between 100° and 250° and for Ant2 the sharp responses are between 285° and 75°, as seen in Fig. 5.39a. For the case of Ant3 of three-port UWB-MIMO antenna (see Fig. 5.39b), the impulse response is very poor at 180° corresponding to the sharp null at its transfer function in Fig. 5.35. This denotes that well formed impulse responses are obtained at all angular regions where the transfer function have high values. Along the elevation plane also the impulse response goes sharper as the intensity

(a) two-port UWB-MIMO antenna

(b) three-port UWB-MIMO antenna

(c) four-port UWB-MIMO antenna
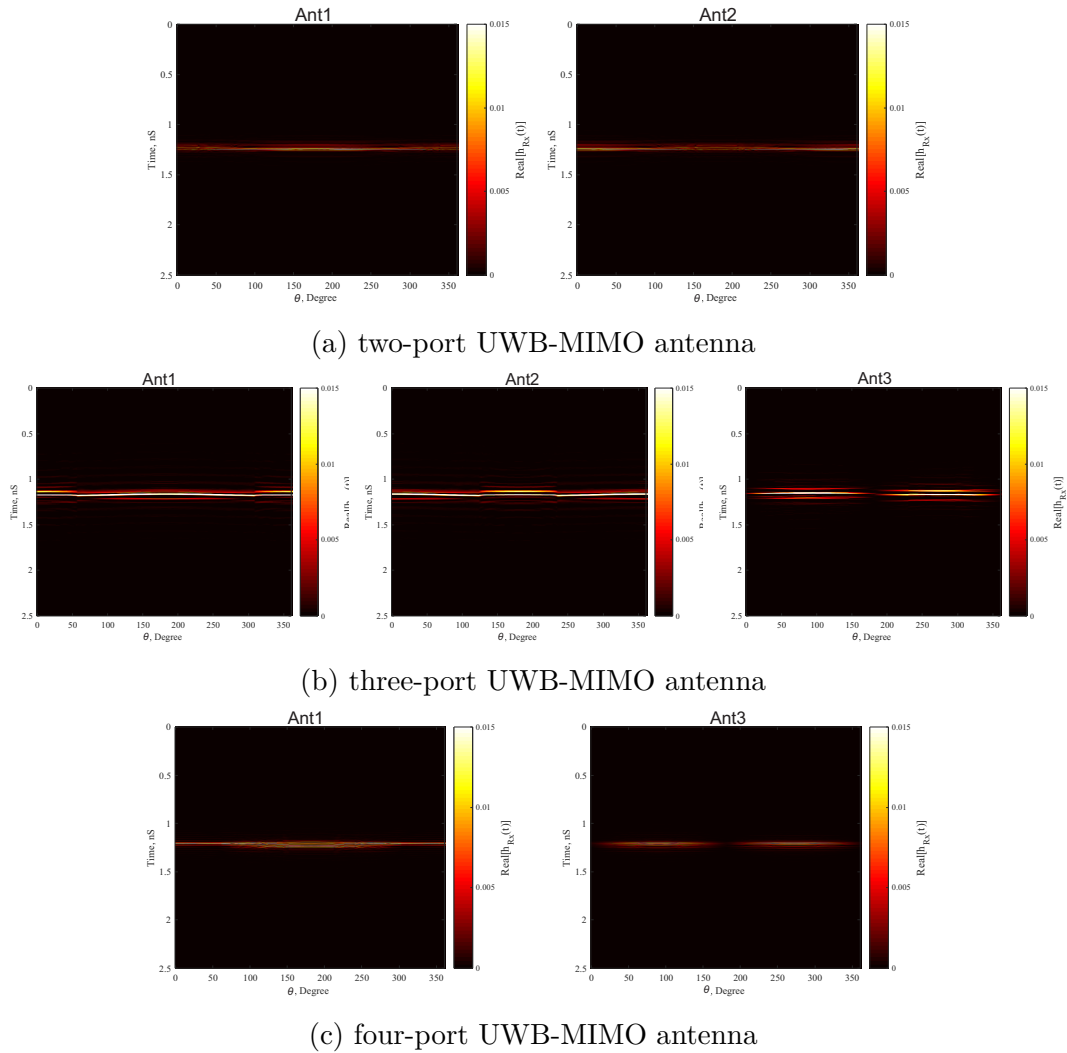
Fig. 5.39 Simulated impulse response in the azimuthal plane for three UWB-MIMO antennas

of transfer function goes higher and have poor response for those angles where the magnitude of transfer function have sharp nulls.

The impulse responses from the measured values of transfer function are depicted in Fig. 5.41 along the azimuthal plane and in Fig. 5.42 along the elevation plane. Here also, the impulse response for the angles at 0°, 90° & 180° are shown for convenience. In both azimuthal and elevation plane the impulse responses, shown in Fig. 5.41a, 5.41b, 5.41c and Fig. 5.42a, 5.42b, 5.42c, goes sharper corresponding to the maximum values of transfer functions in Fig. 5.37a,

(a) two-port UWB-MIMO antenna

(b) three-port UWB-MIMO antenna

(c) four-port UWB-MIMO antenna
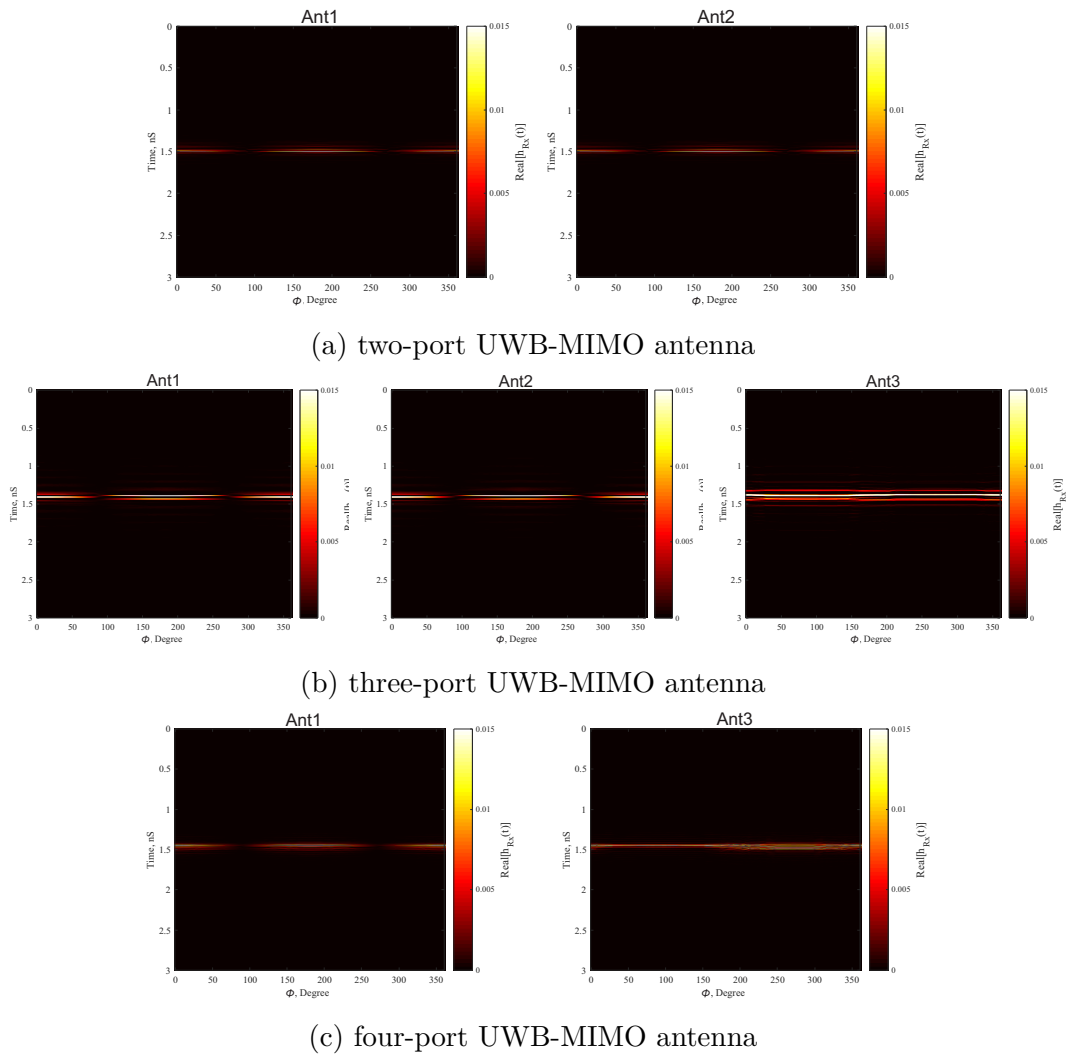
Fig. 5.40 Simulated impulse response in the elevation plane for three UWB-MIMO antennas

5.37b, 5.37c and Fig. 5.38a, 5.38b, 5.38c, respectively. The measured values of impulse responses agrees well with those of simulated one across both azimuthal and elevation angles.

5.4.3   Quality Measures of UWB antennas

The simulated and measured transfer properties are quantified with the help of certain quality measures, as discussed in Section 3.3.3. One of the crucial
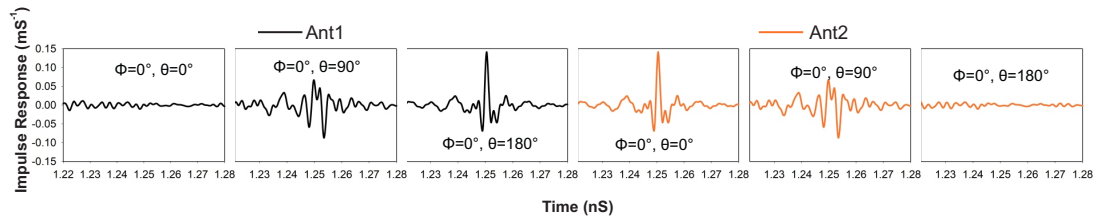
(a) two-port UWB-MIMO antenna
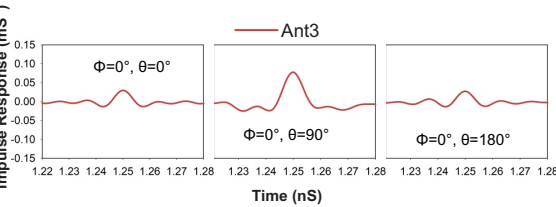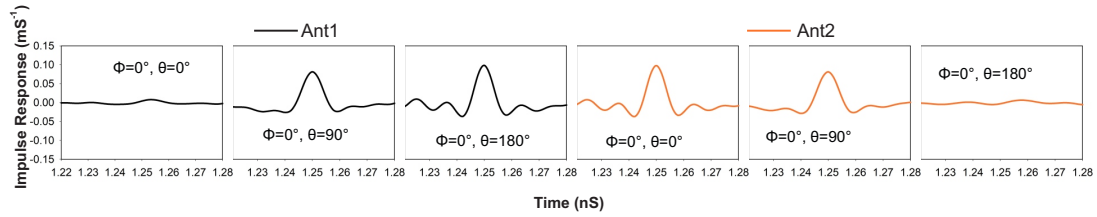
(b) three-port UWB-MIMO antenna
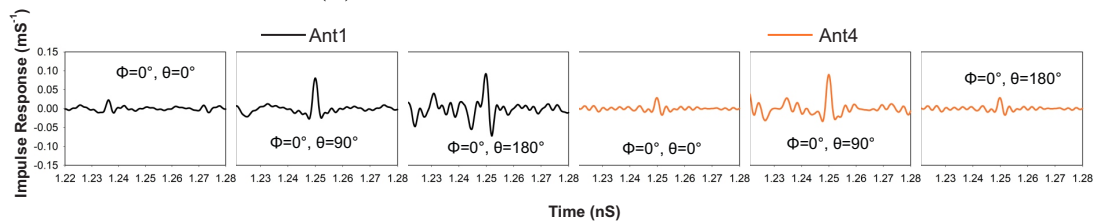
(c) four-port UWB-MIMO antenna

Fig. 5.41 Measured impulse response in the azimuthal plane for three UWB-MIMO antennas

quality measure is the group delay of the antenna. For an ideal scenario the group delay will be flat, showing the linear variation of phase with frequency. Here, the group delay of all the UWB-MIMO antennas are measured and plotted in Fig. 5.44. In order to conduct the group delay measurement, a UWB link is set-up using two identical antennas at a far-field distance of D. For the analysis of one antenna-element, the same element of both the antennas are kept face-to-face, at a distance of D. Fig. 5.43a, 5.43c and 5.43b shows the arrangements for the group delay measurement of all the ports in the case of two-port, three-port and

(a) two-port UWB-MIMO antenna

(b) three-port UWB-MIMO antenna

(c) four-port UWB-MIMO antenna
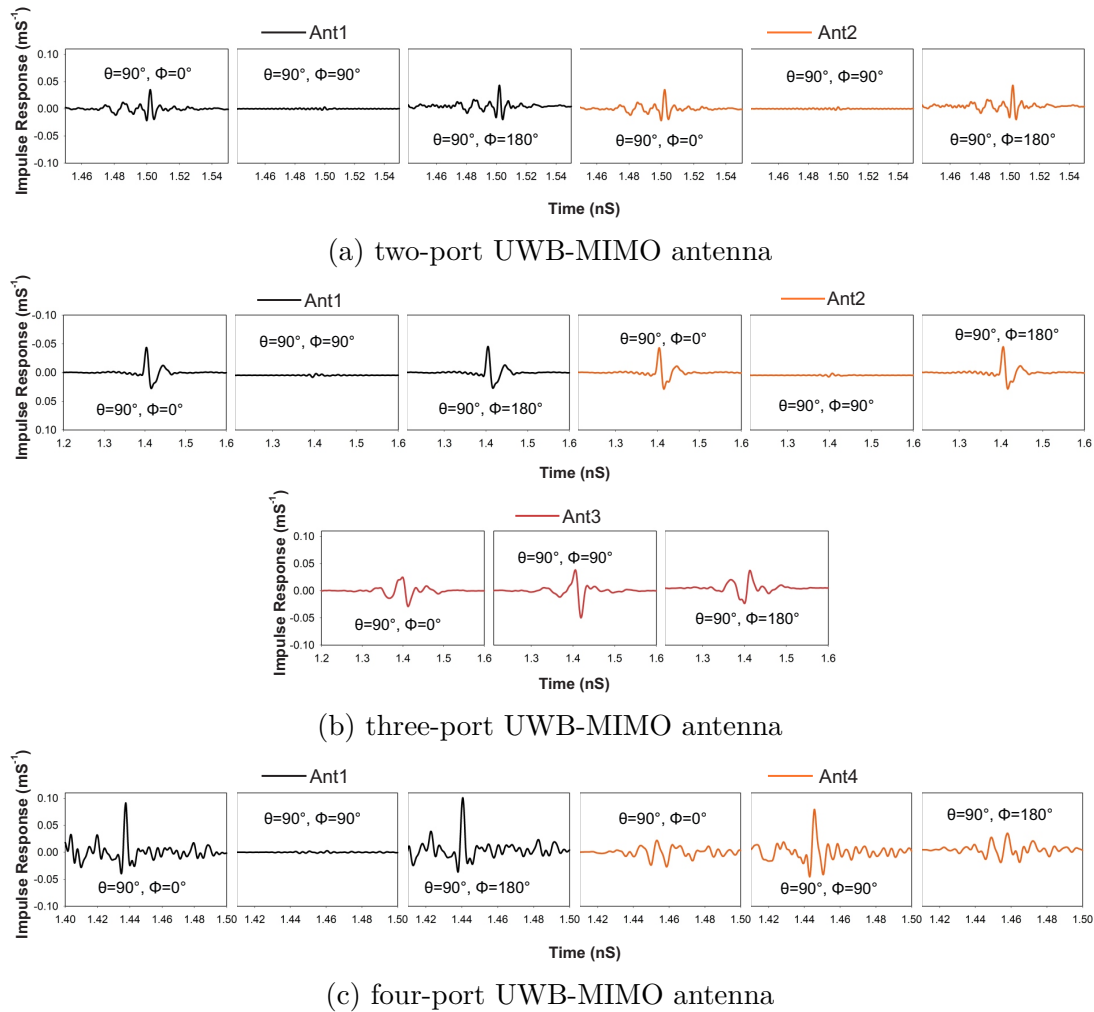
Fig. 5.42 Measured impulse response in the elevation plane for three UWB-MIMO antennas

four-port UWB-MIMO antennas, respectively. For the measurement of one port all the other ports are terminated with matched loads.

Fig. 5.44a shows the group delay of Ant1 and Ant2 in the two-port UWB-MIMO antenna. For Ant1, the group delay varies from 0.46nS to 1.15nS, which gives a variation of ≤0.69nS in the 3.1 - 10.6 GHz operation band. This satisfies the tolerable range of ≤1nS. Similarly, for Ant2 the minimum value of group delay is 0.52nS and maximum value is 1.18nS, which offers a variation of ≤0.66nS only in the UWB band. The group delay values of three-port antenna is shown in Fig. 5.44b, where Ant1 has variation ≤0.67nS, Ant2 has variation ≤0.83nS

(a) two-port UWB-MIMO antenna   (b) four-port UWB-MIMO antenna

(c) three-port UWB-MIMO antenna
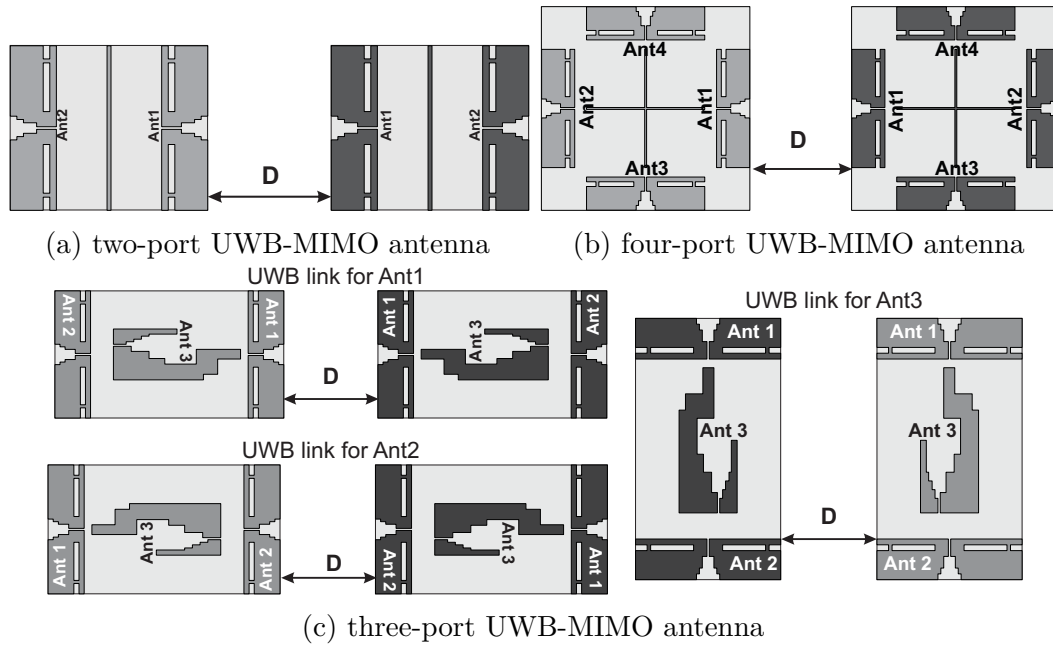
Fig. 5.43 Arrangement of UWB-MIMO antennas for group delay measurement

and Ant3 has variation ≤0.68nS, throughout the band of interest. For the case of four-port UWB-MIMO antenna only group delay measures of Ant1 and Ant3 are shown due to the structural symmetry of the antenna. As seen in Fig. 5.44c Ant1 has variation ≤0.93nS and Ant3 has variation ≤0.83nS within the UWB band of 3.1 - 10.6 GHz. Thus, for all the UWB-MIMO antennas the measured group delays are within the tolerable range of ≤1nS, denoting a linear change of phase with frequency.

The Table 5.4, 5.5 and 5.6 summarizes the values of FWHM, ringing and fidelity factor of two-port, three-port and four-port UWB-MIMO antennas, respectively. These values are calculated from the respective simulated and measured transient responses across their azimuth and elevation planes. These factors gives an idea about the dispersive behaviour of the antennas. It is clear from the table that all the antennas have narrow FWHM and low ringing, which manifests high fidelity factor for their respective planes. This shows that the antennas gives only tolerable distortions to the pulses that are transmitted through them. The measured and simulated values conformed well with each other, in both the azimuthal and elevation planes.

(a) two-port UWB-MIMO antenna

(b) three-port UWB-MIMO antenna

(c) four-port UWB-MIMO antenna
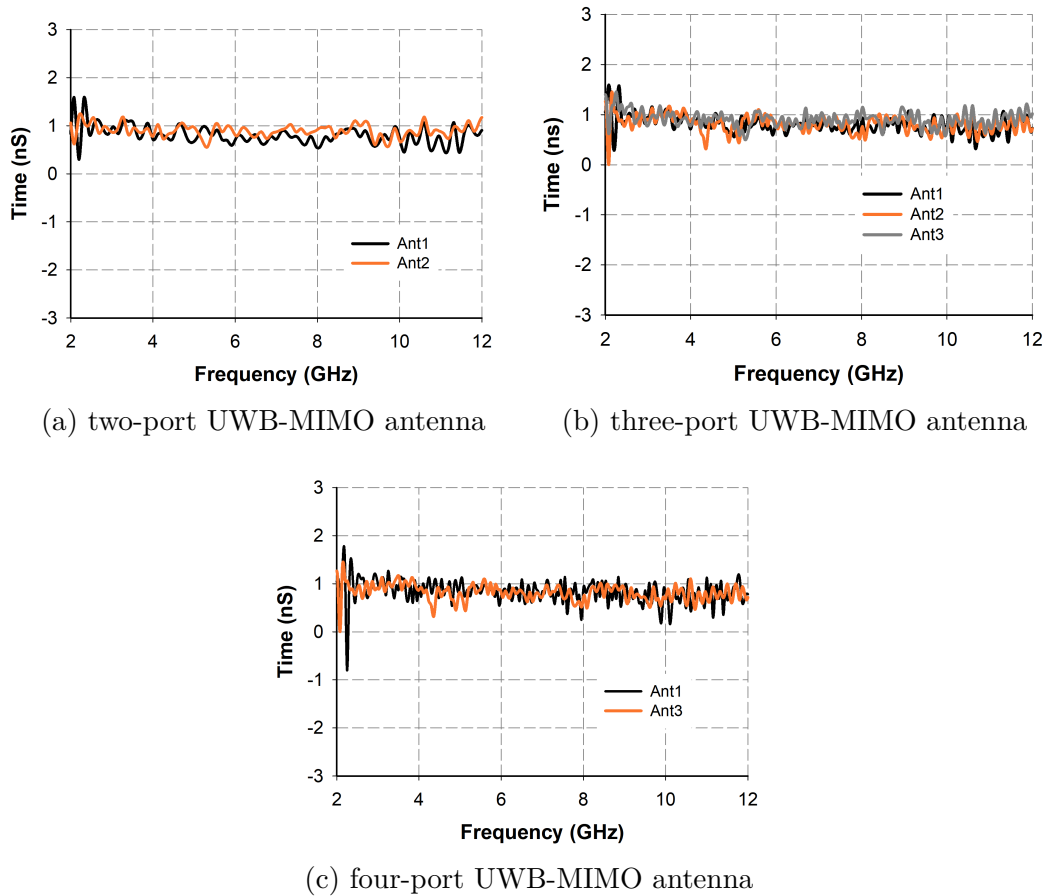
Fig. 5.44 Measured group delay of the three UWB-MIMO antennas

5.5 Spatial-domain Analysis

Spatial-domain analysis gives the knowledge about the fluctuations in the radiation properties around the antenna. This analysis can be performed by calculating the correlation patterns and Pattern Stability Factor (PSF) of the antenna at its respective planes, in the directions of interests, as discussed in section 3.3.4.

In this section, investigations carried out in the spatial-domain for all the three UWB-MIMO antennas are explained in detail, with their simulated as well as measured results. For the analysis of two-port and four-port UWB-MIMO antennas, only the analysis of Ant1 is taken into consideration because of their structural symmetry. The other antenna elements of two-port and four-port

Table 5.4 FWHM, Ringing and Fidelity of two-port UWB-MIMO antenna

		Angle (θ or ϕ)	FWHM (pS)		Ringing (pS)		Fidelity (%)	
			Sim.	Meas.	Sim.	Meas.	Sim.	Meas.
Ant1	Azimuthal	0°	164.1	153	141.9	171.9	90.7	87.2
		90°	152.9	141.2	109.2	132	93.9	90.3
		180°	142	156	87.4	91	91.8	92.3
	Elevation	0°	120.2	109.7	76.5	89.2	91.6	94.32
		90°	152.9	169.3	109.2	130	68.8	87.2
		180°	120.2	113.2	76.5	86.3	97.3	96.6
Ant2	Azimuthal	0°	141.9	156	87.4	101.2	91.8	92.3
		90°	152.9	171.2	109.2	132	93.9	96.7
		180°	163.8	168	141.9	101.2	90.7	90.3
	Elevation	0°	120.1	110	76.4	130	91.6	89.2
		90°	152.9	178.1	109.2	234.6	68.8	73.43
		180°	120.1	103.2	76.4	147	97.3	91.27

UWB-MIMO antennas have similar results as for Ant1. To identify the best reference direction for system design, the correlation patterns of the antennas are determined over the azimuth & elevation plane in the frequency range of 3.1–10.6 GHz, and the results are shown in Fig. 5.45, Fig. 5.46 and Fig. 5.47 . From the correlation patterns the corresponding PSF values are calculated and are listed in Table 5.7 . This gives an idea of the degree of stability the antennas possess in their band of operation. For an ideal antenna the PSF values will be equal to unity and PSF>0.9 is taken as a desirable value for a good all-round performing antenna.

In the case of two-port UWB-MIMO antenna, the correlation pattern of Ant1 over azimuth plane (X-Z plane) is constant, throughout the 3.1 - 10.6 GHz band,

Table 5.5 FWHM, Ringing and Fidelity of three-port UWB-MIMO antenna

		Angle (θ or ϕ)	FWHM (pS)		Ringing (pS)		Fidelity (%)	
			Sim.	Meas.	Sim.	Meas.	Sim.	Meas.
Ant1	Azimuthal	0°	186.6	175.6	98.8	181.4	95.8	94.3
		90°	142.7	132.7	87.8	110	95.4	92.6
		180°	142.7	120.6	87.8	107.89	92.5	93.7
	Elevation	0°	131.7	175	87.8	126.4	97.5	95.5
		90°	142.7	217	131.7	168.3	68.9	78.6
		180°	131.7	185	87.8	143.6	91.8	89.3
Ant2	Azimuthal	0°	76.8	163	67.3	133.5	91.3	92.3
		90°	120.7	183	88.7	198	87.2	90.1
		180°	164.7	178	142.7	230	90.4	94.3
	Elevation	0°	131.7	142.3	70.3	128.2	88.2	90.82
		90°	263.5	197.3	147.1	192.3	90.7	92.9
		180°	120.7	175.5	70.3	131.33	79.97	93.75
Ant3	Azimuthal	0°	142.7	172	369	210	90.74	90.9
		90°	120.7	111.3	130.3	125.3	95.27	96.1
		180°	142.7	167	368.7	217	91.06	95.8
	Elevation	0°	170.2	167.71	208.5	197.32	87.2	90.7
		90°	121.3	145.3	109.8	131.12	91.6	93
		180°	167.3	142.3	197.5	176.3	79.1	87.75

as they are more correlated with all directions on average (see Fig. 5.45). Also, in this plane the antenna shows high values for correlation pattern in all the directions concerned. However, in elevation plane (X-Y plane) the correlation

Table 5.6 FWHM, Ringing and Fidelity of four-port UWB-MIMO antenna

		Angle $(\theta$ or $\phi)$	FWHM (pS)		Ringing (pS)		Fidelity (%)	
			Sim.	Meas.	Sim.	Meas.	Sim.	Meas.
Ant1	Azimuthal	0°	166.6	202	177.7	136	87.23	92.3
		90°	155.5	187	89.7	163	94.3	91.7
		180°	144.4	133.4	111.07	114.3	86.3	90.3
	Elevation	0°	121.5	117.8	88.8	86.5	94.6	96.2
		90°	144.7	192.4	110.9	173.6	82.5	86.6
		180°	121.5	122	88.8	108	87.9	89
Ant4	Azimuthal	0°	155.3	231.2	244	207.3	67.5	73.21
		90°	121.2	140	88.9	121.7	94.71	92.37
		180°	155.4	246	244.4	223.2	67.5	81
	Elevation	0°	144	188	111.2	112.3	94.9	90.1
		90°	120.4	117	87.3	92.3	96.9	93.2
		180°	155.5	206	111.2	87	94.24	86.7

pattern shows dips in the direction of 90° and 270°, which are due to the presence of nulls in the radiation pattern at those directions. This indicates that the reference directions in all the range, other than at these two points at its elevation plane, are the best to use. The PSF values of two-port antenna in Table 5.7 at both azimuth and elevation plane points out an excellent degree of stability for the antenna, as the values are > 0.949 in the 3.1 - 10.6 GHz frequency band.

Similar will be the case for Ant1 and Ant2 of the three-port UWB-MIMO antenna, as seen in Fig. 5.46a and 5.46b, respectively. As Ant3 is in a differently polarized position from that of Ant1 & 2, the correlation patterns of that antenna element has dips at 180° and 360° over its azimuthal plane and is constant over the elevation plane, as shown in Fig. 5.46c. This denotes that, in the case of
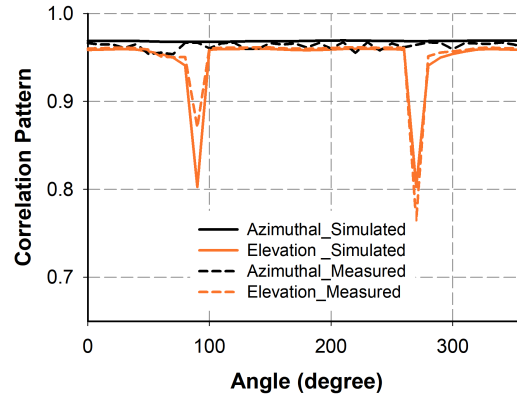
Fig. 5.45 Simulated and measured correlation pattern of two-port UWB-MIMO antenna; $L = 25$mm, $W = 30$mm $G = 16$mm, $W_S = 0.4$mm

Table 5.7 PSF Values for 3.1 - 10.6 GHz band

UWB-MIMO antennas		$\phi = 0°$ (X-Z) Plane		$\theta = 90°$ (X-Y) Plane	
		Sim.	Meas.	Sim.	Meas.
2-port	Ant1	0.969	0.963	0.949	0.952
3-port	Ant1	0.972	0.953	0.968	0.945
	Ant2	0.97	0.965	0.947	0.932
	Ant3	0.9	0.912	0.949	0.95
4-port	Ant1	0.962	0.958	0.948	0.935

Ant3, the pattern are more correlated in all directions along the elevation plane. Moreover, the PSF values are > 0.945 for Ant1, > 0.932 for Ant2 and > 0.9 for Ant3 (refer Table 5.7), along both the planes showing good stability in its radiation characteristics.

The Fig. 5.47 depicts the simulated and measured correlation patterns of Ant1 in the four-port UWB-MIMO antenna, along the azimuthal and elevation plane. Here, Ant1 has constant correlation pattern along the azimuthal plane in the UWB band, whereas correlation pattern had dips in the direction of 90° and 270° along its elevation plane corresponding to the sharp nulls in its radiation pattern.

(a) Ant1

(b) Ant2

(c) Ant3
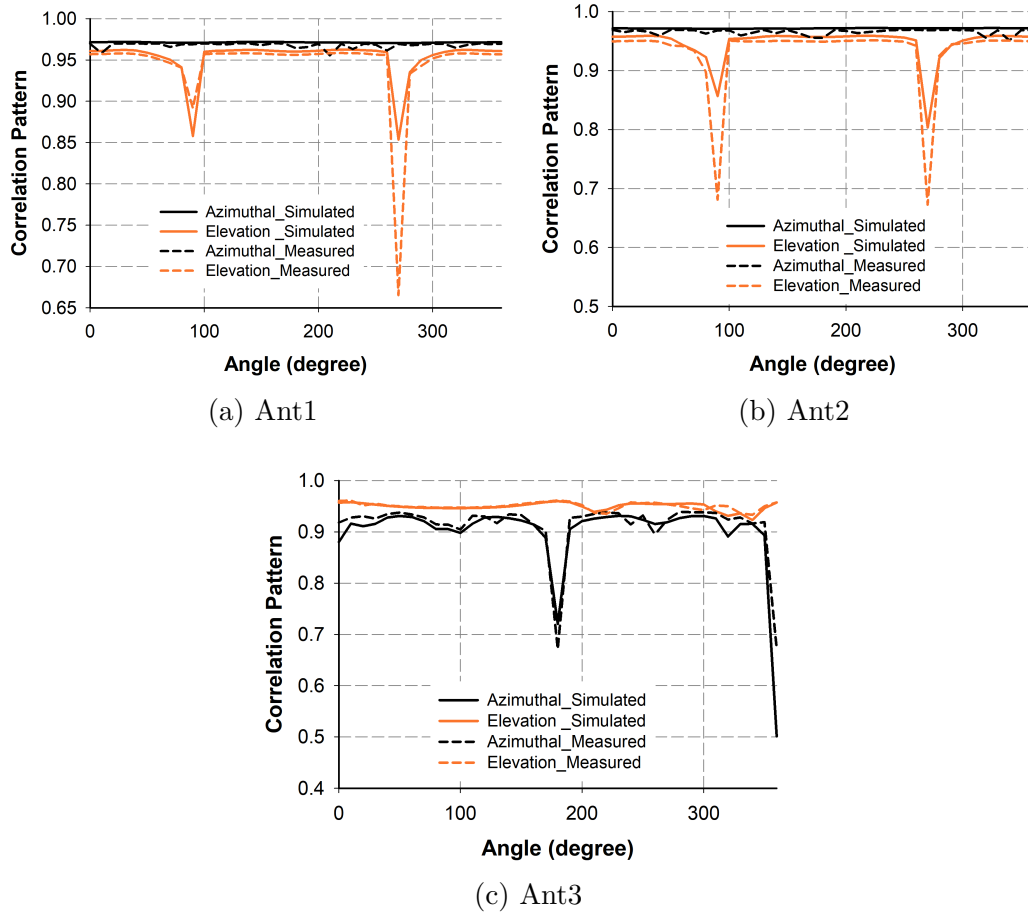
Fig. 5.46 Simulated and measured correlation pattern of three-port UWB MIMO antenna; $L = 25$mm, $W = 45$mm $G = 31$mm, $L_{off} = 7.5$mm, $W_{off} = 4.5$mm

The correlation pattern of Ant2 will be same as that of Ant1, whereas for Ant3 & Ant4 the only difference is that the dips will be present in the azimuthal plane at 180° and 360°. This is due to the orthogonal polarization of Ant3 & Ant4 with Ant1 & Ant2. The values of correlation pattern and PSF will be same as that of Ant1. The PSF values of Ant1 along the azimuthal and elevation plane is listed in Table 5.7 and it shows a value >0.935 throughout the 3.1-10.6 GHz band. Thus, all the three UWB-MIMO antennas have stable performance in their operation band, and both the simulated and measured results conform very well with each other in the band of interest.
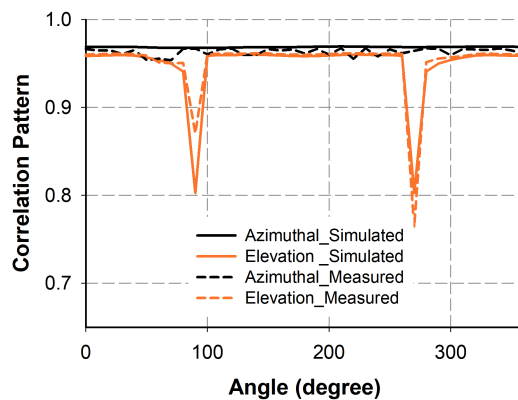
Fig. 5.47 Simulated and measured correlation pattern of four-port UWB-MIMO antenna; $L = 43$mm, $G = 29$mm, $W = 0.4$mm, $S = 12.3$mm

5.6 MIMO/Diversity performance Evaluation

The evaluation of MIMO/diversity performance of a multi-port antenna is important to analyse the credibility of that antenna as a candidate in MIMO communication systems. Section 3.3.5 has discussed various figures-of merit to evaluate the MIMO/diversity performance of a multi-element antenna. These quality-measures analyse the impact of one antenna-element on to the performance of other elements, which are co-located in the same MIMO antenna. Envelope correlation coefficient (ρ_{ij}^e), Mean Effective Gain (MEG), Diversity Gain (DG) and Multiplexing Efficiency (η_{mux}) are the main parameters to be evaluated for the antenna performance in MIMO applications. The detailed theory behind all these parameters and their calculation methods were discussed in section 3.3.5. Here, the subscript ij denotes the figure-of-merit between i^{th} and j^{th} antenna elements and all the results are obtained from the corresponding measured data of antenna-elements.

The guaranteed values of envelope correlation coefficient and the results of mean effective gain MEG of the three UWB-MIMO antennas are plotted against frequency and shown in Fig. 5.48. For all the antennas in this thesis, the correlation coefficient is calculated by incorporating the s-parameters, efficiency and losses of the antennas, in equation (3.47). Thus, the values of correlation coefficient obtained for different frequencies are the worst case values, which
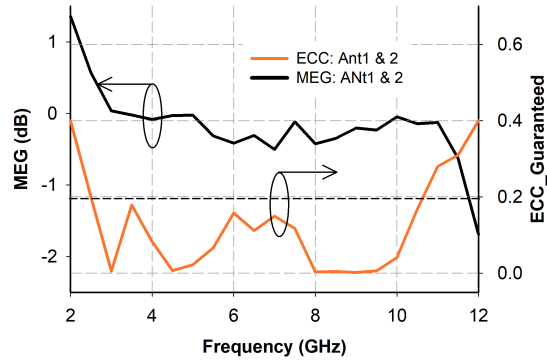
(a) Two-port UWB-MIMO antenna
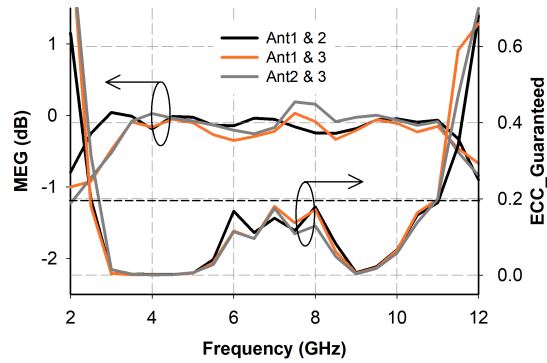
(b) Three-port UWB-MIMO antenna
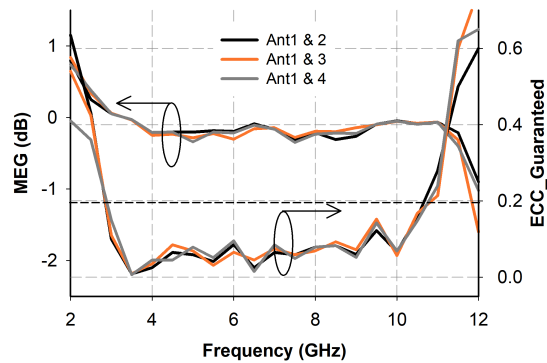
(c) Four-port UWB-MIMO antenna

Fig. 5.48 Envelope correlation coefficient and MEG of the three UWB-MIMO antennas
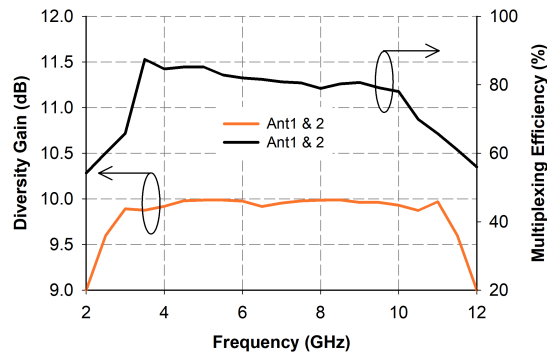
(a) Two-port UWB-MIMO antenna
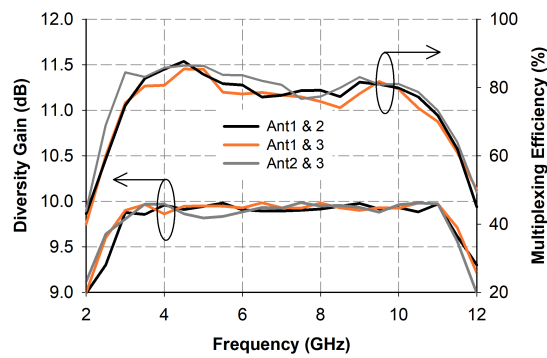
(b) Three-port UWB-MIMO antenna
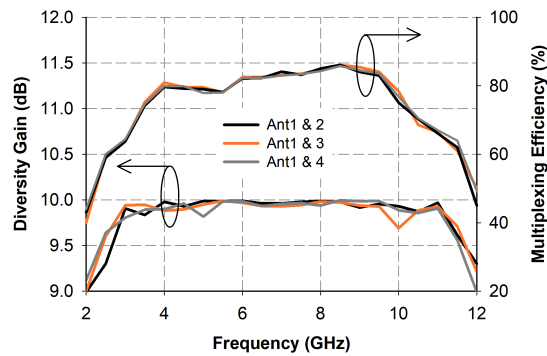
(c) Four-port UWB-MIMO antenna

Fig. 5.49 Diversity gain and Multiplexing efficiency of the three UWB-MIMO antennas

implies that, the actual values are sure to lie below these calculated values. This is termed as guaranteed correlation coefficient or guaranteed envelope

correlation coefficient ($ECC_{guaranteed}$ or $\rho^e_{ij_{guaranteed}}$). Here, the $\rho^e_{ij_{guaranteed}}$ and MEG (calculated using equation (3.50)) are calculated between each antenna-elements and are included in the respective figures. To promise a good channel characteristic and a better diversity performance the MIMO antennas should satisfy the criteria of $\rho^e_{ij}<0.5$ and $MEG_{ij} < \pm3$dB through out the band of interest. The Fig. 5.48ashows the $\rho^e_{ij_{guaranteed}}$ ($ECC_{guaranteed}$) and MEG_{ij} of the two-port UWB-MIMO antenna, where the study is carried out between Ant1 and Ant2. It is clear from the figure that, the guaranteed values of ECC ($ECC_{guaranteed}$) are below 0.2 and that of MEG_{12} (between Ant1 & 2) are less than ±0.5dB, for all frequencies in the operation band. The same parameter values for the three-port UWB-MIMO antenna is depicted in Fig. 5.48b, between Ant1 & 2, Ant1 & 3 and Ant2 & 3. As observed from the figure, the three-port antenna also shows good diversity performance as $\rho^e_{ij_{guaranteed}}$ and MEG_{ij} for all the antenna-element combination are below 0.2 and ±0.5dB, throughout the UWB band. In the case of four-port antenna $\rho^e_{ij_{guaranteed}}$ and MEG_{ij} between Ant1 & 2, Ant1 & 3 and Ant1 & 4 are only shown in the Fig. 5.48c, because of the structural symmetry. The antenna shows $ECC_{guaranteed}$ and MEG_{ij} below 0.2 and ±0.5dB throughout the UWB band, for all the antenna-element combinations. Thus all the MIMO antennas satisfied the required criteria of $\rho^e_{ij}<0.5$ and $MEG_{ij} < \pm3$dB through out the UWB band. This shows that all the elements of UWB-MIMO antennas radiates uncorrelated waveforms that indicates good MIMO/diversity performance. The polarization, spatial and angle diversities obtained in the antenna is responsible for maintaining low correlation coefficient and mean effective gain between the antenna-elements.

Another two important figures-of merit for the evaluation of MIMO antennas are diversity gain (DG) and multiplexing efficiency (η_{mux}), which are plotted in Fig. 5.49 for the case of all UWB-MIMO antennas, described earlier. The DG obtained for the two-port, three-port and four-port UWB-MIMO antennas from the measured results, using equation (3.59), at 99% reliability are depicted in Fig. 5.49a, 5.49b and 5.49c, respectively. For all the antennas, the value of DG is near to 10dB in the UWB frequency band, which is comparable to the ideal scenario and thus validates the efficient diversity performance of the antennas. Similarly, the η_{mux} obtained for the two-port, three-port and four-port UWB-MIMO antenna, using equation (3.61), is shown in Fig. 5.49a, 5.49b and

5.49c, respectively. It is evident from the figure that η_{mux} is similar to the η_{tot} of the respective MIMO antennas; see Fig. 5.14b for two-port, Fig. 5.24b for three-port and Fig. 5.34b for four-port UWB-MIMO antenna to have a look at their total efficiencies. This similarity between η_{mux} and η_{tot} are due to the low values of envelope correlation coefficient (ρ_{ij}^e) and also due to the much alike total efficiencies (η_{tot}) of the antennas in the band of interest. This evaluation study ascertained that all the UWB-MIMO antennas discussed in this chapter are good candidates for the MIMO communication systems operating in the Ultra-wideband frequency range.

5.7 Chapter Summary

This chapter discussed the performance characteristics of three UWB-MIMO antennas, using the developed UWB-I and UWB-II antennas discussed in Chapter4. A two-port UWB-MIMO antenna is realized by placing the antenna elements back-to-back and adding one reflector strip in between them. These two isolation mechanisms helped the antenna to attain reduction in mutual coupling between antenna elements. A three-port UWB-MIMO antenna, having the third element in orthogonal polarization with the other two antenna elements were also discussed in this chapter. This antenna utilized both spatial diversity and polarization diversity to attain adequate isolation between the antenna elements. By placing four similar antenna-elements, a quad-element UWB-MIMO antenna is realized and for proper isolation a cross-shaped reflector is also added in between the antenna elements, in addition to the polarization and spatial separation between them. Thus, an enhanced isolation is obtained for the four-port antenna with the help of these three isolation mechanisms. The radiation characteristics of all the UWB-MIMO antennas are investigated and the simulated results are verified with the experimental results. All the three MIMO antennas acquired angle diversity within their structure which is favourable for its MIMO performance. To analyse the pulse handling capability of these antennas the transfer properties of them are also studied in detail. The group delay of all the antennas are within the desirable limit, which shows the phase linearity of the antennas. The summarized values of quality measures reveals that all the UWB-MIMO antennas have minimum FWHM, less ringing and reasonably good fidelity throughout

their operation band. This verifies the good pulse handling capability of the antennas. The spatial-domain analysis of these antennas are also carried out in their principle planes. The frequency-domain correlation pattern helped to select the best reference directions for the which offers better transfer properties. The PSF values are also calculated and confirmed the stable performance of the UWB-MIMO antennas, in the 3.1-10.6 GHz bandwidth. In addition to this, the MIMO/diversity performance of the antennas are also studied and the results are included in this chapter. All the antennas offered low correlation coefficient and ample Mean Effective Gain (MEG) for all the ports. Also, DG and η_{mux} validated the MIMO/diversity performance of the UWB-MIMO antennas in the frequency band of interest, which shows that these antennas are potential candidates for UWB-MIMO communication systems.

Chapter 6

Channel Performance of UWB-MIMO antennas

In a wireless communication system which are operating in an urban and indoor environments, the wireless terminals are often subjected to strong fading due to the multipath propagation. In such environments the performance of these wireless terminals can be improved by employing spatial. polarization and/or pattern diversities for the transmitting/receiving terminals. This means that, the signals from a wireless communication system having two antennas at their terminals, which are differently positioned or polarized or have diverse radiation patterns, are combined at the receiver in such a way that the combined signal will have shallower fading minima. This corresponds to an improvement on the Signal-to-Noise Ratio (SNR) in the fading dips, which will in-turn reduces the fading margins in the wireless communication link budget. This increase in SNR will also increase the capacity of the communication channel. The wireless communication systems having several antennas on both transmitting and receiving sides are called as MIMO (Multiple-Input Multiple-Output) systems. MIMO systems are mainly characterized by their maximum available channel capacity, which depends on the correlation between the signals on different channels. The correlation is primarily caused due to the mutual coupling between the antenna-elements on both transmitting and receiving terminals. This correlation should be made less to guarantee a good MIMO operation with enhanced channel capacity. The multi-antenna systems which are devoted for diversity performances are characterized

by the diversity gain which is also affected by the mutual coupling between the antenna-elements. Thus, to realize an effective MIMO/diversity system it is necessary to have sufficient uncorrelated signals from isolated antenna elements, at both ends of the wireless link. The degree of correlation or isolation between the antenna elements can be evaluated by utilizing the scattering parameters of the antenna, as discussed in section 3.3.5 and section 5.6 of Chapter 3 and Chapter 5, respectively. Even though, these evaluation studies give knowledge about the credibility of a multi-element antenna for a MIMO communication system, to understand the end-to-end performance of the system employing multiple antennas, in a realistic environment, an Over The Air (OTA) test is essential. The European Cooperation in Science and Technology (COST) 2100, 3rd Generation Partnership Project (3GPP) RAN WG4 and the Cellular Telecommunications Industry Association (CTIA) conducted numerous studies on different approaches to perform this task. The currently available major test methodologies to conduct MIMO OTA test are:

- **Multi-probe anechoic chamber method**, [146]: The principle behind this method is to create an adequate channel model with the help of multiple probe antennas, which are placed at arbitrary positions inside an anechoic chamber, at equal distances from the Device Under Test (DUT). Thus, each antenna will be faded by the channel emulator to obtain the desired temporal component. A system level block diagram of multi-probe configuration
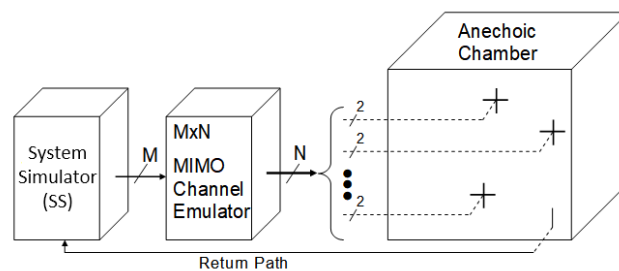
Fig. 6.1 Multi-probe OTA testing method (TR 37.976 [8])

method for OTA tesing is shown in Fig. 6.1.The key components in the for this OTA tesing are:

– Anechoic Chamber

– System Simulator (SS)

– N channel RF emulator, with OTA Channel Generation Features

– N antenna elements configured with V, H or co-located V & H or slant X polarizations

– K azimuthally separated antenna positions with predefined angles at radius R

– Channel Model definition for each test case
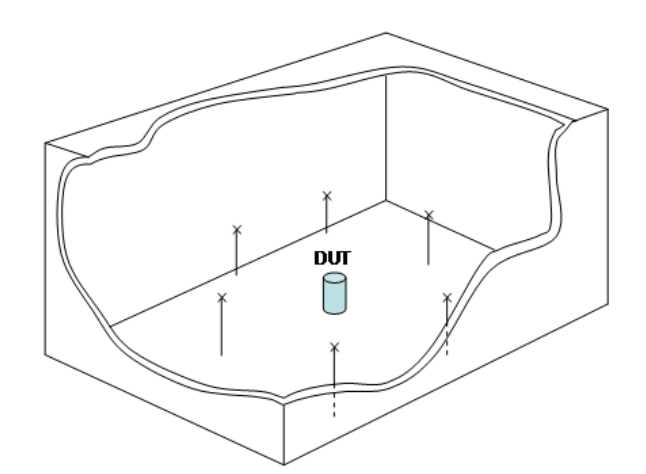
Fig. 6.2 N-Element Anechoic Chamber (Absorbing tiles and cabling not shown) (TR 37.976 [8])

The anechoic chamber implementation is depicted in Fig. 6.2. It consist of a number of source elements surrounding the DUT to create a realistic geometric based spatio-temporal radio channel for testing MIMO performance. A range of potential channels are emulated by making use of specific geometries of test probes in an anechoic chamber. The number and positioning of the antenna probes (source) will be optimized for the best performance, while defining the OTA channel models. Thus, depending upon the range of parameters required for testing and types of adequate channel models, the possibly fewest number of probes are selected to attain the best performance. Generally, the most flexible configurations require the higher number of probes. As observed from the Fig. 6.1, the SS will

generate the M branch MIMO signal, and an RF Channel Emulator with an OTA Channel Generation Feature will properly correlate, fade, scale, delay, and distribute the signal to each test antenna probe in the chamber.

An accurate selection of the number and positioning of the antenna probes one can construct an arbitrarily complex radio propagation environment. This is a conceptually simple method as it has a direct relationship between the required angular spread of the channel and the position of antenna probes. In its simplest configuration, the probes would be located along the azimuthal plane to build a 2D (two-dimensional) environment. Complex 3D environment can also be created by placing additional probes along different planes. In both the cases to test the DUT from all the required angles, it must be mounted on a rotating and tilting platform.

A range of potential channel models and parametrizations will be used to define the most versatile and generic source test probe configuration. The channel model is proposed to be limited in scope or simplified for the proper performance and conformance testing. This will optimize the design and allow it to reduce the number of test probes needed. Therefore, the number of test antenna probes will be picked to meet the best requirements of the test so that the most economical and efficient design can be realized. However, the major demerit of this methodology is the increase in complexity and cost when the number of test probes are increased, compared to the other testing methods.

- **Reverberation chamber method**, [45, 59]: This method is capable of conducting the MIMO OTA testing hastily. It utilizes the intrinsic reflective properties of a mode-stirred reverberation chamber to set up a rich complex multipath signal from a test signal given as input. The pictorial representation of reverberation chamber method is shown in Fig. 6.3. This test setup for receiver diversity performance evaluation consists of a base station emulator, a reverberation chamber equipped with fixed BS wall-mounted antennas, a switch to direct the base station signal to/from one of the BS wall mounted antennas, mechanical metallic stirrers and a rotating platform to hold the DUT. The reverberation chamber is a metallic cavity which can emulate an isotropic multi-path environment.
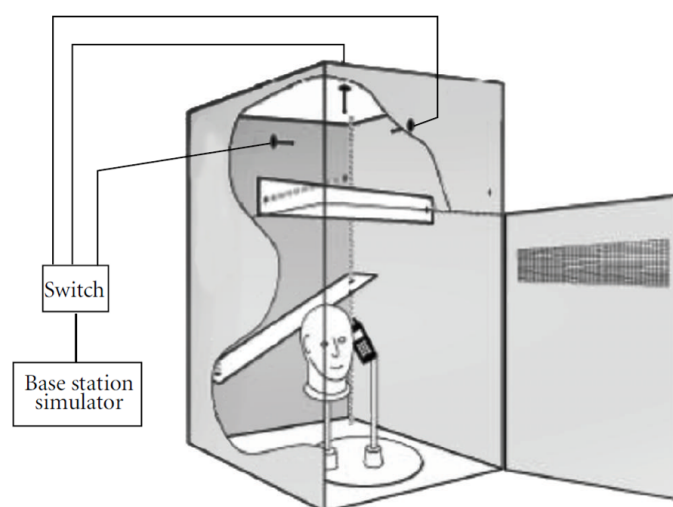
Fig. 6.3 Single cavity Reverberation chamber setup for MIMO OTA testing (TR 37.976 [8])

This environment can act as a reference environment for systems designed to work during fading. This is similar to how the free space "anechoic" reference environment is used for tests of Line-Of-Sight systems. Creating a Rayleigh propagation environment in a reverberation chamber is close to the realistic urban and indoor environments. There is no quiet-zone in reverberation chamber, but as long as the position of DUT is at-least 0.5λ from the chamber walls or metallic stirrers, same result will be obtained within the standard deviation of the chamber. This method produces random spatial characteristics for the signal and thus, enables spatial multiplexing gain due to the diverse signals on each antenna of DUT. The in-built time-domain response of the chamber can be altered by the inclusion of some RF absorptive materials in the reverberation chamber.With the help of mechanical stirrers and corresponding switching of different antenna terminals inside the chamber, the Rayleigh fading is simulated within the chamber. By rotating the device holding platform the accuracy can be further increased. Thus, each position of mechanical stirrers for different platform angles and each fixed BS antenna can represent an arbitrary point of the Rayleigh fading distribution in terms of the received power on the

device antenna. Thereby, a Rayleigh fading is created artificially. From this faded signal the various channel characteristics can be computed. This method provides a fast and repeatable testing way, to evaluate and compare multiple-antenna devices in the mostly using environment, which is crucial for a multi-antenna OTA measurement standard.

- **Two-stage method**, [96]: This two-stage method takes a different approach to conduct the OTA testing of DUT. This method is based on the assumption that the far-field radiation patterns of a MIMO antenna can completely capture the mutual coupling between the antenna-elements and their influence. Thus it is needed to measure the antenna patterns accurately, and for an inactive device the chipset needs to support both amplitude and relative phase measurements. As the name indicates it has two-stages of operation.

In first stage the multiple-antenna system is tested in a traditional anechoic chamber. The DUT is placed inside the chamber using proper positioner, which makes it possible to conduct full three-dimensional far-field radiation pattern measurements for both Txr and Rxr radiated performance. Thus, the 3D far zone pattern are obtained using the conventional SISO measurement way inside an anechoic chamber. Also, it should be possible to measure two orthogonal polarizations (θ and ϕ components as shown in Fig. 6.4) of the multi-element antenna system.

In the second stage, these patterns are convolved with the appropriate MIMO channel model using a channel emulator to create a real channel faded signal from the DUT. This signal is then utilized to evaluate the channel performance of a system employing DUT. The MIMO OTA testing based on two-stage method is illustrated in the Fig. 6.5. A commercial Channel Emulator can emulate the integrated MIMO channel model with both multiple-antenna effect & its multipath channel effect. These faded signals are then send to BS emulator and then to MIMO DUT ports via RF cables to evaluate the further channel characteristics.

This method is adopted to investigate the end-to-end channel performances of the UWB-MIMO antennas discussed in this thesis. The detailed descrip-
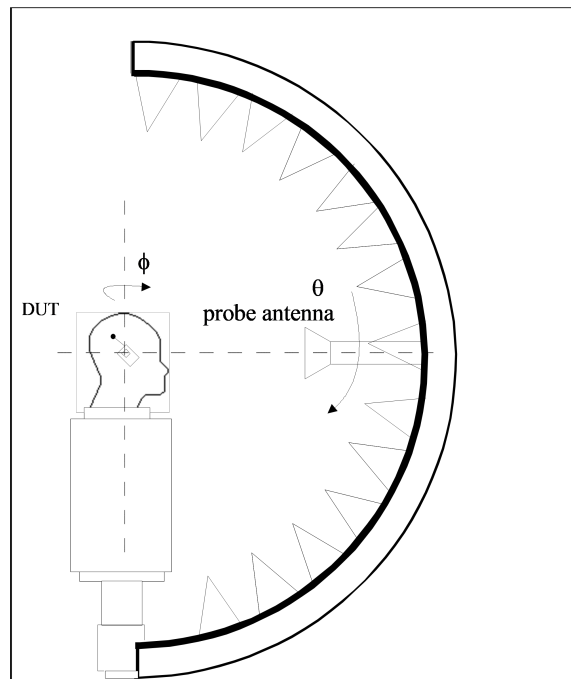
Fig. 6.4 Pattern measurement setup (TR 37.976 [8])
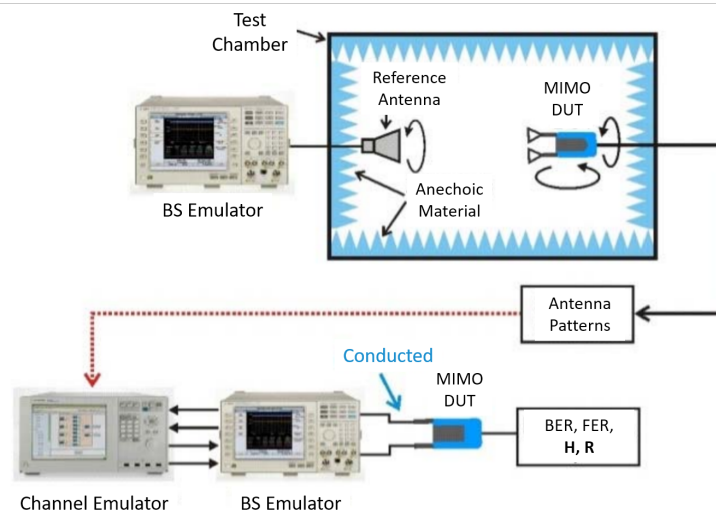
Fig. 6.5 Two-stage MIMO OTA testing method (TR 37.976 [8])

tion about the analysis methods using two-stage method is given in the coming sections.

6.1 The Two-Stage OTA analysis of UWB-MIMO antennas

This section deals with the whereabouts of two-stage OTA method used for the channel performance evaluation of the developed UWB-MIMO antennas. In order to perform this Keysight SystemVue software [7] is utilized, which is a powerful system architecture for analysing antenna performances in a propagation environment. The MIMO Channel Builder of SystemVue can simulate the multi-channel fading by incorporating the antenna patterns. Thus, this two-stage OTA testing method is an efficient alternative to the live hardware method of OTA testing, as it is both economical and repeatable. The two stages involved in this method are depicted in Fig. 6.6 and they are:

1. The radiation patterns of each antenna-elements in a multi-antenna system is obtained either by using the traditional anechoic chamber or using the CST Microwave studio EM simulation software.

2. These radiation patterns are then loaded into the SystemVue MIMO Channel models and these models are then emulated with the incorporated patterns. The SystemVue MIMO Channel model Builder has two different approach to integrate the radiation patterns with MIMO Channel model. One approach is to use a correlation-based model and other is to use the WINNER (Wireless world initiative new radio) II channel model.

After these two stages the real faded channel signal will be obtained, which can then be used to measure MIMO channel capacity, throughput, BLER (Block Error Rate), antenna correlation, CQI (Channel Quality Indicator) etc., [8], of the multi-antenna system. These analysis can also be performed for the case of two channel models: correlation-based channel and WINNER II channel. The detailed description of both these channel models are given in the next section.

6.2 Different Channel Model Approaches

As mentioned above SystemVue's MIMO Channel builder has two channel model approaches, which are used to emulate the antenna patterns with. The two
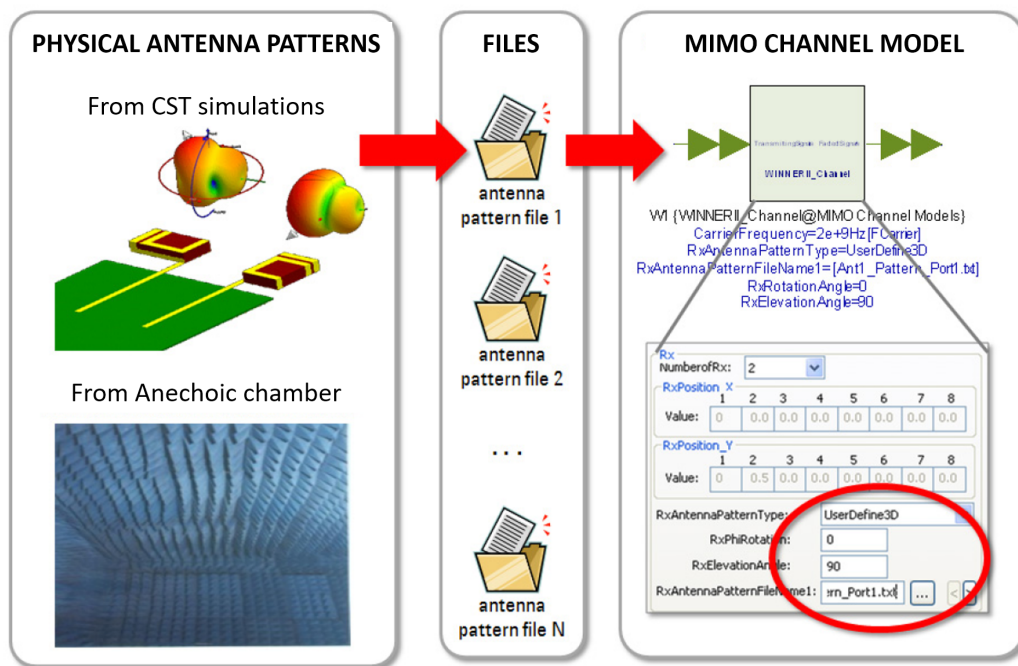
Fig. 6.6 Two-stage SystemVue analysis procedures

Channel models that are used to evaluate the developed UWB-MIMO antennas are:

6.2.1 Correlation-based MIMO Channel Model

The correlation-based channel model is a flexible model for user, in terms of its customization. In this channel model, a correlation matrix composing of the correlations between the different paths of a given channel to be modelled is formed. For the afore mentioned two-stage OTA testing method this model is suitable as it can combine the spatial properties of multiple paths with the spatial characteristics of the transmitter and receiver antenna arrays. Thus for the given antenna radiation patterns, the spatial correlation matrix is given by, [169],

$$\rho_{Tx,mn} = \frac{\int_{-\pi}^{+\pi} e^{-j2\pi \frac{d_{mn}}{\lambda} sin(\theta)} PAS_{Tx}(\theta) \sqrt{G_{Tx,m}(\theta) G_{Tx,n}(\theta)} d\theta}{\sqrt{\int_{-\pi}^{+\pi} PAS_{Tx}(\theta) G_{Tx,m}(\theta) d\theta} \sqrt{\int_{-\pi}^{+\pi} PAS_{Tx}(\theta) G_{Tx,n}(\theta) d\theta}} \tag{6.1}$$

$$\rho_{Rx,mn} = \frac{\int_{-\pi}^{+\pi} e^{-j2\pi\frac{d_{mn}}{\lambda}sin(\theta)} PAS_{Rx}(\theta)\sqrt{G_{Rx,m}(\theta)G_{Rx,n}(\theta)}d\theta}{\sqrt{\int_{-\pi}^{+\pi} PAS_{Rx}(\theta)G_{Rx,m}(\theta)d\theta}\sqrt{\int_{-\pi}^{+\pi} PAS_{Rx}(\theta)G_{Rx,n}(\theta)d\theta}} \tag{6.2}$$

where $PAS(\theta)$ is the power azimuth spectrum of the impinging signal, $G(\theta)$ is the power gain of the radiation pattern. The basic Kronecker model assumes that the transmitter and receiver terminals are uncorrelated and therefore, the spatial correlation matrix R_s can be formulated as,

$$R_s = \frac{1}{tr\{R_{Rx}\}}R_{Tx} \otimes R_{Rx} \tag{6.3}$$

where, $\otimes$ denotes the Kronecker product and R_{Tx} & R_{Rx} are the $N_t \times N_t$ and $N_r \times N_r$ matrices of the spatial correlations of multiple antenna arrays at the receiver and transmitter sides, respectively. The joint correlation matrix R is then given by [34],

$$R = R_s \bullet R_p \tag{6.4}$$

where, R_s is the spatial correlation matrix and R_p is the polarization correlation matrix. The channel coefficients H_s can be generated by

$$H_s = \sqrt{R}H_u \tag{6.5}$$

where, H_u represents the spatially uncorrelated Rayleigh fading sample and that is temporal correlated by the Doppler spectrum.

The Kronecker assumption may not be valid for the generic antenna array. Thus, SystemVue software improved the correlation model based on the basic Kronecker model, by developing a proprietary algorithm that calculates the spatial-polarization and joint correlation characteristics. This algorithm was practically validated and shows that it is an good fit for realistic antennas, [7].

This expanded method can include the effect of different types of antenna-elements and also is compatible with the basic Kronecker model. It offers a flexible method to analyse the antenna performance and its channel effects. In addition to these all, the correlation model admits the user to customize the parameters such as, Angular Spread, different power angular spectrum, Power

Delay Profile (PDP), antenna patterns etc., which helps the users to evaluate their system and antenna performances under varying channel environments.

6.2.2   WINNER II MIMO channel model

The WINNER II channel model is a geometry-based stochastic channel model and is also called as double directional channel model [7, 108]. This approach is used mainly to create a radio channel model which helps in evaluating the link level and system level performances of many wireless communication systems. In this model the locations of scatters won't be specified explicitly, rather it will give informations on the directions of rays. This geometry based modeling of radio channel enables insertion of different antenna configurations, separation of propagation parameters & antennas and diverse patterns of antenna elements. The time variant impulse response matrix of the $U \times S$ MIMO channel is given by [7],

$$H(t;\tau) = \sum_{n=1}^{N} H_n(t;\tau) \tag{6.6}$$

This is the channel impulse response from transmitter antenna element s to the receiver antenna u, where, t is time, τ is delay, N is the number of paths, and n is path index. The impulse response matrix is composed of the antenna array response matrices F_{Tx} and F_{Rx} for the transmitter (Txr) and the receiver (Rxr), respectively. Thus, the channel from the Txr antenna element s to the Rxr element u for cluster n, can be formulated as

$$
\begin{aligned}
H_{u,s,n}(t;\tau) = \sum_{m=1}^{M} & \begin{bmatrix} F_{Rx,u,V}\big(\varphi_{n,m}\big) \\ F_{Rx,u,H}\big(\varphi_{n,m}\big) \end{bmatrix}^T \begin{bmatrix} \alpha_{n,m,VV} & \alpha_{n,m,VH} \\ \alpha_{n,m,HV} & \alpha_{n,m,HH} \end{bmatrix} \begin{bmatrix} F_{Tx,s,V}\big(\phi_{n,m}\big) \\ F_{Tx,s,H}\big(\phi_{n,m}\big) \end{bmatrix} \\
& \times exp\Big(j2\pi\lambda_0^{-1}\big(\bar{\varphi}_{n,m}\cdot\bar{r}_{Rx,u}\big)\Big)\ exp\Big(j2\pi\lambda_0^{-1}\big(\bar{\phi}_{n,m}\cdot\bar{r}_{Tx,s}\big)\Big) \\
& \times exp\Big(j2\pi\upsilon_{n,m}t\Big)\delta\Big(\tau - \tau_{n,m}\Big)
\end{aligned}
\tag{6.7}
$$

Where:

- $F_{Rx,u,V}$ and $F_{Rx,u,H}$ are the antenna element u field patterns for vertical and horizontal polarizations, respectively;

- $F_{Tx,s,V}$ and $F_{Tx,s,H}$ are the antenna element s field patterns for vertical and horizontal polarizations, respectively;

- $\alpha_{n,m,VV}$, $\alpha_{n,m,VH}$, $\alpha_{n,m,HV}$ and $\alpha_{n,m,HH}$ are the complex gains of vertical-to-vertical, horizontal-to-vertical, vertical-to-horizontal and horizontal-to-horizontal polarizations of ray n, m, respectively;

- λ_0 is the wavelength of the carrier frequency;

- $\bar{\phi}_{n,m}$ is the AoD unit vector;

- $\bar{\varphi}_{n,m}$ is the AoA unit vector;

- $\bar{r}_{Tx,s}$ and $\bar{r}_{Rx,u}$ are the location vectors of element s and u, respectively; and

- $\upsilon_{n,m}$ is the Doppler frequency component of ray n, m.

If the radio channel is modelled as dynamic, all the above mentioned small scale parameters are time variant, i.e. function of t.

The propagation environments used is WINNER II channel model are called the propagation scenarios. The WINNER II model cover a wide scope of propagation scenarios and in SystemVue model for 18 such scenarios are developed, that are classified into three: Local, Metropolitan and Wide area [7]. This WINNER II channel model are independent of antennas and are appropriate for the evaluation of transceiver techniques such as equalization, adaptive radio links, modulation and coding. This model is also helpful for link budget calculation and network planning.

6.3   Channel Capacity Measurements

The channel performance analysis and comparative study of the developed UWB-MIMO antennas are carried out with the help of SystemVue software. The channel capacity measurement setup of SystemVue has two steps of analysis. First step is

the generation of correlation matrix by incorporating the radiation patterns of the UWB-MIMO antenna, using the afore mentioned channel model approach. The second step deals with the calculation of channel capacity utilizing the generated correlation matrix corresponding to the Antenna Under Test (AUT). The detailed explanations regarding these two steps are given below.

The correlation matrix generation follows the two-stage analysis method depicted in Fig. 6.6. In the first stage the three dimensional radiation patterns of the developed UWB-MIMO antennas are obtained either from anechoic chamber or from CST Microwave studio simulations. The patterns of each antenna element are saved in separate files. These radiation pattern files are then converted to *.uan format as particularized by the SystemVue. This file format consists of two parts: a parameter description section and a data section. The parameter description section is the header section of the file and the parameter details required for the proper data reading is explained here. An example of such a parameter section used in this thesis is described below:

```
begin_<parameters>
format free
phi_min 0
phi_max 360
phi_inc 5
theta_min 0
theta_max 180
theta_inc 5
complex
mag_phase
pattern gain
magnitude dB
direction degrees
phase degrees
polarization theta_phi
NetInputPower 0.002309593
end_<parameters>
```
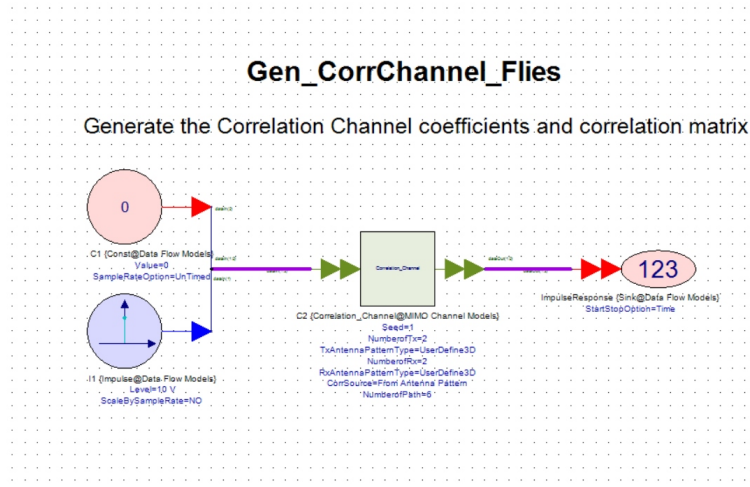
(a) Correlation-based MIMO Channel model
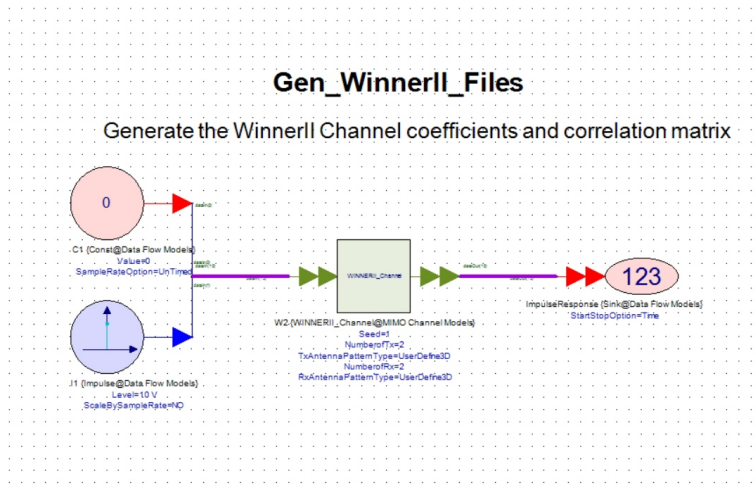
(b) WINNER II MIMO Channel model

Fig. 6.7 MIMO Channel Builders in SystemVue

Thus, this section gave information about the maximum and minimum values of phi and theta angles, the step size with which pattern is obtained, in which format the data is present in the file (magnitude_phase or real_Imaginary), polarization of the antenna, net input power etc.. The data section (corresponding to the above parameter section) will have four columns: theta-angles, phi-angles, theta-gain, phi-gain, theta-phase and phi-phase. Thus, this section has the magnitude (dB) and phase (degrees) values of the far-field radiation patterns, for different theta and phi rotations.

These radiation pattern files and the information regarding number of antenna elements are given to the MIMO channel Builder in the SystemVue software. In this channel builder the user defined radiation patterns are convolved with the channel models to generate the real faded correlation channel coefficients and correlation matrix. Based upon the channel model with which the convolution takes place, two types of correlation matrices are formed in SystemVue. They are correlation-based channel matrix and WINNER II channel matrix. The analysis setup of both are depicted in Fig. 6.7, for a 2x2 MIMO system. According to the number of paths assigned by user, the generated correlation matrix will be a $K \times N$ array, where K is $No.of\ Txr\ antennas\ *\ No.of\ Rxr\ antennas$ and N is $No.of\ Txr\ antennas\ *\ No.of\ Rxr\ antennas\ *\ No.of\ paths$. Thus, the so formed correlation matrices will be saved as three text files, in the specified directory. Out of that, one will be the combined correlation matrix with MIMO antenna gain and power imbalance information for all paths and for all drops. The other two files corresponds to the real and imaginary parts of the correlation matrix.

The channel capacity calculation model utilizes these real and imaginary parts of correlation matrix to calculate the channel capacity of a system. The two capacity models corresponding to the correlation-based channel model and WINNER II channel model are shown in Fig. 6.8. Therefore, these models are used to compute the channel capacity for the MIMO channel, based on the channel correlation matrix and channel coefficients. This model reads two files which have informations regarding number of samples of the drops and real & imaginary parts of corresponding channel correlation matrix R, which is a Kronecker product of transmit and receive correlation matrices. The R is of size $K \times K$, where K is $No.of\ Txr\ antennas\ *\ No.of\ Rxr\ antennas$. This channel correlation matrix R combines all the paths together. The length of the generated channel coefficients is determined by the number of samples given as input.

For the case of a 2×2 MIMO, the combined channel coefficient is

$$\begin{bmatrix} Txr_1Rxr_1 & Txr_2Rxr_1 \\ Txr_1Rxr_2 & Txr_2Rxr_2 \end{bmatrix} \tag{6.8}$$
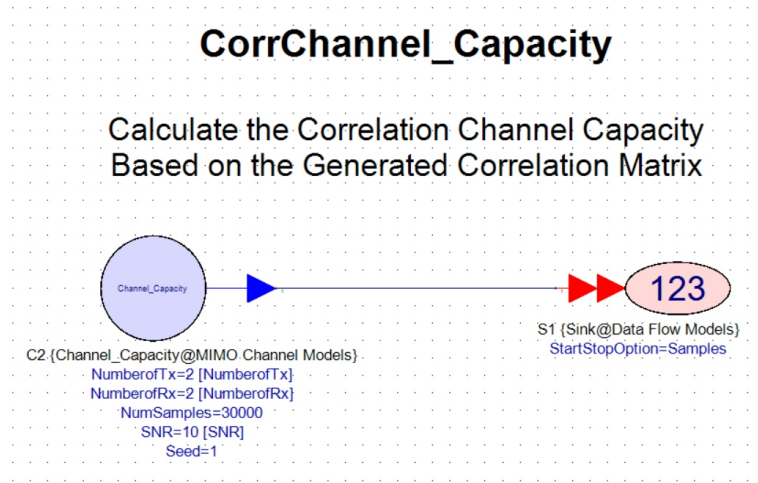
(a) Correlation Channel Capacity model
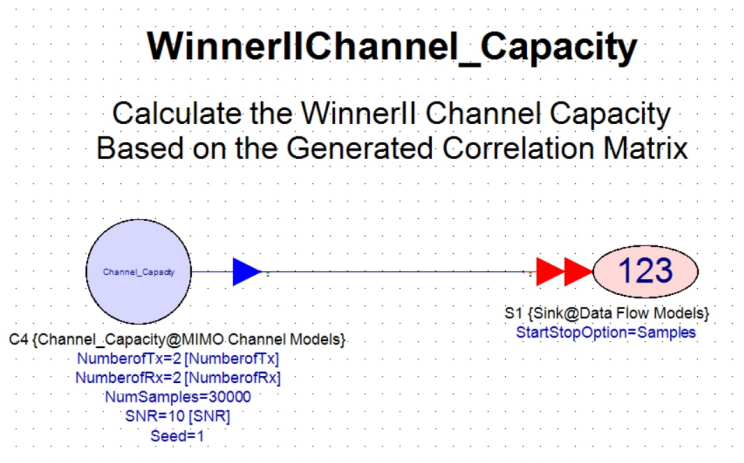
(b) WINNER II Channel Capacity model

Fig. 6.8 Channel Capacity models in SystemVue

and the combined correlation matrix is

$$
\begin{bmatrix}
Txr_1Rxr_1 \\
Txr_1Rxr_2 \\
Txr_2Rxr_1 \\
Txr_2Rxr_2
\end{bmatrix}
\times
\begin{bmatrix}
Txr_1Rxr_1 & Txr_1Rxr_2 & Txr_2Rxr_1 & Txr_2Rxr_2
\end{bmatrix}^*
\tag{6.9}
$$

Thus, the 16 float elements of each file, which is the real or imaginary part of the correlation matrix, is given by $Txr_1Rxr_1 \times Txr_1Rxr_1, Txr_1Rxr_1 \times Txr_1Rxr_2, \ldots Txr_1Rxr_1 \times Txr_2Rxr_2, Txr_1Rxr_2 \times Txr_1Rxr_1, \ldots Txr_2Rxr_2 \times Txr_2Rxr_2$. Hence, the channel capacity is then calculated by, [66],

$$C = \log_2 \det \left[I + \frac{\rho}{N} HH^H \right] (bits/s/Hz) \qquad (6.10)$$

where, ρ is the Signal-to-Noise Ratio (SNR) in dB, N is the number of transmitter antennas, H is the transfer matrix which is the Cholesky decomposition of R multiply channel coefficients.

By following the above described steps, the channel capacities of the three developed UWB-MIMO antennas (AUTs) are computed, and are compared with the channel capacities obtained for an ideal 2×2, 3×3 and 4×4 MIMO systems employing half-wavelength separated omni-directional antennas. The channel capacities obtained for ideal antenna systems are taken as the reference for other capacity calculations, and these calculations incorporates the antenna array performance as well as the correlation between them [221].

The three-dimensional radiation patterns of the two-port, three-port and four-port UWB-MIMO antennas discussed in section 5.1, 5.2 and 5.3 are obtained for 4 GHz and 8 GHz, respectively. These radiation patterns are then loaded to SystemVue and the corresponding channel capacities are calculated for both correlation-based and WINNER II MIMO channel models. These capacity values are then plotted for varying SNR values from 0 to 30 dB, and are compared with the respective ideal (or reference) scenarios. The channel capacity measurements for correlation-based channel model of the two-port UWB-MIMO antenna (in section 5.1) at 4 GHz and 8 GHz are potted in Fig. 6.9a and 6.9b, respectively. It is observed from the figure that, the channel capacity increases from 1.4 bits/s/Hz to 10.7 bits/s/Hz for 4 GHz and from 1.8 bits/s/Hz to 15.5 bits/s/Hz for 8 GHz, for a SNR sweep from 0dB to 30dB.

The correlation-based channel capacity of three-port UWB-MIMO antenna (in section 5.2) employing spatial, polarization and angle diversity is shown in Fig. 6.10. For this antenna, the capacity stood at 3.2 bits/s/Hz at a SNR of 0 dB and got increased to 23.5 bits/s/Hz while the SNR reached 30 dB, at 4 GHz (see
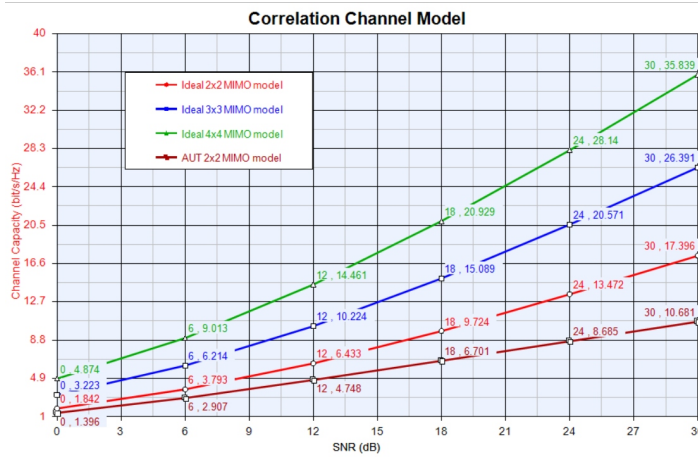
(a) At 4 GHz
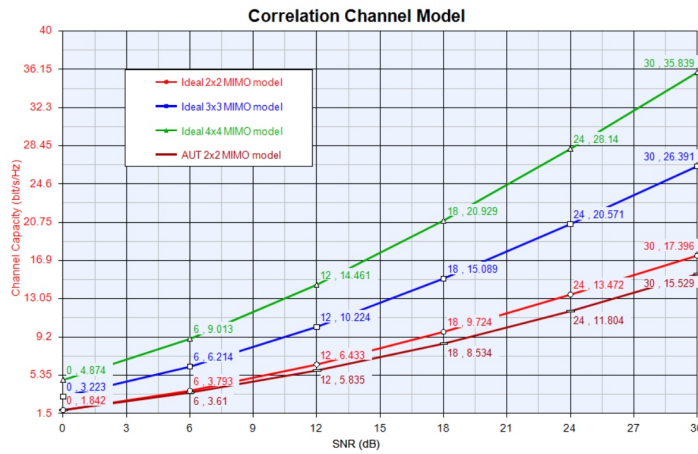
(b) At 8 GHz

Fig. 6.9 Channel Capacity of Two-port UWB-MIMO antenna for Correlation-based Channel model

Fig. 6.10a). At 8 GHz, the channel capacity showed variation from 3.2 bits/s/Hz to 23 bits/s/Hz for a 0-30 dB SNR variation, as shown in Fig. 6.10b.

For the quad-element UWB-MIMO antenna (in section 5.3) the channel capacity for a correlation-based model showed improvement from 4.9 bits/s/Hz to 28.2 bits/s/Hz for an SNR range of 0 dB to 30 dB, at 4 GHz. And, for 8 GHz it ranged from 4.9 bits/s/Hz to 28.4 bits/s/Hz for SNR values from 0 dB to 30 dB.
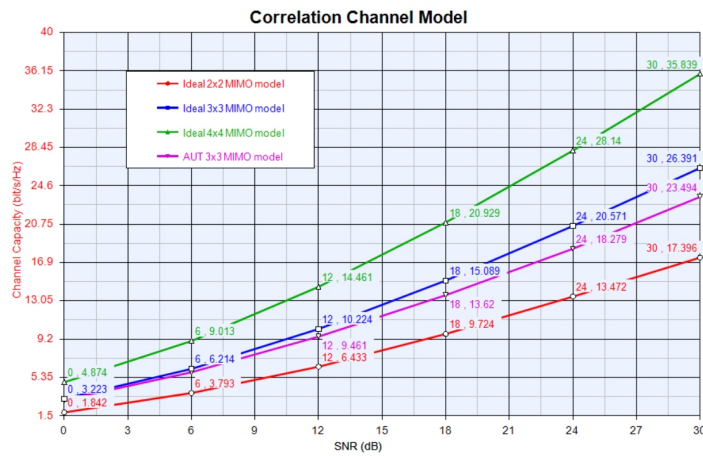
(a) At 4 GHz
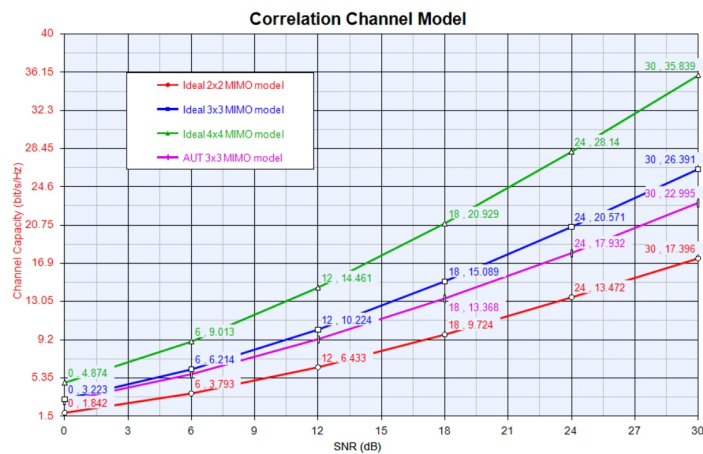
(b) At 8 GHz

Fig. 6.10 Channel Capacity of Three-port UWB-MIMO antenna for Correlation-based Channel model

Similarly, the channel capacities of the UWB-MIMO antennas for WINNER II channel model are also computed for 4 GHz and 8 GHz. The results are depicted in Fig. 6.12, Fig. 6.13 and Fig. 6.14 for two-port, three-port and four-port UWB-MIMO antennas, respectively. It is observed from the figure that, WINNER II channel model possess competitively less channel capacity than that for correlation-model. This is because in WINNER II channel model an urban macro-cell scenario is modeled, which is more closer to a realistic environment. For a 2×2 MIMO system with the developed two-port antenna, the channel
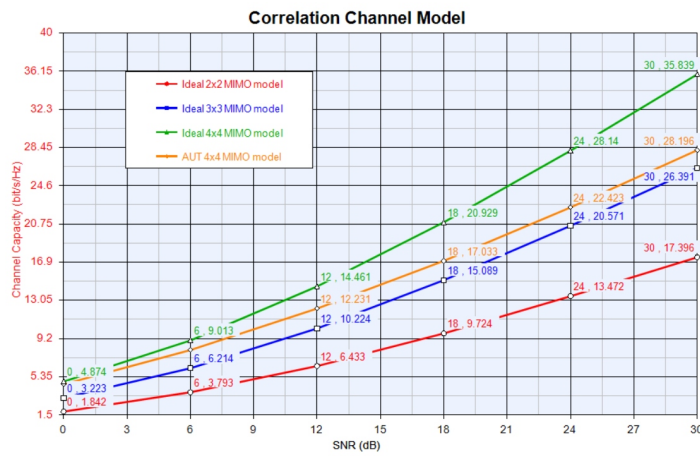
(a) At 4 GHz
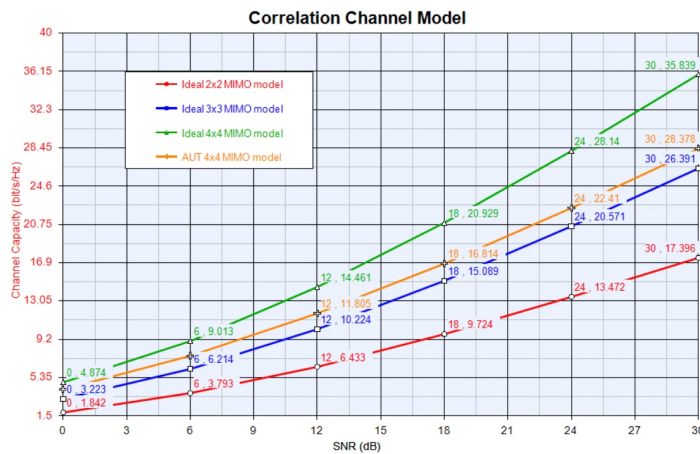
(b) At 8 GHz

Fig. 6.11 Channel Capacity of Four-port UWB-MIMO antenna for Correlation-based Channel model

capacity is found to be increasing from 1.3 bits/s/Hz to 12.5 bits/s/Hz for a SNR range of 0 to 30 dB, at 4 GHz (Fig. 6.12b). In the case at 8 GHz, the capacity stood high at 13.9 bits/s/Hz for a SNR value of 30 dB, as shown in Fig. 6.12b.

The channel capacity analysis of the three-port UWB-MIMO antenna at 4 GHz and 8 GHz is shown in Fig. 6.13. The figure shows values ranging from 2.2 bits/s/Hz to 19.3 bits/s/Hz for a SNRs ranging from 0 dB to 30 dB, at 4 GHz. And, for 8 GHz the capacity increased from 2.2 bits/s/Hz to 19.5 bits/s/Hz for SNR from 0 dB to 30 dB.
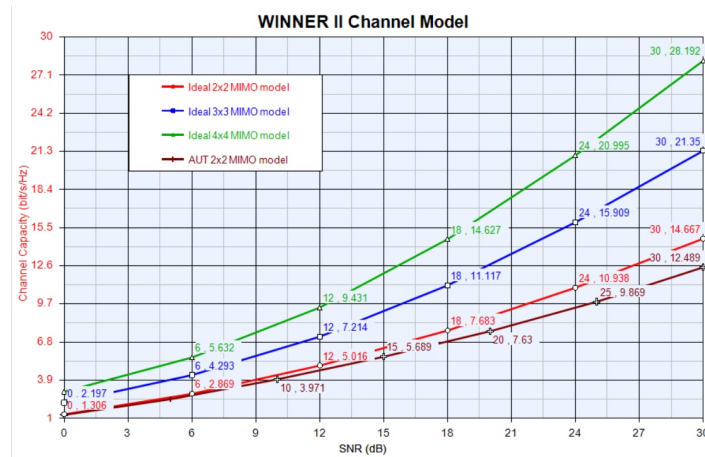
(a) At 4 GHz
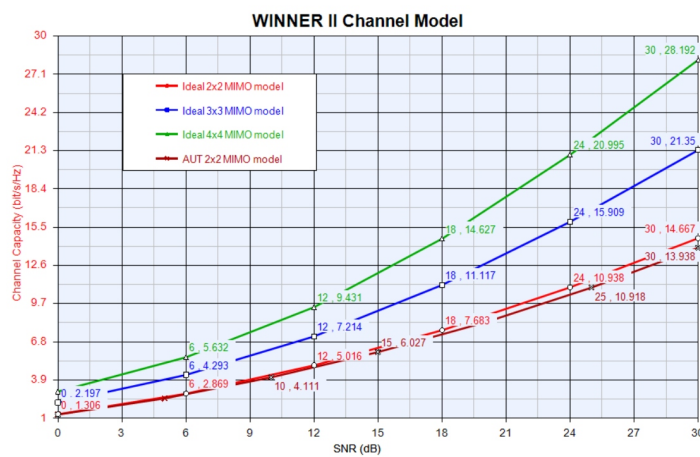
(b) At 8 GHz

Fig. 6.12 Channel Capacity of Two-port UWB-MIMO antenna for WINNER II Channel model

The channel capacity of the four-port UWB-MIMO antenna using WINNER II channel model with varying SNR values ranging from 0 dB to 30 dB shows a capacity improvement from 2.2 bits/s/Hz to 24.8 bits/s/Hz, at 4 GHz. And, at 8 GHz this increment is from 2.2 bits/s/Hz to 25.5 bits/s/Hz for the same SNR range of 0-30 dB. The capacity measures of this four-port antenna at 4 GHz and 8 GHz are shown in Fig. 6.14a and 6.14a, respectively.

From all the channel capacity calculations, it can be inferred that, the channel capacities of the 4×4 MIMO system, using the four-port antenna, are greater as
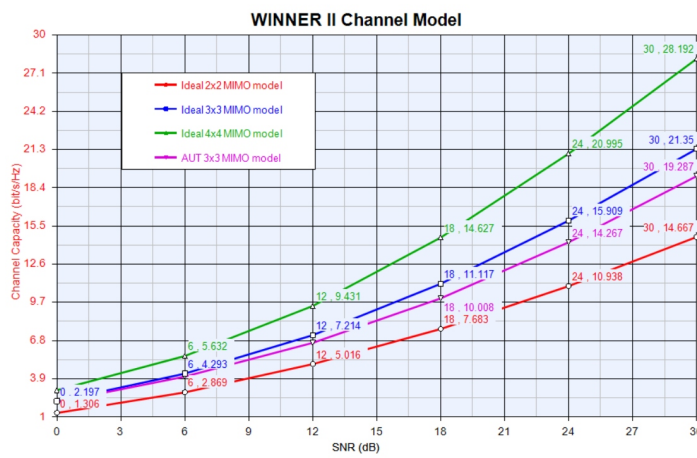
(a) At 4 GHz
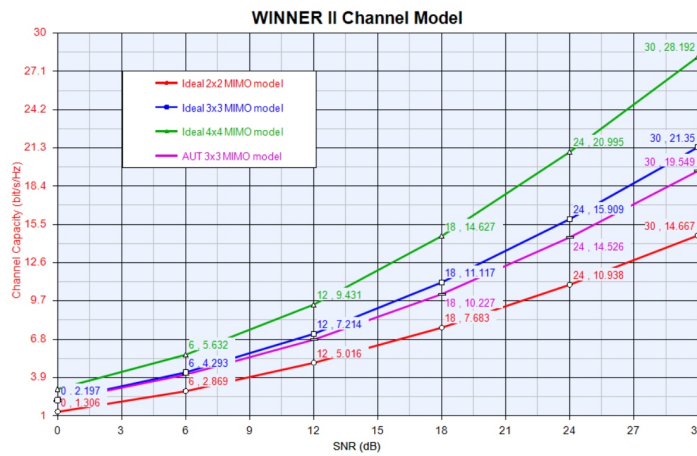
(b) At 8 GHz

Fig. 6.13 Channel Capacity of Three-port UWB-MIMO antenna for WINNER II Channel model

compared to that of 3×3 and 2×2 systems. Also, on comparing the capacity performances of correlation-based and WINNER II channel models, WINNER II shows low capacities for the system employing same MIMO antennas, as it is a geometry-based model which corresponds well with the practical propagation scenarios. Thus, for a UWB-MIMO communication system employing the developed antennas, the channel capacity increases with the number of antenna-elements at both transmitter and receiver side.
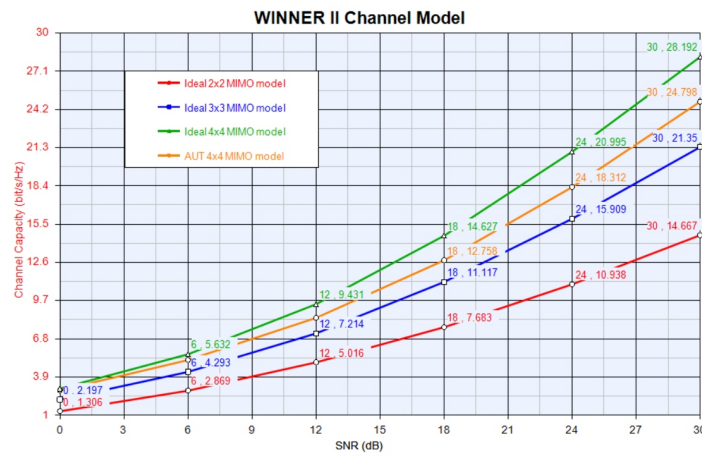
(a) At 4 GHz
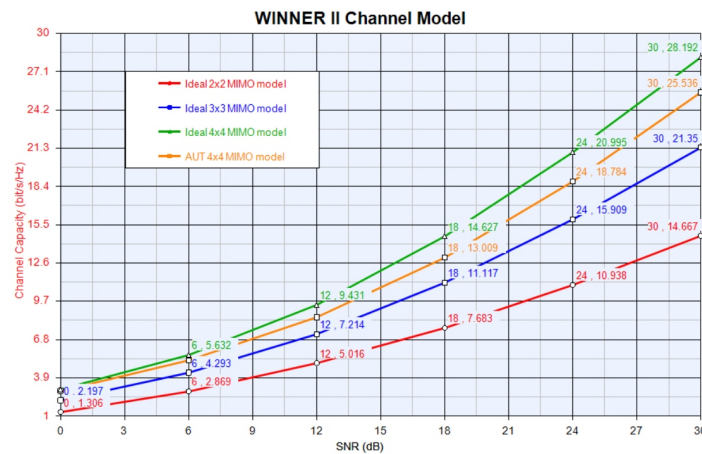
(b) At 8 GHz

Fig. 6.14 Channel Capacity of Four-port UWB-MIMO antenna for WINNER II Channel model

6.4 Chapter Summary

This chapter discussed the channel performance evaluation of the developed UWB-MIMO antennas. The channel performances of the antennas in both correlation-based channel and WINNER II channel were analysed. Also, the channel response of the three UWB-MIMO antennas are compared with the respective ideal scenarios with the help of antennas with omnidirectional radiation patterns. From the above evaluations and comparative studies it can be inferred that the developed UWB-MIMO antennas are capable of exhibiting satisfactory

channel performances, needed for a good communication system. Moreover, the analysis in the chapter validated that as the number of antenna-elements increases the channel capacity of that system also increases. Thus, the 4×4 UWB-MIMO antenna system will perform with a better channel capacity as compared to the 2×2 and 3×3 UWB-MIMO systems. Also, the capacities of all the multi-port antennas conform well with the reference multi-antenna system having omni-directional radiation patterns.

Chapter 7

Conclusion and Future Perspective

This chapter summarizes the conclusions and major findings came out of the study conducted on UWB-MIMO antennas discussed in this thesis. This is followed by some thoughts about the future scope of the works based on UWB-MIMO antennas.

7.1 Conclusions

The main objective of the thesis was to develop multiple-element antennas for UWB-MIMO applications, and to investigate their radiation characteristics in favour of the aforesaid applications. This thesis presented the basic trends in wireless communication which eventually lead to the invention of two leading wireless technologies: UWB and MIMO. A brief introduction about the UWB technology and their basic concepts were also discussed. The regulations that were framed for their application in different propagation environment, were included. Similarly, various aspects of MIMO technology along with different MIMO communication techniques were discussed briefly in this thesis. Principally, the thesis presented the scope of incorporating UWB technology with MIMO communication and their benefits. Moreover, various methodologies adopted to develop the antennas and to investigate them accordingly, were deliberated concisely.

For the realization of co-located UWB-MIMO antennas, two compact coplanar antennas were built, which are capable of giving efficient transmission/reception over the UWB range of operation. Utilizing these two UWB antennas, three co-located UWB-MIMO antennas were developed and validated their capabilities for operation in a MIMO communication system, for UWB applications. To accomplish best MIMO/diversity performance, a combination of spatial, polarization and angle diversity techniques were applied to the MIMO antennas. Also, a method of isolating the antenna-elements using a simple metal strip was included. Moreover, the evolution of the antenna structure were discussed in order to get an insight into their wideband, MIMO/diversity behaviour at each stage.

The performance analysis of UWB-MIMO antennas were carried out using distinct quality measures in different domain of computations. These include transfer properties, spatial-domain characteristics and figures-of-merit for effective MIMO behavioural evaluations. To have a knowledge about the channel characteristics of the MIMO communications system, employing the developed UWB-MIMO antennas, a two-stage OTA testing was conducted. A channel emulator software aided in accomplishing this OTA test using the farfield radiation patterns of the antenna and thus, evaluated the channel capacities of the developed UWB-MIMO antennas for varying SNR values. It is found that, the channel capacities of the communication systems increases as the number of elements in the transmitter/receiver increased.

In this thesis, two-port, three-port and four-port UWB-MIMO antennas were developed and analysed their performance characteristics. Their channel performance evaluation studies revealed that the UWB-MIMO system with four-port antenna at transmitter/receiver achieved more channel capacity compared to the other two.

7.2 Thesis Highlights

The key findings of the study conducted on various antennas are summarized in this section.

- **CPS fed UWB antenna:UWB-I** :- A coplanar stripline (CPS) fed UWB antenna was realized on a FR-4 substrate of thickness 1.6mm, ϵ_r of 4.3 and

tan(δ) of 0.02, in chapter 4. This antenna utilized the staircase-shaped slots and shorted slit at the bottom of the antenna to realize the wideband operation. The CPS-fed antenna is excited in its dipole mode, and a wideband operation covering the required UWB band (3.1 - 10.6 GHz) was obtained with the help of staircase-shaped slots and shorted slit at the bottom of the antenna. This antenna is very compact which has an overall size of $25mm \times 7mm$ only. It offered a wide bandwidth from 3 GHz to 11 GHz with an average gain of 2.15 dBi and radiation efficiency better than 75%, throughout the operation band. The antenna possessed omni-directional coverage in its lower UWB band and slightly directive radiation behaviour in the higher UWB band. The transfer properties of the antenna verified the capability of the antenna to handle pulse transmission/reception, without impinging any distortion to it. Moreover, the antenna retained stable radiation characteristics towards the 3.1 - 10.6 GHz band with the pattern stability factor (PSF) of 0.96 along azimuth plane and 0.93 along elevation plane.

- **ACS fed UWB antenna:UWB-II** :- Another coplanar UWB antenna using asymmetric coplanar strip (ACS) feeding technique is presented in chapter 4. The antenna is realized on a small profile of FR-4 substrate of size $25mm \times 10mm \times 1.6mm$, with ϵ_r of 4.3 and $tan(\delta)$ of 0.02. This antenna also utilized the principle of step-slots on its asymmetric lateral strips to achieve wide bandwidth. It offered a 2:1 VSWR bandwidth from 3 GHz to 12.5 GHz, thus covering the required 3.1 - 10.6 GHz bandwidth for UWB radio systems. Antenna showed partially omni-directional pattern in its lower UWB band and slightly directive patterns in its higher frequency band. Within the UWB band the antenna obtained an average gain of 2.6 dBi and radiation efficiency better than 75%. The time-domain analysis validated the antennas pulse handling capability and has group delay ≤1nS for Face-to-Face and Side-to-Side mode of transmission/reception. The antenna obtained PSF values of 0.97 and 0.9 along azimuth and elevation plane, respectively. This denoted that the best direction of operation of this antenna along its azimuthal plane.

- **Two-port UWB-MIMO antenna** :- By arranging two CPS-fed UWB antennas (UWB-I), one two-element UWB-MIMO antenna was realized and their performance characteristics was investigated in chapter 5 (section 5.1). The two antenna-elements are arranged back-to-back with a spatial separation of 16mm. This diversity in space reduced the mutual coupling between the elements across 7.5 - 11 GHz bandwidth. In addition to this, a metal strip of size $25mm \times 0.4mm$ placed between them provided an isolation improvement of about 10 dB across 3.1 - 7.5 GHz band, as compared to the geometry without metal strip. The two-port MIMO antenna for UWB application was realized on a small prototype of size $25mm \times 30mm$, and in-spite of its small size it obtained a minimum isolation of 20dB between the antenna-elements, throughout the UWB operation bandwidth of 3.1 - 10.6 GHz. Both the antenna-elements succeeded in reproducing the input pulses efficiently, as their transfer properties met the requirements. The metal strip between the elements acted as a reflector for the lower frequency band and improved the gain of the antenna for those frequencies. Due to the presence of reflector and the antenna configuration, the radiation pattern of both elements are slightly directive and are spatially separated by an angle of 180°. This helped the MIMO antenna to attain angle diversity across the UWB band with an average gain of 4.1 dBi and radiation efficiency better than 83% for both the ports. The addition of reflector strip made a gain improvement of 1 dBi possible, in the lower UWB band. The PSF values >0.96 in X-Z plane and >0.95 in the X-Y plane proved the pattern stability of the antenna in 3.1 - 10.6 GHz band. The ECC values of the two-port antenna is below 0.2 and MEG is found to be $\leq \pm 0.5dB$ throughout the UWB band. Also, the diversity gain (DG) matched well with the ideal scenario of 10dB and η_{mux} conformed well with the total efficiency of the antenna, which guaranteed good MIMO/diversity performance.

- **Three-port UWB-MIMO antenna** :- A three-element antenna suitable for the UWB-MIMO communication is realized by including the UWB-II in between the two-port antenna, discussed above. With the three UWB antenna-elements the overall size of the MIMO antenna became $25mm \times 45mm$ and achieved 2:1 VSWR bandwidth from 3.1 GHz to 11.3

GHz. Two antenna-elements were arranged back-to-back with adequate spatial separation and the third antenna element is placed orthogonally between them. This configuration of antenna-elements ensured a minimum isolation of 19dB between all the elements. All the radiation patterns are slightly directive and are directed towards three different directions, thus providing angle diversity for the MIMO antenna. Spatial, polarization and angle diversity mechanism are utilized in this MIMO antenna to obtain adequate inter-element isolation within the small profile. An average gain of 3.5 dBi and radiation efficiency >72% is obtained for the three-port antenna. Good transient transmission/reception were exhibited by the antenna and has stable radiation characteristics in the 3.1 - 10.6 GHz band. The antenna has PSF values of 0.95, 0.96 & 0.9 along X-Z plane and 0.95, 0.93, & 0.95 along X-Y plane for Ant1, Ant2 & Ant3, respectively. The criteria for good MIMO performance such as ECC<0.5, MEG$\leq \pm$3dB, DG$\cong$10dB & $\eta_{mux} \cong \eta_{tot}$ has been fulfilled by the three-port antenna.

- **Four-port UWB-MIMO antenna** :- By arranging four UWB-I antenna-elements, a quad-element UWB-MIMO antenna is created and its overall size is only $43mm \times 43mm$ on the FR-4 substrate, which is presented in chapter 5. This antenna exhibited good impedance matching from 3.1 GHz to 11 GHz, which enabled it to cover the required bandwidth for UWB radio systems. In addition to the four antenna-elements, one cross-shaped reflector is placed in the center of the antenna to isolate the antenna-elements along the axes. Moreover, two antenna elements are arranged orthogonally with respect to the other two elements. These arrangements of the antenna-elements and the cross-shaped reflector enabled the antenna to attain slightly directive radiation patterns to four different directions. Thus, along with the cross-reflector, the spatial, polarization & angle diversity enhanced the inter-element isolation of the antenna to be better than 20dB within the small size. The antenna offered a stable gain with a peak gain of 6.7 dBi and variation less than 2.2dBi within the UWB band. The radiation efficiency is found to be better than 80% in the UWB spectrum. The group delay of all the antenna-elements are below 1nS and PSF values are <0.95 in X-Z plane & <0.94 in X-Y plane. These ensured excellent transient

characteristics and stable patterns for the four-port UWB-MIMO antenna. Moreover, the ECC and MEG stayed below 0.2 and ± 0.5dB, respectively. Also, DG and η_{mux} conformed well with the ideal scenarios. These results ensured better MIMO/diversity performances of the four-port antenna.

- **MIMO Channel performance Evaluation** :- Using the two-stage OTA method the MIMO channel performance evaluation of the developed MIMO antennas are conducted from their far-field radiation patterns. The correlation-based and WINNER II MIMO channel models in the SystemVue are utilized to compute the channel capacities of the MIMO system employing these antennas. The channel capacities are obtained for different SNR values from 0dB to 30dB to authenticate and compare the performances of all the three UWB-MIMO antennas. The two-port UWB-MIMO antenna show a channel capacity of 10.7 bits/s/Hz at 4 GHz and 15.5 bits/s/Hz at 8 GHz for a SNR value of 30 dB, in the case of correlation-based MIMO channel. For WINNER II channel, the capacity is found to be 12.5 bits/s/Hz at 4 GHz and 13.9 bits/s/Hz at 8 GHz for a 30dB SNR value. In a correlation-based channel, the three-port UWB-MIMO antenna exhibited a channel capacity of 23.5 bits/s/Hz at 4 GHz and 23 bits/s/Hz at 8 GHz of operation, for 30dB SNR. Whereas, for WINNER II channel model, the capacity stood at 19.3 bits/s/Hz at 4 GHz and 19.5 bits/s/Hz at 8 GHz for a SNR value of 30dB. The channel capacity of a MIMO system with the quad-element UWB antenna exhibited high values of 28.2 bits/s/Hz at 4 GHz and 28.4 bits/s/Hz at 8 GHz for 30dB SNR, in the case of a correlation-based channel model. And, for WINNER II channel model the capacity remained at 24.8 bits/s/Hz at 4 GHz and at 25.5 bits/s/Hz at 8 GHz. The channel performance studies revealed that the capacities obtained for two MIMO channel models are different as well as the results of each UWB-MIMO antennas differ from one another. The correlation-based MIMO model exhibited better channel capacities compared to WINNER II model. This is because the WINNER II model is close to a real channel for an urban environment. It is concluded from the results that, the quad-element UWB-MIMO antenna possessed higher channel capacities for both channel models, compared to the other two. This capacity increase is attributed

to the principle of increase in channel capacity with increase in number of antennas at transmitter/receiver.

7.3   In Future...

The future of an antenna designing lies in fulfilling the upcoming needs of the modern wireless strategies. One of the crucial challenge is to make antennas, which possess the requirements such wide bandwidth, high efficiency & gain, high isolation & low correlation between the antenna elements etc., all in a small space. A trade-off between these basic requirements escalates the challenge mainly for wideband antennas. This results in many design constraints regarding the size and performance of the antenna.

In this thesis the time-domain analysis of UWB-MIMO antennas was carried out by taking measurements in frequency-domain and then undergoing Fourier Transform. The results will be more accurate if direct time-domain measurements are possible using pulse generator and spectrum analyzer.

As a future design technique the UWB-MIMO can be designed on Low Temperature Co-fired Ceramic (LTCC) substrates which makes the direct integration of the antenna with monolithic microwave circuits possible. This makes the antenna module designing simpler and accurate.

Active integrated UWB-MIMO antennas are an interesting aspect as they proved to be beneficial in terms of gain and diversity performance. Integrating pulse generator with the antenna avoids the need of a transmission line between RF device/generator and the antenna. This eliminates the need of balun as it prevents the excitation of common-mode currents. Another future interest will be integrating Low Noise Amplifier (LNA) with UWB antenna, which is proved to be effective in its receiver mode. This is because a typical UWB receiver needs a LNA to detect signals as the UWB systems operate with very low power levels. These integration can enhance the overall performance of the communication system employing these antennas.

Another future investigation for the UWB-MIMO antenna will be the detailed channel evaluation, which will be beneficial for the MIMO antennas. This can be accomplished by using real test equipments and realistic propagation scenarios which will give an idea about the actual channel effects, improvement in reliability,

spectrum efficiency etc.. By selecting the actual urban or noisy environments, realistic antenna solutions can be drawn at the design stage itself. The main limitations faced for the channel evaluation in UWB-MIMO antennas are the availability of adequate equipments that can operated in the UWB range of operation. Most of the MIMO testing equipments will be of narrow band range, which can test the channel effects for certain frequencies only.

UWB-MIMO antennas can be incorporated with RFID (Radio Frequency Identification Device) technology to enhance the reliability as well as speed of transmission/reception. The challenge in this scenario is to examine the near-field characteristics thoroughly for its performance analysis.

Wireless Body Area Network (WBAN) is devoted mainly to short-range communication, and employing UWB-MIMO antennas in those systems will increase the reliability and data rate of it tremendously. This opens up a fresh area to ponder, and to come up with efficient systems that can aid the fast growing requirements of the medical field. In addition to this, a further reduction of overall size of the antenna can be accomplished by using high dielectric substrates, DGS based surface, metamaterials etc.. This is a future investigation for the antenna discussed in this thesis.

References

[1] (1979). IEEE Standard Test Procedures for Antennas. *IEEE Std 149-1979.*

[2] (1984). Cellular Telecommunications Industry Association. *CTIA.* http://www.ctia.org/.

[3] (1998). The 3rd Generation Partnership Project. *3GPP.* http://www.3gpp.org/.

[4] (2009). Agilent PNA Microwave Network Analyzers-Data sheet. *Keysight Technologies.* https://www.keysight.com.

[5] (2009). User manual. *CST-Microwave Studio.* https://www.cst.com/products/cstmws.

[6] (2011). COST Action 2100Pervasive Mobile & Ambient Wireless Communications. *COST2100.* http://www.cost2100.org/.

[7] (2014). Accounting for Antenna and MIMO Channel Effects Using Keysight SystemVue. *Keysight Technologies.* https://www.keysight.com.

[8] 3GPP (2012). Measurement of radiated performance for mimo and multiple antenna reception for hspa and lte terminals. *in Tech. Rep. ETSI TR 137 976,* v11.0.0.

[9] Adamiuk, G. et al. (2009). Dual-orthogonal polarized antenna for UWB-IR technology. *IEEE Antennas and Wireless Propagation Letters,* 8:981–984.

[10] Addaci, R. et al. (2012). Dual-band WLAN diversity antenna system with high port-to-port isolation. *IEEE Antennas and Wireless Propagation Letters,* 11:244–247.

[11] Addaci, R. et al. (2014). Dual-band WLAN multiantenna system and Diversity/MIMO performance evaluation. *IEEE Transactions on Antennas and Propagation,* 62(3):1409–1415.

[12] Ahmed, O. and Sebak, A. R. (2008). A printed monopole antenna with two steps and a circular slot for UWB applications. *IEEE Antennas and Wireless Propagation Letters,* 7:411–413.

[13] Al-Rawi, A. et al. (2014). A new compact wideband MIMO antenna—the double-sided tapered self-grounded monopole array. *IEEE Transactions on Antennas and Propagation*, 62(6):3365–3369.

[14] Alishir MoradiKordalivand, T. A. R. and Khalily, M. (2014). Common elements wideband mimo antenna system for WiFi/LTE access-point applications. *IEEE Antennas and Wireless Propagation Letters*, 13:1601–1604.

[15] Alsath, M. G. N. and Kanagasabai, M. (2015). Compact UWB monopole antenna for automotive communications. *IEEE Transactions on Antennas and Propagation*, 63(9):4204–4208.

[16] Amman, M. J. et al. (2004). On pattern stability of the crossed planar monopole. *Microwave and Optical Technology Lett*, 40(4):294–296.

[17] Angelopoulos, E. S. et al. (2006). Circular and elliptical CPW-fed slot and microstrip-fed antennas for ultrawideband applications. *IEEE Antennas and Wireless Propagation Letters*, 5:294–297.

[18] Angus C. K. Mak, C. R. R. and Murch, R. D. (2008). Isolation enhancement between two closely packed antennas. *IEEE Transactions on Antennas and Propagation*, 56(11):3411–3419.

[19] Anil Kr Gautam, S. Y. and Kanaujia, B. K. (2013). A CPW-fed compact UWB microstrip antenna. *IEEE Antennas and Wireless Propagation Letters*, 12:151–154.

[20] Baccarelli, E. et al. (2004). A novel multi-antenna impulse radio UWB transceiver for broadband high-throughput 4G WLANs. *IEEE Communication Letters*, 8(7):419–421.

[21] Balanis, C. A. (1997). *Antenna Theory: Analysis and Design.* John Wiley and Sons, Newyork, USA, second edition.

[22] Balanis, C. A. (2005). *Antenna theory: Analysis and Design.* Wiley, Newyork, third edition.

[23] Balanis, C. A. and Ioannides, P. I. (2007). *Introduction to Smart Antennas.* Morgan & Claypool Publishers, Newyork, first edition.

[24] Ban, Y.-L. et al. (2014). Decoupled hepta-band antenna array for WWAN/LTE smartphone applications. *IEEE Antennas and Wireless Propagation Letters*, 13:999–1002.

[25] Bartlett, F. A. (1941). A dual diversity preselector. *QST*, XXV:37–39.

[26] Beverage, H. H. and Peterson, H. O. (1931). Diversity receiving system of r.c.a. communications, inc., for radiotelegraphy. *Proceedings of the Institute of Radio Engineers*, 19(4):531–561.

[27] Bilal, M. et al. (2017). An FSS-based nonplanar quad-element UWB-MIMO antenna system. *IEEE Antennas and Wireless Propagation Letters*, 16:987–990.

[28] Bondyopadhyay, P. K. (1998). Sir J. C. Bose's Diode Detector Received Marconi's First Transatlantic Wireless Signal of December 1901 (The "Italian Navy Coherer" Scandal Revisited). *Proc. of IEEE*, 86(1):259–285.

[29] Brillouin, L. N. (Nov 30, 1948). Broad band antenna. *US Patent*, US 2,454,766 A.

[30] BRITTAIN, J. E. (2008). Electrical engineering hall of fame: Harold h. beverage. *Proceedings of the IEEE*, 96(9):1551–1554.

[31] Bybi P. Chacko, G. A. and Denidni, T. A. (2013). Uniplanar polarisation diversity antenna for ultrawideband systems. *IET Microwaves, Antennas & Propagation*, 7(10):851–857.

[32] C. E. Baum, E. G. F. and Giri, D. V. (1998). Review of impulse-radiating antennas. *Sensor and Simulation Notes, Air Force Research Laboratory*, pages 1–33. USA.

[33] C. Waldschmidt, T. F. and Wiesbeck, W. (2002). Spiral and dipole antennas for indoor mimo-systems. *IEEE Antennas and Wireless Propagation Letters*, 1:176–178.

[34] C802.16m-07/062, I. (2007). Draft channel model for 802.16m - advanced air interface.

[35] Carter, P. S. (Dec 5, 1939). Wideband, short wave antenna and transmission line system. *US Patent*, US 2,181,870 A.

[36] Chadi Abou-Rjeily, N. D. and Belfiore, J.-C. (2006). Space–Time coding for multiuser Ultra-Wideband communications. *IEEE Transactions on Communications*, 54(11):1960–1972.

[37] Chao-Ming Luo, J.-S. H. and Zhong, L.-L. (2015). Isolation enhancement of a very compact UWB-MIMO slot antenna with two defected ground structures. *IEEE Antennas and Wireless Propagation Letters*, 14:1766–1769.

[38] Chen, Z. N. (2004). Considerations for source pulses and antennas in UWB radio systems. *IEEE Transactions on Antennas and Propagation*, 52(7):1739–1748.

[39] Chen-Nee Chuah, David N. C. Tse, J. M. K. and Valenzuela, R. A. (2002). Capacity scaling in mimo wireless systems under correlated fading. *IEEE Transactions on Information Theory*, 48(3):637–650.

[40] Chiu, C.-W. and Li, C.-S. (2009). A CPW-fed band-notched slot antenna for UWB applications. *Microwave and Optical Technology Letters*, 51(6):1587–1592.

[41] Chiu, C.-Y. et al. (2007). Reduction of mutual coupling between closely-packed antenna elements. *IEEE Transactions on Antennas and Propagation*, 55(6):1732–1738.

[42] Clarke, R. H. (1968). A statistical theory of mobile-radio reception. *Bell System Technical Journal*, 47(6):957–1000.

[43] Claus Kupferschmidt, E. D. and Kaiser, T. (2009). Multiple antenna UWB systems WP3 of the EUWB-Project. *The 2009 International Conference on Advanced Technologies for Communications*, pages 295–299.

[44] Collin, R. E. (2001). *Foundations for microwave engineering.* John Wiley and Sons, United Kingdom, second edition.

[45] Communications, S. (2009). 3GPP r4-094673 evaluating channel models for MIMO OTA.

[46] Costa, J. R. et al. (2011). Evaluation of a new wideband slot array for MIMO performance enhancement in indoor WLANs. *IEEE Transactions on Antennas and Propagation*, 59(4):1200–1206.

[47] Cover, T. M. and Thomas, J. A. (2006). *Elements of Information Theory.* Wiley, United States of America, second edition.

[48] Cravotta, N. (2002). Ultrawideband: the next wireless panacea. *EDN Network*, pages 51–58. Oct 17.

[49] Denidni, T. and Habib, M. (2006). Broadband printed CPW-fed circular slot antenna. *IET Electronic Letters*, 42(3):135–136.

[50] Dezfooliyan, A. and Weiner, A. M. (2012). Experimental test-bed for studying multiple antenna beamforming over ultra wideband channels up to 12 GHz. *IEEE Wireless Communications Letters*, 1(5):520–523.

[51] Dhar, S. K. et al. (2016). An active integrated ultra-wideband MIMO antenna. *IEEE Transactions on Antennas and Propagation*, 64(4):1573–1578.

[52] Diallo, A. et al. (2008). Enhanced two-antenna structures for universal mobile telecommunications system diversity terminals. *IET Microwaves, Antennas & Propagation*, 2(1):93–101.

[53] Ding, Y. et al. (2007). A novel dual-band printed diversity antenna for mobile terminals. *IEEE Transactions on Antennas and Propagation*, 55(7):2088–2096.

[54] Dioum, I. et al. (2014). A novel compact dual-band LTE antenna-system for MIMO operation. *IEEE Transactions on Antennas and Propagation*, 62(4):2291–2296.

[55] Dissanayake, T. and Esselle, K. P. (2006). Correlation-based pattern stability analysis and a figure of merit for UWB antennas. *IEEE Transactions on Antennas and Propagation*, 54(11):3184–3191.

[56] D.R. Melo, M. N. Kawakatsu, D. C. N. and Dmitriev, V. (2012). A planar monopole UWB antennas with rounded patch and ground plane possessing improved impedance matching. *Microwave and Optical Technology Letters*, 54(2):335–338.

[57] Dubost, G. and Zisler, S. (1976). *Antennes à large bande: théorie et applications.* Masson, Paris.

[58] E. Antonino-Daviu, M. Cabedo-Fabre´s, M. F.-B. and Valero-Nogueira, A. (2003). Wideband double-fed planar monopole antennas. *IET Electronics Letters*, 39(23):1635–1636.

[59] Elektrobit (2009). 3gpp r4-093959 veri
cation of the anechoic chamber and fading emulator based mimo ota method.

[60] Ersin Yetisir, C.-C. C. and Volakis, J. L. (2014). Low-profile UWB 2-port antenna with high isolation. *IEEE Antennas and Wireless Propagation Letters*, 13:55–58.

[61] et al, B. O. (2005). Wideband LTCC CPW-fed two-layered monopole antenna. *IET Electronics Letters*, 41(16):889–890.

[62] et al, Y. J. C. (2006). A miniature UWB planar monopole antenna with 5-GHz band-rejection filter and the time-domain characteristics. *IEEE Transactions on Antennas and Propagation*, 54(5):1453–1460.

[63] Evans, J. A. and Ammann, M. J. (Sept 1999). Planar trapezoidal and pentagonal monopoles with impedance bandwidth in excess of 10:1. *IEEE Antennas and Propagation International Symposium (Digest)*, pages 1558–1561.

[64] FCC (2002). First report and order in et docket no. 98-153, 17 fcc rcd 7435. April, 22.

[65] Foschini, G. J. (1996). Layered space-time architecture for wireless communication in a fading environment when using multi-element antennas. *Bell Labs Technical Journal*, pages 41–59.

[66] Foschini, G. J. and Gans, M. J. (1998). On limits of wireless communications in a fading environment when using multiple antennas. *Wireless Personal Communications*, 6:311–335.

[67] Gao, P. et al. (2014). Compact printed UWB diversity slot antenna with 5.5-GHz band-notched characteristics. *IEEE Antennas and Wireless Propagation Letters*, 13:376–379.

[68] Gesbert, D. et al. (2003). From theory to practice: An overview of MIMO space–time coded wireless systems. *IEEE Journal on selected areas in communications*, 21(3):281–302.

[69] Gibson, P. J. (Sept 1979). The vivaldi aerial. *IEEE 9th European Microwave Conference*, pages 101–105.

[70] Gopikrishna, M. et al. (2009a). Design of a compact semi-elliptic monopole slot antenna for UWB systems. *IEEE Transactions on Antennas and Propagation*, 57(6):1834–1837.

[71] Gopikrishna, M. et al. (2009b). Design of a microstrip fed stepslot antenna for UWB communication. *Microwave and Optical Technology Letters*, 51(4):1126–129.

[72] H. O. Peterson, H. H. B. and Moore, J. B. (1931). Diversity telephone receiving system of r.c.a. communications, inc. *Proceedings of the Institute of Radio Engineers*, 19(4):562–584.

[73] Hallbjörner, P. (2005). The significance of radiation efficiencies when using s-parameters to calculate the received signal correlation from two antennas. *IEEE Antennas and Wireless Propagation Letters*, 4:97–99.

[74] Haykin, S. (2002). *Adaptive Filter Theory.* Prentice Hall, Upper Saddle River, NJ, fourth edition.

[75] Horn, R. A. and Johnson, C. R. (1986). *Matrix Analysis.* Cambridge University Press, Cambridge, UK.

[76] Huang, C. Y. and Hsia, W. C. (2005). Planar elliptical antenna for ultrawideband communications. *IET Electronic Letters*, 41(6):296–297.

[77] Hussain, M. G. M. (2002). Principles of space–time array processing for ultrawide-band impulse radar and radio communications. *IEEE Transactions on Vehicular Technology*, 51(3):393–403.

[78] Hussain, M. G. M. (2005). Theory and analysis of adaptive cylindrical array antenna for ultrawideband wireless communications. *IEEE Transactions on Wireless Communications*, 4(6):3075–3083.

[79] Irahhauten, Z. et al. (2004). The effect of antenna and pulse waveform on ultra wideband link budget with impulse radio transmission. *Proceedings of 34th European Microwave Conference*, pages 113–116. Amsterdam, Netherlands.

[80] J. Yang, Y. Sun, J. S. and Pem, N. (2003). Channel estimation for wireless communications using space-time block coding techniques. *Proceedings of the 2003 International Symposium on Circuits and Systems (ISCAS) 2003*, 2:220–223.

[81] Jafarkhani, H. (2005). *Space-Time Coding:Theory and Practice*. Cambridge University Press, Cambridge, UK, first edition.

[82] Jafri, S. I. et al. (2016). Compact reconfigurable multiple-input multiple-output antenna for ultra wideband applications. *IET Microwaves, Antennas & Propagation*, 10(4):413–419.

[83] Jang, Y. W. (2000). Broadband cross-shaped microstrip-fed slot antenna. *IET Electronic Letters*, 36(25):2056–2057.

[84] Jang, Y. W. (2001). Experimental study of large bandwidth three-offset microstripline-fed slot antenna. *IEEE Microwave and Wireless Components Letters*, 11(10):425–427.

[85] Jeongpyo Kim, Taeyeoul Yoon, J. K. and Choi, J. (2005). Design of an ultra wide-band printed monopole antenna using FDTD and genetic algorithm. *IEEE Microwave and Wireless Components Letters*, 15(6):395–397.

[86] Jiang, J.-B. et al. (2009). Band-notched UWB printed antenna with an inverted-L-slotted ground. *Microwave and Optical Technology Letters*, 51(1):260–263.

[87] Jianjun Liu, S. Z. and Esselle, K. P. (2011). A printed elliptical monopole antenna with modified feeding structure for bandwidth enhancement. *IEEE Transactions on Antennas and Propagation*, 59(2):667–670.

[88] Jianxin Liang, Choo C. Chiau, X. C. and Parini, C. G. (2005). Study of a printed circular disc monopole antenna for uwb systems. *IEEE Transactions on Antennas and Propagation*, 53(11):3500–3504.

[89] Jorge R. Costa, C. R. M. and Fernandes, C. A. (2009). Performance of a crossed exponentially tapered slot antenna for UWB systems. *IEEE Transactions on Antennas and Propagation*, 57(5):1345–1352.

[90] K. Chung, T. Y. and Choi, J. (2004). Wideband CPW-fed monopole antenna with parasitic elements and slots. *IET Electronic Letters*, 40(17):1038–1040.

[91] Kahn, W. K. (1969). Active reflection coefficient and element efficiency in arbitrary antenna arrays. *IEEE Transactions on Antennas and Propagation*, 17(5):653–654.

[92] Kaiser, T. and Zheng, F. (2010). *Ultra Wideband Systems with MIMO*. Wiley, New York, USA.

[93] Karimian, R. et al. (2013). Novel F-Shaped quad-band printed slot antenna for WLAN and WiMAX MIMO systems. *IEEE Antennas and Wireless Propagation Letters*, 12:405–408.

[94] Kay, S. M. (1993). *Fundamentals of Statistical Signal Processing: Estimation Theory*. Prentice Hall, Upper Saddle River, NJ.

[95] Keignart, J. et al. (2006). UWB SIMO channel measurements and simulations. *IEEE Transactions on Microwave Theory and Techniques*, 54(4):1812–1819.

[96] Keysight (2009). 3GPP r4-093094 performance analysis of two-stage MIMO OTA method versus SCM approximation method.

[97] Khan, M. et al. (2015a). Compact 4×4 UWB-MIMO antenna with WLAN band rejected operation. *IET Electronic Letters*, 51(14):1048–1050.

[98] Khan, M. et al. (2015b). Compact planar UWB MIMO antenna with on-demand WLAN rejection. *IET Electronic Letters*, 51(13):963–964.

[99] Khan, M. S. et al. (2017). A compact CSRR-enabled UWB diversity antenna. *IEEE Antennas and Wireless Propagation Letters*, 16:808–812.

[100] Kim, D. O. and Kim, C. Y. (2010). CPW-fed ultra-wideband antenna with triple-band notch function. *IET Electronic Letters*, 46(18):1246–1248.

[101] Kim, Y. and Kwon, D.-H. (2004). CPW-fed planar ultra wideband antenna having a frequency band notch function. *IET Electronic Letters*, 40(7):403–405.

[102] Kin-Lu Wong, C.-H. W. and Su, S.-W. (2005). Ultrawide-band square planar metal-plate monopole antenna with a trident-shaped feeding strip. *IEEE Transactions on Antennas and Propagation*, 53(4):1262–1269.

[103] Ko, S. C. K. and Murch, R. D. (2001). Compact integrated diversity antenna for wireless communications. *IEEE Transactions on Antennas and Propagation*, 49(6):954–960.

[104] Kotyrba, G. and Chaloupka, H. J. (2005). On signal distortion in compact UWB arrays due to element interaction. *Proc. of IEEE Int. Symp. Antennas Propag.*, pages 614–617. Washington, DC, USA.

[105] Krishna, R. V. S. R. and Kumar, R. (2016). A dual-polarized square-ring slot antenna for UWB, imaging, and radar applications. *IEEE Antennas and Wireless Propagation Letters*, 15:195–198.

[106] Kulkarni, M. K. and Kasabegoudar, V. G. (2013). A CPW-Fed triangular monopole antenna with staircase ground for UWB applications. *International Journal of Wireless Communications and Mobile Computing*, 4(1):129–135.

[107] Kunisch, J. and Pamp, J. (2003). Uwb radio channel modeling considerations. *Proc. of International Conference on Electromagnetics in Advanced Applications (ICEAA '03)*, pages 277–284. Torino, Italy.

[108] Kyösti, P. et al. (2007). IST-4-027756 WINNER II D1.1.2 V1.2. *WINNER II Channel Models*, 1.1.

[109] Kyungho Chung, J. K. and Choi, J. (2005). Wideband microstrip-fed monopole antenna having frequency band-notch function. *IEEE Microwave and Wireless Components Letters*, 15(11):766–768.

[110] Lamensdorf, D. and Susman, L. (1994). Baseband-pulse-antenna techniques. *IEEE Antennas and Propagation Magazine*, 36(1):20–30.

[111] Le Kang, Hui Li, X. W. and Shi, X. (2015). Compact offset microstrip-fed MIMO antenna for band-notched UWB applications. *IEEE Antennas and Wireless Propagation Letters*, 14:1754–1757.

[112] Lee, J.-M. et al. (2012). A compact ultrawideband MIMO antenna with WLAN band-rejected operation for mobile devices. *IEEE Antennas and Wireless Propagation Letters*, 11:990–993.

[113] Lee Paulsen, James B. West, W. F. P. and Kraus, J. (June 2003). Recent investigations on the volcano smoke antenna. *IEEE Antennas and Propagation International Symposium (Digest)*, pages 845–848.

[114] Leonardo Lizzi, Renzo Azaro, G. O. and Massa, A. (2011). Printed uwb antenna operating over multiple mobile wireless standards. *IEEE Antennas and Wireless Propagation Letters*, 10:1429–1432.

[115] Lewallen, R. W. (1985). Baluns: What they do and how they do it. *ARRL Antenna Compendium*, 1:157–164.

[116] Li, D. and fa Mao, J. (2012). A koch-like sided fractal bow-tie dipole antenna. *IEEE Transactions on Antennas and Propagation*, 60(5):2242–2251.

[117] Li, J.-F. et al. (2013). Compact dual band-notched UWB MIMO antenna with high isolation. *IEEE Transactions on Antennas and Propagation*, 61(9):4759–4766.

[118] Li, M.-Y. et al. (2017). Eight-port orthogonally dual-polarised MIMO antennas using loop structures for 5G smartphone. *IET Microwaves, Antennas & Propagation*, 11(12):1810–1816.

[119] Li, Q. et al. (2015). Miniaturized double-layer EBG structures for broadband mutual coupling reduction between UWB monopoles. *IEEE Transactions on Antennas and Propagation*, 63(3):1168–1171.

[120] Li-Chun Wang, W.-C. L. and Shieh, K.-J. (2005). On the performance of using multiple transmit and receive antennas in pulse-based ultrawideband systems. *IEEE Transactions on Wireless Communications*, 4(6):2738–2750.

[121] Li Liu, S. W. C. and Yuk, T. I. (2013). Compact MIMO antenna for portable devices in UWB applications. *IEEE Transactions on Antennas and Propagation*, 61(8):4257–4264.

[122] Li Liu, S. W. C. and Yuk, T. I. (2014). Compact multiple-input–multiple-output antenna using quasi-self-complementary antenna structures for ultrawideband applications. *IET Microwaves, Antennas & Propagation*, 8(13):1021–1029.

[123] Liang, X. L. (2012). *Ultra-Wideband Antenna and Design.* INTECH open access, Chapter 7, first edition.

[124] Liao, W.-J. et al. (2015). Inverted-F/Slot integrated dual-band four-antenna system for WLAN access points. *IEEE Antennas and Wireless Propagation Letters*, 14:847–850.

[125] Lin, G.-S. et al. (2017). Isolation improvement in UWB MIMO antenna system using carbon black film. *IEEE Antennas and Wireless Propagation Letters*, 16:222–225.

[126] Lindenblad, N. E. (April 29, 1941). Wide band antenna. *US Patent*, US 2,239,724 A.

[127] Liu, L. et al. (2008). A compact printed antenna using slot-type CSRR for 5.2GHz/5.8GHz band-notched UWB application. *Microwave and Optical Technology Letters*, 50(12):3239–3242.

[128] Liu, Y.-Y. and Tu, Z.-H. (2017). Compact differential band-notched stepped-slot UWB-MIMO antenna with common-mode suppression. *IEEE Antennas and Wireless Propagation Letters*, 16:593–596.

[129] Lodge, O. J. (Aug 16, 1898). Electric telegraphy. *US Patent*, US 609,154 A.

[130] Lui, W. J. et al. (2005). Frequency notched ultra-wideband microstrip slot antenna with fractal tuning stub. *IET Electronic Letters*, 41(6):294–296.

[131] Luis Inclán-Sánchez, J.-L. V.-R. and Rajo-Iglesias, E. (2008). High isolation proximity coupled multilayer patch antenna for dual-frequency operation. *IEEE Transactions on Antennas and Propagation*, 56(4):1180–1183.

[132] Luna, A. E. (1973). Parallel coplanar strips on a dielectric substrate. Master's thesis, M.E.E. thesis, Dep. Eng., Naval Postgraduate School, Monterey, California.

[133] Luo, Y. et al. (2013). A planar H-Shaped directive antenna and its application in compact MIMO antenna. *IEEE Transactions on Antennas and Propagation*, 61(9):4810–4814.

[134] M. Klemm, I. Z. Koves, G. F. P. and Troster, G. (2005). Novel small-size directional antenna for UWB WBAN/WPAN applications. *IEEE Transactions on Antennas and Propagation*, 53(12):3884–3896.

[135] M. Schwartz, W. R. B. and Stein, S. (1965). *Communication Systems and Techniques.* McGraw-Hill, NewYork, NY, USA.

[136] Ma, T.-G. and Jeng, S.-K. (2005). Planar miniature tapered-slot-fed annular slot antennas for ultrawide-band radios. *IEEE Transactions on Antennas and Propagation*, 53(3):1194–1202.

[137] Malik, W. Q. (2008). Spatial correlation in ultrawideband channels. *IEEE Transactions on Wireless Communications*, 7(2):604–610.

[138] Malik, W. Q. and Edwards, D. J. (2007). Measured MIMO capacity and diversity gain with spatial and polar arrays in ultrawideband channels. *IEEE Transactions on Communications*, 55(12):2361–2370.

[139] Mao, C.-X. and Chu, Q.-X. (2014). Compact coradiator UWB-MIMO antenna with dual polarization. *IEEE Transactions on Antennas and Propagation*, 62(9):4474–4480.

[140] Mao, S.-G. and Chen, S.-L. (2007). Frequency- and time-domain characterizations of ultrawideband tapered loop antennas. *IEEE Transactions on Antennas and Propagation*, 55(12):3698–3701.

[141] Masters, R. W. (Nov 4, 1947). Antenna. *US Patent*, US 2,430,353 A.

[142] Mei Sun, Y. P. Z. and Lu, Y. (2010). Miniaturization of planar monopole antenna for ultrawideband radios. *IEEE Transactions on Antennas and Propagation*, 58(7):2420–2425.

[143] Migliore, M. D. et al. (2008). An investigation on UWB-MIMO communication systems based on an experimental channel characterization. *IEEE Transactions on Antennas and Propagation*, 56(9):3081–3083.

[144] Nandi, S. and Mohan, A. (2017). A compact dual-band MIMO slot antenna for WLAN applications. *IEEE Antennas and Wireless Propagation Letters*, 16:2457–2460.

[145] Narayan Prasad Agrawall, G. K. and Ray, K. P. (1998). Wide-band planar monopole antennas. *IEEE Transactions on Antennas and Propagation*, 46(2):294–295.

[146] Okano, Y. (2009). Evaluation of ota performance for mobile terminal antennas reflecting practical usage and improvement of measurement efficiency. *NTT docomo technical journal*, 11(2):17–25.

[147] Pourahmadazar, J. et al. (2011). Broadband CPW-Fed circularly polarized square slot antenna with inverted-L strips for UWB applications. *IEEE Antennas and Wireless Propagation Letters*, 10:369–372.

[148] Price, E. and Woodruff, D. P. (2012). Applications of the shannon-hartley theorem to data streams and sparse recovery. *IEEE International Symposium on Information Theory Proceedings*, pages 2446–2450.

[149] Proakis, J. G. (1995). *Digital Communications*. McGraw-Hill, NewYork, NY, USA, second edition.

[150] Qi Wu, Ronghong Jin, J. G. and Ding, M. (2008). Printed omni-directional UWB monopole antenna with very compact size. *IEEE Transactions on Antennas and Propagation*, 56(3):896–899.

[151] R. Azim, M. I. and Misran, N. (2011). Ground modified double-sided printed compact UWB antenna. *IET Electronic Letters*, 47(1):9–11.

[152] R. K. Jongh, M. H. and Ligthart, L. P. (1997). Antenna time-domain measurement techniques. *IEEE Antennas and Propagation Magazine*, 39(5):7–12.

[153] R. Tian, B. K. L. and Ying, Z. (2011). Multiplexing efficiency of MIMO antennas. *IEEE Antennas and Wireless Propagation Letters*, 10:183–186.

[154] Rajagopalan, A. et al. (2007). Increasing channel capacity of an ultrawide-band MIMO system using vector antennas. *IEEE Transactions on Antennas and Propagation*, 55(10):2880–2887.

[155] Raleigh, G. G. and Ciofi, J. M. (1998). Spatio-temporal coding for wireless communication. *IEEE Transactions on Communications*, 46(3):357–366.

[156] Reddy, G. S. et al. (2015). Cross-configured directional UWB antennas for multidirectional pattern diversity characteristics. *IEEE Transactions on Antennas and Propagation*, 63(2):853–858.

[157] Ren, J. et al. (2014). Compact printed MIMO antenna for UWB applications. *IEEE Antennas and Wireless Propagation Letters*, 13:1517–1520.

[158] Rezaul Azim, M. T. I. and Misran, N. (2011). Compact tapered-shape slot antenna for UWB applications. *IEEE Antennas and Wireless Propagation Letters*, 10:1190–1193.

[159] Ries, S. and Kaiser, T. (2006). Ultra wideband impulse beamforming: It is a different world. *Elsevier Signal Processing*, 86:2198–2207.

[160] Ruiyuan Tian, B. K. L. and Ying, Z. (2012). Multiplexing efficiency of mimo antennas with user effects. *Proc. of IEEE Antennas and Propagation Society International Symposium (APSURSI), 2012.* Chicago, IL, USA.

[161] S. Blanch, J. R. and Corbella, I. (2003). Exact representation of antenna system diversity performance from input parameter description. *Electronics letters*, 39(9):705–707.

[162] S. Zhang, P. Z. and He, S. (2010). Printed mimo antenna system of four closely-spaced elements with large bandwidth and high isolation. *IET Electronic Letters*, 46(15):1052–1053.

[163] Saleem, R. et al. (2015). Eight-element UWB-MIMO array with three distinct isolation mechanisms. *IET Electronic Letters*, 51(4):311–313.

[164] Salvatore Bellofiore, Consfan fine A. Balanis, J. F. and Spanias, A. S. (2002). Smart-antenna systems for mobile communication networks part i: Overview and antenna design. *IEEE Antennas and Propagation Magazine*, 44(3):145–154.

[165] Samardzija, D. and Mandayam, N. (2003). Pilot-assisted estimation of mimo fading channel response and achievable data rates. *IEEE Transactions on Signal Processing*, 51(11):2882–2890.

[166] Saou-Wen Su, K.-L. W. and Tang, C.-L. (2004). Ultra-wideband square planar antenna for IEEE 802.16a operating in the 2–11 GHz band. *Microwave and Optical Technology Letters*, 42(6):463–466.

[167] Sarkar, D. et al. (2015). Four-element quad-band multiple-input multiple-output antenna employing split-ring resonator and inter-digital capacitor. *IET Microwaves, Antennas & Propagation*, 9(13):1453–1460.

[168] Schantz, H. G. (2002). Radiation efficiency of UWB antennas. *Proceedings of the 2002 IEEE UWBST Conference.*

[169] Schumacher, L. and Raghothaman, B. (2005). Closed-form expressions for the correlation coefficient of directive antennas impinged by a multimodal truncated laplacian PAS. *IEEE transactions on wireless communications*, 4(4):1351–1359.

[170] See, T. S. P. and Chen, Z. N. (2009). An ultrawideband diversity antenna. *IEEE Transactions on Antennas and Propagation*, 57(6):1597–1605.

[171] Seok H. Choi, Jong K. Park, S. K. K. and Park, J. Y. (2004). A new ultra-wideband antenna for uwb applications. *Microwave and Optical Technology Letters*, 40(5):399–401.

[172] Seong-Youp Suh, W. L. S. and Davis, W. A. (2004). A new ultrawideband printed monopole antenna: The Planar Inverted Cone Antenna (PICA). *IEEE Transactions on Antennas and Propagation*, 52(5):1361–1365.

[173] Shameena, V. A. et al. (Feb 2011). A compact CPW fed serrated UWB antenna. *IEEE International Conference on Communications and Signal Processing (ICCSP)*, pages 108–111.

[174] Shannon, C. E. (1948). A mathematical theory of communication. *The Bell System Technical Journal*, 27(3):379–423.

[175] Sharawi, M. S. et al. (2012). A dual-element dual-band MIMO antenna system with enhanced isolation for mobile terminals. *IEEE Antennas and Wireless Propagation Letters*, 11:1006–1009.

[176] Shrivishal Tripathi, A. M. and Yadav, S. (2015). A compact koch fractal UWB MIMO antenna with WLAN band-rejection. *IEEE Antennas and Wireless Propagation Letters*, 14:1565–1568.

[177] Shun-Shi Zhong, X.-L. L. and Wang, W. (2007). Compact elliptical monopole antenna with impedance bandwidth in excess of 21:1. *IEEE Transactions on Antennas and Propagation*, 55(11):3082–3085.

[178] Siddharth Ray, M. M. and Zheng, L. (Nov 2004). On MIMO capacity in the ultra-wideband regime. *Conference Record of the Thirty-Eighth Asilomar Conference on Signals, Systems and Computers*, pages 1516–1520.

[179] Siriwongpairat, W. P. et al. (2006). Multiband-OFDM MIMO coding framework for UWB communication systems. *IEEE Transactions on Signal Processing*, 54(1):214–224.

[180] Sklar, B. (1997). Rayleigh fading channelsin mobile digital communication systems part1: Characterization. *IEEE Communications Magazine*, 35(7):90–100.

[181] SOBOL, H. (1984). Microwave communications—an historical perspective. *IEEE Transactions on Microwave Theory and Techniques*, 32(9):1170–1181.

[182] Solis, M. A. P. and Aguilar, H. J. (June 2005). Ultra-wideband planar monopole antenna for operation in the 3-20 GHz band. *IEEE 6th International Symposium on Electromagnetic Compatibility and Electromagnetic Ecology*, pages 97–100.

[183] Sonkki, M. et al. (2015). Wideband dual-polarized cross-shaped vivaldi antenna. *IEEE Transactions on Antennas and Propagation*, 63(6):2813–2819.

[184] Srivastava, G. and Mohan, A. (2016). Compact MIMO slot antenna for UWB applications. *IEEE Antennas and Wireless Propagation Letters*, 15:1057–1060.

[185] Stohr, W. (Jan 16, 1968). Broadband ellipsoidal dipole antenna. *US Patent*, US 3,364,491 A.

[186] Sujith, R. et al. (2010). Compact CPW-fed ground defected H-shaped slot antenna with harmonic suppression and stable radiation characteristics. *IET Electronic Letters*, 46(12):812–814.

[187] Taga, T. (1990). Analysis for mean effective gain of mobile antennas in land mobile radio environments. *IEEE Transactions on Vehicular Technology*, 39(2):117–131.

[188] Tang, I. T. et al. (2008). Miniaturized 5.2GHz notched UWB CPW-fed antenna using dual reverse split trapezoid slots. *Microwave and Optical Technology Letters*, 50(3):652–655.

[189] Tang, T.-C. and Lin, K.-H. (2014). An ultrawideband MIMO antenna with dual band-notched function. *IEEE Antennas and Wireless Propagation Letters*, 13:1076–1079.

[190] Taylor, J. D. (1995). *Introduction to ultrawideband radar systems*. CRC Press, USA.

[191] Thomas Kaiser, F. Z. and Dimitrov, E. (2009). An overview of Ultra-Wide-Band systems with MIMO. *Proceedings of the IEEE*, 97(2):285–312.

[192] Toh, W. K. et al. (2009). A planar UWB diversity antenna. *IEEE Transactions on Antennas and Propagation*, 57(11):3467–3473.

[193] Toktas, A. and Akdagli, A. (2015). Compact multiple-input multiple-output antenna with low correlation for ultra-wideband applications. *IET Microwaves, Antennas & Propagation*, 9(8):822–829.

[194] Tran, V. and Sibille, A. (2006). Spatial multiplexing in UWB MIMO communications. *IET Electronic Letters*, 42(16):931–932.

[195] V. Plicanic, B. K. Lau, A. D. and Ying, Z. (2009). Actual diversity performance of a multiband diversity antenna with hand and head effects. *IEEE Transactions on Antennas and Propagation*, 57(5):1547–1556.

[196] V. Tarokh, A. Naguib, N. S. and Calderbank, A. R. (1999). Space-time codes for high data rate wireless communication: performance criteria in the presence of channel estimation errors, mobility, and multiple paths. *IEEE Transactions on Communications*, 47(2):199–207.

[197] Vaughan, R. and Andersen, J. B. (2003). *Channels, propagation and antennas for mobile communications*. IET, United Kingdom, first edition.

[198] Vaughan, R. G. and Andersen, J. B. (1987). Antenna diversity in mobile communications. *IEEE Transactions on Vehicular Technology*, 36(64):149–172.

[199] Vivek, R. et al. (2018). Coplanar Waveguide (CPW)-Fed Compact Dual Band Antenna for Wireless Applications. *Proc. of IEEE International Symposium on Antennas and Propagation and USNC-URSI Radio Science Meeting (AP-S/URSI), 2018*, pages 1021–1022. Boston, Massachusetts, USA.

[200] W. Sorgel, S. K. and Wiesbeck, W. (2003). Measurement and evaluation of ultra wideband antennas for communications. *Proc. of International ITG Conference on Antennas-INICA2003*, pages 377–380.

[201] W. Wiesbeck, G. A. and Sturm, C. (2009). Basic properties and design principles of UWB antennas. *Proceedings of the IEEE*, 97(2):372–386.

[202] Wang, H. et al. (2014). Wideband tri-port MIMO antenna with compact size and directional radiation pattern. *IET Electronic Letters*, 50(18):1561–1262.

[203] Wasim Q. Malik, B. A. and Edwards, D. J. (Sep 2006). A simple adaptive beamformer for ultrawideband wireless systems. *IEEE 2006 International Conference on Ultra-Wideband*, pages 453–458.

[204] Wen, C. P. (1969). Coplanar waveguide: A surface strip transmission line suitable for nonreciprocal gyromagnetic device applications. *IEEE Microwave Theory and Techniques*, 17(12):1087–1090.

[205] Werner Sörgel, C. S. and Wiesbeck, W. (2005b). Influence of antennas on ultrawideband transmisson. *EURASIP J. App. Signal Processing*, 3:296–305.

[206] Werner Sörgel, C. S. and Wiesbeck, W. (Sep 2005a). Impulse responses of linear uwb antenna arrays and the application to beam steering. *IEEE International Conference on Ultra-Wideband*, pages 275–280.

[207] Win, M. Z. and Scholtz, R. A. (2000). Ultra-wide bandwidth time-hopping spread-spectrum impulse radio for wireless multiple-access communications. *IEEE Transactions on Communications*, 48(4):679–691.

[208] Winters, J. H. (1987). On the capacity of radio communication systems with diversity in a Rayleigh fading environment. *IEEE Journal on Selected Areas in Communications*, 5(5):871–878.

[209] Wu, B. Q. and Luk, K.-M. (2009). A wideband, low-profile, conical-beam antenna with horizontal polarization for indoor wireless communications. *IEEE Antennas and Wireless Propagation Letters*, 8:634–636.

[210] X. L. Liang, S. S. Zhong, W. W. and Yao, F. W. (2006). Printed annular monopole antenna for ultra-wideband applications. *IET Electronic Letters*, 42(2):71–72.

[211] Xian-Ling Liang, S.-S. Z. and Wang, W. (2006). Tapered CPW-fed printed monopole antenna. *Microwave and Optical Technology Letters*, 48(7):1242–1244.

[212] Xian Ling Liang, S. S. Z. and Wang, W. (2006). UWB printed circular monopole antenna. *Microwave and Optical Technology Letters*, 48(8):1532–1534.

[213] Y. Duroc, T. P. V. and Tedjini, S. (2007a). A time/frequency model for ultrawideband antennas. *IEEE Transactions on Antennas and Propagation*, 55(8):2342–2350.

[214] Y. Duroc, A. Ghiotto, T. P. V. and Tedjini, S. (2007b). UWB antennas:systems with transfer functions and impulse response. *IEEE Transactions on Antennas and Propagation*, 55(5):1449–1451.

[215] Yang, G. M. et al. (2009). Ultrawideband (UWB) antennas with multiresonant split-ring loops. *IEEE Transactions on Antennas and Propagation*, 57(1):256–260.

[216] Yang, L. and Giannakis, G. B. (2004). Analog space–time coding for multi-antenna ultra-wideband transmissions. *IEEE Transactions on Communications*, 52(3):507–517.

[217] Yang, Y. et al. (2012). Design of a UWB wide-slot antenna with 5.2-/5.8-GHz dual notched bands using modified electromagnetic band-gap structures. *Microwave and Optical Technology Letters*, 54(4):1069–1075.

[218] Yazdandoost, K. Y. and Kohno, R. (June 2004). Bow-tie antenna for UWB communication frequency. *IEEE Antennas and Propagation Society International Symposium*, pages 2520–2523.

[219] Yuan-Fu Liu, P. W. and Qin, H. (2014). Compact ACS-fed UWB monopole antenna with extra bluetooth band. *IET Electronic Letters*, 50(18):1263–1264.

[220] Yue Gao, Xiaodong Chen, Z. Y. and Parini, C. (2007). Design and performance investigation of a dual-element PIFA array at 2.5 GHz for MIMO terminal. *IEEE Transactions on Antennas and Propagation*, 55(12):3433–3441.

[221] Yun, J. X. and Vaughan, R. G. (2012). Multiple element antenna efficiency and its impact on diversity and capacity. *IEEE Transactions on Antennas and Propagation*, 60(2):529–539.

[222] Z. Chen, J. Y. and Vucetic, B. (2005). Analysis of transmit antenna selection/maximal-ratio combining in rayleigh fading channels. *IEEE Transactions on Vehicular Technology*, 54(4):1312–1321.

[223] Z. L. Zhou, L. L. and Hong, J. S. (2011). Compact UWB printed monopole antenna with dual narrow band notches for WiMAX/WLAN bands. *IET Electronic Letters*, 47(20):1111–1112.

[224] Z. N. Low, J. H. C. and Law, C. L. (2005). Low-Cost PCB antenna for UWB applications. *IEEE Antennas and Wireless Propagation Letters*, 4:237–1181.

[225] Zhang, J.-Y. et al. (2015). ACS-fed UWB-MIMO antenna with shared radiator. *IET Electronic Letters*, 51(17):1301–1302.

[226] Zhang, L. N. et al. (2009a). Compact omnidirectional band-notch ultra-wideband antenna. *IET Electronic Letters*, 45(13):659–660.

[227] Zhang, S. et al. (2009b). Ultrawideband MIMO/diversity antennas with a tree-like structure to enhance wideband isolation. *IEEE Antennas and Wireless Propagation Letters*, 8:1279–1282.

[228] Zhang, S. et al. (2013). Adaptive quad-element multi-wideband antenna array for user-effective LTE MIMO mobile terminals. *IEEE Transactions on Antennas and Propagation*, 61(8):4275–4283.

[229] Zhang, S. and Pedersen, G. F. (2016). Mutual coupling reduction for UWB MIMO antennas with a wideband neutralization line. *IEEE Antennas and Wireless Propagation Letters*, 15:166–169.

[230] Zhao, Y.-L. et al. (2008). Compact planar monopole UWB antenna with band-notched characteristic. *Microwave and Optical Technology Letters*, 50(10):2656–2658.

[231] Zheng, F. and Kaiser, T. (2008). On the evaluation of channel capacity of UWB indoor wireless systems. *IEEE Transactions on Signal Processing*, 56(12):6106–6113.

[232] Zhu, J. and Eleftheriades, G. V. (2010). A simple approach for reducing mutual coupling in two closely spaced metamaterial-inspired monopole antennas. *IEEE Antennas and Wireless Propagation Letters*, 9:379–382.

[233] Zhu, J. et al. (2016). Compact dual-polarized UWB quasi-self-complementary MIMO/Diversity antenna with band-rejection capability. *IEEE Antennas and Wireless Propagation Letters*, 15:905–908.

[234] Zwierzchowski, S. and Jazayeri, P. (2003). Derivation and determination of the antenna transfer function for use in ultra-wideband communications analysis. *Proc. of Wireless 2003 15th International Conference*, pages 533–544. Calgary, Canada.

Appendix A

Modified Bowtie Antenna for DVB-H application

The rapid development of various wireless protocols increases the needs for antennas having low profile, compact size and light weight with ease of fabrication. Many techniques have been developed to achieve compactness in the antenna design such as integrating shorting walls on the radiating element, using stacked structures and fractal geometries [1–4]. Recently, Composite Right/Left Handed (CRLH) Transmission Lines (TLs), composed of shunt inductors and series capacitors periodically loaded along the host TLs, have drawn increasing attention because of its many unusual properties [5–7]. One of the unusual properties is the zeroth-order resonance at which the phase constant, β is zero for a non-zero frequency. This enables the resonant frequency to be independent of the antenna dimension [8–10]. A 75% reduction in the footprint area of the structure can be achieved compared to a conventional patch antenna by using meander-line inductor [11]. In CRLH TLs, the quasi lumped element implementation of shunt inductance and series capacitance are obtained by vias to ground plane and inter-digital capacitors respectively [12]. This makes the fabrication difficult and tedious. In [13] and [14], a chip inductor was embedded in the printed monopole antennas, which results a decrease in the resonant length of the fundamental mode.

In this chapter, a Zeroth Order Resonant Antenna (ZORA) using a chip inductor is discussed and studied. The chip inductor reduces the overall antenna

size. Here the unique property of the CRLH TLs, i.e., zeroth order resonance, is accomplished on a bowtie structure, since it is simple to fabricate. The features of the bowtie include wider bandwidth, higher gain, lower front-to-back ratio, lower cross-polarization level and smaller size [15]. A conventional CRLH TL is composed of a series inductance and capacitance as well as shunt inductance and capacitance. The zeroth-order mode is determined by the shunt components in the case of an open ended transmission line and by series components in short ended transmission line. By increasing the shunt inductance, the zeroth-order resonant frequency can be decreased, so that the antenna size can be made much smaller. In this proposed structure, the shunt inductance is accomplished by embedding a chip inductor on one of the strip of the bowtie antenna. Thus it omits the need for vias to the ground. The series capacitor of a traditional CRLH TL is taken away in order to reduce both size and structural complexity, which makes the system devoid of left-handed (LH) transmission but retaining the zeroth-order resonance and right-handed transmission [16]. The proposed antenna with dimension $0.0186\lambda_0$ X $0.020\lambda_0$ X $0.003\lambda_0$ mm^3 has a zeroth order resonance at 503MHz, which makes it electrically very small [18], where λ_0 is the free space wavelength corresponding to the resonant frequency. In addition the high gain wide band of the original bowtie antenna at higher frequencies [15] is retained. The optimization of the antenna dimensions is carried out using Ansoft HFSS.

A.1   Antenna geometry

Fig.A.1 shows the modified bowtie antenna with an inductor. The prototype is fabricated on a substrate of relative permittivity (ϵ_r) 4.3 and thickness (h) 1.588mm. The antenna requires a small footprint of $0.0186\lambda_0$ X $0.020\lambda_0$ X $0.003\lambda_0$ mm^3 only.

A 0603CS 120nH Coilcraft surface mount inductor is mounted on one of the arm of bowtie antenna as shown in Fig. A.1. The effect of the loaded chip inductor is an increase in the electrical length of the bowtie antenna, and thus lowering the resonant frequency.

The circuit model of the bowtie antenna loaded with inductor is shown in Fig. A.2a. The parasitic components can be modeled using series inductance (L_R)
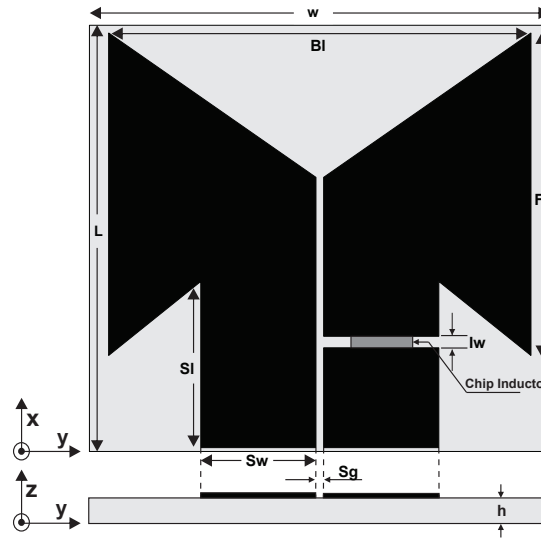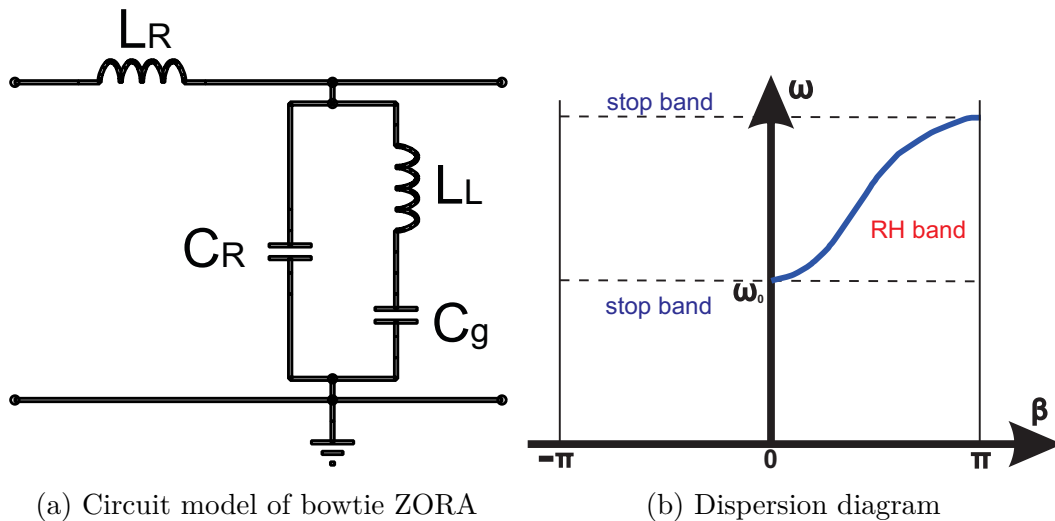
Fig. A.1 Geometry of modified bowtie antenna; Bl=11mm, Fl=8.4mm, Sl=4mm, Sw=3mm, Sg=0.2mm, Iw=0.3mm, h=1.6mm, L=11.1mm, W=12mm

(a) Circuit model of bowtie ZORA   (b) Dispersion diagram

Fig. A.2 Circuit model and dispersion diagram of modified bowtie antenna

and shunt capacitance (C_R). The bow (flaring) corresponding to the inductor loaded strip, acts as a metal patch and provides a capacitance C_g to the ground. When C_g is large, it provides a virtual ground voltage [19, 20] and thus realizes the shunt inductance (L_L). This condition triggers the zeroth order mode of the structure at lower frequencies. At higher frequencies the virtual ground effect fails

as the inductor impedance increases and results in the right-handed transmission. Fig. A.2b shows a schematic representation of the proposed dispersion diagram corresponding to the circuit model.

A.2 Theory

The modified bowtie antenna with inductor suppresses the left handed transmission (phase advance) but possess zero phase constant and right-handed transmission (phase delay) [6]. The suppression of LH transmission took place since there is no series capacitance (C_L) [16] as in Fig. A.2a

By applying boundary condition related to Bloch-floquet theorem [12] to the structure, the dispersion relation, $\beta(\omega)$, of the simplified TL in Fig. A.2a, is obtained as

$$\beta(\omega) = \cos^{-1}(1 + \frac{ZY}{2}) \tag{A.1}$$

Where the series impedence (Z) and the shunt admittance (Y) are given by

$$Z(\omega) = j(\omega L_R) \tag{A.2}$$

$$Y(\omega) = j(\omega C_R - \frac{1}{\omega L_L - \frac{1}{\omega C_g}}) \tag{A.3}$$

when $\omega L_L \gg \frac{1}{\omega C_g}$ then $Y(\omega)$ approaches the admittance of $L_L C_R$ tank resonator and therefore C_g has less influence on the propagation characteristics[18]. By applying Taylor series approximation, (A.1) becomes

$$\beta(\omega) = \sqrt{\omega^2 L_R C_R - \frac{L_R}{L_L - \frac{1}{\omega^2 C_g}}} \tag{A.4}$$

As the propagation constant approaches zero, the zeroth order resonance (infinite wavelength resonance) results. Here the structure acts as an open ended transmission line, so the zeroth mode frequency is determined by shunt circuit [18].

$$\omega = \omega_0 = \sqrt{\omega_{sh}^2 + \omega_g^2} \tag{A.5}$$

where $\omega_{sh} = \frac{1}{\sqrt{L_R C_R}}$ and $\omega_g = \frac{1}{\sqrt{L_L C_g}}$

As L_L, C_R and C_g are increased, the resonant frequency decreases. It is more effective to increase L_L rather than C_R and C_g, by simply increasing the value of the chip inductor. When L_L becomes larger, the zeroth-mode resonance shifts to lower frequency region, making the antenna more compact in size.

A.3 Simulation and Experimental results

Agilent PNA E8362B network analyzer is used for experimental analysis. The modified ZOR antenna with a 120nH chip inductor was fabricated and measured. A photograph of the antenna is shown in Fig. A.3. Fig. A.4 shows the simulated and measured reflection coefficient as well as the transmission coefficient of the antenna. The slight discrepancy in the S_{11} curve is due to the coupling of the SMA connector, which is not considered in the simulation.
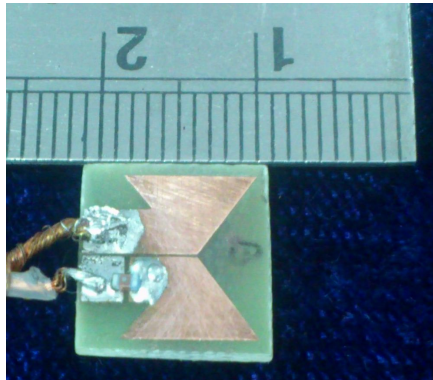

Fig. A.3 Photograph of the fabricated prototype; Bl=11mm, Fl=8.4mm, Sl=4mm, Sw=3mm, Sg=0.2mm, Iw=0.3mm, h=1.6mm, L=11.1mm, W=12mm

Fig. A.5 depicts the comparison of reflection characteristics at higher frequency region, between the bowtie antennas with and without inductor. A bowtie antenna without embedding any chip inductor has only n=+1 mode. From Fig. A.4 & A.5 it is clear that for the proposed antenna the higher resonance is still determined by the bowtie structure while the lower resonance is due to the presence of a 120nH inductor. For this inductor-loaded antenna, n=0 mode is the lowest mode, because it does not support backward wave like the CRLH TL. The n=0 mode resonates at 503MHz with a reflection coefficient of -35dB and a 3:1 VSWR
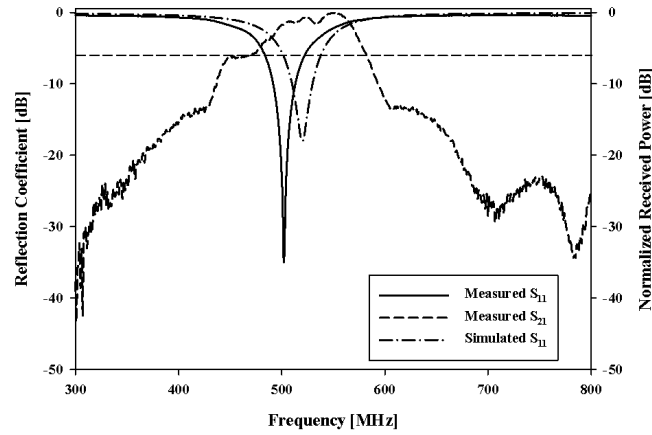
Fig. A.4 Transmission and reflection characteristics of modified bowtie antenna; Bl=11mm, Fl=8.4mm, Sl=4mm, Sw=3mm, Sg=0.2mm, Iw=0.3mm, h=1.6mm, L=11.1mm, W=12mm
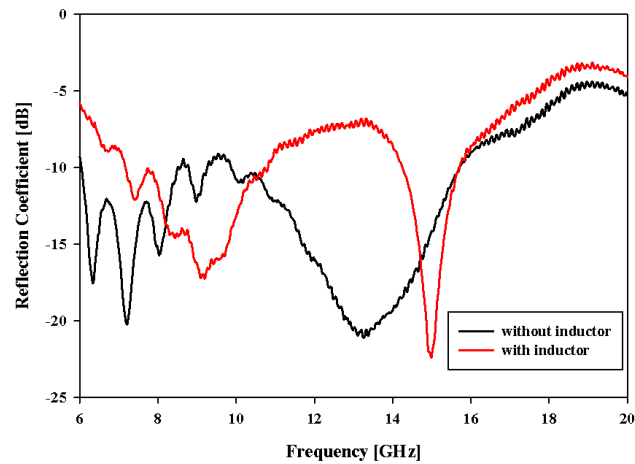
Fig. A.5 Reflection coefficient of bowtie antenna with and without inductor; Bl=11mm, Fl=8.4mm, Sl=4mm, Sw=3mm, Sg=0.2mm, Iw=0.3mm, h=1.6mm, L=11.1mm, W=12mm

bandwidth of 39MHz and for n=+1 mode the resonance is at 9.15GHz with a reflection coefficient of -17dB as shown in Fig. A.4 & A.5

The electric field distribution for n=0 (β=0) and n=+1 (β>0) are analyzed. At 503MHz (n=0) the electric fields are uniformly distributed and are in-phase
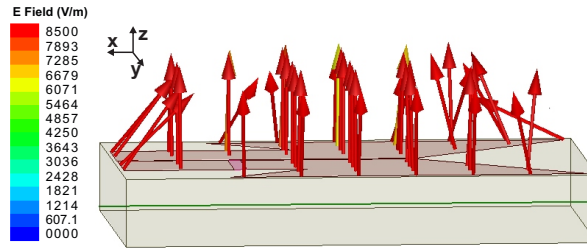
(a) EF distribution at n=0 mode
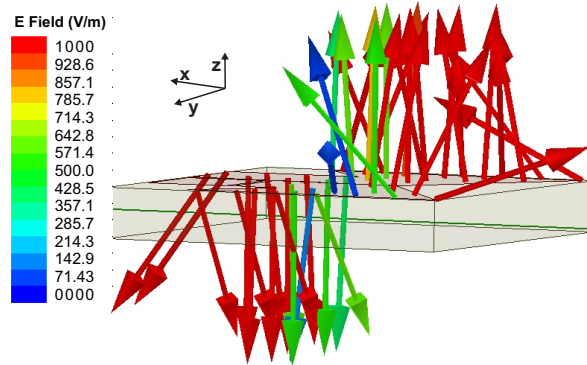
(b) EF distribution at n=+1 mode

Fig. A.6 Vector electric field distribution of modified bowtie antenna for two modes of operation; Bl=11mm, Fl=8.4mm, Sl=4mm, Sw=3mm, Sg=0.2mm, Iw=0.3mm, h=1.6mm, L=11.1mm, W=12mm

as in Fig. A.6a. This verifies the infinite wavelength resonance condition [16, 17]. While at 9.15GHz (n=+1) the electric field is sinusoidally distributed and are out of phase corresponding to a half-wavelength, as in Fig. A.6b. This shows the right-handed wave propagation through the structure.
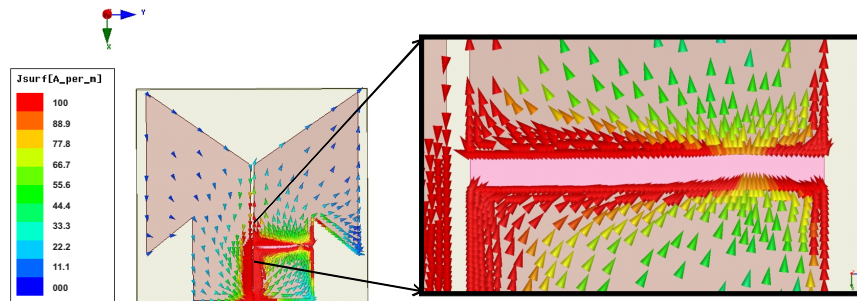

Fig. A.7 Surface current distribution at 503MHz; Bl=11mm, Fl=8.4mm, Sl=4mm, Sw=3mm, Sg=0.2mm, Iw=0.3mm, h=1.6mm, L=11.1mm, W=12mm

The surface current distribution on the antenna at 503MHz is depicted in Fig. A.7. It is found that the surface current at the slot edges are anti-parallel to each other. So an inductor placed across that slot have a shunt effect which makes the chip inductor to represent the shunt inductance (L_L) in the equivalent model of the antenna.
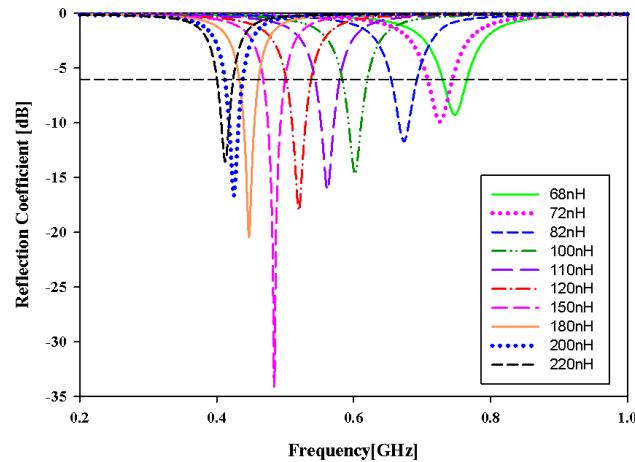

Fig. A.8 Resonant frequency variation with chip inductor value; Bl=11mm, Fl=8.4mm, Sl=4mm, Sw=3mm, Sg=0.2mm, Iw=0.3mm, h=1.6mm, L=11.1mm, W=12mm

Rigorous parametric analysis has been conducted to find out the effect of various antenna parameters on the radiation performance. Fig. A.8 shows the variation of the resonant frequency with the value of chip inductor. The resonant frequency does decrease with increased inductance value, while the antenna size is maintained the same. The resonant frequency is inversely proportional to the square root of the chip inductance. The effect of flare length(Fl), strip gap(Sg) & strip width(Sw) on the resonant characteristics are shown in Fig. A.9a, A.9b & A.9c respectively. A lowering in the resonant frequency is obtained when C_R and C_g is increased, which is accomplished by an increase in strip width and/or decrease in strip gap. But this will lead to the re-fabrication of the whole structure. Instead resonant frequency can be tuned by simply changing the value of chip inductor.

The measured radiation pattern of the modified zeroth order bowtie antenna is shown in Fig. A.10a & A.10b. An omni-directional radiation pattern is obtained

(a) Varying flare length

(b) Varying strip gap

(c) Varying strip width
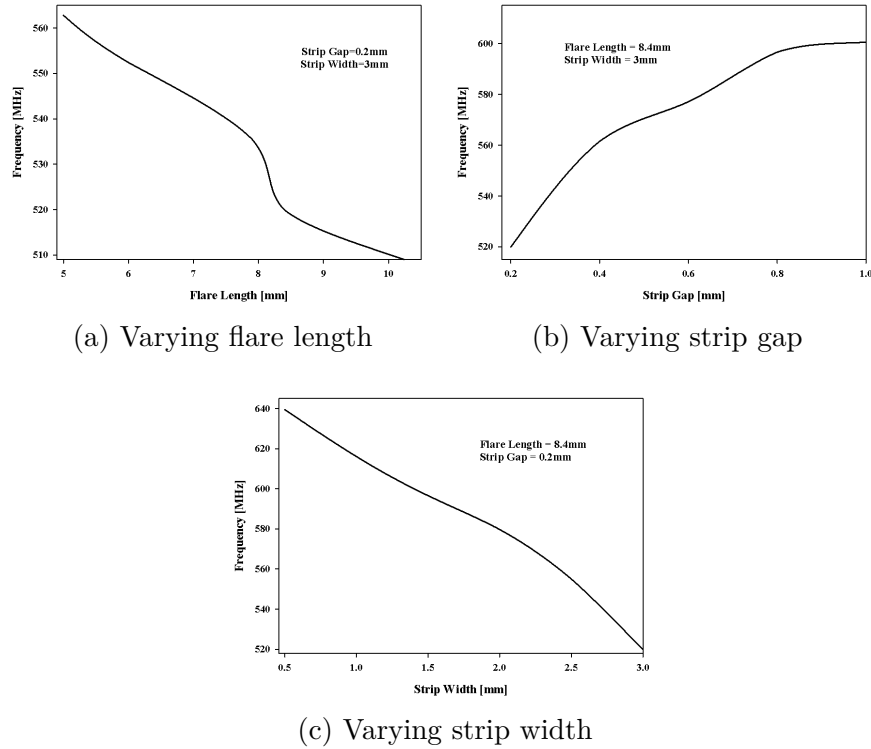
Fig. A.9 Change in reflection coefficient of the modifies bowtie antenna while varying various parameters; Bl=11mm, Sl=4mm, Iw=0.3mm, h=1.6mm, L=11.1mm, W=12mm

at the zeroth order frequency (503 MHz), since the electric field distribution for n=0 mode does not change much within the bandwidth. The monopolar radiation is maintained over the bandwidth. The cross polarization level for E-plane is 12.8dB and for the H-plane it is 12.5dB. The measured peak gain of the antenna using three antenna method is -9.2dBi and measured radiation efficiency using Wheeler Cap method [21] is 37% at 503 MHz. Both the gain and radiation efficiency stands within the DVB-H specification [22]. The physical area of a circular patch antenna fabricated on the same substrate and operating at the same frequency is 15836.76 mm^2, while that of the proposed antenna is only 133.2 mm^2. Thus a 99.1% reduction in the overall physical area of the structure is obtained compared to circular patch antenna.

(a) E-Plane   (b) H-Plane
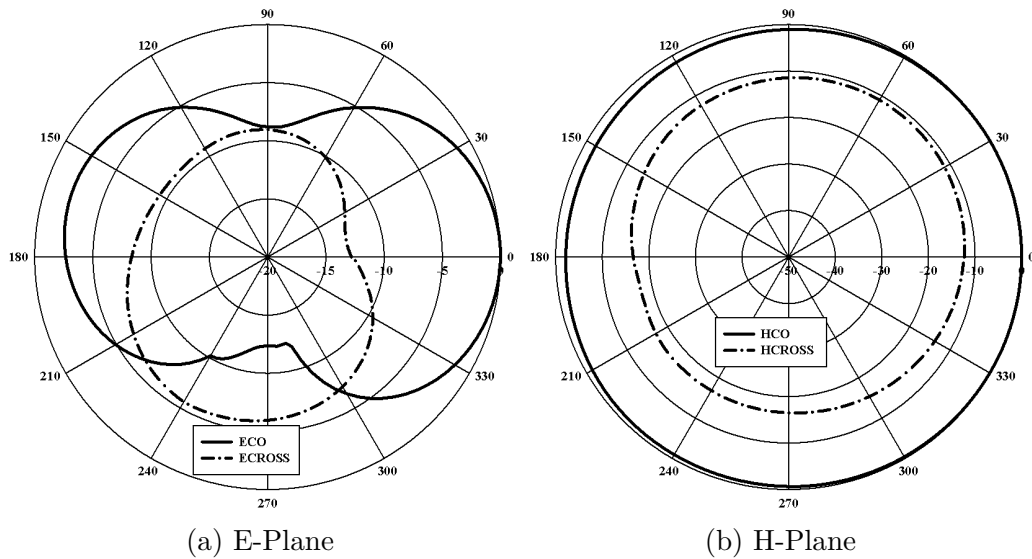
Fig. A.10 Measured radiation pattern of modified bowtie antenna at 503 MHz; Bl=11mm, Fl=8.4mm, Sl=4mm, Sw=3mm, Sg=0.2mm, Iw=0.3mm, h=1.6mm, L=11.1mm, W=12mm

A.4   Summary

In this chapter a novel low profile, extremely compact, zeroth order bowtie antenna for DVB-H application, with less structural complexity is presented. By loading a chip inductor on one of the bowtie strip a lower resonance independent of the antenna size is obtained. A 99.1% of overall size reduction is achieved as compared to a conventional circular patch antenna operating at the same frequency. The operating principle of the antenna is explained in terms of circuit parameters. The antenna exhibits a zeroth order resonance at 503MHz with -35 dB reflection coefficient and has 3:1 VSWR bandwidth of 39MHz with a gain of -9.2dBi and radiation efficiency of 37% which are in agreement with the DVB-H specification.

References

[1] J. Xiong, Z. Ying, and S. He, "A broadband lowprofile patch antenna of compact size with three resonances," *IEEE Trans. Antennas Propag.*, Vol. 57, No. 6, pp. 1838—1843, Jun. 2009.

[2] O. Kramer, T. Djerafi, and K. Wu, "Vertically multilayer-stacked Yagi antenna with single and dual polarizations," *IEEE Trans. Antennas Propag.*, Vol. 58, No. 4, pp. 1022—1030, Apr. 2010.

[3] M. Z. Azad and M. Ali, "A miniature implanted inverted-F antenna for GPS application," *IEEE Trans. Antennas Propag.*, Vol. 57, No. 6, pp. 1854-–1858, Jun. 2009.

[4] D. D. Krishna, M. Gopikrishna, C. K. Aanandan, P. Mohanan, and K. Vasudevan, "Compact wideband Koch fractal printed slot antenna," *Microw. Antennas Propag.*, Vol. 3, No. 5, pp. 782-–789, 2009.

[5] A. Sanada, C. Caloz, and T. Itoh, "Characteristics of the composite right/left-handed transmission line," *IEEE Microw. Wireless Compon. Lett.*, Vol. 14, No. 2, pp. 68-–70, Feb. 2004.

[6] C. Caloz and T. Itoh, "Electromagnetic metamaterials: transmission line theory and microwave applications: the engineering approach, 2006," *Wiley-IEEE Press*, USA, 2006.

[7] W. Liu, Z. Zhang and Z. Feng, "A bidirectional circularly polarized array of the same sense based on crlh transmission line," *Progress In Electromagnetics Research*, Vol. 141, pp. 537–552, 2013.

[8] A. Rennings, T. Liebig, S. Abielmona, C. Caloz, and P. Waldow, "Triband and dual-polarized antenna based on composite right/left-handed transmission line," *Proceedings of 37th Eur. Microw. Conf.*, Munich, pp. 720—723, 9–12 Oct. 2007.

[9] C. J. Lee, K. M. K. H Leong, and T. Itoh, "Compact dual-band antenna using an anisotropic metamaterial," *Proc. 36th Eur. Microw. Conf.*, Manchester, pp. 1044—1047, 10–15 Sept. 2006.

[10] J. G. Lee and J. H. Lee, "Zeroth order resonance loop antenna," *IEEE Trans. Antennas Propag.*, Vol. 55, No. 3, pp. 994–997, Mar. 2007.

[11] A. Sanada, M. Kimura, I. Awai, C. Caloz, and T. Itoh, "A planar zerothorder resonator antenna using a left-handed transmission line," *Proc. 34th Eur. Microw. Conf.*, Amsterdam, Vol. 3, pp. 1341–1344, 12–14 Oct. 2004.

[12] A. Lai, C. Caloz and T. Itoh, "Composite Right/Left-Handed transmission line metamaterials," *IEEE Microwave Mag.*, Vol. 5, No. 3, pp. 34–50, Sept. 2004.

[13] K. Wong and S. Chen, "Printed single-strip monopole using a chip inductor for penta-band WWAN operation in the mobile phone," *IEEE Trans. Antennas Propag.*, Vol. 58, No. 3, pp. 1011—1014, Mar. 2010.

[14] T. Kang and K. Wong, "Chip-inductor-embedded small-size printed strip monopole for WWAN operation in the mobile phone," *Microw. Opt. Technol. Lett.*, Vol. 51, No. 4, pp. 996-–971, Apr. 2009.

[15] A. A. Eldek, A. Z. Elsherbeni, and C. E. Smith, "Wideband microstrip-fed printed bow-tie antenna for phased-array systems," *Microwave and Optical Technology Letters*, Vol. 43, No. 2, pp. 123-–126, Oct. 2004.

[16] W. Han, J. Zhao, and Y. Feng, "Omni-directional microstrip ring antenna based on a simplified left-handed transmission line structure," *International symposium on Biophotonics, Nanophotonics and Metamaterials, 2006*, Hangzhou, pp. 455–458, 16–18 Oct. 2006.

[17] A. Lai, S. Member, K. M. K. H. Leong, and T. Itoh, "infinite wavelength resonant antenna With Monopolar Radiation Pattern Based on Periodic Structures," *IEEE Trans. Antennas Propag.* Vol. 55, No. 3, pp. 868-–876, Mar. 2007.

[18] R. E. Collin and S. Rothschild, "Evaluation of antenna Q," *IEEE Transactions on antennas and propagation*, Vol. 12, No. 1, pp. 23-27, Jan. 1964.

[19] A. Sanada, K. Murakami, S. Aso, and H. Kubo, "A Via-Free Microstrip Left-Handed Transmission Line," *Microwave Symposium Digest, 2004 IEEE MTT-S International*, Texas, Vol. 1, pp. 301–304, 6–11 June 2004.

[20] G. N. Satish, K. V Srivastava, A. Biswas, and D. Kettle, "A via-free left-handed Transmission Line with Radial Stubs," *Microwave Conference, 2009. APMC 2009. Asia Pacific*, Singapore, pp. 2501–2504, 7–10 Dec. 2009.

[21] H. Choo, R. Rogers, and H. Ling, "On the wheeler cap measurement of the efficiency of microstip antennas," *IEEE Trans. Antennas Propag.*, Vol. 53, No. 7, pp. 2328-–2332, Jul. 2005.

[22] ETSI, TR 102 377, "Digital Video Broadcasting (DVB); DVB-H Implementation Guidelines," V1.2.1 (2005-11).

Appendix B

A Compact Coplanar Stripline fed Antenna for Wireless Applications

Recently, owing to rapid developments in WLAN and ISM communications, high gain compact planar antennas operating in 5-6 GHz band are becoming demanding in practical applications. The United States Federal Communication Commission (FCC) has allocated new frequency bands in the 5-6 GHz range under the Unlicensed National Information Infrastructure (U-NII) for high speed WLAN at low cost. Among the IEEE 802.11 group, IEEE 802.11a uses the U-NII band. The U-NII operates over four frequency ranges and they are named as U-NII Low (U-NII-1): 5.15-5.25 GHz, U-NII Mid (U-NII-2): 5.25-5.35 GHz, U-NII Worldwide (U-NII-2e): 5.47-5.725 GHz and U-NII Upper (U-NII-3): 5.725-5.825 GHz [1]. ISM 5.8 uses the U-NII Upper band. On the other hand the HIPERLAN2 specifies two bands of 5.15-5.35 GHz and 5.47-5.725 GHz [2–4].

Combining resonant structures with microstrip line slot antennas for efficient radiation in some desired bands has been studied before [?]. In [13], a wideband rectangular slot antenna with U-shaped strip for WLAN application is presented. The overall size of this antenna is 75×75 mm^2 and is not well suited for practical applications. Another multiband antenna with U-shaped resonator is presented in [14]. It has a moderate gain and a high dielectric constant of 10 is needed to improve broadband matching. A wideband packaged antenna

that can support the IEEE 802.11a WLAN bands is presented in [15]. But its fabrication is arduous and also the peak gain is only 1.8dBi. Whereas [16] proposes coplanar waveguide fed slot antenna with high gain in spite of its low bandwidth performance. In addition, due to steady growth of wireless communication systems, antenna providing more operational bandwidth with high gain has been considered crucially. In this chapter a novel, open stub loaded planar antenna which meets the bandwidth requirements of many application bands, while belonging to the class of simply-structured and compact coplanar strip fed antennas. In the proposed antenna the actual radiation element is the arc shaped structure and hence it excites the un-guided mode of propagation. An open stub of length $\lambda_g/4$ is used for impedance matching. To reduce the overall size of the antenna a slanted stub is used in this study. The antenna has a 2:1 VSWR bandwidth of 23.6% from 4.6-5.38 GHz covering IEEE 802.11a (5.15-5.35 GHz, 5.725-5.825 GHz), HIPERLAN2 (5.45-5.725 GHz), HiSWANa (5.15-5.25 GHz), WiMAX (5.25-5.83 GHz) and ISM 5.8 (5.725-5.825 GHz) communication bands.
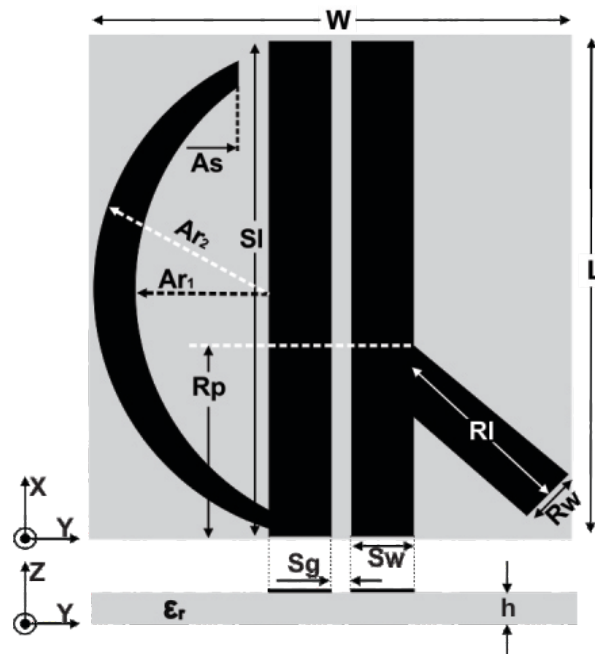

Fig. B.1 Geometry of the proposed antenna; W=23mm, L=24mm, Sl=24mm, Sg=1mm, Sw=3mm, Rl=8.85mm, Rw=2.83mm, Rp=9.25mm, Ar_1=6.5mm, Ar_2=8.5mm, As=1.5mm, h=1.6mm

B.1 Antenna geometry

Fig. B.1 depicts the geometry of the proposed antenna and its optimized parameters. The arc shaped strip of radius Ar_1, at the left side of the coplanar strip is employed to produce the resonance between 5-6 GHz, while a quarter wave $(\lambda_g/4)$ open stub connected to the right side of the coplanar strip improves the impedance matching for the above produced resonance. The open stub of size $Rl \times Rw$ is placed at a distance $\lambda_g/4$ away from the feed point in X-direction to obtain adequate impedance matching. Stripline gap (Sg) and stripline width (Sw) is optimized for getting maximum impedance matching. The resonant frequency is inversely proportional to the stripline length as expected. The prototype is fabricated on a FR-4 substrate of relative permittivity (ϵ_r) 4.4 and loss tangent $(tan(\delta))$ 0.02. The antenna requires a small footprint of $24mm \times 23mm \times 1.6mm$ only and is fed by a 50Ω coaxial cable.
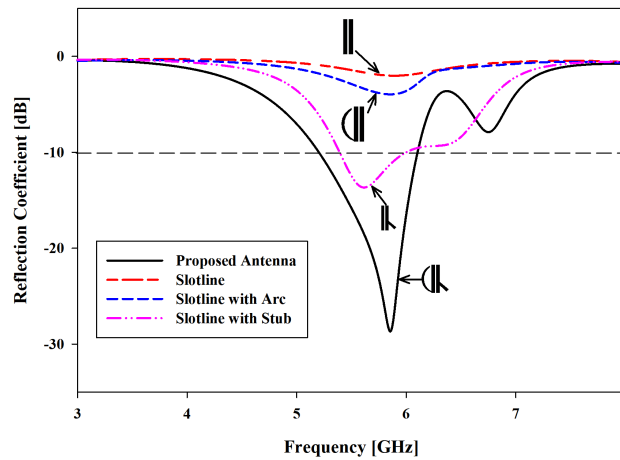

Fig. B.2 Simulated reflection characteristics of different antenna structures

B.2 Results and Discussion

The stub loaded asymmetric coplanar stripline antenna is simulated using Ansoft HFSS. Various parameters of the proposed antenna are optimized to obtain the resonance in the above mentioned application bands. The variation in the

reflection coefficient with the evolution of the present antenna from the guided coplanar stripline is shown in Fig. B.2. It is clear from figure that the conventional coplanar stripline antenna hardly has a resonance in the 5-6 GHz band, while by introducing an arc on the left side, the resonance in the 5-6 GHz band has been introduced, with poor impedance matching. The bandwidth improvement with better impedance match is achieved by inserting a slanted quarter wave ($\lambda_g/4$) open stub on the right side of the coplanar stripline. The optimized design is fabricated and experimentally verified using Agilent PNA E8362B network analyzer.
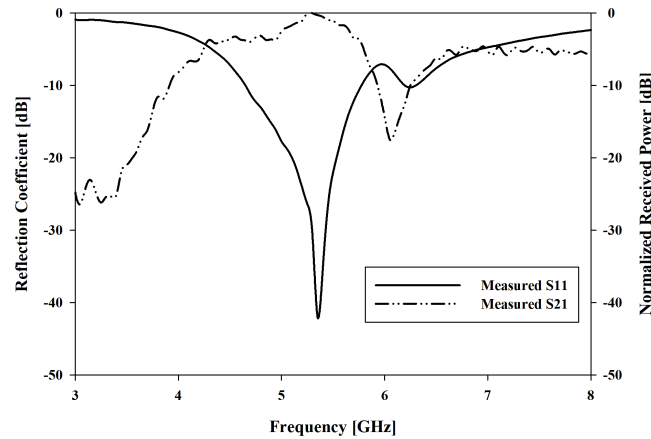
Fig. B.3 Measured reflection and radiation characteristics of the proposed antenna; W=23mm, L=24mm, Sl=24mm, Sg=1mm, Sw=3mm, Rl=8.85mm, Rw=2.83mm, Rp=9.25mm, Ar_1=6.5mm, Ar_2=8.5mm, As=1.5mm, h=1.6mm

Fig. B.3 depicts the measured reflection and radiation characteristics of the proposed antenna. It is evident from the graph that the proposed antenna can effectively operate over 4.6-5.83 GHz frequency band, with 2:1 VSWR bandwidth of 23.69% about the center frequency 5.35 GHz.

The influence of open stub position (Rp) and length (Rl) is exhibited in Fig. B.4a and B.4b, respectively. It is observed that the location of the stub has large influence on the impedance characteristics of the antenna. The stub should be placed at proper location at which the impedance is matched with 50Ω. Impedance matching of the antenna with the length of the stub is shown in Fig. B.4b. It is found that the position of open circuited $\lambda_g/4$ stub from the feed

(a) Open stub position (Rp)

(b) Open stub length (Rl)
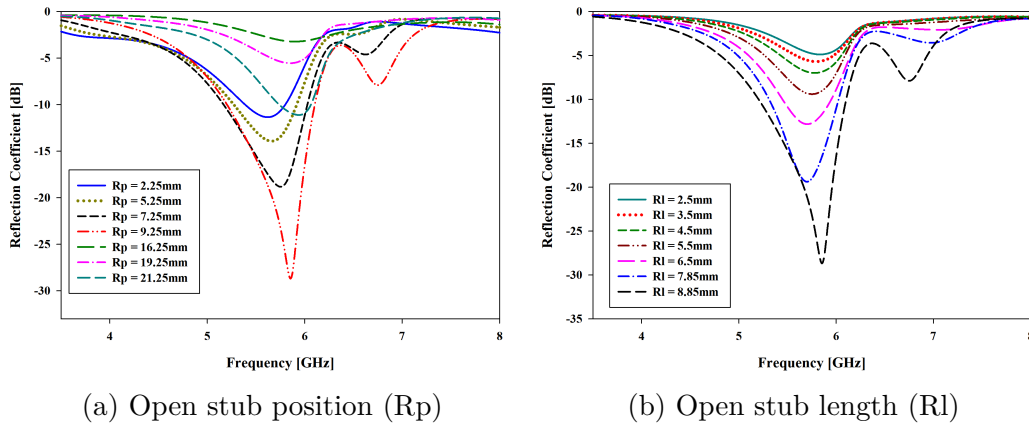
Fig. B.4 Change in reflection coefficient while changing the open stub parameters

should be around $\lambda_g/4$, where λ_g is the guided wavelength corresponding to the center frequency of the antenna.
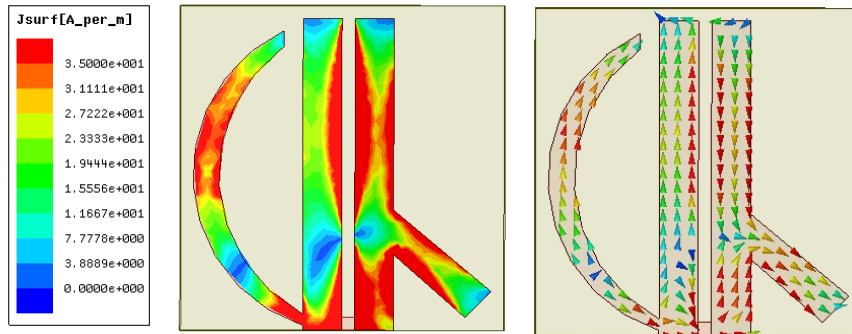
Fig. B.5 Surface Current Distribution of the antenna at 5.35 GHz; W=23mm, L=24mm, Sl=24mm, Sg=1mm, Sw=3mm, Rl=8.85mm, Rw=2.83mm, Rp=9.25mm, Ar_1=6.5mm, Ar_2=8.5mm, As=1.5mm, h=1.6mm

The surface current distribution of the proposed antenna at 5.35 GHz is illustrated in Fig. B.5. It is evident from the current density plot that the resonance at 5.35 GHz is due to the arc shaped strip.

Fig. B.6a and B.6b represents the measured radiation patterns at the center frequency. It is apparent that the radiation pattern is omni-directional in nature with reasonable cross polarization level in the proposed application band. The cross polarization level for E-plane (Y-Z plane) is 16dB and for H-plane (X-

(a) E-plane   (b) H-Plane
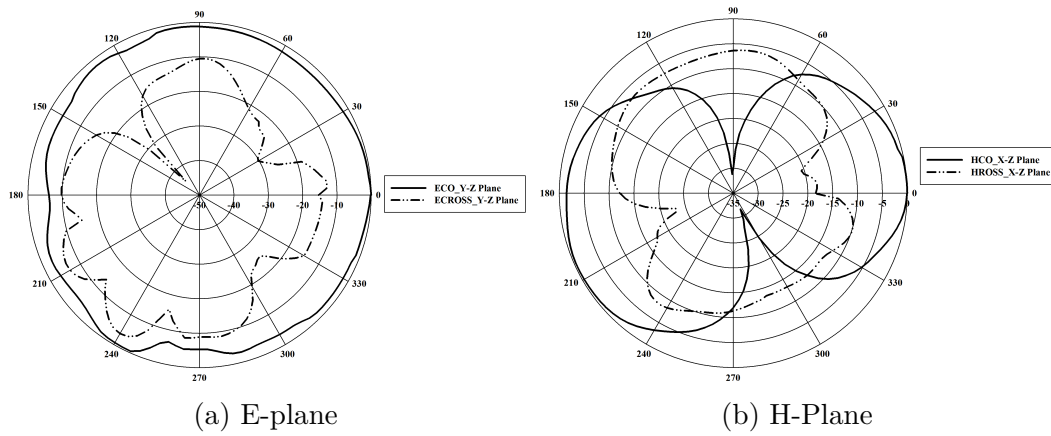
Fig. B.6 Measured radiation pattern of proposed antenna at 5.35 GHz

Z plane) is 19dB. A small tilt in the E-plane radiation pattern is due to the asymmetry of the structure.

(a) Gain   (b) Radiation Efficiency
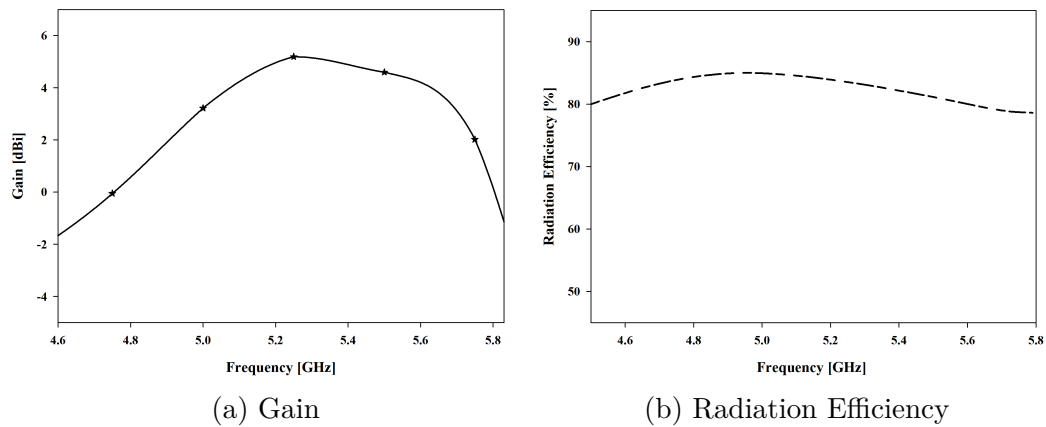
Fig. B.7 Measured gain and radiation efficiency of the proposed antenna

Measured gain and radiation efficiency of the proposed antenna is depicted in Fig. B.7a and B.7b, respectively. A high gain of 5.20dBi and a good radiation efficiency of 84.75% are obtained. The radiation efficiency is measured using Wheeler Cap Method [17]. The proposed antenna is small in size and provides high gain.

B.3   Summary

A novel open stub loaded asymmetric coplanar stripline antenna for wireless communication has been proposed and studied experimentally. With the use of an arc shaped strip and an open stub on either side of coplanar stripline, a 2:1 VSWR bandwidth of 23.69% is achieved. This is enough for covering IEEE 802.11a, HIPERLAN2, HiSWANa, WiMAX (IEEE 802.11e) and ISM 5.8 application bands. The proposed antenna also provides high gain and good radiation efficiency.

References

[1] S. Raghavan, T. Shanmuganantham, and M.S. Kishore Kumar, "Reconfigurable patch antenna with switchable L- shaped slots for circular polarization diversity," *Microwave Opt Technol Lett.*, Vol. 50, pp. 2348—2350, 2008.

[2] S. Raghavan, D. Sriram Kumar, and M.S. Kishore Kumar, "Reconfigurable patch slot antenna for circular polarization diversity," *Int J Microwave Opt Technol.*, Vol. 50, pp. 419—425, 2008.

[3] W. Diels, K. Vaesen, P. Wambacq, S. Donnay, W. Raedt, M. Engels, and I. Bolsens, "Single-package integration of RF blocks for a 5GHz WLAN application," *IEEE Trans Adv Packing.*, Vol. 24, pp. 384—391, 2001.

[4] F. Brauchler, S. Robertson, J. East, and L. P. B. Katehi, "W-band finite ground plane coplanar (FGC) line circuit elements," *1996 IEEE Int. Microwave Symposium Digest.*, San Francisco, CA, June 17—21, pp. 1845—1848, 1996.

[5] Y. Yoshimura, "A microstirpline slot antenna," *IEEE Trans Microwave Theory Tech 11.*, 760—762, 1972.

[6] T. Morioka, S. Araki, and K. Hirasawa, "Slot antenna with parasitic element for dual band operation," *Electron Lett 33*, pp. 2093—2094, 1997.

[7] J.-Y. Sze and K.-L. Wong, "Bandwidth enhancement of a microstrip-line-fed printed wide-slot antenna," *IEEE Trans Antennas Propag* , pp. 1020—1024, 2001.

[8] S.-Y. Lin and K.-L. Wong, "A dual-frequency microstrip-line-fed printed slot antenna," *Microwave Opt Technol Lett*, 28, pp. 373—375, 2001.

[9] A. Buerkle, K. Sarabandi, and H. Mosallaei, "Compact slot and dielectric resonator antenna with dual-resonance, broadband characteristics," *IEEE Trans Antennas Propag*, 53, pp. 1020—1027, 2004.

[10] G. Khunead, J. Nakasuwan, N. Songthanapitak, and N. Anantrasirichai, "Investigate rectangular slot antenna with L-shape strip," *PIERS Online*, Vol. 3, pp. 1076—1079, 2007.

[11] F.-T. Zha, S.-X. Gong, G. Liu, H.-Y. Yang, and S.-G. Lin, "Compact slot antenna for 2.4 GHz/UWB with dual band-notched characteristic," *Microwave Opt Technol Lett*, Vol. 51, pp. 1859—1862, 2009.

[12] R. Fallahi, A. A. Kalteh, and M. G. Roozbahani, "A novel UWB elliptical slot antenna with band-notched characteristics," *Prog Electromagn Res.*, Vol. 82, pp. 127—136, 2008.

[13] J.-W. Wu, H.-M. Hsiao, J.-H. Lu, and S.-H. Chang, "Dual broadband design of rectangular slot antenna for 2.4 and 5 GHz wireless communication," *Electron Lett.*, Vol. 40, pp. 1461—1463, 2004.

[14] R. Flores-Leal, "Reduced microstrip slot multiband antenna with AU-shaped resonator for wlan applications," *Microw. Opt. Technol. Lett.*, Vol. 54, pp. 2684—2689, 2012.

[15] M. Ali, T. Sittironnarit, H.-S. Hwang, R. a. Sadler, and G. J. Hayes, "Wide-Band/Dual-Band Packaged Antenna for 5–6 GHz WLAN Application," *IEEE Trans. Antennas Propag*, Vol. 52, No. 2, pp. 610—615, Feb. 2004.

[16] T. Shanmuganantham, and S. Raghavan, "NOVEL PRINTED CPW-FED SLOT ANTENNA FOR WIRELESS," *Microwave Opt Technol Lett*, Vol. 52, No. 6, pp. 1258—1261, 2010.

[17] H. Choo, R. Rogers, and H. Ling, "On the wheeler cap measurement of the efficiency of microstip antennas," *IEEE Trans. Antennas Propag.* Vol. 53, No. 7, pp. 2328—2332, Jul. 2005.

Resume of the Author

T K Roshna
Senior Research Fellow
Department of Electronics
Cochin University of Science and Technology
Kerala, India
E-mail : roshnatk03@gmail.com

Summary

- **6 years** of research experience in microwave communication field
- **Publications-30; International journals-14; Conferences-16**
- Proficiency in **Design and Development of Multiple-Input Multiple-Output antennas**
- Proficiency in **Time and frequency domain analysis of Ultra Wide-Band antennas**
- Proficiency in **conducting Finite Difference Time Domain analysis**

Honours, Awards & Achievements

- Qualified **National Eligibility Test (NET)** for lectureship by University Grants Commission (UGC) Government of India
- Awarded **Junior Research Fellowship** by Kerala State Council for Science, Technology and Environment (KSCSTE), Government of Kerala.
- **University First Rank Holder** in M Sc. Electronics from Cochin University of Science and Technology, Kochi, Kerala
- Qualified **DAT 2009** of Cochin University of Science and Technology
- **University First Rank Holder** in B Sc. Electronics from University of Calicut, Kozhikode, Kerala

Areas of Interest

Ultra WideBand (UWB) antennas, Multiple-Input Multiple Output (MIMO) antennas, FDTD, Filters, Reconfigurable antennas, RF Circuits, Implantable and Wearable antennas, Electrically small antennas, Zeroth Order Antennas, RFID, Microwave Sensors etc.

Technical Skills

- Have a good hands on experience with Vector Network Analyzers like HP 8510C, Agilent PNA E8362B & R&S ZVB20 and Anritsu Spectrum Analyzer. Have conducted measurements like S parameters and far field characteristics of antennas inside Anechoic chamber.

- Familiar with various Antenna and RF/Microwave circuit design tools like Ansys HFSS, CST MWS, Agilent ADS, EMPro etc.

- Gained six years of experience in using FEM based high frequency simulation software HFSS from Ansys for the analysis and design of many single band, multi band and wide band MIMO antennas. The optimization of antennas have been carried out using the parametric analysis of HFSS. HFSS has been extensively used for the scattering and far field analysis of antennas. Scattering analysis is conducted in HFSS while designing the stepped impedance resonator and RFIDs, and Eigenmode analysis is extensively used for the characterisation of the unit cells of periodic structures while finding the dispersion diagram. It is also used for the design and analysis of a dielectric based biomedical sensor. Well experienced in using different types of excitations in HFSS.

- Experienced in microwave absorption studies, material characterisation and cavity perturbation method

- Involved in the design and analysis of different types of antennas for Ultra wideband communication, RFID and for MIMO, ISM, DVB-H, High gain and WLAN applications

- Involved in the designing of biomedical sensor for the measurement of blood sugar based on dielectric resonator.

- Hands-on experience in antenna prototyping using photolithography and CNC tool.

- Experienced in FDTD analysis and Image processing

- Experienced in RADAR Cross Section (RCS) Measurements

- Experienced in programming with languages like, C, C++, Python, Matlab etc

Scholarly work and services

- Active member in IEEE Antenna Propagation Society & IEEE Women In Engineering.

- Member, Organizing Committee, Antennas and Propagation Symposium (APSYM), 2010

- Member, Organizing Committee, International Symposium on Ocean Electronics (SYMPOL) 2011

- Member, Organizing Committee, Antennas and Propagation Symposium (APSYM), 2012
- Member, Organizing Committee, International Symposium on Ocean Electronics (SYMPOL) 2013
- Member, Organizing Committee, Antennas and Propagation Symposium (APSYM), 2014
- Member, Organizing Committee, International Symposium on Ocean Electronics (SYMPOL) 2015
- Actively engaged in organizing various events and workshops
- Attended National and International Conferences and presented research papers

Work experience including research projects

2007-2008: **Device Switching using password:** Successfully developed a PIC microcontroller based system to switch ON/OFF devices using password

2008-2009: **ZigBee based vehicle speed governing system:** A device which is used to govern the speed of the vehicle through ZigBee communication

2010-2011: **Near Field to Far Field Transformation:** Developed a GUI to derive the far field data from the measured near field electric field data

2011-2012: **Worked as a guest lecturer and a project trainee:** This gave a proficient lecturing ability and a good exposure in the image processing area, dealing with Iris detection, Finger print detection and Steganography using wavelet . This was so helpful in improving my team-leading & leadership qualities, since I got chances to conduct laboratory works and lead few modules of the project

2012-Present: **Pursuing PhD,** at Centre for Research in Electromagnetics and Antennas (CREMA), Cochin University of Science and Technology, India - working on the design, development and analysis of Ultra wideband Multiple-Input Multiple-Output antennas. The Ph.D. work is nearing completion. Meanwhile I am also involved in the design and development of Electrically small antennas, zeroth order antennas, high gain antennas, circularly polarized antennas and Chip less RFID tags, which are booming technologies of the current era.

Education

2012– ongoing **Pursuing PhD**, *From Department of Electronics, Cochin University of Science and Technology*, Kerala, India, .
Specialized in UWB-MIMO antennas

2009–2011 **Master of Science(M.Sc)**, *From Department of Electronics, Cochin University of Science and Technology*, Kerala, India, .
Specialized in Electronics

2006–2009	**Bachelor of Science (B.Sc)**, *From Calicut University*, Kerala, India, . Specialized in Electronics
2004–2006	**Higher Secondary: MCC HSS**, *Kerala Board of Higher Secondary Education*, Medical College Campus Higher Secondary School,Chevayur, Kerala , India, .
2003-2004	**Tenth: Chinmaya Vidhyalaya HSS**, *Kerala Board of Secondary Education*, Chinmaya Vidhyalaya Higher Secondary School, Thondayad, Kerala, India, .

Personal Vitae

Date Of Birth	03.09.1988
Gender	Female
Blood Group	B positive
Marital Status	Married
Nationality	Indian
Address	28/2701-C, Roshvilla
	Mythrinagar
	Nellicode P. O.
	Kozhikode-673016, Kerala
	India.

List of Publications

International Journals

1. **T. K. Roshna**, U. Deepak, V. R. Saijtha, K. Vasudevan and P. Mohanan, "Modified Bowtie Antenna for Zeroth Order Resonance", *Progress In Electromagnetics Research C*, Vol. 48, pp 45-52, 2014.

2. **T. K. Roshna**, U. Deepak, Nijas C. M., Sajitha V. R. and Mohanan P., "A high gain Compact Coplanar Stripline fed Antenna for Wireless Application", *Microwave and Optical Technology Letters* , Vol. 56, No. 8, August 2014.

3. **T. K. Roshna**, U. Deepak, V. R. Sajitha, and P. Mohanan, "A coplanar stripline fed compact UWB antenna", *Electronics Letters*, vol. 50, no. 17, pp. 1181-1182, Aug. 2014.

4. **T. K. Roshna**, U. Deepak, V. R. Sajitha, K. Vasudevan, and P. Mohanan, "A Compact UWB MIMO Antenna with Reflector to Enhance Isolation", *IEEE Transactions on Antennas and Propagation*, Vol. 63, No. 4, pp. 1873-1877, Jan. 2015.

5. **T. K. Roshna**, U. Deepak, and P. Mohanan, "A coplanar stripline fed compact UWB antenna", *Elseiver Procedia Computer Science*, Vol. 46, pp. 1365-1370, 2015.

6. **T. K. Roshna**, U. Deepak, V. R. Sajitha and P. Mohanan, "An ACS-fed Compact Antenna for UWB Applications", *International Journal of Advances in Microwave Technology (IJAMT)*, Vol. 1, No. 1, May 2016.

7. **T. K. Roshna**, U. Deepak and P. Mohanan, "Compact UWB MIMO antenna for tridirectional pattern diversity characteristics", *IET Microwaves, Antennas & Propagation*, Vol. 11, No. 14, Dec 2017.

8. U. Deepak, **T. K. Roshna**, C. M. Nijas, and P. Mohanan, "Compact CPW fed electrically small antenna for WLAN application", *Electronics Letters*, vol. 50, no. 2, pp. 62-64, Jan. 2014.

9. S Mathew, R Anitha, **T. K. Roshna**, C. M. Nijas, C. K. Aanandan, P. Mohanan, and K. Vasudevan, "A Fan-Shaped Circularly Polarized Patch Antenna for UMTS Band", *Progress In Electromagnetics Research C*, Vol. 52, pp. 101-107, 2014.

10. U. Deepak, **T. K. Roshna**, C. M. Nijas, K. Vasudevan, and P. Mohanan, "A Dual Band SIR Coupled Dipole Antenna for 2.4/5.2/5.8 GHz Applications", *IEEE Transactions on Antennas and Propagation*, Vol. 63, No. 4, pp. 1514-1520, Jan. 2015.

11. V. R. Sajitha, C. M. Nijas, **T. K. Roshna** and P. Mohanan, "Compact Chip Inductor Loaded multiband Antenna," *European Journal of Advances in Engineering and Technology (EJAET)*, Vol. 2, No. 4, 2015.

12. V. R. Sajitha, C. M. Nijas, **T. K. Roshna**, R. Vivek, K. Vasudevan and P. Mohanan "Polarization Independent Chipless RFID Tag", *Microwave and Optical Technology Letters* , Vol. 57, No. 8, August 2015.

13. U. Deepak, **T. K. Roshna**, and P. Mohanan, "A Dual Band SIR Coupled Dipole Antenna for 2.4/5.2/5.8 GHz Applications", *Elseiver Procedia Computer Science*, Vol. 46, pp. 1311-1316, 2015.

14. V. R. Sajitha, C. M. Nijas, **T. K. Roshna**, K. Vasudevan and P. Mohanan "Compact cross loop resonator based chipless RFID tag with polarization insensitivity", *Microwave and Optical Technology Letters* , Vol. 58, No. 4, April 2016.

Conference papers

1. U. Deepak, **T. K. Roshna**, C. M. Nijas, R. Dinesh, and P. Mohanan, "Compact CPW fed ZOR antenna for WLAN application," 2013 IEEE Antennas Propag. Soc. Int. Symp., pp. 984-985, Jul. 2013.

2. Deepak U., **T. K. Roshna**, Nijas C. M., Mohanan P., "An SIR loaded modified dipole antenna" IEEE XXXIth URSI General Assembly and Scientific Symposium (URSI GASS). 2014.

3. **T. K. Roshna**, Deepak U., Sujith R. and Mohanan P., "A high gain Compact Coplanar Stripline fed Antenna for Wireless Application", IEEE XXXIth URSI General Assembly and Scientific Symposium (URSI GASS). 2014.

4. U. Deepak, **T. K. Roshna**, C. M. Nijas, K. Vasudevan and P. Mohanan, "A Dual Band SIR Coupled Dipole Antenna for 2.4/5.2/5.8 GHz Applications", International Conference on Information and Communication Technologies (ICICT), Kerala, India, Dec. 2014.

5. **T. K. Roshna**, U. Deepak, and P. Mohanan, "A coplanar stripline fed compact UWB antenna", International Conference on Information and Communication Technologies (ICICT), Kerala, India, Dec. 2014.

6. U. Deepak, Susan Thomas, **T. K. Roshna** and P Mohanan, "A Compact ACS fed Electrically Small Antenna", Antennas and propagation Symposium (APSYM), Kerala, India. Dec. 2014.

7. U. Deepak, Susan Thomas, **T. K. Roshna** and P. Mohanan , "An Electrically Small ACS fed Compact Antenna ", Future of Electromagnetic Communication and Materials, SPECTRUM 2014 Proceedings, Kerala, India

8. **T. K. Roshna**, Deepak U. and Mohanan P , "A Coplanar Stripline fed High Gain Compact Antenna ", Future of Electromagnetic Communication and Materials, SPECTRUM 2014 Proceedings, Kerala, India.

9. U. Deepak, **T. K. Roshna**, V. R. Sajitha and P. Mohanan, "A Capacitively Coupled Meanderline Loaded Electrically Small Antenna ", Recent Advancements in Electronic Communication and Allied Areas Conference Proceedings, Kerala, India, 2015

10. **T. K. Roshna**, U. Deepak, V. R. Sajitha, Sumitha Mathew and P. Mohanan, "A Reflector based UWB MIMO Antenna", Antennas and propagation Symposium (APSYM), Kerala, India. Dec. 2014

11. **T. K. Roshna**, U. Deepak, V. R. Sajitha, Sumitha Mathew and P. Mohanan, "A Reflector based UWB MIMO Antenna", Antennas and propagation Symposium (APSYM), Kerala, India. Dec. 2014.

12. U. Deepak, **T. K. Roshna** and P. Mohanan, "An SIR excited ESA for 2.4 GHz band", Appied Electromagnetic Conference (AEMC) 2015.

13. **T. K. Roshna**, U. Deepak, V. R. Sajitha and P. Mohanan, "A 3 port UWB MIMO antenna with enhanced isolation", Appied Electromagnetic Conference (AEMC) 2015.

14. V. R. Sajitha, C. M. Nijas, **T. K. Roshna**, and P. Mohanan, âĂIJChipless RFID tag based on stepped impedance resonators," Antennas and propagation Symposium (APSYM), Kerala, India, Dec. 2014.

15. **T. K. Roshna**, U. Deepak and P. Mohanan, âĂIJA 4-port mimo antenna for high speed uwb applications," 28th Kerala Science Congress, University of Calicut, Thenhipalam, Malappuram, India, Jan. 2016.

16. **T. K. Roshna**, U. Deepak and P. Mohanan, "A Compact Coplanar 4-Port MIMO Antenna For High-Speed UWB Applications", International Conference on Electromagnetics in Advanced Applications and IEEE-APS Topical Conference on Antennas and Propagation in Wireless Communications (ICEAA & IEEE APWC 2016), Cairns, Australia, Sept. 2016.